MAGNETIC RESONANCE IMAGING STUDIES
OF
ANGIOGENESIS AND STEM CELL IMPLANTATIONS
IN
RODENT MODELS OF CEREBRAL LESIONS

Inaugural Dissertation

zur

Erlangung

des

Doktorgrades

der

Mathematisch-Naturwissenschaftlichen Fakultät

der

Universität zu Köln

vorgelegt von

Diplom Physiker

Philipp Böhm-Sturm

aus Tübingen

MAX-PLANCK-GESELLSCHAFT

Universität zu Köln

Max-Planck-Institut
für neurologische Forschung
Köln

Berichterstatter:	Prof. Dr. Peter Reiter
	PD Dr. Heike Endepols
	Prof. Dr. Michal Neeman

Tag der mündlichen Prüfung: 15. Januar 2013

Vorwort

Angiogenese ist das Neuwachstum von Gefäßen aus einem bereits existierenden Gefäßnetzwerk. Ein besseres Verständnis der Angiogenese könnte zu neuen Therapien zerebraler Läsionen führen, z.B. bei Tumorerkrankungen oder nach Schlaganfall. Ein weiterer Hoffnungsträger für die Regeneration geschädigten Hirngewebes sind transplantierte Stammzellen. Diese Dissertation handelt von der Entwicklung magnetresonanztomographischer Verfahren zur Bildgebung der Angiogenese und transplantierter Stammzellen. Sie ist vom 01. Oktober 2009 bis 31. Januar 2013 am Max-Planck-Institut für neurologische Forschung in Köln in der “In-Vivo-NMR” Gruppe von Prof. Dr. Mathias Hoehn entstanden unter der Betreuung von Prof. Dr. Peter Reiter von der Universität zu Köln. Die Arbeit wurde von der mathematisch-naturwissenschaftlichen Fakultät der Universität zu Köln zur Promotion angenommen. Die mündliche Prüfung erfolgte am 15. Januar 2013. Referenten waren Prof. Dr. Peter Reiter (1. Gutachter), PD Dr. Heike Endepols (2. Gutachter) und Prof. Dr. Michal Neeman (externer Gutachter).

Table of Contents

1 INTRODUCTION 7

1.1 ANGIOGENESIS 7

1.1.1 Angiogenesis in tumors 8

1.1.2 Angiogenesis after stroke 8

1.2 IMAGING ANGIOGENESIS 9

1.2.1 Overview 9

1.2.2 Steady state contrast enhanced MRI 9

1.3 NEURAL STEM CELLS 12

1.3.1 General properties 12

1.3.2 Neural stem cell implantation in the healthy and stroke-damaged brain 13

1.4 IMAGING IMPLANTED NEURAL STEM CELLS 14

1.4.1 Overview 14

1.4.2 Cell tracking with ^{1}H MRI 15

1.4.3 Cell tracking with ^{19}F MRI 17

1.5 AIMS OF THIS DISSERTATION 19

2 ORIGINAL PAPERS AND MANUSCRIPTS 21

3 DISCUSSION AND OUTLOOK 107

3.1 MRI OF ANGIOGENESIS 107

3.1.1 Biological aspects 107

3.1.2 Methodological aspects 108

3.2 MRI OF STEM CELL IMPLANTATIONS 114

3.2.1 Biological aspects 114

3.2.2 Methodological aspects 115

3.3 INTERACTIONS OF ANGIOGENESIS AND STEM CELLS AFTER CEREBRAL LESIONS 123

3.4 CONCLUSION 124

4 REFERENCES 125

5 SUMMARY/ZUSAMMENFASSUNG 139

5.1 SUMMARY 139

5.2 ZUSAMMENFASSUNG 141

6 APPENDIX 143

1 Introduction

One of the challenges of basic neurological research is to identify potential targets for treatment of diseases, for which little or no therapeutic options exist today. Examples are brain tumors, stroke, or aging-related diseases such as Alzheimer's or Parkinson's disease. A shift of paradigm has been proposed, motivated by advances in molecular biology, cellular biology, and genomics, towards manipulating the molecular and cellular events underlying the disease, which would be an appealing and efficient way of treatment. In this context, angiogenesis, i.e. the regrowth of new vessels from the existing vascular network, has been identified as a major player in the progression of brain tumors and, more recently, in regeneration after stroke. Another intriguing approach to treat cerebral lesions has been triggered by advances in stem cell research. Donation of stem cells to the damaged brain may help to replace damaged tissue or improve tissue at risk through release of protective factors.

However, before angiogenesis-targeted therapies and stem cell implantations can be used for the treatment of patients, their action and role need to be better understood in animal models of disease. Here, development of noninvasive imaging tools is of importance to better understand the spatio-temporal profile of pathophysiological processes in the individual animal and to have quantitative measures for the response to molecular/cellular therapy. In this dissertation, the potential of magnetic resonance imaging (MRI) to image angiogenesis and stem cell implantations is exploited. MRI is a particularly powerful modality due to its (i) noninvasiveness (non-ionizing radiation), (ii) high tissue penetration depth, (iii) high spatial resolution compared to most other imaging modalities, (iv) high flexibility in image generation, which can be optimized to visualize the tissue/biological process of interest, and (v) good scaling properties, i.e. many methods established in small animals can potentially be translated to humans.

In the following paragraphs, angiogenesis and its role in brain tumor and in ischemic stroke will be briefly introduced. Furthermore, basic terms used in stem cell research will be discussed including prospects of stem cell therapy of the central nervous system, particularly after stroke. Modalities that allow to image angiogenesis and implanted cells will be reviewed with a focus on MRI methods.

1.1 Angiogenesis

Angiogenesis is the growth of new vessels from an existing vascular network. Angiogenic processes are strictly regulated in the healthy adult brain but can be highly upregulated under pathological conditions such as ischemia, metabolic challenge, mechanical stress, or inflammation [1], [2]. The pathology leads to an imbalance of pro- and anti-angiogenic molecules towards the pro-angiogenic factors, the most prominent being vascular endothelial growth factor (VEGF-A) and its primary receptor VEGFR-2. Many more pro-angiogenic molecules have been identified including others of the VEGF family (VEGF-B to D, placenta growth factor PlGF, and VEGFR-1), fibroblast growth factor (aFGF, bFGF), transforming growth factor beta (TGF-β), neuropilins, angiopoietins (Ang-1 and 2) and their receptors Tie-1 and Tie-2, and erythropoietin (Epo). Upregulation of these molecules is often accompanied by downregulation of anti-angiogenic factors, e.g. thrombospondin and angiostatin [3], [4]. The imbalance of factors leads to destabilization of vessel walls and subsequent proliferation of endothelial cells, formation of microvessel branches, followed by stabilization of the new vessel walls, and finally perfusion of the newly formed vasculature [5]. The different stages of angiogenesis are illustrated in Fig. 1.

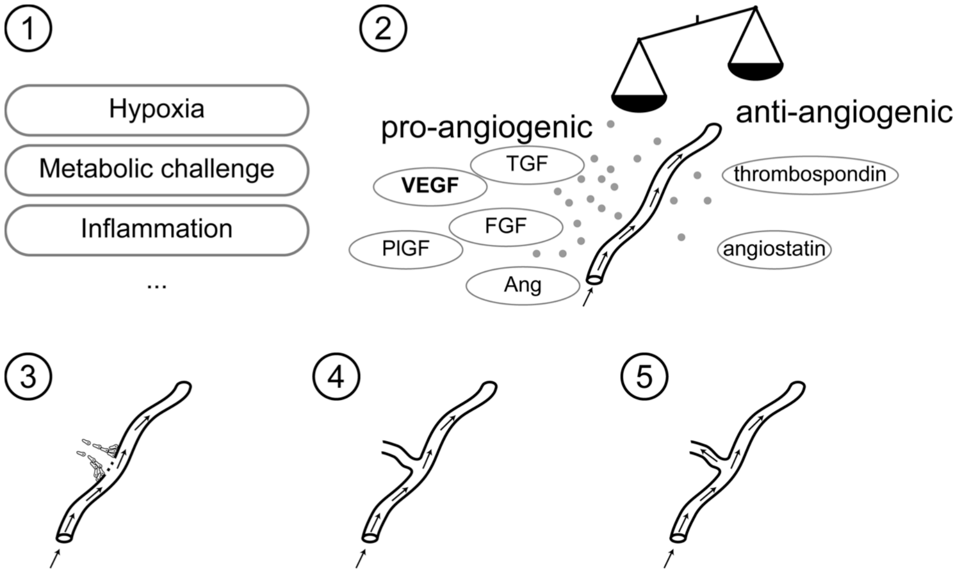

Figure 1: Angiogenesis in the adult brain. A pathological condition (1) can stimulate upgregulation of pro-angiogenic and downregulation of anti-angiogenic factors (2). Subsequently, vessels become permeable, endothelial cells start to proliferate and endothelial progenitor cells are recruited from the blood stream. Endothelial cells migrate and form new vascular buds (3). After stabilization of vessel walls (4) the newly formed vessel is perfused (5).

1.1.1 Angiogenesis in tumors

Small carcinomas are supplied with oxygen and nutrients by the already existing vasculature by diffusion through tissue. Even for strongly proliferating, i.e. very malignant tumor cells the high number of newly formed cells can for a long time be compensated by high number of cells undergoing apoptosis due to the lack of supporting vasculature. In this stage, tumor size is usually restricted to a few mm^3 [6]. For many tumor types, however, a part of the tumor cells can start to upregulate pro-angiogenic and downregulate anti-angiogenic factors, which leads to recruitment of new capillaries and allows the whole tumor to grow further. This “angiogenic switch” is a key step in the progression of primary tumors and metastases [7]. Its importance has triggered the development of substances for anti-angiogenic tumor therapies, mainly inhibitors of VEGF and its receptors [8], [9], which also holds for the drugs used in studies of this dissertation: Bevacizumab (commercial name Avastin, Roche) and PTK 787 (commercial name Vatalanib, Novartis). However, results in the clinic are variable. Unsolved problems include resistance, toxicity, or a change of tumor phenotype in response to therapy from angiogenic to infiltrative phenotype as seen for example in brain tumors [10], [11].

1.1.2 Angiogenesis after stroke

In an ischemic stroke, a blood clot blocks a supplying artery in the brain, which leads to decreased blood flow to brain tissue and finally to permanent cell loss and loss of function associated with the damaged area of the brain. The ischemia triggers a complex cascade of molecular events, some of which can promote angiogenesis [4], [12]. The most dominant contribution to angiogenesis is hypoxia in affected tissue, which induces stabilization of hypoxia-inducible transcription factor alpha (HIF-α) and subsequent upregulation of VEGF-A and its main receptor VEGFR-2. The time scale, by which upregulation of pro-angiogenic molecules and subsequent new vessel formation occur after ischemia, begins within a few hours after the infarct and cumulates over several days [4]. In 1994, Kuprinski and colleagues reported vessel sprouting and increased microvessel densities in the peri-infarct zone on post-mortem tissue of stroke patients, which was correlated with longer survival times [13]. Almost a decade later, the same group was then the first to detect angiogenesis after experimental stroke in rats using vascular casts and electron microscopy [14]. Since angiogenesis bears promise to restore blood flow to damaged, ischemic tissue, pro-angiogenic therapy of stroke has been under investigation in animal studies, e.g. by delivery of growth factors or cells [15], [16].

1.2 Imaging angiogenesis

1.2.1 Overview

Since angiogenesis is an important contributor to outcome in brain tumor and in stroke, the ability to examine this process noninvasively with imaging would be of great benefit. Imaging modalities to study the molecular events of angiogenesis (steps 1-2 of Fig. 1) include fluorescence, bioluminescence, or MR imaging of vessel-specific “reporter genes”, i.e. artificial proteins that are detectable by imaging and that are expressed only in presence of the specific molecule of interest. This requires however the generation of transgenic cells, thus is almost exceptionally applicable in animals due to safety issues. Permeability of vessels (step 3 of Fig. 1) can be detected with dynamic contrast enhanced MRI. A T_1 contrast agent (usually Gadolinium-based) is administered i.v. and leakage of the agent into the tissue is detected via decrease of the T_1 relaxation time. Perfused vessels (step 5 of Fig. 1) can be directly detected via angiography (MRI or computed tomography), by changes in perfusion (positron emission tomography, computed tomography, ultrasonography, dynamic susceptibility contrast MRI or arterial spin labeling techniques), by changes in blood volume (contrast-enhanced MRI), or by changes in blood oxygenation through the blood-oxygen-level dependent (BOLD) effect [17–20]. Again, MRI represents one of the most appealing modalities although the resolution is too low (~100 µm) to directly detect newly formed microvessels (~10 µm). Despite this drawback, important statistical microvessel characteristics can be calculated from MRI data by mathematical modeling of the vascular network. In this dissertation, steady-state contrast-enhanced MRI (SSCE MRI) was optimized and used to assess blood volume, mean vessel density, and mean vessel size. The mathematical model and experimental strategy underlying SSCE MRI are introduced in the next sections.

1.2.2 Steady state contrast enhanced MRI

Basic principle

The basic strategy of SSCE MRI is outlined in Fig. 2. The MRI signal from a vascular network is measured before injection of an intravascular contrast agent and again after the contrast agent is equilibrated in the blood (is in a steady state). A mathematical model can be used to predict the changes in MRI signal intensities, which generally depend on the geometry of the vascular network. If the model is bijective (i.e. forward and backward problem are solved unambiguously), measurements of MRI signal changes due to injection of the agent allow conclusions about vessel geometry. This can be used for biological applications. In the next section the most commonly used model of MRI signal in vasculature is introduced.

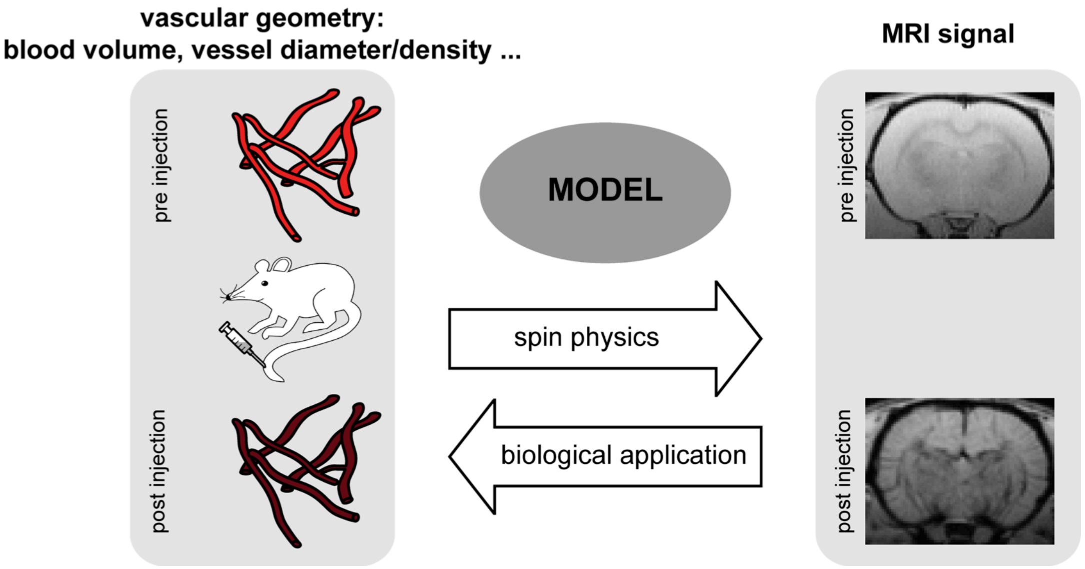

Figure 2: Basic principle of steady state contrast-enhanced MRI. A (super) paramagnetic contrast agent is injected into the blood pool and spreads homogeneously over the vascular network of a certain geometry (left). This leads to a change in MRI signal as shown here on representative coronal gradient echo images of a healthy rat brain before and after superparamagnetic iron oxide injection (right). The challenges are to find a good set of parameters describing the vascular geometry and to find a model, which not only quantifies the changes in MRI signal given the vascular geometry but also solves the inverse problem. This can be used to probe the vasculature with MRI in biological applications.

Cylinder model of the vasculature

In the cylinder model, tissue is assumed to consist of an intravascular compartment (blood) and an extravascular compartment (tissue), which exhibit a constant difference in magnetic susceptibility χ. Vessels are modeled as randomly distributed, infinitely long cylinders. Analytical expressions of the MR signal from a voxel were developed in the works of Haacke, Yablonskiy, Kiselev, and Posse by solving the Bloch/Bloch-Torrey differential equations for the case of one vessel and by averaging over all diffusion paths and possible vessel positions and radii [21–24]. The procedure is outlined for the extravascular signal in Fig. 3 along the lines of Kiselev and Posse [22]. Under certain assumptions, which will be discussed in more detail in chapter 3.1, the signal contribution of the cylinders can simply be described by shifts of relaxation rates, i.e. $1/T_2 = R_2 \to R_2 + \Delta R_2$ for the spin echo experiment and $1/T_2^* = R_2^* \to R_2^* + \Delta R_2^*$ for the gradient echo experiment. In other words, the signal post-injection is characterized by an additional monoexponential decay compared to the signal pre-injection $S_{post} = S_{pre} \cdot \exp(-B \cdot t); \quad B = \Delta R_2 / \Delta R_2^*$.

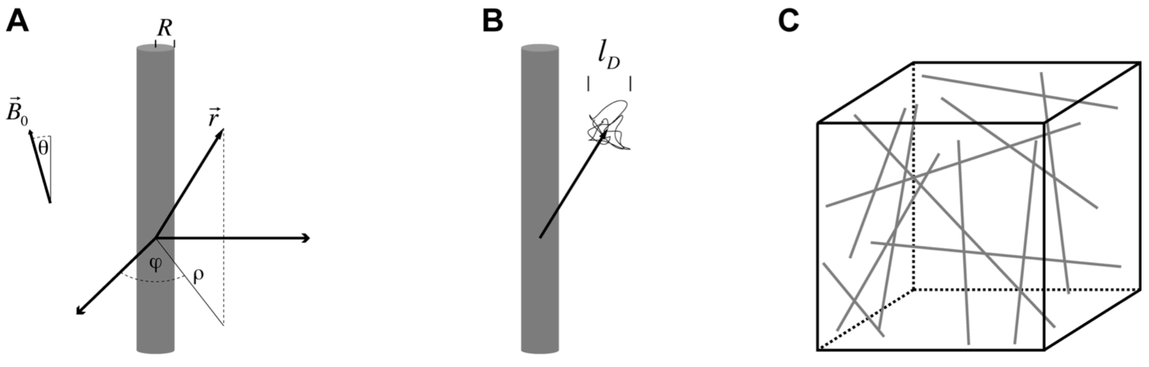

$$\omega(\vec{r}) = \omega_0 + 2\pi\gamma\chi B_0 \frac{R^2}{\rho^2}\cos 2\varphi \sin^2 \vartheta \qquad \Psi(\vec{r},t) = \exp\left\{-i\omega(\vec{r})t - \frac{D}{3}\left[\nabla\omega(\vec{r})\right]^2 t^3\right\} \qquad s(t) = \int \prod_{n=1}^{N} d\Omega_n \Psi$$

Figure 3: Analytical model of MR signal in a network of randomly distributed cylindrical vessels. Two basic mechanisms attenuate the MR signal near a cylindrical vessel of radius R, angle ϑ to the external field $\vec{B}_0$, and susceptibility difference χ compared to tissue. First, the additional magnetic field of the vessel leads to a shift of the basic Larmor frequency $\omega_0 = 2\pi\gamma B_0$, thus to a loss of phase coherence of spins at different positions (A). Second, spins can diffuse through the field gradient $\nabla\omega(\vec{r})$ during the imaging experiment and pick up a random phase. The diffusion leads to an exponential decay in the magnetization density $\Psi(\vec{r},t)$ (first term denotes phase offset described in (A), second term the diffusion effect) after averaging over all diffusion paths that end at $\vec{r}$ (B). This exponential factor is well known from diffusion MRI. MR signal from a voxel containing many cylinders is obtained via averaging over $\vec{r}$, which is equivalent to averaging over positions, orientations, and radii of all cylinders in the voxel (C). γ : gyromagnetic ratio, D : diffusivity of tissue, l_D : mean diffusion length during MR experiment, $\int d\Omega_n$: integration over position, orientation, and radius of the nth cylinder. Equations are only shown for the extravascular compartment. The complete mathematical description can be found in [22].

Importantly, a sensitivity of ΔR_2 to the mean vessel radius R within a voxel was found in the analytical expressions and confirmed by Monte-Carlo simulations of Boxermann et al. [25]. ΔR_2^* depends on volume fraction of the intravascular compartment, i.e. blood volume fraction ξ_0.

$$\Delta R_2 = 0.694 \cdot \left(2\pi\gamma\chi B_0\right)^{2/3} D^{1/3} \xi_0 R^{-2/3} \tag{1}$$

$$\Delta R_2^* = \tfrac{4}{3}\pi\gamma\chi B_0 \xi_0 \tag{2}$$

Dennie et al. were the first to demonstrate how this can be used in the experiment to measure changes of vessel morphology due to angiogenesis in tumors [26]. Since then, the experimental framework has been developed further and is commonly referred to as "vessel size imaging" [27]. The (slightly modified) framework was also used for this dissertation and is illustrated in Fig. 4. Changes in relaxation rates ΔR_2 and ΔR_2^* are assessed by spin echo and gradient echo MRI, respectively. The changes in relaxation rates are relative measures of blood volume in small vessels (ΔR_2) and overall blood volume (ΔR_2^*). Additional measurements of diffusivity in tissue D and of susceptibility changes in blood χ allow calculation of mean vessel radius R and areal vessel density N via equations (1) and (2) (in cgs units [27–30]):

$$R = 0.425\left(\frac{D}{\gamma\chi B_0}\right)^{1/2}\left(\frac{\Delta R_2^*}{\Delta R_2}\right)^{3/2} \tag{3}$$

$$N = 0.218\cdot\frac{1}{D}\frac{\left(\Delta R_2\right)^3}{\left(\Delta R_2^*\right)^2} \tag{4}$$

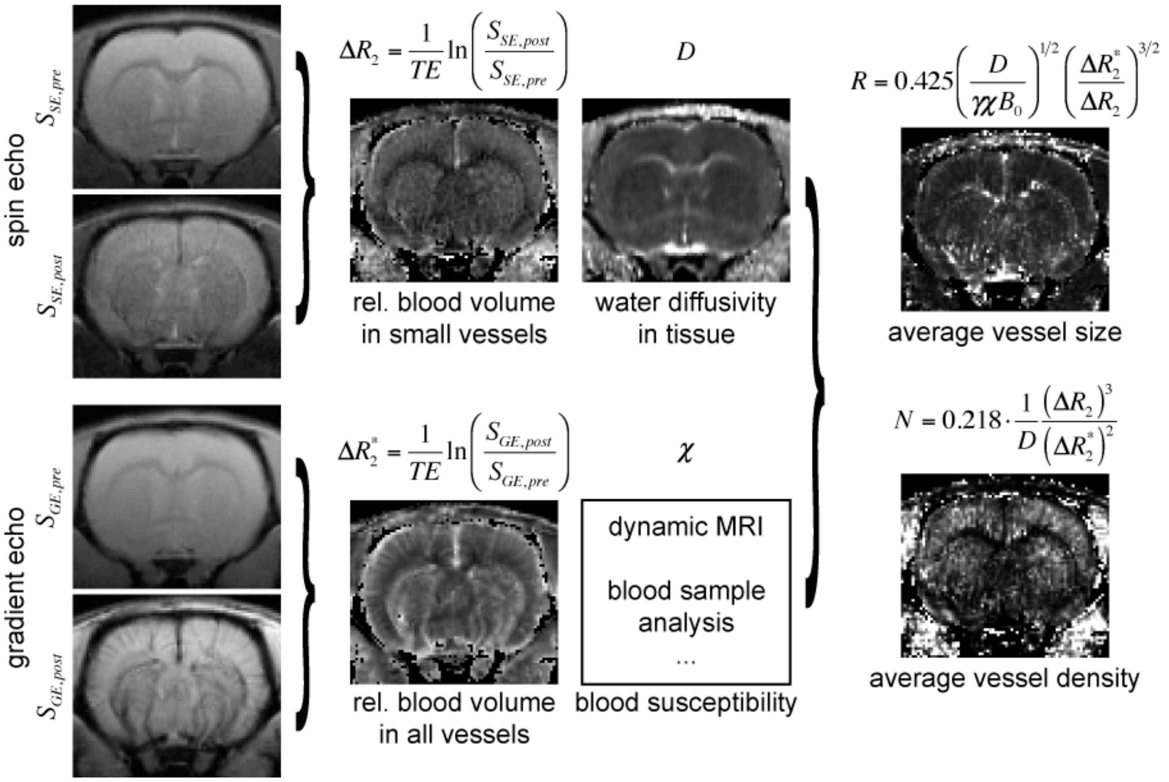
spin echo
$S_{SE,pre}$
$S_{SE,post}$
gradient echo
$S_{GE,pre}$
$S_{GE,post}$
$\Delta R_2 = \frac{1}{TE}\ln\left(\frac{S_{SE,post}}{S_{SE,pre}}\right)$
D
rel. blood volume in small vessels
water diffusivity in tissue
$\Delta R_2^* = \frac{1}{TE}\ln\left(\frac{S_{GE,post}}{S_{GE,pre}}\right)$
χ
dynamic MRI
blood sample analysis
...
rel. blood volume in all vessels
blood susceptibility
$R = 0.425\left(\frac{D}{\gamma\chi B_0}\right)^{1/2}\left(\frac{\Delta R_2^*}{\Delta R_2}\right)^{3/2}$
average vessel size
$N = 0.218\cdot\frac{1}{D}\frac{\left(\Delta R_2\right)^3}{\left(\Delta R_2^*\right)^2}$
average vessel density

Figure 4: Typical SSCE MRI data acquisition and post-processing framework for imaging blood volume, vessel size (radius), and vessel density. Gradient echo and spin echo MR images are acquired pre and post i.v. injection of superparamagnetic iron oxide particles. From the changes in signal, changes in relaxation rates ΔR_2 and ΔR_2^* are calculated, which are relative measures of blood volume. Together with measurements of tissue diffusivity and blood susceptibility, absolute vessel size and vessel density maps are generated. Representative coronal brain images of a healthy rat before and after contrast agent injection (30 mg Fe/kg) are shown. TE: echo time.

1.3 Neural stem cells

1.3.1 General properties

Neural stem cells (NSCs) are immature, proliferating cells that can generate all major cells of the central nervous system, i.e. are multipotent, and that have the capacity of self-renewal [31] although more stringent definitions exist [32]. NSCs are the progeny of embryonic stem cells. They can themselves differentiate into neuronal and glial progenitor cells and finally give rise to mature neurons and glia (Fig. 5). It was long believed that NSCs only play a role during embryonic and fetal development. However, it is known today that NSC niches exist in the adult brain, predominantly in the granular layer of the dentate gyrus in the hippocampus and in the subventricular zone [33], [34]. The NSCs of the adult brain can give rise to new neurons (neurogenesis). In the healthy mammalian brain, neural progenitor cells from the subventricular zone migrate to the olfactory bulb and generate new neurons [34] whereas adult hippocampal neurogenesis is speculated to play a role in accommodating the brain to establish a more complex neuronal network [35].

NSCs are highly investigated for therapies of neurological disorders such as Parkinson's disease, stroke, and multiple sclerosis, since the clinical syndromes of these diseases are caused by a loss of glia and neurons [36]. Two major strategies are proposed: (i) to "boost" neurogenesis or to prevent cell death of endogenous NSCs and (ii) implantation of NSCs to replace damaged tissue [37]. The latter will be introduced in more detail in the following section with a focus on stroke.

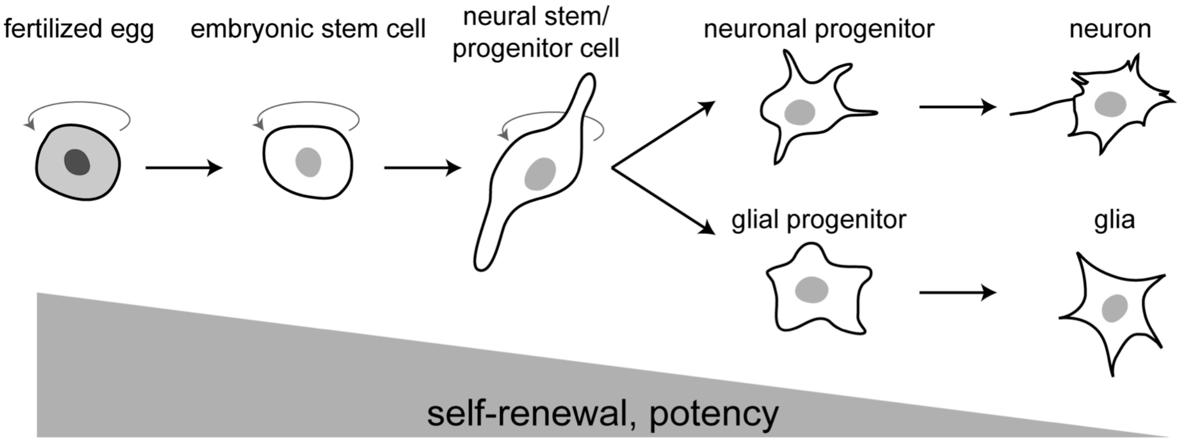

Figure 5: Schematic illustration of different stem cell levels of potency and commitment for differentiation into neurons and glia. Black arrows indicate default pathway for development of specialized cells and fate restriction. Rounded arrows indicate the capacity for self-renewal. Modified from [46].

1.3.2 Neural stem cell implantation in the healthy and stroke-damaged brain

To generate the large number of cells needed for implantations, NSCs can be derived from embryonic stem cells, the fetal or the adult brain and expanded in vitro in neurosphere [38] or monolayer [39], [40] cultures. Alternatively, NSCs can be derived from induced pluripotent stem (iPS) cells [41]. These cells are generated by genetic modification of differentiated cells, e.g. skin cells, a process also referred to as reprogramming or de-differentiation. Despite the high impact of this technology, which resulted in the Nobel price in physiology or medicine for one of the pioneers Shinya Yamanaka in 2012, there is still debate on safety of iPS cells and whether or not iPS cells are equivalent to normal stem cells [42]. The NSCs used in this dissertation were provided by our collaborator Zaal Kokaia from the Laboratory of Neural Stem Cell Biology and Therapy, Department of Clinical Sciences, Stem Cell Center, Lund, Sweden. They are derived from the human fetal brain and expanded in vitro as neurospheres. Since these NSCs are of human origin they represent a particularly promising candidate for a clinical translation [37]. In previous, invasive studies in Lund, these cells were well characterized in terms of differentiation potential, survival, and integration into host tissue both in the healthy rodent brain and under pathological conditions [43–47]. Importantly, tumor formation was never observed in vivo.

Implantation in the healthy rodent brain is used to study survival, migration, and differentiation of NSCs under in vivo conditions. In studies of this dissertation, NSCs were implanted in the adult mouse brain and the neonatal rat brain. Since the neonatal brain is rich in instructive, developmental signals it serves as an intermediate step between the artificial, controlled in vitro environment and the less plastic adult brain [46]. Moreover, immune response and risk of graft rejection is lower in neonates than in adults [48–50], rendering pharmacological immune suppression, e.g. with the drug Cyclosporine, unnecessary. This is particularly important for long-term studies since most immunosuppressants are toxic and should not be used for longer times (> 4 weeks).

A large number of reports on human NSC implantation studies after stroke exist for rats [44], [45], [51–54], but also for mice [55], Mongolian gerbils [56], and non-human primates [57]. The cells survived robustly depending on the proximity of the graft to the lesion, migrated predominantly towards the damaged area and the migrating cells mainly differentiated to cells with neuronal phenotype [58]. A reduction of infarct volume compared to control animals was observed in [56]. Neurological function of stroke animals with NSC implantation improved significantly compared to controls that received a vehicle transplant [51], [55], [56]. However, functional improvement after cell implantation in stroke is generally believed to be rather due to release of trophic factors than direct tissue replacement. These factors possibly promote endogenous repair mechanisms, reduce cell death, and stimulate angiogenesis and neurogenesis [59].

Before NSC implantations can be used for the treatment of stroke patients a number of fundamental questions need to be answered [60]: Which patients would profit most from such a treatment (age, anatomical location and size of the lesion, …)? What is the best cell type? What is the optimal timing and site for implantation? Which delivery route should be preferred? What numbers and concentration of cells should be used and how can graft rejection by the host immune system be avoided?

As cell-mediated regeneration processes develop continuously over long times, noninvasive imaging is essential to answer some of these questions. Noninvasive imaging allows to follow the cells in space and time over long periods and, ideally, permits to assess their functional fate [61]. In turn, imaging can provide readouts of host response to the cellular therapeutic. For example, lesion size can be measured on T_2 weighted MRI and functional recovery can be assessed by functional MRI [62].

1.4 Imaging implanted neural stem cells

1.4.1 Overview

The discrimination of implanted neural stem cells from surrounding cells in brain tissue is very challenging since the physical properties of implant and tissue are almost identical. Thus it is necessary to label the cells for detection with imaging. In principal, two labeling approaches exist: genetic labeling and external labeling before implantation. For genetic labeling, a gene (the “reporter gene”) is introduced in the DNA of cells. The genetically modified cell is forced to produce a foreign protein, which can either be directly detected or enhances binding of a substance (the “reporter probe”) detectable by imaging. For external labeling, cells are forced to take up a detectable agent before implantation. If the cells keep the label after implantation, the agent can be used to indirectly locate the cells with imaging. External labels have the disadvantage of label dilution when the cells divide after implantation. Furthermore, an external label may still remain in place when the cells die leading to false positive signal. On the other hand, the chemistry of external labels can be optimized to a much higher extent, which generally leads to higher sensitivity compared to reporter gene approaches. Moreover, genetic labeling requires generation of genetically modified cells, which raises safety issues for use in humans whereas external labels can be chemically designed as to minimize adverse effects. In the following, an overview of labels and imaging modalities is given (reviewed in [63–65]).

For optical imaging, the most prominent reporter gene is the green fluorescent protein (GFP), which originates from the genome of jellyfish. Upon excitation with light in the ultraviolet range, the protein emits green light, which can be detected with an optical camera. Numerous other fluorescent proteins of different excitation/emission spectra are available nowadays for planar or tomographic fluorescence imaging. External labels for optical imaging include a wide range of fluorophores or quantum dots, which yield order of magnitude higher light emission. Another class of optical reporter genes is represented by the luciferases of the firefly, click beetle, renilla, gaussia, or some types of bacteria. Genetically modified cells produce the luciferase and are detected via light emission during an enzymatic reaction with an exogenously delivered substrate. Since luciferases are absent in normal tissue of mammals, cells can very sensitively be detected against background. However, scattering and absorption of light in tissue limits the use of optical imaging to cell culture or small animals. In vivo, the typical penetration depth is only a few mm and 3D tomographic methods are in their infancy. Still, optical methods remain the Gold standard for histology. Therefore, novel imaging approaches, as presented in this dissertation, need to be verified by optical techniques, e.g. microscopy on brain slices.

Positron emission tomography (PET) and single-photon emission computed tomography (SPECT) sensitively detect radioisotopes or positron emitters in vivo in deep tissues, e.g. the brain. They allow acquisition of true 3D tomographic data. However, the spatial resolution is poor (> 1 mm), approximately one order of magnitude lower than in MRI. An example of a PET/SPECT reporter gene is the herpes simplex virus type 1 thymidine kinase. Externally administered, radiolabeled probes for PET and SPECT detection accumulate only in cells expressing the herpes thymidine kinase. Cells can also be pre-labeled with a radionuclide and tracked with PET/SPECT after implantation. Due to radioactive decay of the tracer, this is only useful for short-term studies with time-spans at the order of tracer half-life.

Of all imaging modalities, MRI is the least invasive and provides most detailed anatomical information of deep tissues. Most isotopes used for MRI are stable, thus enabling long-term studies. Reporter genes for MRI may be classified in four categories: (i) metalloproteins that promote iron accumulation detectable via the T_2/ T_2^* effect, (ii) cell surface molecules that specifically bind an externally administered MR contrast agent, (iii) enzymes which turn on the contrast of an externally administered agent, (iv) proteins detectable via the chemical exchange saturation transfer effect [62]. However, MR reporter genes are still in their infancy and wide-spread use has been hampered by low sensitivity and safety issues [64]. The most widely used external labels for MRI cell tracking are superparamagnetic iron oxide particles (SPIOs). Cells labeled with SPIOs are traced with conventional ^{1}H MRI via their T_2 and T_2^* effect. More recently, fluorinated labels are investigated for cell detection with ^{19}F MRI. Advantages and drawbacks of these cell tracking methods will be introduced in the following sections.

1.4.2 Cell tracking with ^{1}H MRI

MRI of cells that have been labeled with SPIO contrast agents before implantation can provide insight into location and – less reliably – numbers of grafted cells. Using SPIO labels, our group was the first to noninvasively image migration of implanted stem cells from the healthy towards the stroke-damaged hemisphere [67]. However, the murine stem cell line (C17.2) used in that study carries an oncogene for more convenient handling in cell culture thus is not well suited for therapy. Later studies by other groups employed long-term ^{1}H MRI of SPIO labeled, clinically more relevant, human NSCs in the neonatal, healthy adult, and the stroke-induced rat brain [68]. These revealed distinct migration patterns of cells depending on their microenvironment.

SPIOs usually consist of an iron oxide crystal core (magnetite, Fe_3O_4) surrounded by a dextran/carboxydextran coating. Depending on the hydrodynamic diameter, iron oxide particles are categorized in micron-sized iron oxide particles (MPIOs, ~1 µm), SPIOs (50-180 nm), ultrasmall SPIOs (USPIOs, 10-50 nm), or very small SPIOs (VSPIOs, <10 nm) [69]. For this dissertation, the commercially available dextran-coated SPIO formulation Endorem (~200 nm, Guerbet, France) was used for all studies. NSCs take up the particles through endocytosis, and endosomes filled with SPIOs accumulate in the cytoplasm. In the large magnetic field of an MRI scanner, the magnetization of intracellular SPIOs generates a broader magnetic field distribution in the voxel containing the cell(s). Effectively, this induces faster dephasing of nearby ^{1}H spins, i.e. a signal dropout on T_2/ T_2^* weighted MR images. As many ^{1}H nuclei in the surrounding of the contrast agent particles are affected in their MR signal, the method is very sensitive when cells are imaged against magnetically homogeneous background (Fig. 6 A). In vivo, however, the hypointensity generated by SPIO labeled cells can easily be confounded with other sources of magnetic inhomogeneities such as blood vessels (iron in hemoglobin) or dense anatomical structures such as bone and cartilage (Fig. 6 B). The specificity of the contrast induced by cells may become even worse under pathological conditions (e.g. bleedings, iron accumulations in scars). Furthermore, the underlying T_2/ T_2^* contrast mechanisms make quantification of cell numbers in a region of interest very difficult. For homogeneous solutions of contrast agent, e.g. in water, iron oxide concentrations c can, for a wide range, be assessed through the simple proportionality of relaxation rates $R_1 \sim c$ and $R_2^* \sim c$. Usually, the same holds true for cell concentrations (Fig. 6 C). For clusters of cells, an analytical model is needed to quantify cell densities. Such models exist, e.g. for small cylindrical shapes in analogy to chapter 1.2.2 or small spherical "blobs" of cells. Again, calculations usually lead to $R_2^* \sim c_{cells}$. However, even for homogeneous cell distribution or simple shapes, the signal may decay too fast to be sampled with MRI, especially for high iron oxide densities. Generally, the cell graft forms an arbitrary shape and cells are heterogeneously distributed within the graft. Both shape and distribution are not known a priori. The magnetic field distribution then becomes too complex rendering quantification of cell densities very challenging.

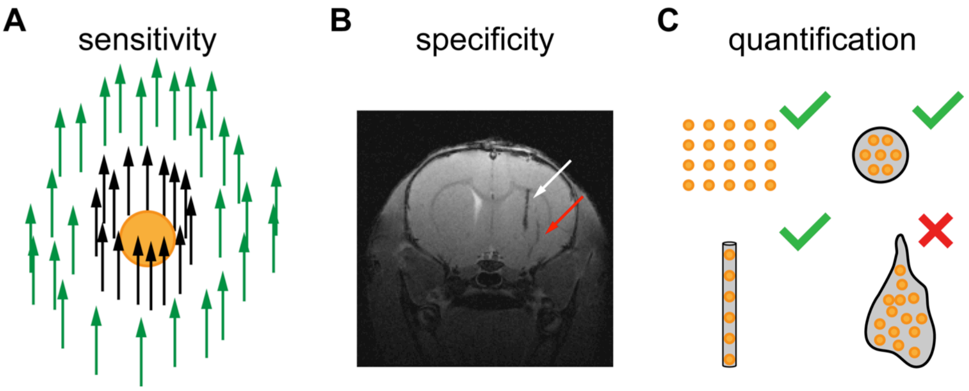

Figure 6: ^{1}H MRI of magnetically labeled cells. A: A cell (yellow sphere) loaded with SPIO particles can effectively dephase spins in its vicinity (black arrows) inducing a hypointensity on MR images compared to spins in background tissue (green arrows). One cell can affect many spins enabling very sensitive detection against homogeneous background. B: Gradient echo MR image of a rat with intrastriatal implantation of 100,000 SPIO labeled human NSCs. Cells are clearly depicted as a hypointensity (white arrow). However, the graft can easily be confounded with other sources of magnetic inhomogeneities, e.g. blood vessels (red arrow). C: Quantification of cell numbers can be possible for homogeneous distribution of cells, spherical, cylindrical and other simple geometric shapes for which the magnetic field distribution can be calculated. However, a cell graft is usually arbitrarily shaped and cell distribution within the graft is not known rendering quantification very challenging.

1.4.3 Cell tracking with ^{19}F MRI

Due to the drawbacks of iron oxide labels, a new class of fluorinated labels for cell tracking with MRI has emerged over the past few years since the seminal paper by Ahrens et al. in 2005 [70]. The stable isotope ^{19}F is >99% abundant in nature. It has the second highest gyromagnetic ratio after ^{1}H ($\gamma_{19F}/\gamma_{1H}=0.94$), thus has only 17% less equilibrium MR signal (i.e. signal at defined concentration neglecting relaxation times). In order to track cells with fluorine agents, cells are pre-labeled, and both ^{1}H and ^{19}F MRI are performed after implantation. As the Larmor frequencies of ^{1}H and ^{19}F are well separated by 6%, signal from one nucleus does not “leak” into the image of the other nucleus. The conventional ^{1}H image provides anatomical context whereas the ^{19}F image intensity depends only on in vivo concentrations of ^{19}F. When the ^{19}F image is acquired in the same position of the animal, it can be overlaid on the ^{1}H image and cells can be located in the body. Since the ^{19}F magnetization is detected directly - in contrast to the indirect mechanism for detection of iron oxide labels discussed in the previous section – cell tracking with ^{19}F MRI is considerably less sensitive (Fig. 7 A). Therefore, most studies employed perfluorocarbon (PFC) based cellular labels, since these contain a large number of ^{19}F per molecule [71]. One of the main advantages of ^{19}F MRI is that endogenous ^{19}F concentrations in the body are well below detectability ($<<10^{-3}$ mol/L). This guarantees that only labeled cells contribute to the signal on a ^{19}F MR image with no confounding background signal (Fig. 7 B). It is noted, that this statement is not true for anesthetized animals since the most widely used and most convenient gas anesthetics (e.g. Halothane, Isoflurane) are fluorinated gases. These gases can accumulate in MR detectable concentrations especially in fatty tissue. This can be used to study the uptake and elimination of these gases in vivo [72] but it is confounding for cell tracking studies. Thus it is necessary to switch to alternative forms of anesthesia. Due to the direct detection of ^{19}F, the ^{19}F MR signal is simply proportional to concentration $S_{19F} \sim c_{19F}$. If the average ^{19}F loading per cell is known and a reference tube with defined ^{19}F concentration is placed next to the object of interest, this can be used to quantify cell density directly from the image data [73] (Fig. 7 C).

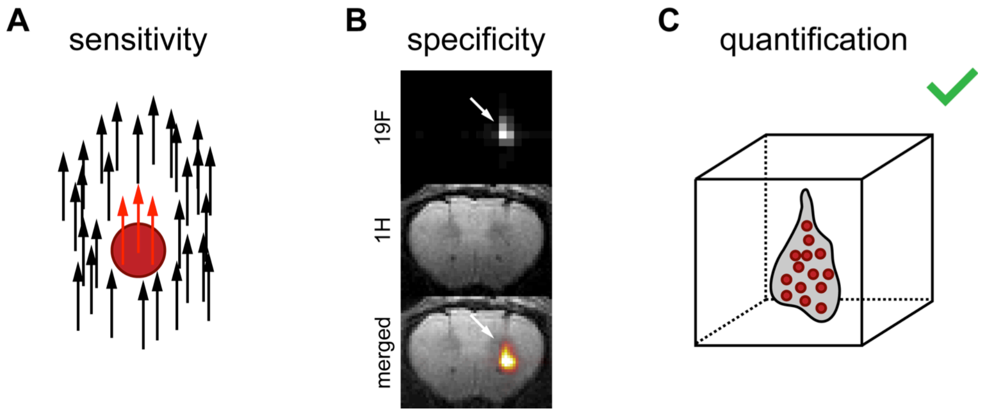

Figure 7: MRI of ^{19}F labeled cells. A: ^{19}F spins (red arrows) within a cell (red sphere) are directly detected in the ^{19}F MR experiment. ^{1}H MR signal of proton spins in the vicinity (black arrows) is unchanged. High ^{19}F concentrations in the mM range are needed to be detectable by ^{19}F MRI, thus cell detection is considerably less sensitive than using SPIO labels. B: ^{19}F MR, anatomical ^{1}H MR, and merged images of a mouse with intrastriatal implant of 300,000 PFC labeled murine neural stem cells (white arrow). ^{19}F image interpolated to ^{1}H resolution and pseudo-colored for the merged image. Due to absence of ^{19}F in the body, only the cell graft generates significant signal on the ^{19}F image. C: As long as the number of cells within a voxel exceeds the detection limit, quantification is possible via a linear relationship of image intensity and cell number. This holds for arbitrary geometric distribution of cells within the voxel, i.e. graft shape and distribution do not need to be known a priori for quantification.

Most published studies focused on tracking and quantification of PFC labeled immune cells. In vivo ^{19}F MRI of dendritic cells and T-cells was shown after focal injection or intravenous infusion of cells for therapeutic purpose in rodent models of cancer vaccination [70], [74–77], diabetes [78], or inflammation [79]. In a proof of concept, Ruiz-Cabello et al. showed the feasibility to detect C17.2 murine NSCs after implantation to the healthy adult mouse brain indicating that ^{19}F MRI may be a valuable tool in the field of brain cell replacement therapy [80].

1.5 Aims of this dissertation

The aims of this dissertation were to develop and optimize MRI methods to image angiogenesis and implanted neural stem cells. The detailed aims were to:

1. Implement and optimize SSCE MRI to image vessel size and density. This included the design of a transmit radiofrequency (RF) coil, optimization of MRI pulse sequences, and the development of MRI data analysis strategies.
2. Design a setup for in vitro MRI and develop image data processing strategies for analysis of in vivo MRI of SPIO labeled NSCs.
3. Develop a setup for ^{19}F MRI including design of dedicated RF coils, holders for in vitro and in vivo MRS and MRI.
4. Evaluate cell detection limits of ^{19}F MRI of NSCs, improve sensitivity by optimization of MRI pulse sequences, and develop cell quantification strategies.

In contrast to a purely methodological work, I wanted to prove the usefulness of developed hardware and methods in biological studies in collaboration with biologists and physicians. We therefore aimed to (corresponding papers as numbered in the next chapter):

1. Follow vascular changes in tumors and in response to anti-angiogenic treatment (papers I+II)
2. Follow vascular changes after stroke (paper III).
3. Monitor the fate of NSCs after implantation (papers IV-VI).

2 Original papers and manuscripts

This thesis is based on the following papers (* indicates equal contribution):

I. Roland T. Ullrich*, Jan Jikeli*, Michael Diedenhofen, Philipp Böhm-Sturm, Meike Unruh, Stefan Vollmar, and Mathias Hoehn (2011). In-vivo visualization of tumor microvessel density and response to anti-angiogenic treatment by high resolution MRI in mice. PLoS ONE, 6(5), e19592. doi:10.1371/journal.pone.0019592

II. Thomas Viel*, Philipp Boehm-Sturm*, Sara Rapic, Parisa Monfared, Bernd Neumaier, Mathias Hoehn, and Andreas H Jacobs (2013) Non-invasive imaging of glioma vessel size and densities in correlation with tumour cell proliferation by small animal PET and MRI. European Journal of Nuclear Medicine and Molecular Imaging, 1–12. doi:10.1007/s00259-013-2464-1 (Epub ahead of print)

III. Philipp Boehm-Sturm*, Tracy D. Farr*, Joanna Adamczak, Jan Jikeli, Luam Mengler, Dirk Wiedermann, Therése Kallur, Valerij Kiselev, and Mathias Hoehn (2012), Vascular changes after stroke in the rat: a longitudinal study using optimized magnetic resonance imaging. Contrast Media & Molecular Imaging, 8(5), 383–392. doi:10.1002/cmmi.1534

IV. Therése Kallur, Tracy D. Farr, Philipp Böhm-Sturm, Zaal Kokaia, and Mathias Hoehn (2011). Spatio-temporal dynamics, differentiation and viability of human neural stem cells after implantation into neonatal rat brain. European Journal of Neuroscience, 34(3), 382-393. doi:10.1111/j.1460-9568.2011.07759.x

V. Philipp Boehm-Sturm, Luam Mengler, Stefan Wecker, Mathias Hoehn, and Therése Kallur (2011). In Vivo Tracking of Human Neural Stem Cells with 19F Magnetic Resonance Imaging. PloS ONE, 6(12), e29040. doi:10.1371/journal.pone.0029040

VI. Mangala Srinivas, Philipp Boehm-Sturm, Jolanda de Vries, Carl Figdor, Mathias Hoehn (2012), Labeling cells for in vivo cell tracking with 19F MRI. Biomaterials, 33(34), 8830–40. doi:10.1016/j.biomaterials.2012.08.048.

In-Vivo Visualization of Tumor Microvessel Density and Response to Anti-Angiogenic Treatment by High Resolution MRI in Mice

I

OPEN ACCESS Freely available online

PLoS one

In-Vivo Visualization of Tumor Microvessel Density and Response to Anti-Angiogenic Treatment by High Resolution MRI in Mice

Roland T. Ullrich[1,2,3]*[❡], Jan F. Jikeli[1❡], Michael Diedenhofen[1], Philipp Böhm-Sturm[1], Maike Unruh[1], Stefan Vollmar[1], Mathias Hoehn[1]

1 Max Planck Institute for Neurological Research, Cologne, Germany, **2** Center of Molecular Medicine, Cologne, Germany, **3** Department I of Internal Medicine, University Hospital, Cologne, Germany

Abstract

Purpose: Inhibition of angiogenesis has shown clinical success in patients with cancer. Thus, imaging approaches that allow for the identification of angiogenic tumors and the detection of response to anti-angiogenic treatment are of high clinical relevance.

Experimental Design: We established an in vivo magnetic resonance imaging (MRI) approach that allows us to simultaneously image tumor microvessel density and tumor vessel size in a NSCLC model in mice.

Results: Using microvessel density imaging we demonstrated an increase in microvessel density within 8 days after tumor implantation, while tumor vessel size decreased indicating a switch from macro- to microvessels during tumor growth. Moreover, we could monitor in vivo inhibition of angiogenesis induced by the angiogenesis inhibitor PTK787, resulting in a decrease of microvessel density and a slight increase in tumor vessel size.

Conclusions: We present an in vivo imaging approach that allows us to monitor both tumor microvessel density and tumor vessel size in the tumor. Moreover, this approach enables us to assess, early-on, treatment effects on tumor microvessel density as well as on tumor vessel size. Thus, this imaging-based strategy of validating anti-angiogenic treatment effects has high potential in applications to preclinical and clinical trials.

Citation: Ullrich RT, Jikeli JF, Diedenhofen M, Böhm-Sturm P, Unruh M, et al. (2011) In-Vivo Visualization of Tumor Microvessel Density and Response to Anti-Angiogenic Treatment by High Resolution MRI in Mice. PLoS ONE 6(5): e19592. doi:10.1371/journal.pone.0019592

Editor: John D. Minna, Univesity of Texas Southwestern Medical Center at Dallas, United States of America

Received October 1, 2010; **Accepted** April 12, 2011; **Published** May 5, 2011

Copyright: © 2011 Ullrich et al. This is an open-access article distributed under the terms of the Creative Commons Attribution License, which permits unrestricted use, distribution, and reproduction in any medium, provided the original author and source are credited.

Funding: This work was supported in part by a grant from the Deutsche Forschungsgemeinschaft through SFB 832 (to R.T.U.), and by European funds (project ENCITE) under the 7th Framework HEALTH-F5-2008-201842 (to M.H.). The funders had no role in study design, data collection and analysis, decision to publish, or preparation of the manuscript.

Competing Interests: The authors have declared that no competing interests exist.

* E-mail: ullrich@nf.mpg.de

❡ These authors contributed equally to this work.

Introduction

In the past years preclinical and clinical studies have demonstrated the essential role of angiogenesis for initiation of tumor growth [1,2]. Treatment strategies inhibiting angiogenic processes mainly targeting the vascular endothelial growth factor (VEGF) and its receptor (VEGFR) have been implicated in clinical trials. Thus, non-invasive methods to visualize and to monitor tumor angiogenesis, and its inhibition, respectively, are of high clinical relevance.

Currently, dynamic contrast enhanced magnetic resonance imaging (DCE-MRI) is in clinical use for the assessment of anti-angiogenic treatment effects [3,4]. DCE-MRI represents an indirect measure of angiogenesis since it mainly reflects leakage of the vascular bed by measuring the transfer of contrast agent into the interstitial space. Due to high VEGF levels within tumors vascular leakage is increased in tumor microvessels. Thus, DCE imaging is proposed to be an accurate marker to detect therapeutic VEGF inhibition. Gadolinium-based contrast agents are mostly used for DCE-MRI.

Dennie et al proposed the use of the ratio of gradient echo and spin echo relaxation rate changes ($\Delta R^*_2/\Delta R_2$) after injection of a high molecular weight contrast agent to measure average microvessel density within a voxel [5]. These authors found a good correlation between the MRI derived in vivo data and histology. Based on these findings Jensen and Chandra proposed to map the ratio of $Q = \Delta R_2/(\Delta R^*_2)^{2/3}$ and demonstrated that Q is dependent on water diffusion but independent of the concentration of the contrast agent [6]. Because of the heterogeneity of diffusion within tumors and changes of diffusion during tumor growth [7] we sought to establish a multi-echo spin echo sequence that takes the tumor diffusion into account for the determination of tumor microvessel density and tumor vessel size.

In this study, we present an in vivo MRI approach that allows for simultaneous assessment of tumor microvessel density and vessel size by the use of a superparamagnetic iron oxyde (SPIO) at a very high spatial resolution. We validated the accuracy of this approach by monitoring tumor angiogenesis and detecting response to the VEGFR/PDGFR tyrosine kinase inhibitor vatalanib in a NSCLC xenograft model in mice.

Materials and Methods

Cell Culture

We used the NSCLC cell line H1975 [8]. Cells were maintained in RPMI 1640 supplemented with 10% heat inactivated fetal bovine serum (FBS, Roche Diagnostics, Mannheim, Germany), 1% penicillin and 1% streptomycin (P/S, Life Technologies) at 37°C in a 5% CO2/95% air atmosphere.

Xenograft model

All animal procedures were in accordance with the German Laws for Animal Protection and were approved by the local animal committee and the local authorities (LANUV, Recklinghausen, reference number: 8.87-50.10.31.08.331).

Tumors were generated by s. c. injecting 5×10^6 H1975 tumor cells into *nu/nu* athymic male mice as described recently [8] (Janvier, Europe). In the first set, we longitudinally measured animals on days 1 (n = 4), 4 (n = 6, 2 sacrificed for immunohistochemistry), 8 (n = 6, 2 sacrificed for immunohistochemistry), 14 (n = 6, 2 sacrificed for immunohistochemistry), 21 (n = 6, 2 sacrificed for immunohistochemistry) after tumor cell injections. In the second set, animals were randomized into two groups, vehicle treated (control) and vatalanalib (PTK787) treated. Vehicle and PTK787 animals were studied on day 8 (start of treatment) 14, and 21 after tumor cell implantation (vehicle n = 6, PTK787 n = 6; 2 sacrificed for immunohistochemistry on day 21). Mice were treated daily by oral gavage of 75 mg/kg PTK787. PTK787 was dissolved at 1% DMSO and 0.5% Tween 80 in distilled water. All controls were dosed with the same volume of vehicle (1% DMSO and 0.5% Tween 80).

Immunohistochemistry

After the last MRI measurements, animals were sacrificed and s.c. tumors were extracted. Tumors were embedded in tissue freezing medium (Jung, Nussloch, Germany) and cut in 10-µm frozen sections. Hematoxylin Eosin staining on the tissue was performed according to standard protocols. Microvessel density was assessed with CD31 staining (1:50 dilution, Mat.-No. 550274, BD Pharmingen^{TM}). CD31 positive endothelial cells or cell cluster were counted. In order to determine the mean number of microvessel density within the tumor, the number of CD31 positive cells was determined by 3 different areas with maximal, moderate, and minimal endothelial density. The mean number of microvessels was determined as (F1+F2+F3)/3.

Magnetic Resonance Imaging (MRI)

All experiments were performed on an experimental animal scanner at 7T (Bruker BioSpec; Bruker) equipped with a gradient set of 400 mT/m. Radio frequency (RF) irradiation and signal detection was achieved with custom-built coils: a 8-cm-diameter Helmholtz coil arrangement for RF excitation, and a 16 mm diameter surface coil for signal detection.

To determine ΔR2 and ΔR2* maps multi slice multi spin echo (MSME) and multi gradient echo (MGE) pulse sequences, respectively, were performed before and after injection of iron oxide nanoparticles (Endorem®, Guerbet Inc.) at a dose of 30 mg Fe/kg. The postcontrast image acquisition was delayed by 2 min to ensure a steady-state distribution of contrast agent in the vascular network.

MSME and MGE MR images were obtained with the same Field of View (FOV) (16 mm×16 mm), and matrix size (64×64), and a slice thickness of 0.3 mm (Matrix size 250×250×300 µm^2).

MSME was acquired with TR = 5000 ms and TE = (10.9, 21.8,…,109)ms. MGE was acquired with TR = 1400 ms and TE = (4, 8,…,32) ms with a 60° hermite pulse.

To map the apparent diffusion coefficient (ADC) of water, two diffusion-weighted images with b = 300, b = 800 s/mm^2, in both, x and z directions of the gradient system were acquired, together with a reference image (b≈0 s/mm^2) at the following parameters: voxel size = 0.5×0.25×0.3 mm^3, zero-filled to 0.25×0.25×0.3 mm^3, matrix 64×64. The total scan time was 49 min and 16 seconds. We started the measurement with the ADC map. Then, we acquired the MSME and MGE pre CA-injection datasets. The post injection scan time was 16 min and 38 sec. The signal intensity after contrast agent injection was stable within half an hour.

Data analysis

The co-registration of the images was performed using FSL software (FLIRT, Oxford, UK). IDL was used for image processing (Interactive data language, ITT, VIS). We used a volume of interest (VOI) of the entire tumor to assess the global values of the ADC, MDI and VSI. The in-house developed software VINCI was used for volume of interest (VOI) analysis of MR images [9].

The ADC map was calculated from the diffusion-weighted images with a mono-exponential fit of the signal intensity of the three different b values (b_0, 300, 800 s/mm^2).

The $\Delta R*_2$ maps were determined with the second echo (TE = 8 ms) by

$$\Delta R*_2 = \frac{2}{3}\delta\omega\xi_0 = \frac{\ln\left(\frac{GE_{pre}}{GE_{post}}\right)}{TE} \qquad (1)$$

[10,11] and a modified calculation for multi-spin echo sequences with the third echo (TE = 32.7 ms)

$$\Delta R_2 = 0.694\delta\omega^{2/3}\xi_0\#^{2/3}ADC^{1/3}R^{-2/3} = \frac{\ln\left(\frac{SE_{pre}}{SE_{post}}\right)}{TE} \qquad (2)$$

[12] (ξ_0 = Blood Volume fraction; $\delta\omega = 2\pi\gamma\Delta X B_0$ = frequency shift, # = number of 180° pulses; R = Vessel Size Index (VSI) ΔX = changes in the susceptibility, B_0 = magnitude of the magnetic field, γ = gyromagnetic ratio). The prefactor 0.694 had been calculated in [12].

Based on equation (2) we calculated the microvessel density index (MDI) from

$$MDI = \xi_0/(2\pi R^2) = 1.327\#^2\frac{Q^3}{ADC} = 1.327\#^2\frac{\left(\frac{\Delta R2}{(\Delta R2*)^{2/3}}\right)^3}{ADC} \qquad (3)$$

As such, measurement values are independent of the local contrast agent concentration. The process is schematically depicted in Fig. 1.

The combination of equation (1) and (2) leads to the term of the VSI

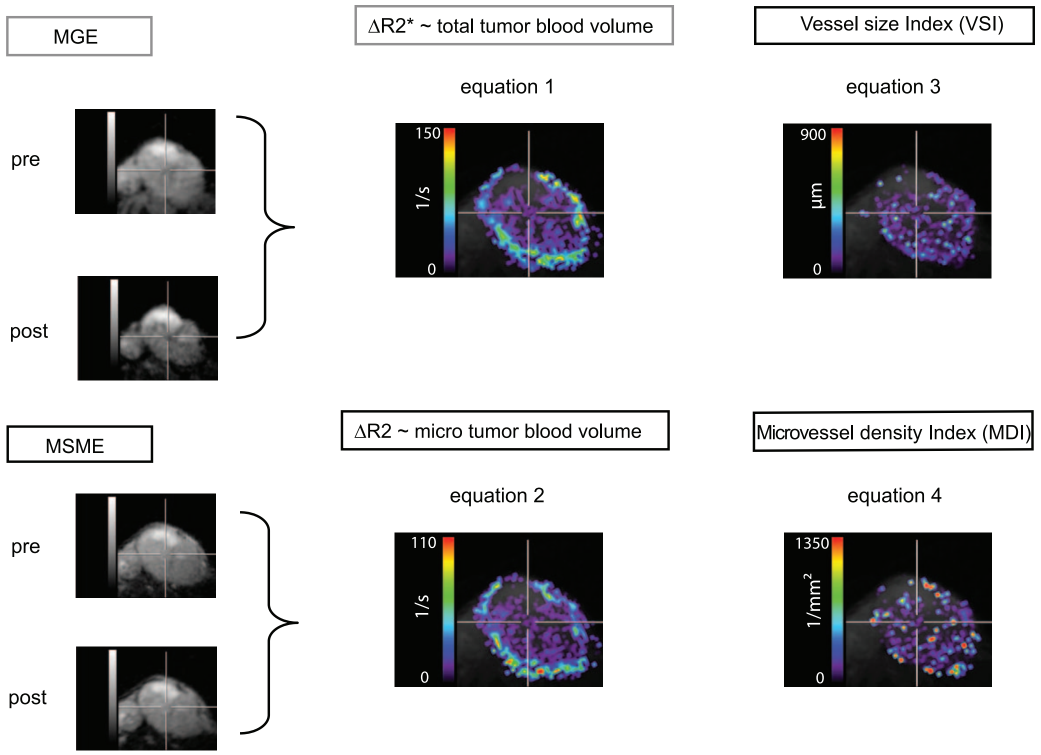

Figure 1. Schematic of data calculation for the microvessel density index (MDI) and the vessel size index (VSI).
doi:10.1371/journal.pone.0019592.g001

$$VSI = R = 0.425\#\left(\frac{ADC}{\delta\omega}\right)^{1/2}(\Delta R_2/\Delta R*_2)^{3/2};$$
$$\delta\omega = 2\pi\Delta X B_0 \text{ with } \Delta X = 1\times 10^{-3}. \qquad (4)$$
$$(\Delta X = \text{susceptibility change})$$

[13].

Statistical analysis

Statistical tests were performed using SPSS software (release 18.0 SPSS, Inc., Chicago. IL.USA). To assess statistical significance we used the Spearman correlation and the t-test. Statistical significance was set at $p<0.05$. Values are indicated as mean and standard deviations.

Results

Model

Equation (2) considers the number of 180°-pulses (#) within the MSME sequence. The calculation of the VSI map and the MDI map are based on equation (2). To our knowledge, we take for the first time the number of 180°-pulses into account by calculating VSI and MDI maps.

Comparison of the image derived MDI values with histology

In order to validate our image-derived data for microvessel density we compared the MDI values to the in vitro microvessel density. The in vitro microvessel density index was immunohistochemically assessed by CD31 positive microvessels at different time points directly after the MRI measurements. Here, we found a significant correlation between the in vivo derived MDI values and the microvessel density index of CD31 positive cells (r = 0.8, p = 0.0006; *Spearman correlation*) (Fig. 2). Furthermore, tumor areas with high VSI values showed also large vessel size in histology (Fig. 2A).

Monitoring tumor microvessel density and vessel size

We analyzed the growth of tumor microvessels as detected by the MDI map from day 1 to day 4, 8, 14, and 21. Already one day following s.c. inocculation of the tumor xenograft we observed high intra- and subcutaneous MDI values around the tumor. On day 4 we found an increasing number of tumor microvessels within the tumor (MDI value: 198±28). The maximum was reached 8 days after tumor cell inocculation (MDI value: 297±73). The MDI values then slightly decreased at day 14 (247±94) and day 21 (230±72). We did not find significant changes between day 1 and 4, day 4 and 8, day 8 and 14, day 14 and 2. Of note, at later time points we found a rather homogeneous distribution of the microvessels within the center as well as in the outer rim of the tumor (Fig. 3). This was accompanied with a homogeneous, rather low ADC value on days 14 and 21 (Fig. 3).

Using maps of the vessel size index (VSI) we estimated the vessel diameter over time. Interestingly, we found inverse behavior of the vessel size and vessel density changes: an increase in MDI from day 4 to day 14 was accompanied by a decrease in VSI, indicating a switch from larger to smaller vessel sizes (VSI, day 4: 68.7±40.8; day 14: 50.7±1.8). Tumor vessels with larger diameter were found in the outer rim of the tumor with their diameter still increasing during the following days (Fig. 3).

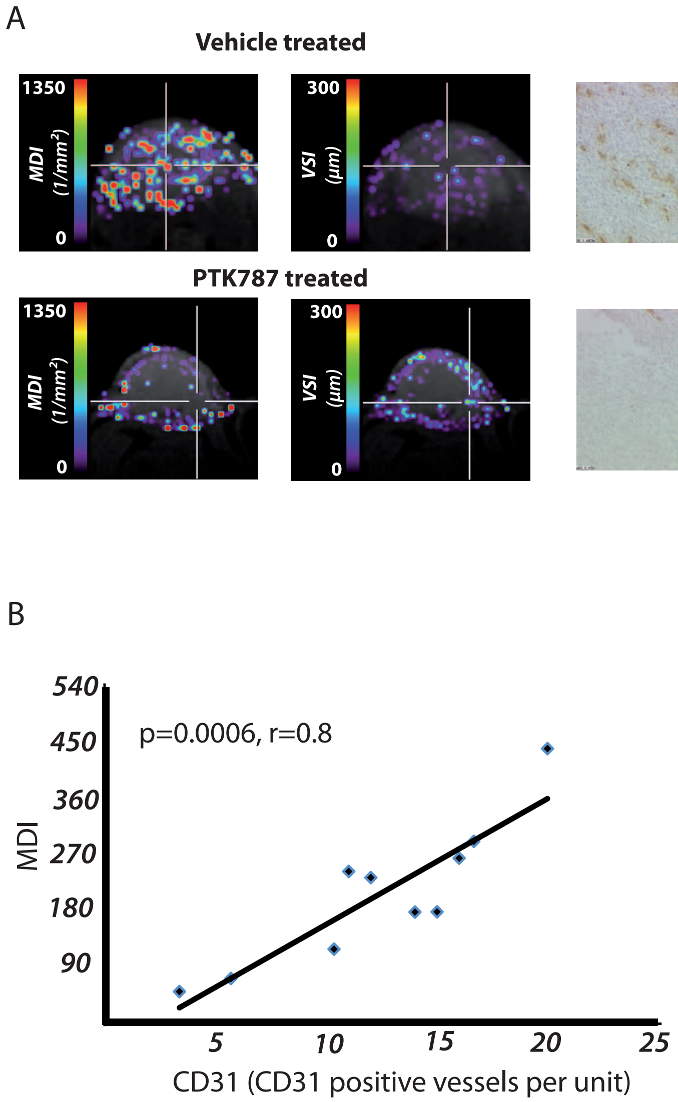

Figure 2. Comparison of the image derived values of MDI and VSI to CD31 positive endothelial cell staining. (A) a vehicle treated (upper row) tumor presenting a high microvessel density index (MDI (1/mm^2)) in MRI and a low vessel index (VSI (µm)). The PTK787-treated tumor (lower row) presents low MDI values with high VSI values. (B) correlation between CD31 positive vessels per area unit and the imaged derived MDI values (n = 10).
doi:10.1371/journal.pone.0019592.g002

ADC values showed a decrease within the first 8 days reflecting a decline in extracellular diffusion, most probably due to an increase in tumor cell density.

Response to PTK787 treatment

We determined the potential of our protocol to assess response to anti-angiogenic treatment. Tumors were grown for 8 days and MDI, ADC and VSI were measured. We then started PTK787 treatment and monitored response to treatment after 6 and 13 days by calculating percentage changes in MDI, VSI and ADC. Already after 6 days of oral PTK787 treatment, we found a significant decline in the MDI values in comparison to the vehicle group ($p = 0.021$) (see Table 1 and Fig. 4). This was confirmed after 13 days of treatment ($p = 0.005$). In contrast, the VSI decreased in the control group over time whereas in the treated tumors the VSI remained nearly stable at day 6 and even increased till day 13. This indicates a switch from macro- to microvessels in the vehicle group. On the other hand, PTK787 treatment induces the inverse effect resulting in a shift from micro- to macrovessels.

In parallel we observed a decrease in the ADC value after 6 days of PTK787 treatment whereas there was nearly no change in the ADC in the vehicle treated tumors. The ADC value then increased till day 13 during PTK787 treatment (Tab. 1 and Fig. 4).

Discussion

In this study we demonstrate the feasibility to non-invasively determine microvessel density in an experimental NSCLC model by the use of the MRI derived MDI map. Moreover, we propose a

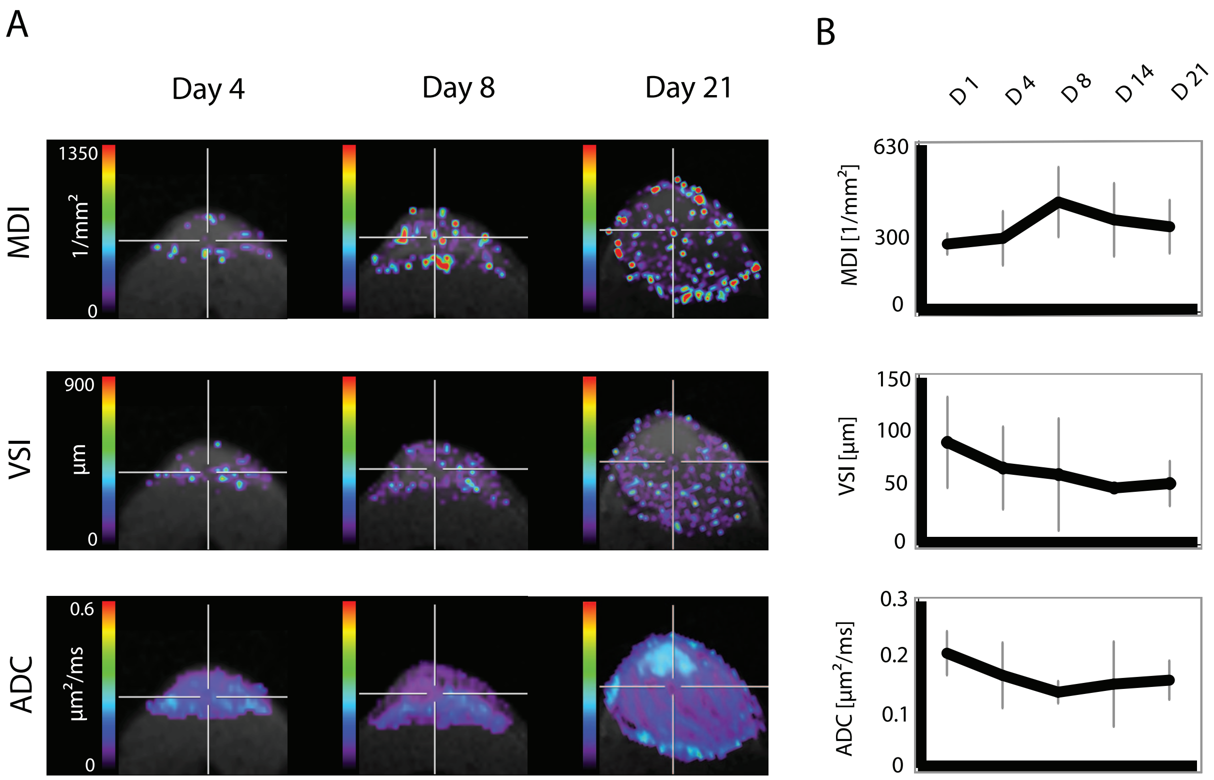

Figure 3. Longitudinal investigation of vascular dynamics during tumor growth. Simultaneous in vivo monitoring of tumor depiction with T2-weighted imaging, microvessel density (MDI), vessel size (VSI) and apparent diffusion coefficient (ADC) during tumor growth on day 1, day 4, day 8, day 14, and day 21 (D1, D4, D8, D14, D21).
doi:10.1371/journal.pone.0019592.g003

protocol permitting simultaneous monitoring of tumor vessel size (VSI) and tumor microvessel density (MDI). We show that the values obtained by the MDI map reflect the microvessel density as assessed by immunohistochemical CD31 staining. Most importantly, the MDI allows to monitor PTK787 induced reduction in microvessel density as early as 6 days after start of treatment. Finally, repetitive MR imaging reveals a shift of vessel diameter toward larger lumen in PTK787 treated tumors in vivo.

Currently, there are numerous anti-angiogenic agents in clinical trials ([14]; http://www.cancer.gov/clinicaltrials). Likewise, new imaging modalities are required that allow to monitor tumor microvessel density growth and the detection of anti-angiogenic treatment effects. As reported previously, MR imaging offers the detection of capillaries with a diameter of 10 to 30 μm, reflecting the range of the diameter of tumor microvessels [6,10]. Jensen [15] first proposed the Q-map for the assessment of microvessel density in vivo. Based on this approach, Wu et al found reasonable Q-map values within the healthy mouse brain when comparing the results with histological analysis [16]. However, as indicated by Jensen in 2006 [15], the diffusion within the tissue affects the calculation of microvessel density (cf. Eq. 3). This is particularly true for tumor tissue since the diffusion within the tumor is highly variable. Therefore, we established a new protocol for vessel density imaging that includes the ADC map, to take the function of the diffusion heterogeneity within the tumor into consideration for the determination of the MDI. Herewith, we received a clear improvement of the vessel density values, as demonstrated with the significant correlation to the microvessel density assessed by immunohistochemistry. Of note, the same calculation without the ADC map showed no correlation to immunohistochemically assessed by microvessel density (data not shown).

Table 1. Percent changes (relative to day 0) in T2, MDI, VSI and ADC values after 6 days and 13 days of PTK787/vehicle treatment.

	PTK787 treated				*Vehicle treated*			
	day 6		**day 13**		**day 6**		**day 13**	
	Mean	**SD**	**mean**	**SD**	**mean**	**SD**	**mean**	**SD**
T2	−4.79	3.85	−0.93	16.85	−5.69	5.08	−22.55	16.85
MDI	−225.10	169.88	−199.52	104.80	41.30	2.17	−3.82	23.22
VSI	−15.85	64.90	31.63	26.60	−194.20	45.30	−53.10	87.90
ADC	−14.61	18.32	11.71	11.45	0.22	26.72	2.84	18.97

doi:10.1371/journal.pone.0019592.t001

The theoretical description of Kiselev et al [11] has been made for a single echo experiment. Nevertheless, multi echo experiments were used to calculate the Q-maps or the VSI [17]. The gradients for the 180 degree pulses induce diffusion weighting. By using multi spin echo sequences this diffusion weighting is usually not considered. Therefore, the calculation of delta R2 via the fitting on multi echo sequences leads to incorrect results for the VSI and MDI. Thus, we applied the correction factor as suggested by

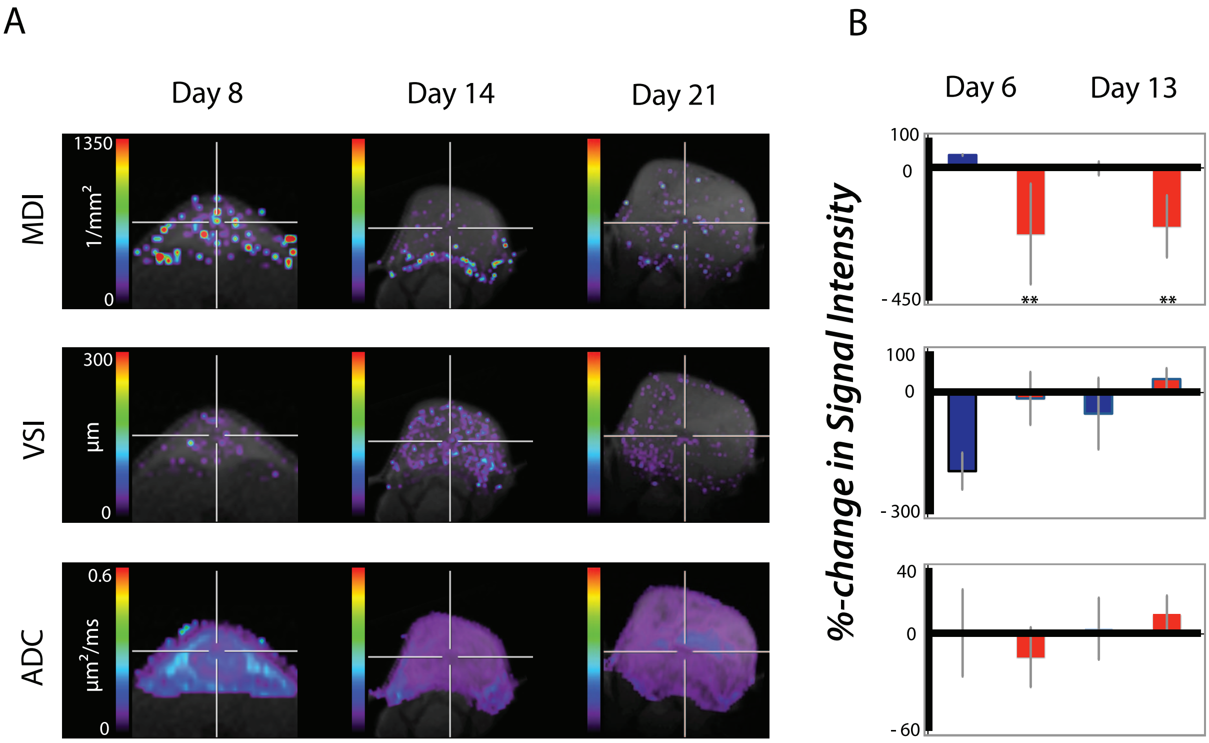

Figure 4. Effect of treatment on tumor angiogenesis. (A) Monitoring PTK787 treatment effects on changes in tumor microvessel density index (MDI), tumor vessel size (VSI) and apparent diffusion coefficient (ADC) during tumor growth and treatment. PTK787 treatment started at day 8 after tumor inoculation. (B) Quantitative analysis of vascular variables after 6 days and 13 days of PTK787 treatment. The blue bars represent the vehicle treated tumors and the red bars the PTK787 treated tumors.
doi:10.1371/journal.pone.0019592.g004

Kiselev [12] to take the diffusion weighting into account. As the correction factor is considered in the formula (3) and (4) both the second and the third echo can be used. However, by using further 180°-pulses we found an increase of the obtained MDI that did not reflect the results from the immunohistochemistry. Thus, we conclude that it is important to use a spin echo sequences with the appropriate echo time to calculate the MDI and VSI.

We have presented a new strategy for the simultaneous estimation of the vessel size index (VSI) and the microvessel density index (MDI) by the use of a multi spin echo sequence. With this tool, we could demonstrate in vivo that in untreated tumors the decrease in the mean tumor vessel size is paralleled by an increase in microvessel density. These findings are in line with a study by Drevs et al. [18] who observed a shift of vessel diameter toward larger lumen in PTK787 treated tumors in comparison to the vehicle group in vitro. This observation is reasonable since it reflects the sprouting of smaller tumor microvessels from pre-existing larger vessels during tumor growth that is inhibited by PTK787.

After 6 days of PTK787 treatment, we found a decrease in the ADC value. It is well known that inhibition of VEGF/VEGFR2 results in a reduction in vascular permeability [19]. We hypothesize that the PTK787 induced decline in vessel permeability reduces interstitial edema and, thus, intra-tumoral diffusion that is reflected by the observed decrease in ADC map. Moreover, after 13 days of treatment there was again a slight increase in the ADC value most probably due to necrotic tumor transformation [20,21,22,23].

Finally, we have demonstrated that the MDI method permits the characterization of microvessel density in vivo in longitudinal studies. Further, the MDI detected the PTK787 treatment induced reduction of microvessel density as early as 6 days of treatment. This is of high clinical interest since it allows for monitoring effects of anti-angiogenic treatments based on the growth and sprouting of tumor microvessels. Of note, the iron oxide nanoparticle Endorem^{R} is a true intravascular contrast agent with a long plasma half-life (T1/2>2.5 h) [24], already approved for human use. Severe side effects have been reported for the gadolinium based contrast agents [25]. Thus, Endorem represents a highly promising contrast agent for clinical studies. Moreover, using Gd-complexes the changes of the signal induced by the susceptibility is weak. Since Endorem is a paramagnetic CA the changes of the local susceptibility in the steady state is much higher than induced by gadolinium complexes.

In summary, we present an in vivo imaging approach for simultaneous monitoring of tumor microvessel density (MDI) and tumor vessel size (VSI). This approach enables the early assessment of treatment effects on microvessel density as well as on tumor vessel size. Thus, this imaging method bears high potential for monitoring anti-angiogenic treatment effects in preclinical and clinical trials.

Acknowledgments

We wish to acknowledge Dr Kiselev (University of Freiburg) for fruitful discussions and calculations. We thank Stefan Wecker and Jörg Seehafer (medres, Cologne) for support in the technical setup and Daniel Kalthoff for helpful discussions.

Author Contributions

Conceived and designed the experiments: RTU MH JFJ PB-S SV. Performed the experiments: RTU JFJ PB-S MU MD. Analyzed the data: RTU JFJ PB-S. Contributed reagents/materials/analysis tools: RTU MH MU SV. Wrote the paper: RTU JFJ PB-S MH.

References

1. Folkman J (1995) Angiogenesis in cancer, vascular, rheumatoid and other disease. Nat Med 1: 27–31.
2. Carmeliet P (2005) Angiogenesis in life, disease and medicine. Nature 438: 932–936.
3. Wong CI, Koh TS, Soo R, Hartono S, Thng CH, et al. (2009) Phase I and biomarker study of ABT-869, a multiple receptor tyrosine kinase inhibitor, in patients with refractory solid malignancies. J Clin Oncol 27: 4718–4726.
4. Drevs J, Siegert P, Medinger M, Mross K, Strecker R, et al. (2007) Phase I clinical study of AZD2171, an oral vascular endothelial growth factor signaling inhibitor, in patients with advanced solid tumors. J Clin Oncol 25: 3045–3054.
5. Dennie J, Mandeville JB, Boxerman JL, Packard SD, Rosen BR, et al. (1998) NMR imaging of changes in vascular morphology due to tumor angiogenesis. Magn Reson Med 40: 793–799.
6. Jensen JH, Chandra R (2000) MR imaging of microvasculature. Magn Reson Med 44: 224–230.
7. Eis M, Els T, Hoehn-Berlage M (1995) High resolution quantitative relaxation and diffusion MRI of three different experimental brain tumors in rat. Magn Reson Med 34: 835–844.
8. Ullrich RT, Zander T, Neumaier B, Koker M, Shimamura T, et al. (2008) Early detection of erlotinib treatment response in NSCLC by 3′-deoxy-3′-[F]-fluoro-L-thymidine ([F]FLT) positron emission tomography (PET). PLoS One 3: e3908.
9. Cizek J, Herholz K, Vollmar S, Schrader R, Klein J, et al. (2004) Fast and robust registration of PET and MR images of human brain. Neuroimage 22: 434–442.
10. Tropres I, Grimault S, Vaeth A, Grillon E, Julien C, et al. (2001) Vessel size imaging. Magn Reson Med 45: 397–408.
11. Kiselev VG, Posse S (1999) Analytical model of susceptibility-induced MR signal dephasing: effect of diffusion in a microvascular network. Magn Reson Med 41: 499–509.
12. Kiselev VG (2010) Spin Echo Amplitude in Biological Tissue with Implications for Vessel Size Imaging. Joint Annual Meeting ISMRM-ESMRMB, Stockholm (01-07052010) 1: 1792 (Proc.).
13. Zwick S, Strecker R, Kiselev V, Gall P, Huppert J, et al. (2009) Assessment of vascular remodeling under antiangiogenic therapy using DCE-MRI and vessel size imaging. J Magn Reson Imaging 29: 1125–1133.
14. Ivy SP, Wick JY, Kaufman BM (2009) An overview of small-molecule inhibitors of VEGFR signaling. Nat Rev Clin Oncol 6: 569–579.
15. Jensen JH, Lu H, Inglese M (2006) Microvessel density estimation in the human brain by means of dynamic contrast-enhanced echo-planar imaging. Magn Reson Med 56: 1145–1150.
16. Wu EX, Tang H, Jensen JH (2004) High-resolution MR imaging of mouse brain microvasculature using the relaxation rate shift index Q. NMR Biomed 17: 507–512.
17. Lin CY, Chang C, Cheung WM, Lin MH, Chen JJ, et al. (2008) Dynamic changes in vascular permeability, cerebral blood volume, vascular density, and size after transient focal cerebral ischemia in rats: evaluation with contrast-enhanced magnetic resonance imaging. J Cereb Blood Flow Metab 28: 1491–1501.
18. Drevs J, Muller-Driver R, Wittig C, Fuxius S, Esser N, et al. (2002) PTK787/ZK 222584, a specific vascular endothelial growth factor-receptor tyrosine kinase inhibitor, affects the anatomy of the tumor vascular bed and the functional vascular properties as detected by dynamic enhanced magnetic resonance imaging. Cancer Res 62: 4015–4022.
19. Jain RK (2005) Normalization of tumor vasculature: an emerging concept in antiangiogenic therapy. Science 307: 58–62.
20. Huang MQ, Pickup S, Nelson DS, Qiao H, Xu HN, et al. (2008) Monitoring response to chemotherapy of non-Hodgkin's lymphoma xenografts by T(2)-weighted and diffusion-weighted MRI. NMR Biomed 21: 1021–1029.
21. Valonen PK, Lehtimaki KK, Vaisanen TH, Kettunen MI, Grohn OH, et al. (2004) Water diffusion in a rat glioma during ganciclovir-thymidine kinase gene therapy-induced programmed cell death in vivo: correlation with cell density. J Magn Reson Imaging 19: 389–396.
22. Chenevert TL, McKeever PE, Ross BD (1997) Monitoring early response of experimental brain tumors to therapy using diffusion magnetic resonance imaging. Clin Cancer Res 3: 1457–1466.
23. Hamstra DA, Chenevert TL, Moffat BA, Johnson TD, Meyer CR, et al. (2005) Evaluation of the functional diffusion map as an early biomarker of time-to-progression and overall survival in high-grade glioma. Proc Natl Acad Sci U S A 102: 16759–16764.
24. Schwarz AJ, Reese T, Gozzi A, Bifone A (2003) Functional MRI using intravascular contrast agents: detrending of the relative cerebrovascular (rCBV) time course. Magn Reson Imaging 21: 1191–1200.
25. Wertman R, Altun E, Martin DR, Mitchell DG, Leyendecker JR, et al. (2008) Risk of nephrogenic systemic fibrosis: evaluation of gadolinium chelate contrast agents at four American universities. Radiology 248: 799–806.

Non-invasive imaging of glioma vessel size and densities in correlation with tumour cell proliferation by small animal PET and MRI

II

Eur J Nucl Med Mol Imaging
DOI 10.1007/s00259-013-2464-1

ORIGINAL ARTICLE

Non-invasive imaging of glioma vessel size and densities in correlation with tumour cell proliferation by small animal PET and MRI

Thomas Viel · Philipp Boehm-Sturm · Sara Rapic · Parisa Monfared · Bernd Neumaier · Mathias Hoehn · Andreas H. Jacobs

Received: 8 March 2013 / Accepted: 9 May 2013
© Springer-Verlag Berlin Heidelberg 2013

Abstract
Purpose Angiogenesis is a key event in the progression of glioblastomas (GBM). Our goal was to measure different anatomical and physiological parameters of GBM vessels using steady-state contrast-enhanced magnetic resonance imaging (SSCE-MRI), together with the assessment of biochemical parameters on GBM proliferation and angiogenesis using [^{11}C]methyl-L-methionine (MET) and 3′-deoxy-3′-[^{18}F]fluorothymidine (FLT) and positron emission tomography (PET). We focused on how these anatomical and biochemical read-outs correlate with one another and with immunohistochemistry.

Methods SSCE-MRI together with ^{11}C-MET and ^{18}F-FLT PET were performed 3 weeks after intracranial implantation of human GBM spheroids in nude rats (n=8). Total cerebral blood volume (tCBV), blood volume present in microvessels (μCBV), vessel density and size were calculated. Rats were treated with bevacizumab (n=4) or vehicle (n=4) for 3 weeks. Imaging was repeated at week 6, and thereafter immunohistochemistry was performed.

Results Three weeks after implantation, MRI showed an increase of vessel density and μCBV in the tumour compared to the contralateral brain. At week 6, non-treated rats showed a pronounced increase of ^{11}C-MET and ^{18}F-FLT tumour uptake. Between weeks 3 and 6, tCBV and vessel size increased, whereas vessel density and μCBV decreased. In rats treated with bevacizumab μCBV values were significantly smaller at week 6 than in non-treated rats, whereas the mean vessel size was higher. Accumulation of both radiotracers was lower for the treated versus the non-treated group. Most importantly, non-invasive measurement of tumour vessel characteristics and tumour proliferation correlated to immunohistochemistry findings.

Conclusion Our study demonstrates that SSCE-MRI enables non-invasive assessment of the anatomy and physiology of the vasculature of experimental gliomas. Combined SSCE-MRI and ^{11}C-MET/^{18}F-FLT PET for monitoring biochemical markers of angiogenesis and proliferation in addition to vessel anatomy could be useful to improve our understanding of therapy response of gliomas.

Keywords Glioblastoma · Angiogenesis · Proliferation · MRI · PET

Thomas Viel and Philipp Boehm-Sturm contributed equally to this work.

Electronic supplementary material The online version of this article (doi:10.1007/s00259-013-2464-1) contains supplementary material, which is available to authorized users.

T. Viel · S. Rapic · P. Monfared · A. H. Jacobs
European Institute for Molecular Imaging (EIMI) and Department of Nuclear Medicine of the University Hospital of Münster,
Westfälische Wilhelms-Universität (WWU),
Münster, Germany

T. Viel · P. Boehm-Sturm · S. Rapic · P. Monfared · B. Neumaier · M. Hoehn · A. H. Jacobs
Max Planck Institute for Neurological Research,
Cologne, Germany

A. H. Jacobs
Department of Geriatric Medicine, Evangelische Kliniken,
Johanniter Krankenhaus,
Bonn, Germany

A. H. Jacobs (✉)
European Institute for Molecular Imaging (EIMI),
Westfälische Wilhelms-Universität Münster (WWU),
Technologiehof, Mendelstr. 11, 48149 Münster, Germany
e-mail: ahjacobs@uni-muenster.de

Published online: 11 June 2013

Introduction

Treatment of patients with glioblastoma (GBM) remains challenging, and mean survival of these patients is currently limited to 1–3 years [1]. Due to the essential role of angiogenesis during tumour development, treatments targeting vascular development are being evaluated in preclinical and clinical studies [2, 3]. However, despite promising results in animal models [4], anti-angiogenic treatments in patients with gliomas may result in tumour resistance and the development of an infiltrative tumour phenotype [5]. Therefore, non-invasive molecular imaging methods allowing a longitudinal assessment of the tumour vasculature together with tumour proliferation and progression are essential to fully understand the dynamic changes of gliomas during therapy [6, 7].

Dynamic contrast-enhanced MRI (DCE-MRI) is in clinical use for the assessment of brain tumour vasculature [8]. DCE-MRI measures changes in T1, T2 or T2* relaxivity due to leakage of a contrast agent into the extravascular space [9]. Adapted MR sequences allow the calculation of parameters such as blood or plasma volume, fraction of the extravascular/extracellular space, blood-to-tissue transfer constant or blood flow [10]. Another approach was introduced by Dennie et al. based on the ratio of gradient and spin echo relaxation rate changes ($\Delta R^*_2/\Delta R_2$) after injection of an iron oxide-based superparamagnetic contrast agent of high molecular weight [11]. Since $\Delta R2^*/\Delta R2$ increases with increasing vessel size, this method enables calculation of the average vessel size within a voxel, which reveals an additional important parameter of the angiogenic process. Based on these findings, Jensen and Chandra proposed to map the ratio of $Q = \Delta R_2/(\Delta R^*_2)^{2/3}$. Indeed, for a certain threshold of the concentration of the contrast agent, in combination with appropriate echo times, Q has the advantage of being independent of the concentration of the contrast agent [12]. Q depends only on intrinsic tissue properties such as water diffusivity and has been shown to correlate with vessel density [13, 14]. Recently, Ullrich et al. improved the imaging protocols for vessel density and size calculation by including diffusion-weighted MR sequences to take into account that diffusion is not homogeneous inside tumour tissue [15].

In the current study, we evaluated the use of steady-state contrast-enhanced MRI (SSCE-MRI) sequences developed by Ullrich et al. [15] in an intracranial rat model of human GBM. We combined SSCE-MRI with [^{11}C]methyl-L-methionine (MET) and 3′-deoxy-3′-[^{18}F]fluorothymidine (FLT) small animal positron emission tomography (PET). The overall purpose of the study was to assess how the physiological read-outs obtained by MRI correlate with the biochemical read-outs obtained by PET at various biological tumour stages and in response to an anti-angiogenic treatment. It should be pointed out that the focus of this work was the evaluation of the imaging methodologies with validation of the imaging findings by immunohistochemical methods. The results concerning the use of these imaging techniques for monitoring response to bevacizumab should be regarded as preliminary.

Materials and methods

Tissue culture

Tissue samples from a human glioblastoma were minced into ~0.5 mm fragments and placed into 80 cm^2 tissue culture flasks (Nunc) base-coated with 0.75 % agar (Difco). The spheroids were maintained in a standard tissue culture incubator with 5 % CO_2 and 100 % relative humidity at 37 °C. Spheroids with diameters between 400 and 600 μm were selected for intracerebral implantation.

Animal experiments

All animal procedures were in accordance with the German Laws for Animal Protection and were approved by the local animal care committees. Nude rats were housed at constant temperature (23 °C) and relative humidity (40 %), under a regular light/dark schedule. Food and water were freely available.

Intracranial implantation of glioblastoma spheroids into the cortex of nude rats (n=8) was performed as described previously [16]. Three weeks after spheroid implantation, sequential small animal PET and MRI were performed. Thereafter, rats were divided into two groups. Rats in the first group received weekly intravenous (i.v.) injections of 10 mg/kg bevacizumab (Roche, Mannheim, Germany), whereas rats in the second group were injected with saline (100–150 μl). After 3 weeks of treatment, sequential small animal PET/MRI were performed again on each rat, except for one non-treated rat, which died before the final ^{11}C-MET PET. After the last imaging session, rats were deeply anaesthetized and perfused transcardially with saline for 5 min, followed by 4 % paraformaldehyde (PFA) for 2 min. Brains were post-fixed in PFA overnight.

Small animal PET

Rats were anaesthetized with isoflurane (induction 3.0 %, maintenance 1.0–2.0 %; DeltaSelect) vaporized in a mix of O_2 and N_2O (1:2). Body temperature was measured using a rectal probe and maintained at 37 °C using a feedback controlled system (medres, Cologne, Germany). Rats were imaged using a R4 microPET scanner (Concorde Microsystems, Inc., Knoxville, TN, USA).

Radiochemical synthesis of ^{11}C-MET and ^{18}F-FLT was performed as described previously [17, 18]. No-carrier-added ^{11}C-MET was injected i.v. at a dose of 30 MBq/rat. Small animal PET images were acquired over 30 min, starting 20 min after tracer injection. No-carrier-added ^{18}F-FLT was administered i.v. at a dose of 15 MBq/rat, and small animal PET images were acquired over 30 min, starting 60 min after tracer injection. Every scan was followed by a 10-min transmission scan using a ^{57}Co source to correct for attenuation.

PET data were reconstructed using two-dimensional filtered backprojection with a ramp filter and corrected for photon attenuation.

Small animal MRI

Rats were anaesthetized with isoflurane. A tail vein catheter was put in place for i.v. injections during MRI acquisition. Body temperature was measured using a rectal probe and maintained at 37 °C using a feedback controlled system (medres, Cologne, Germany). MRI was conducted on a 7.0 T BioSpec animal scanner (Bruker BioSpin, Ettlingen, Germany) with 20-cm wide actively shielded gradient coils (200 mT/m). Radiofrequency transmission was achieved with home-built Helmholtz coils (12 cm diameter); signal was detected using a 2.2-cm surface coil.

The following protocol was applied: a gradient echo pilot scan was performed for accurate positioning of the animal. Afterwards, a spin echo diffusion map, a T2 map and a T2* map were acquired. Thereafter, the rat was injected i.v. with superparamagnetic iron oxide (SPIO) nanoparticles (30 mg/kg Fe, Endorem, Guerbet, Paris, France). After 2 min delay to ensure a steady-state distribution of contrast agent in the vascular network, a second T2 map was acquired, followed by a second T2* map.

Spin echo diffusion maps were acquired with the following acquisition parameters: field of view (FOV) = 2.56×2.56 cm^2, image matrix = 128×64, reconstructed to 128×128 (isotropic in-plane resolution of 200 μm), 8 consecutive slices of 1 mm, echo time (TE) = 40.7 ms, repetition time (TR) = 4,000 ms, excitation/refocusing flip angle (FA) = 90°/180°, 1 diffusion direction medial-lateral in the animal coordinate system, effective b values = 0.26, 600.26 and 1,500.26 s/mm^2 and total acquisition time (TA) = 12:48 min.

T2-weighted (T2w) images/T2 maps were acquired using a multislice multiple spin echo sequence: FOV = 2.56×2.56 cm^2, image matrix = 128×128 (isotropic in-plane resolution of 200 μm), 12 consecutive slices of 1 mm (geometry of central 8 slices identical to diffusion map), echo time spacing (ΔTE) = 13.6 ms, 10 equidistant echo images, TR = 4,000 ms, FA = 90°/180° and TA = 8:32 min.

T2*-weighted (T2*w) images/T2* maps were acquired using a multiple gradient echo sequence: geometry identical to T2 maps, ΔTE = 5.0 ms, 8 equidistant echo images, TR = 2,000 ms, FA = 60°, 2 averages and TA = 8:32 min.

MRI data processing

MRI data sets of each imaging session were coregistered with a rigid body linear transformation to the first echo image of the multiple spin echo scan pre-SPIO injection using FMRIB Software Library (http://www.fmrib.ox.ac.uk/fsl/).

MR images were further processed with custom scripts written in Interactive Data Language (IDL, ITT Visual Information Solutions, Boulder, CO, USA). T2 and T2* maps were fitted voxel-wise with a monoexponential decay curve $S(TE) = A*\exp(-TE/B) + C$, with equilibrium signal A, relaxation time B = T2 (T2*), signal in each echo image S(TE) and a constant offset C to reduce bias in areas with low signal to noise ratio (SNR) [19]. Apparent diffusion coefficient (ADC) maps were calculated by fitting a monoexponential decay curve $S(b) = A*\exp(-b*ADC) + C$ to the signal intensities S(b) for different b values (A is the equilibrium signal and C an offset constant).

ΔR_2 [relative blood volume present in microvessels (μCBV)], ΔR_2^* [relative total cerebral blood volume (tCBV)], microvascular density index (MDI) and vessel size index (VSI) were calculated as described before [15, 20]. As we did not measure the iron concentration in the blood, we used a dimensionless VSI, defined as $VSI = (ADC/D_{lit})^{1/2}*(\Delta R_2^*/\Delta R_2)^{3/2}$. The first term denotes the local variation of ADC from an average diffusivity value in the healthy rat brain (D_{lit} = 664 μm^2/s) reported previously in the literature [21].

To ensure sufficient quality of the underlying data, voxels with an SNR < 5 in the b = 0.26 s/mm^2 image (diffusion sequence) or first echo image (all T2 and T2* map sequences) were excluded from the analysis. Furthermore, thresholding was applied to voxels with non-physical values $\Delta R_2 < 0$, $\Delta R_2^* < 0$ or $\Delta R_2^* < \Delta R_2$. At week 3, 6±7 % of the voxels within tumours had to be excluded in the tCBV, μCBV, vessel size and vessel density maps. At week 6, the percentage of excluded voxels was 9±10 % for the non-treated rats and 21±20 % for the treated rats where more necrosis and dilated vessels were observed.

PET and MRI data analysis

Coregistration of the different PET and MR images was performed using the VINCI software (Vinci v 2.55; http://www.nf.mpg.de/vinci3/) [22]. T2w images were used to delineate the tumours and to draw the volumes of interest (VOI). Reference regions were mirror regions of the tumours drawn in the contralateral brain hemisphere in order to determine tumour to background (T/B) ratios. PET images were analysed using VINCI in order to determine the maximal and mean per cent of injected dose per cm^3 (%ID/cm^3) in the tumours and in the reference regions. Quantification of the mean tumour and contralateral brain hemisphere values on T2, ADC, μCBV, tCBV, vessel size and vessel density maps was performed using ImageJ (ImageJ 1.46o; Rasband WS, ImageJ, NIH, http://rsb.info.nih.gov/ij).

Immunostaining of paraffin sections

Rat brains fixed in 4 % PFA were embedded in paraffin, cut in 5-μm sections and prepared for immunohistochemical analyses (three of four non-treated and three of four treated rats). After rehydrating and heat-induced epitope retrieval for 30 min in citrate buffer (pH 6.0), sections were incubated in peroxidase blocking solution (S3022, DAKO, Hamburg, Germany) for 5 min and treated with serum-blocking solution for 15 min. Sections were incubated overnight at 4 °C with monoclonal rabbit anti-Ki-67 antibody (dilution 1:100; SP6, ab16667, Abcam, Munich, Germany) or with polyclonal rabbit anti-von Willebrand factor (vWF, dilution 1:250; ab6994, Abcam, Munich, Germany). Labelling of the primary antibody was performed using a commercial avidin-biotin complex detection kit based on a biotinylated anti-rabbit antibody (Vector Laboratories, Lörrach, Germany) according to the manufacturer's manual followed by treatment with 3,3′-diaminobenzidine (DAB, D-5637, Sigma) for 5 min. Sections were counterstained with haematoxylin, dehydrated and mounted using Entellan (Merck, Darmstadt, Germany). Iron staining was performed using the Prussian blue-based Accustain Iron Stain kit from Sigma-Aldrich (HT20, Sigma-Aldrich, Steinheim, Germany) following the manufacturer's recommendations. For TUNEL staining, sections fixed in acetone were permeabilized in sodium citrate solution (0.1 g in 100 ml). Sample sections were incubated 60 min at 37 °C with 25 μl TUNEL reaction mixture according to the manufacturer's manual (In situ TUNEL kit assay, Roche Inc.). Sections were finally covered with 4′-6-diamidino-2-phenylindole (DAPI) containing mounting medium (Vector). Histological analysis was performed using a Nikon Eclipse 90i light microscope (Nikon, Düsseldorf, Germany) and the NIS-Elements software package (Nikon).

Quantification of Ki-67 and vWF stainings (three different areas per tumour and four per contralateral brain) was performed employing the Fiji software [23]. In brief, colour images were deconvolved (H-DAB colour deconvolution) and the resulting monochrome images were thresholded. Thereafter, the positive counts per FOV were quantified using the "Analyse particles" plugin. The total area with positive vWF staining inside the FOV was divided by the number of vWF-positive particles per FOV to calculate the average area per vessel in per cent of FOV.

Statistical analysis

Mean values ± standard deviation of MRI parameters as well as radiotracer %ID/cm^3 and T/B ratios were calculated. Student's *t* test, or Mann–Whitney rank sum test (when the variance tests failed), as well as Pearson's correlation test were performed using SigmaStat 3.0 (SPSS, Inc., Chicago, IL, USA).

Results

Tumour growth-dependent alterations of small animal PET and MRI parameters

^{11}C-MET and ^{18}F-FLT PET in addition to SSCE-MRI were performed in nude rats 3 and 6 weeks after implantation of human GBM spheroids (Fig. 1). At week 3, small tumours were detected on T2w images. Maps of μCBV and vessel density revealed higher values in the area of the tumour compared to healthy brain. Tumour vessel size at this stage was similar in tumour and healthy brain areas. At this stage, only a slight increase of ^{11}C-MET and ^{18}F-FLT uptake was observed in some tumours. At week 6, tumours were characterized by high values of tCBV, μCBV, ^{11}C-MET uptake and ^{18}F-FLT uptake compared to the contralateral brain hemisphere (Fig. 1b). In contrast, vessel density was smaller in the tumour than in healthy tissue. Images were quantified (Fig. 2, Table 1). At week 3, tCBV and μCBV T/B ratios were 1.25±0.08 and 1.17±0.02, respectively, with no significant (NS) difference between tumour and contralateral brain hemisphere. Between weeks 3 and 6, μCBV T/B ratios within the glioma were decreased from 7.2 % ($p<0.05$), while tCBV T/B ratios were increased from 40.9 % ($p<0.01$). At week 3, the VSI was 8.0±0.3 for the healthy cortex and 8.7±0.3 for the glioma tissue (Table 1; difference NS). The average microvessel density (MDI) was 655±99 mm^{-2} for the healthy cortex and 811±73 mm^{-2} for the glioma, giving a T/B ratio of 1.25±0.13 (Table 1; difference NS). The mean tumour VSI was 90.8 % higher at week 3 than at week 6, with values reaching 16.6±2.1 for the tumour tissue (T/B ratio of 2.13±0.33, $p<0.01$). On the other hand, tumour MDI was significantly decreased from 61.3 % between weeks 3 and 6. At week 6, tumour MDI was 58.9 % lower than the vascularized contralateral healthy brain (314±62 mm^{-2} for the tumour versus 770±167 mm^{-2} for the contralateral brain, $p<0.01$). This observation may be explained by high tumour cell proliferation leading to increased cell density with increased spacing between vessels (as demonstrated by Sakariassen et al. [24]) and by the presence of necrotic regions. At week 3, ^{11}C-MET maximum tumour uptake in the tumour was 0.37±0.08 %ID/cm^3 giving a T/B ratio of 1.16±0.08. At this stage, ^{18}F-FLT maximum tumour accumulation in the

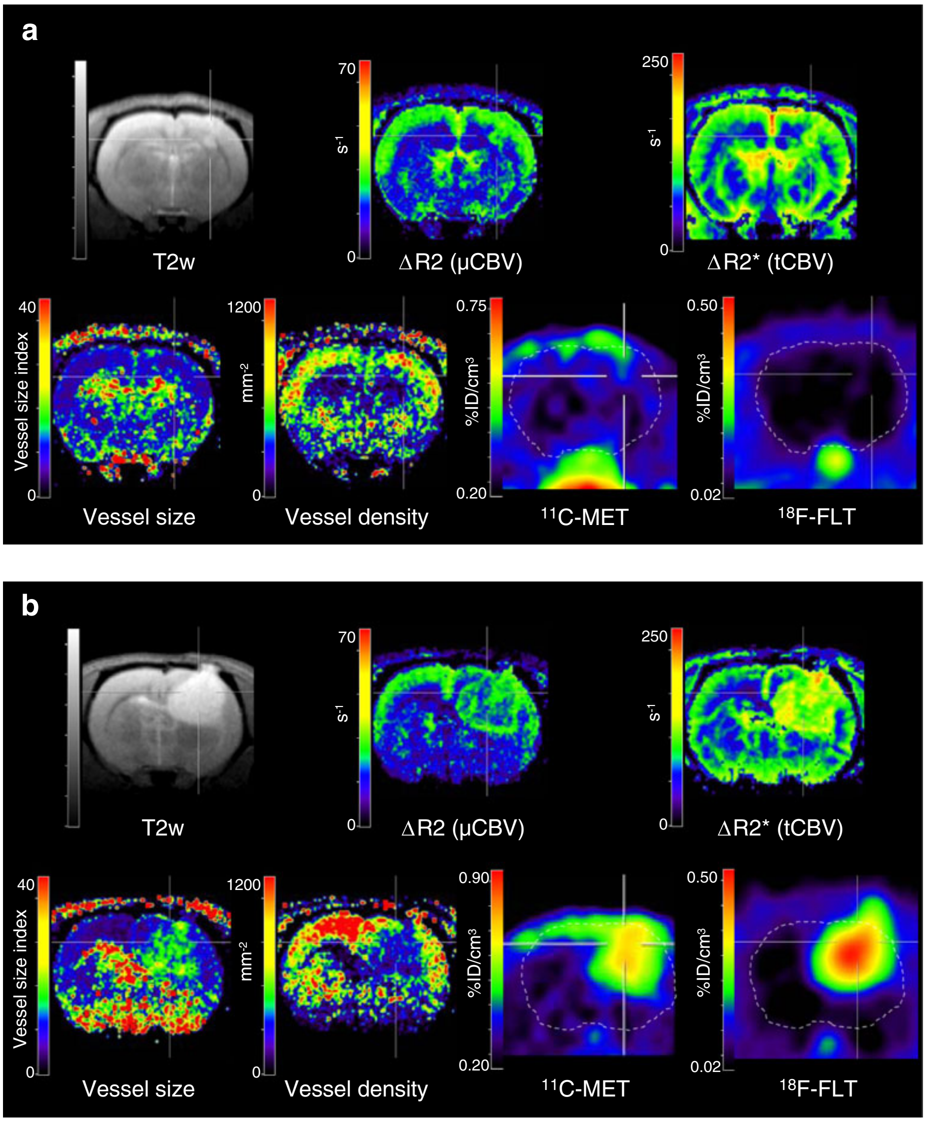
a
T2w
70
s-1
0
ΔR2 (μCBV)
250
s-1
0
ΔR2* (tCBV)
40
Vessel size index
0
Vessel size
1200
mm-2
0
Vessel density
0.75
%ID/cm3
0.20
11C-MET
0.50
%ID/cm3
0.02
18F-FLT
b
T2w
70
s-1
0
ΔR2 (μCBV)
250
s-1
0
ΔR2* (tCBV)
40
Vessel size index
0
Vessel size
1200
mm-2
0
Vessel density
0.90
%ID/cm3
0.20
11C-MET
0.50
%ID/cm3
0.02
18F-FLT

Fig. 1 Multimodal small animal PET and MRI. SSCE-MRI, ^{11}C-MET and ^{18}F-FLT PET were performed 3 (**a**) and 6 (**b**) weeks after implantation of human glioma spheroids into the brain of nude rats. MR parametric maps were calculated and coregistered with the T2w and PET images. Transaxial sections of the different coregistered images of the brain of a representative rat are presented

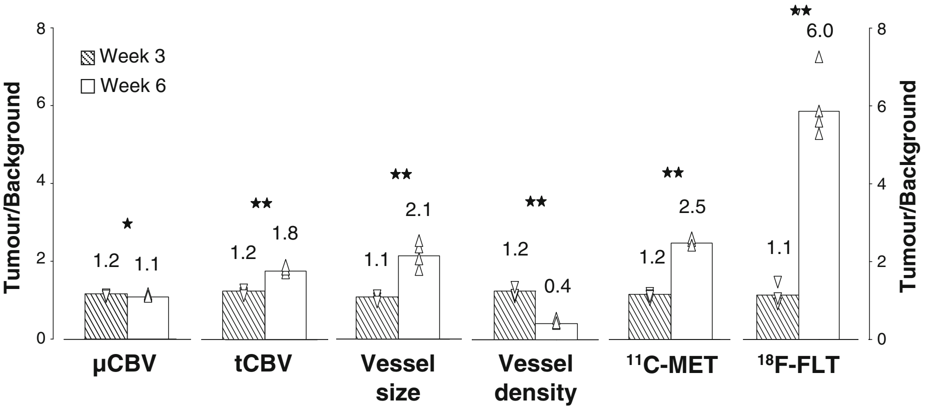

Fig. 2 Quantification of small animal PET and MR imaging results. MR maps and PET images were used to determine T/B ratios of PET tracer uptake and MR-derived parameters 3 (*striped bars*) and 6 weeks (*white bars*) after spheroid implantation in nude rats (n=4). * and **: significant difference between weeks 3 and 6 (p<0.05 and 0.01, respectively)

Table 1 Quantification of PET and MR images (mean ± standard deviation)

		Week 3		Week 6	
		Non-treated	Treated	Non-treated	Treated
Vessel size index	Tumour	8.7 ±0.3	8.7 ±0.5	16.6 ±2.1**##	28.5 ±10.7*##
	Brain	8.0 ±0.3	8.0 ±1.2	7.9 ±1.1	8.2 ±1.4
Vessel density (mm^{-2})	Tumour	810.8 ±72.6	809.8 ±204.6	314.0 ±62.4**##	206.7 ±55.1**##
	Brain	655.1 ±99.4	689.4 ±166.8	770.3 ±166.9	820.2 ±102.3
^{11}C-MET (%ID/cm^3)	Tumour	0.37 ±0.08	0.40 ±0.11	1.06 ±0.40*	0.68 ±0.09**##
	Brain	0.32 ±0.07	0.34 ±0.08	0.43 ±0.18	0.41 ±0.09
^{18}F-FLT (%ID/cm^3)	Tumour	0.12 ±0.08	0.16 ±0.03	0.75 ±0.44*#	0.44 ±0.01**##
	Brain	0.10 ±0.05	0.13 ±0.03	0.13 ±0.08	0.10 ±0.01

* and **: significant difference between weeks 3 and 6 ($p < 0.05$ and 0.01, respectively); # and ##: significant difference between tumour and contralateral brain ($p < 0.05$ and 0.01, respectively)

tumour was very low (0.12±0.08 %ID/cm^3, T/B ratio of 1.14±0.27). Tumour development between weeks 3 and 6 led to a significant ($p<0.01$) increase of ^{11}C-MET and ^{18}F-FLT maximum tumour uptake with T/B ratio reaching 2.47±0.10 and 5.96±0.87 for ^{11}C-MET and ^{18}F-FLT, respectively. The quantitative PET tracer uptake values indicated in Figs. 2, 4 and 6 and Table 1 are the maximum tumour uptake values. We chose to present the maximum uptake values for the following reasons: due to the lack of anatomical information on the PET images, the partial volume effect and the eventual presence of necrotic area, the mean tumour uptake is less robust and more observer dependent than the maximum uptake value. In addition, tumour progression can be driven by the proliferative rim of a tumour presenting therefore a high FLT maximum tumour uptake, even if the FLT mean tumour uptake is low due to the presence of central necrosis for example. However, the same conclusions can be drawn from the analyses of the mean tumour uptake values as from the analyses of the maximum tumour uptake values (Online Resources 1 and 2).

Treatment-dependent alterations of small animal PET and MRI parameters

Small animal MR and PET images were acquired for rats receiving bevacizumab between weeks 3 and 6 (Figs. 3 and 4). In some MR parametric maps (e.g. columns 3, 5 and 6), black voxels are observed in the centre of the tumour. Those voxels were excluded during post-processing due to non-physical values (SNR<5, $\Delta R2<0$, $\Delta R2^*<0$ or $\Delta R2^*<\Delta R2$). As confirmed by haematoxylin and eosin (H&E) and TUNEL staining (Fig. 5), they correspond to necrotic regions, where the assumptions of SSCE-MRI are no longer valid. The mean μCBV T/B ratio (Fig. 4a) was 25.0 % smaller in treated rats compared to non-treated rats (0.81±0.16 versus 1.08±0.03, $p<0.05$). In contrast, the mean tCBV T/B ratio for the treated group was similar to the value obtained from the non-treated rats (T/B ratio of 1.63±0.29 and 1.75±0.08, respectively, NS). The mean VSI T/B ratio was 60.6 % higher for the treated compared to the non-treated rats (T/B ratio of 3.42±0.68 for the treated rats versus 2.13±0.33 for the non-treated, $p<0.05$). In contrast, the mean tumour vessel density (MDI) T/B ratio was 39.0 % smaller for the treated versus the non-treated animals (T/B ratio of 0.25±0.07 for the treated group versus 0.41±0.06 for the non-treated, $p<0.05$). ^{11}C-MET T/B ratio uptake at week 6 was 31.2 % lower in treated rats compared to non-treated (1.70±0.18 versus 2.47±0.10;,$p<0.01$). ^{18}F-FLT T/B ratio uptake was 22.6 % smaller in treated rats compared to non-treated (4.61±0.36 versus 5.96±0.87, $p<0.05$).

^{11}C-MET and ^{18}F-FLT PET T/B ratios were plotted over MRI measures of T/B ratios of vessel density and size obtained at week 6 (Fig. 4b). A significant positive linear correlation was observed between T/B ratios of ^{11}C-MET uptake and T/B ratios of vessel density and vessel size (^{11}C-MET and vessel density: $r=0.93$, $p=0.002$; ^{11}C-MET and vessel size: $r=-0.89$, $p=0.008$, Pearson's correlation). T/B ratios of ^{18}F-FLT uptake and T/B ratios of vessel density and vessel size were also correlated, which did not reach a significant level.

Immunohistochemical analyses confirmed the results of non-invasive imaging

After the last imaging scan, rats were sacrificed for detailed immunohistochemical analyses. H&E (Fig. 5a) and TUNEL (Online Resource 3) staining revealed the presence of necrotic areas in the tumours, in particular for the treated group. Those regions presenting no viable tissue and blood vessels correspond to the regions where some voxels in the MR parametric maps had to be excluded due to small SNR or to non-physical values ($\Delta R2 < 0$, $\Delta R2^* < 0$ or $\Delta R2^* < \Delta R2$). Only very few iron particles could be observed on Prussian blue stainings (Online Resource 3) indicating that leakage of contrast agent was rather limited. Ki-67 staining (Fig. 5b) revealed active tumour cell proliferation for both groups of rats. However, proliferation as assessed by

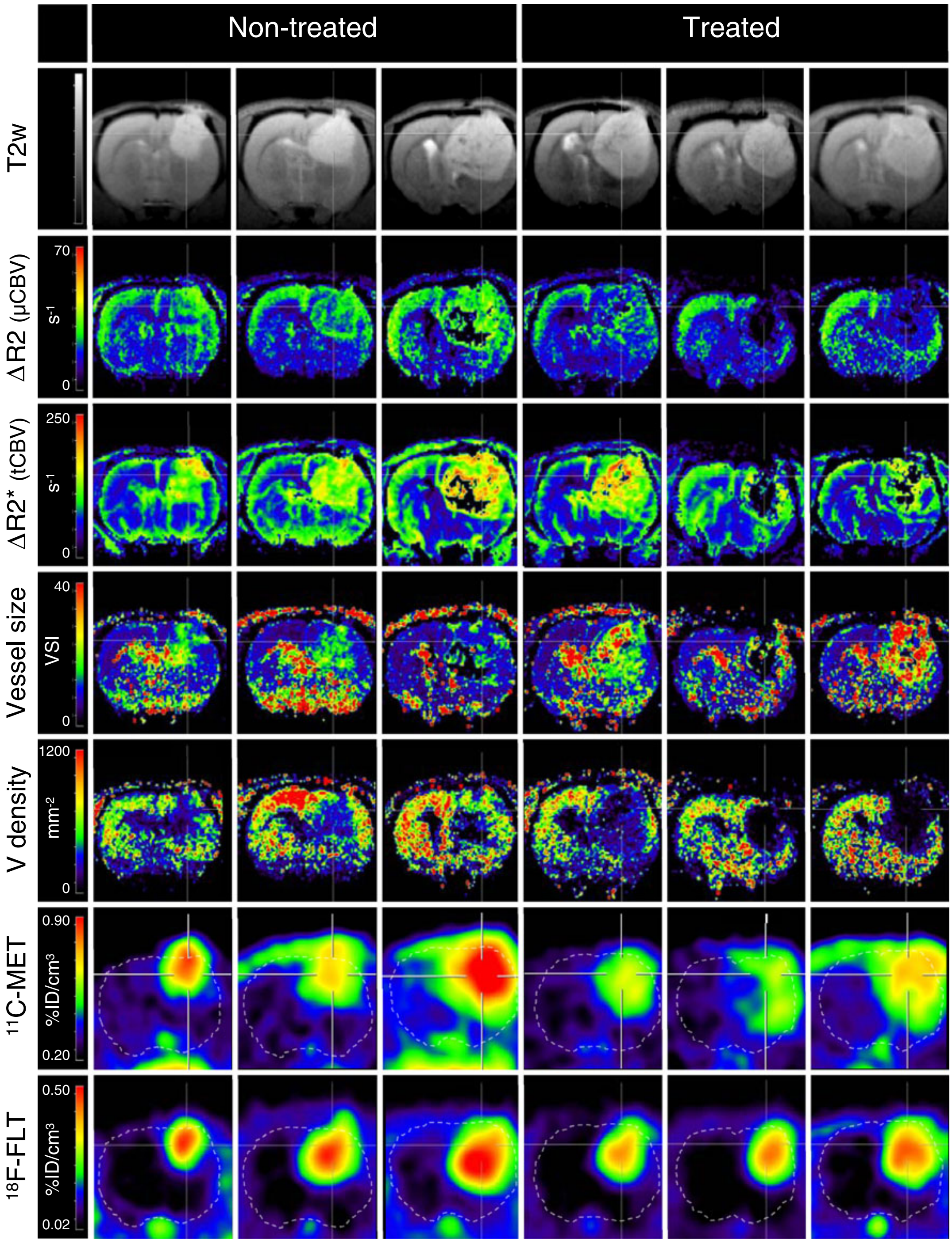
Non-treated
Treated
T2w
ΔR2 (μCBV)
s-1
70
0
ΔR2* (tCBV)
250
0
Vessel size
VSI
40
0
V density
mm-2
1200
0
11C-MET
%ID/cm3
0.90
0.20
18F-FLT
%ID/cm3
0.50
0.02

Fig. 3 Impact on vascular targeted therapy on imaging parameters. In addition to non-treated rats (columns 1–3), SSCE-MRI, ^{11}C-MET and ^{18}F-FLT PET were also performed in rats treated with bevacizumab between weeks 3 and 6 (columns 4–6). Transaxial sections of the different coregistered images of the brain of six of eight rats are presented

quantification of Ki-67 staining (Fig. 6a) was 37.5 % higher for the non-treated group than for the treated group (Ki-67 index of 0.53±0.09 versus 0.39±0.08, respectively, $p<0.01$). Ki-67 indexes were in good agreement with the ^{18}F-FLT T/B uptake values (Fig. 6c). vWF staining (Fig. 5c) revealed the presence of small and large vessels in the non-treated tumours and confirmed that the vessel density was lower in the tumour compared to the contralateral brain

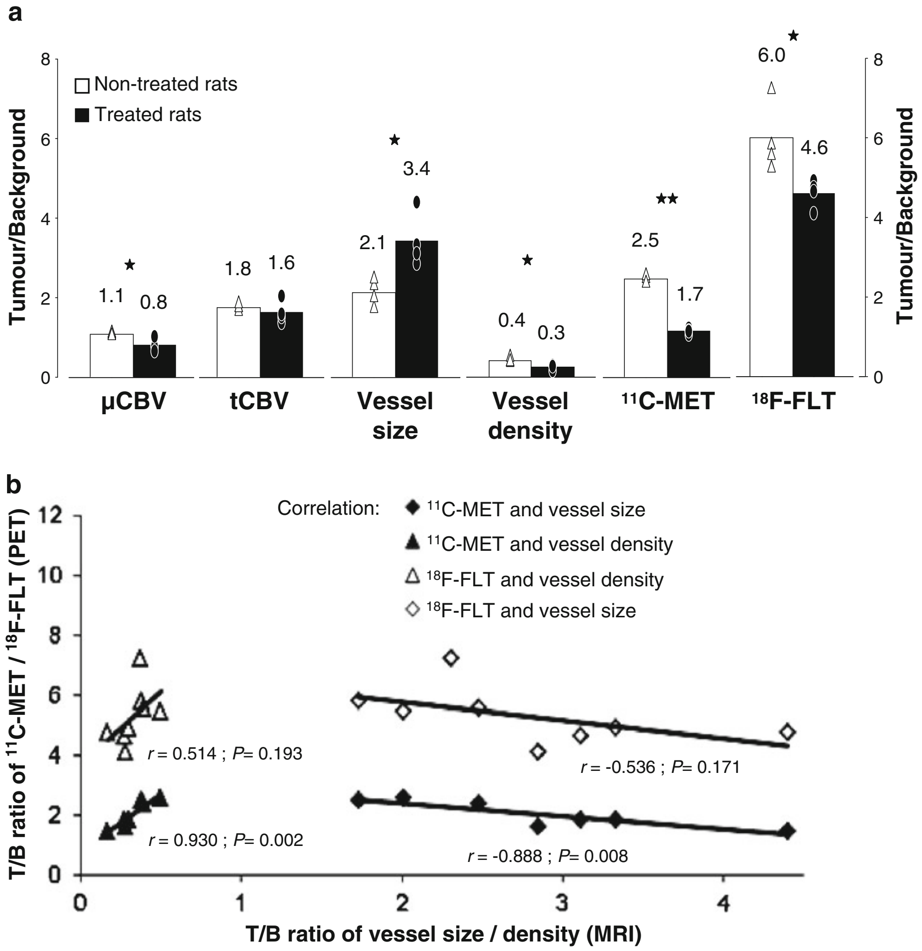

Fig. 4 Quantification of small animal PET and MR imaging results. **a** MR maps and PET images were used to determine T/B ratios of PET tracer uptake and MR-derived parameters for treated (*black bars*) or non-treated (*white bars*) rats. * and **: significant difference between treated and non-treated rats ($p<0.05$ and 0.01, respectively). **b** T/B ratios of ^{11}C-MET and ^{18}F-FLT uptake were plotted over T/B ratios of MRI measures of vessel size/density obtained at week 6. Correlation coefficients and significance were determined using Pearson's correlation analysis

hemisphere, most likely due to high tumour cell density (vWF-positive particle per FOV of 150±28 for the brain versus 108±10 for the tumour, $p<0.01$). The vessel density was 38.2 % smaller in tumour growing in treated rats than in tumour growing in non-treated animals (vWF-positive particle per FOV of 67±30 for the treated rats versus 108±10 for the non-treated tumours, $p=0.012$). On the contrary, the mean size of tumour vessels was 106.1 % higher in treated than in non-treated rats most likely due to inhibition of small vessel formation (average area per vessel in % FOV of 0.06 ±0.02 for the treated rats versus 0.03±0.01 for the non-treated tumours, $p<0.01$), confirming the MRI-derived measures (Fig. 6d).

Discussion

To our knowledge this is the first study presenting a combination of SSCE-MRI with ^{11}C-MET and ^{18}F-FLT PET in a rat model of human glioma. The presented imaging protocol enabled us to non-invasively quantify various important anatomical, physiological and biochemical features related to proliferation and neovascularization in gliomas (proliferation, amino acid uptake, cerebral blood volume, microvessel density, vessel size). PET- and MRI-derived parameters were related to each other and were in good agreement with immunohistochemical findings. Although our relatively preliminary findings warrant further confirmation, they clearly demonstrate the potential of these imaging techniques as imaging biomarkers for monitoring the therapy of patients with gliomas.

Different methods have been developed to non-invasively image GBM vasculature. In particular, MRI allows the calculation of physiological parameters such as blood volume, blood-to-tissue transfer constant, blood–brain barrier integrity or blood flow [25]. PET imaging, on the other hand, allows the measurement of biochemical parameters such as for example the concentration of $\alpha_v\beta_3$ integrin, a surrogate marker of angiogenic activity, through the use of the tracer ^{18}F-galacto-arginine-glycine-aspartic acid (RGD) [26]. As angiogenesis is a complex mechanism involving formation of abnormally dilated vessels and proliferation of microvessels [27],

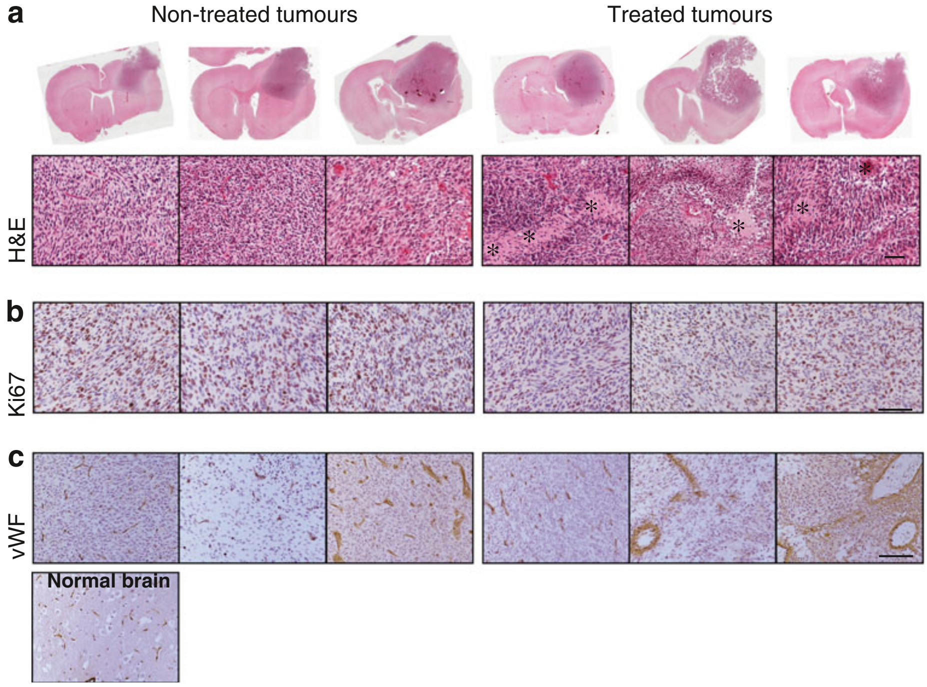

Fig. 5 Immunohistochemistry of tumour tissue from non-treated and bevacizumab-treated rats at week 6. The same rats are presented here as in Fig. 3. **a** H&E staining revealed the presence of necrotic areas (*asterisks*). **b** Ki-67 staining showed active tumour cell proliferation in the treated and in the non-treated GBM. **c** vWF staining revealed the presence of small and large vessels in the non-treated tumours and the presence of large abnormal vessels in the treated xenografts. *Scale bars* 100 μm

implementation of methods to measure the size and the density of tumour vessels can offer additional important information. Using SSCE-MRI, we found values of brain vessel density in reasonable agreement with the histological values given by Klein et al. (456–497 capillary sections/mm^2 for different cortex regions) [28]. The higher values obtained in our study may be explained by species differences (Sprague–Dawley versus nude rat) and the methodology employed for the histological determination of MDI [29]. In our glioma model, T/B ratios of tCBV and μCBV were similar at week 3 (1.25±0.08 and 1.17±0.02, respectively), indicating the appearance and proliferation of microvessels. Upon glioma development, tumour VSI was increased by a factor of 1.9, indicating progression of angiogenesis by formation of large blood vessels. The 2.1-fold higher VSI in tumour compared to normal brain observed at week 6 is in good correlation with the study of Pannetier et al. using dynamic susceptibility contrast (DSC-) and SSCE-MRI [healthy brain: VSI(SSCE) = 7.5 μm, VSI(DSC) = 6.5 μm; GBM: VSI(SSCE) = 19.4 μm, VSI(DSC) = 16.6 μm] [14]. On the other hand, the vessel density significantly decreased from 61.3 % over time in the densely packed gliomas. This result confirms the observation of von Baumgarten et al. [30]. Using intravital microscopy, the authors observed an augmentation of the vessel diameter and vascular volume upon glioma development together with a reduction of the number of vessel branches. Although a good agreement was observed between imaging-derived parameters and immunohistochemistry, the validation of the presented methods warrants further extended studies. In particular, the approximations underlying the SSCE-MRI theoretical model (e.g. vascular network idealized as a random distribution of infinite length cylinders, low blood volume fraction and contrast agent assumed to be truly intravascular) need to be further addressed [13, 31].

The mean tumour vessel density obtained from the rats receiving bevacizumab was 34.2 % smaller than the values measured in non-treated rats ($p<0.05$), whereas the mean tumour vessel size was 71.7 % higher (NS). These results indicate that bevacizumab treatment may prevent the formation of new small vessels in the presented model. Reduction of microvessels in tumours treated with anti-angiogenic molecules was also observed in previous studies employing immunohistochemistry and electron microscopy [32], two-photon intravital microscopy [30] and SSCE-MRI [15]. It should be recalled, however, that our aim was the detailed evaluation of the imaging methodologies. Results concerning imaging of the response of gliomas to bevacizumab, although in good agreement with previously published work [15, 30, 32], should be regarded as preliminary due to the small sample size of animals. The use of rodents to study GBM angiogenesis suffers from the intrinsic limitation coming from the difference between rodent and human vasculature. Combination of bevacizumab, mainly targeting the vascular endothelial growth factor (VEGF) produced by the human tumour cells, with an antibody targeting the rat VEGF may improve the experimental treatment design and be closer to the clinical situation. The methodologies presented in this manuscript, in combination with other methods of vascular imaging, have a determinant role in characterizing the rodent vascular

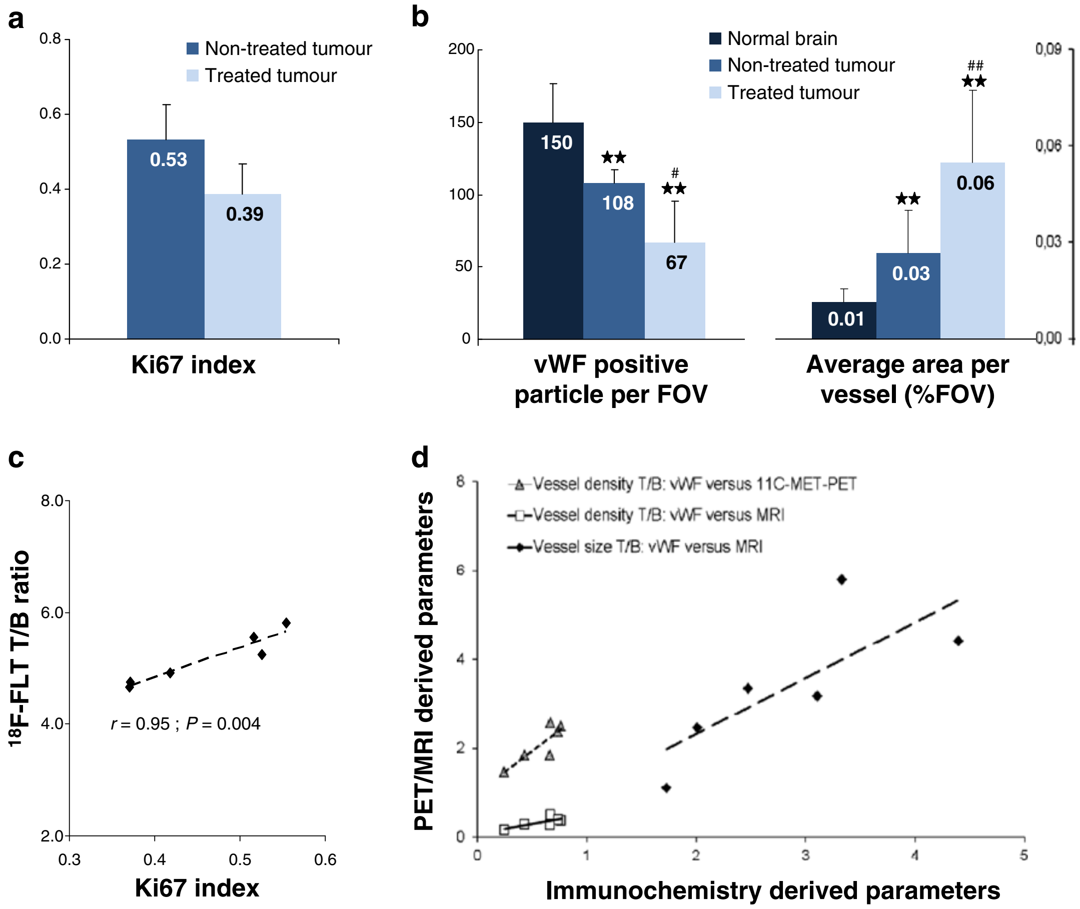

Fig. 6 Quantification of vWF and Ki-67 immunostaining is in good agreement with the in vivo imaging results. **a** Determination of Ki-67 index indicated that proliferation was higher for the non-treated group. **b** The number of tumour vessels per FOV was smaller in the treated compared to the non-treated rats, while the average area per vessel was higher. **c** Ki-67 indexes were in good agreement with the T/B ratios of ^{18}F-FLT uptake. **d** vWF staining was in good agreement with the vessel size/density as determined by SSCE-MRI. T/B ratios of vessel density derived from the immunohistochemistry were correlated with T/B ratios of ^{11}C-MET uptake. * and **: significant difference between tumour and contralateral brain tissue ($p<0.05$ and 0.01, respectively). # and ##: significant difference between treated and non-treated tumours ($p<0.05$ and 0.01, respectively). Correlation coefficients and significance were determined using Pearson's correlation analysis

network and understanding possible discrepancies between preclinical and clinical results.

In addition, it should be pointed out that the measurement of tumour vasculature may not be sufficient to evaluate the efficacy of anti-angiogenic treatments in GBM. Indeed, GBM are able to progress through angiogenic-independent mechanisms [5, 33]. We therefore combined SSCE-MRI with ^{11}C-MET and ^{18}F-FLT PET. At early stages, ^{11}C-MET uptake in the tumour is slightly higher than in normal brain, whereas almost no contrast could be seen on ^{18}F-FLT images. Low ^{18}F-FLT tumour uptake at the early time points may be explained by the limited transport of thymidine analogues across the intact blood–brain barrier and confirms the higher sensitivity of ^{11}C-MET compared to ^{18}F-FLT in the detection of early glioma development [16]. We observed a good correlation between inhibition of angiogenesis and uptake of PET tracers, showing the relation between tumour vessel remodelling, L-type amino acid transporter 1 (LAT1) expression (^{11}C-MET) and tumour proliferation (^{18}F-FLT). The correlation of ^{11}C-MET uptake with microvessel density (r=0.93, p=0.002, Pearson) confirms previous studies demonstrating high ^{11}C-MET uptake in areas of high angiogenesis-related microvessel density [34, 35]. Our results are also in agreement with two prospective clinical studies highlighting the potential of ^{18}F-FLT PET to predict anti-angiogenic treatment outcome in patients with gliomas [36, 37].

Our study demonstrates that the changes in tumour vessels during glioma progression and in response to an anti-angiogenic treatment can be non-invasively assessed by advanced MR imaging. Combination of SSCE-MRI with ^{11}C-MET and ^{18}F-FLT PET affords anatomical, physiological and biochemical information concerning markers of angiogenesis and proliferation. Considering the complexity and the spatial heterogeneity of the glioma response to anti-angiogenic therapy, a multimodal imaging approach appears necessary to fully characterize the induced changes in the tumour. The presented methods might be used for monitoring treatments and to further understand the mechanisms that lead to tumour resistance to therapy.

Acknowledgments The authors thank Irmgard Hoppe and Christa Möllmann (EIMI, Münster) for the technical assistance with immunohistochemistry. This work is supported in part by BMBF (Bundesministerium für Bildung und Forschung) grant MoBiMed and the European Union Framework Program 7 project HEALTH-F5-2008-201842 (ENCITE).

Conflicts of interest None.

References

1. Jemal A, Siegel R, Ward E, Hao Y, Xu J, Thun MJ. Cancer statistics, 2009. CA Cancer J Clin 2009;59:225–49.
2. Vredenburgh JJ, Desjardins A, Herndon 2nd JE, Dowell JM, Reardon DA, Quinn JA, et al. Phase II trial of bevacizumab and irinotecan in recurrent malignant glioma. Clin Cancer Res 2007;13:1253–9.
3. Friedman HS, Prados MD, Wen PY, Mikkelsen T, Schiff D, Abrey LE, et al. Bevacizumab alone and in combination with irinotecan in recurrent glioblastoma. J Clin Oncol 2009;27:4733–40.
4. Kim KJ, Li B, Winer J, Armanini M, Gillett N, Phillips HS, et al. Inhibition of vascular endothelial growth factor-induced angiogenesis suppresses tumour growth in vivo. Nature 1993;362:841–4.
5. Verhoeff JJ, van Tellingen O, Claes A, Stalpers LJ, van Linde ME, Richel DJ, et al. Concerns about anti-angiogenic treatment in patients with glioblastoma multiforme. BMC Cancer 2009;9:444–53.
6. Dhermain FG, Hau P, Lanfermann H, Jacobs AH, van den Bent MJ. Advanced MRI and PET imaging for assessment of treatment response in patients with gliomas. Lancet Neurol 2010;9:906–20.
7. Waerzeggers Y, Monfared P, Viel T, Winkeler A, Jacobs AH. Mouse models in neurological disorders: applications of non-invasive imaging. Biochim Biophys Acta 2010;1802:819–39.
8. Hylton N. Dynamic contrast-enhanced magnetic resonance imaging as an imaging biomarker. J Clin Oncol 2006;24:3293–8.
9. Tofts PS, Brix G, Buckley DL, Evelhoch JL, Henderson E, Knopp MV, et al. Estimating kinetic parameters from dynamic contrast-enhanced T(1)-weighted MRI of a diffusable tracer: standardized quantities and symbols. J Magn Reson Imaging 1999;10:223–32.
10. Koh TS, Zeman V, Darko J, Lee TY, Milosevic MF, Haider M, et al. The inclusion of capillary distribution in the adiabatic tissue homogeneity model of blood flow. Phys Med Biol 2001;46:1519–38.
11. Dennie J, Mandeville JB, Boxerman JL, Packard SD, Rosen BR, Weisskoff RM. NMR imaging of changes in vascular morphology due to tumour angiogenesis. Magn Reson Med 1998;40:793–9.
12. Jensen JH, Chandra R. MR imaging of microvasculature. Magn Reson Med 2000;44:224–30.
13. Wu EX, Tang H, Jensen JH. High-resolution MR imaging of mouse brain microvasculature using the relaxation rate shift index Q. NMR Biomed 2004;17:507–12.
14. Pannetier N, Lemasson B, Christen T, Tachrount M, Troprès I, Farion R, et al. Vessel size index measurements in a rat model of glioma: comparison of the dynamic (Gd) and steady-state (iron-oxide) susceptibility contrast MRI approaches. NMR Biomed 2012;25:218–26.
15. Ullrich RT, Jikeli JF, Diedenhofen M, Böhm-Sturm P, Unruh M, Vollmar S, et al. In-vivo visualization of tumour microvessel density and response to anti-angiogenic treatment by high resolution MRI in mice. PLoS One 2011;6:e19592.
16. Viel T, Talasila KM, Monfared P, Wang J, Jikeli JF, Waerzeggers Y, et al. Analysis of the growth dynamics of angiogenesis-dependent and -independent experimental glioblastomas by multi-modal small-animal PET and MRI. J Nucl Med 2012;53:1135–45.
17. Jacobs AH, Thomas A, Kracht LW, Li H, Dittmar C, Garlip G, et al. 18F-fluoro-L-thymidine and 11C-methylmethionine as markers of increased transport and proliferation in brain tumors. J Nucl Med 2005;46:1948–58.
18. Machulla HJ, Blocher A, Kuntzsch M, Piert M, Wei R, Grierson JR. Simplified labeling approach for synthesizing 3′-deoxy-3′-[18F]fluorothymidine ([18F]FLT). J Radioanal Nucl Chem 2000;243:843–6.
19. Miller AJ, Joseph PM. The use of power images to perform quantitative analysis on low SNR MR images. Magn Reson Imaging 1993;11:1051–6.
20. Kiselev VG. Spin echo amplitude in biological tissue with implications for vessel size imaging. Joint Annual Meeting ISMRM-ESMRMB, Stockholm. 2010;01–07052010(1):1792.
21. Hoehn-Berlage M, Eis M, Schmitz B. Regional and directional anisotropy of apparent diffusion coefficient in rat brain. NMR Biomed 1999;12:45–50.
22. Vollmar SCJ, Sue M, Klein J, Jacobs AH, Herholz K. VINCI - volume imaging in neurological research, co-registration and ROIs included. In: Kremer K, Macho V, editors. Research and Scientific Computing 2003. Göttingen: Gesellschaft für wissenschaftliche Datenverarbeitung; 2004. p. 115–31.
23. Schindelin J, Arganda-Carreras I, Frise E, Kaynig V, Longair M, Pietzsch T, et al. Fiji: an open-source platform for biological-image analysis. Nature Methods 2012;9:676–82.
24. Sakariassen PØ, Prestegarden L, Wang J, Skaftnesmo KO, Mahesparan R, Molthoff C, et al. Angiogenesis-independent tumour growth mediated by stem-like cancer cells. Proc Natl Acad Sci U S A 2006;103:16466–71.
25. Keunen O, Johansson M, Oudin A, Sanzey M, Rahim SA, Fack F, et al. Anti-VEGF treatment reduces blood supply and increases tumor cell invasion in glioblastoma. Proc Natl Acad Sci U S A 2011;108:3749–54.
26. Beer AJ, Schwaiger M. Imaging of integrin alphavbeta3 expression. Cancer Metastasis Rev 2008;27:631–44.
27. Jain RK, di Tomaso E, Duda DG, Loeffler JS, Sorensen AG, Batchelor TT. Angiogenesis in brain tumours. Nat Rev Neurosci 2007;8:610–22.
28. Klein B, Kuschinsky W, Schröck H, Vetterlein F. Interdependency of local capillary density, blood flow, and metabolism in rat brains. Am J Physiol 1986;251:H1333–40.
29. Schor AM, Pendleton N, Pazouki S, Smither RL, Morris J, Lessan K, et al. Assessment of vascularity in histological sections: effects of methodology and value as an index of angiogenesis in breast tumours. Histochem J 1998;30:849–56.
30. von Baumgarten L, Brucker D, Tirniceru A, Kienast Y, Grau S, Burgold S, et al. Bevacizumab has differential and dose-dependent effects on glioma blood vessels and tumor cells. Clin Cancer Res 2011;17:6192–205.
31. Kiselev VG, Posse S. Analytical model of susceptibility-induced MR signal dephasing: effect of diffusion in a microvascular network. Magn Reson Med 1999;41:499–509.
32. Drevs J, Müller-Driver R, Wittig C, Fuxius S, Esser N, Hugenschmidt H, et al. PTK787/ZK 222584, a specific vascular endothelial growth factor-receptor tyrosine kinase inhibitor, affects the anatomy of the tumor vascular bed and the

functional vascular properties as detected by dynamic enhanced magnetic resonance imaging. Cancer Res 2002;62:4015–22.

33. Miletic H, Niclou SP, Johansson M, Bjerkvig R. Anti-VEGF therapies for malignant glioma: treatment effects and escape mechanisms. Expert Opin Ther Targets 2009;13:455–68.
34. Okubo S, Zhen HN, Kawai N, Nishiyama Y, Haba R, Tamiya T. Correlation of L-methyl-11C-methionine (MET) uptake with L-type amino acid transporter 1 in human gliomas. J Neurooncol 2010;99:217–25.
35. Kracht LW, Friese M, Herholz K, Schroeder R, Bauer B, Jacobs A, et al. Methyl-[11C]-l-methionine uptake as measured by positron emission tomography correlates to microvessel density in patients with glioma. Eur J Nucl Med Mol Imaging 2003;30:868–73.
36. Chen W, Delaloye S, Silverman DH, Geist C, Czernin J, Sayre J, et al. Predicting treatment response of malignant gliomas to bevacizumab and irinotecan by imaging proliferation with [18F] fluorothymidine positron emission tomography: a pilot study. J Clin Oncol 2007;25:4714–21.
37. Schwarzenberg J, Czernin J, Cloughesy TF, Ellingson BM, Pope WB, Geist C, et al. 3'-deoxy-3'-18F-fluorothymidine PET and MRI for early survival predictions in patients with recurrent malignant glioma treated with bevacizumab. J Nucl Med 2012;53:29–36.

Online Resource 1

a

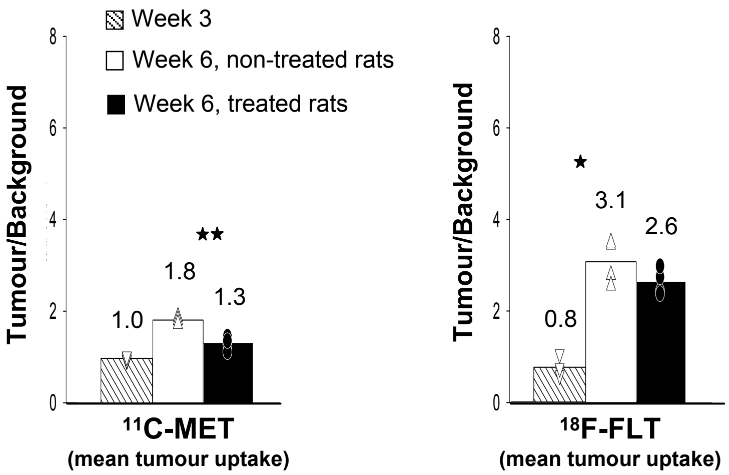

b

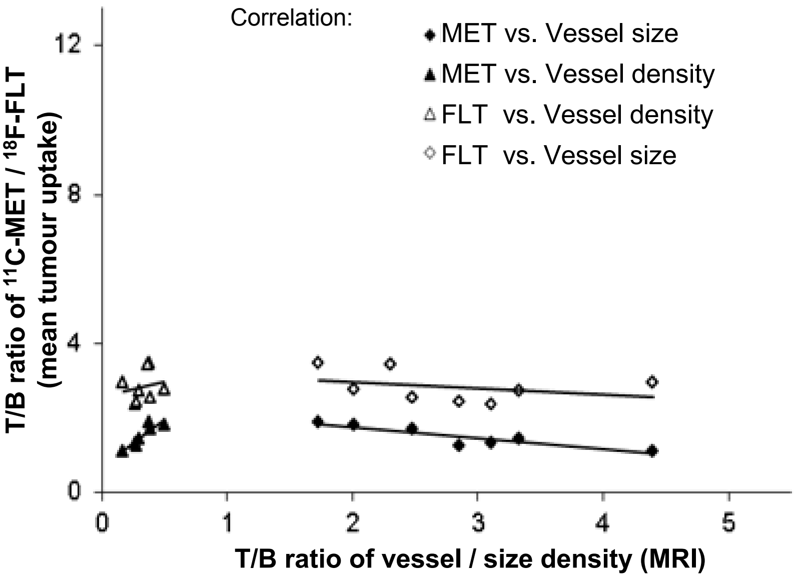

c

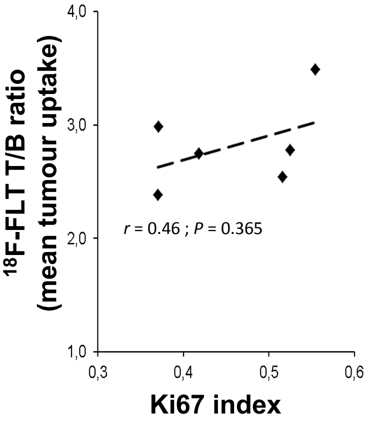

d

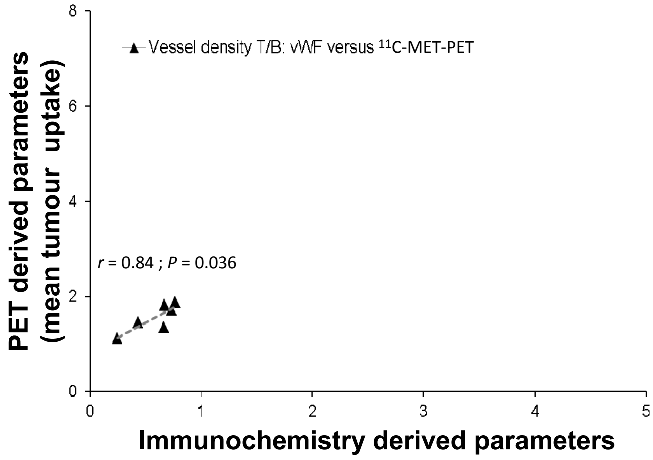

Online Resource 1: Quantification of small animal PET imaging results (mean tumour uptake). **a.** PET images were used to determine T/B ratios of mean tumour uptake of the PET tracers at 3 week (striped bars) and 6 weeks (white bars: non-treated rats; black bars: treated rats) after spheroid implantation in nude rats (n = 4). **b.** T/B ratios of ^{11}C-MET and ^{18}F-FLT mean tumour uptake were plotted over T/B ratios of MRI measures of vessel size/density obtained at week 6. **c.** Ki67 index was plotted over the T/B ratios of ^{18}F-FLT mean tumour uptake. **d.** T/B ratios of vessel density derived from the immunohistochemistry were correlated with T/B ratios of ^{11}C-MET mean tumour uptake.
**: significant difference between treated and non-treated rats ($P < 0.01$). Correlation coefficients and significance were determined using the Pearson correlation analysis.

Online Resource 2

		Week 3		**Week 6**	
		Non-treated	**Treated**	**Non-treated**	**Treated**
^{11}C-MET$_{mean}$ (%ID/cm^3)	**Tumour**	**0.31** ±0.06	**0.30** ±0.05	**0.77** ±0.29*	**0.52** ±0.06**
^{18}F-FLT$_{mean}$ (%ID/cm^3)	**Tumour**	**0.08** ±0.05	**0.10** ±0.01	**0.37** ±0.18*	**0.25** ±0.03**

* and **: significant difference between weeks 3 and 6 ($P < 0.05$ and 0.01, respectively)

Online Resource 2: Quantification of the mean tumour uptake of the PET tracers (Mean ± standard deviation)

Online Resource 3

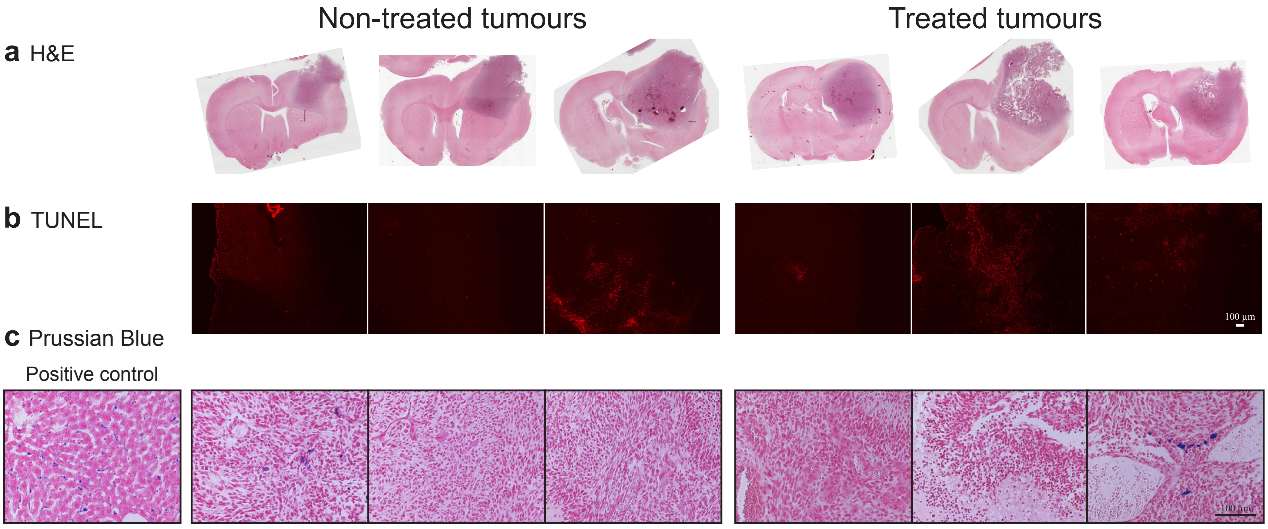
Non-treated tumours
Treated tumours
a H&E
b TUNEL
c Prussian Blue
Positive control
100 µm
100 µm

Online Resource 3: Immuno-histochemistry of tumour tissue from control and bevacizumab treated rats at week 6. The same rats are presented here as in Figure 3. **a.** H&E staining revealed the presence of necrotic areas, especially for the treated tumours. **b.** TUNEL staining confirmed the presence of tumour cell death. **c.** Only very few iron particles could be observed using Prussian blue staining, showing that leakage of iron contrast agent was very limited. The liver of a mouse injected with endorem was used as positive control for Prussian blue staining. Scale bars: 100 µm.

Vascular changes after stroke in the rat – a longitudinal study using optimized magnetic resonance imaging

III

Full Paper

CONTRAST MEDIA & MOLECULAR IMAGING

Received: 24 August 2012, Revised: 30 November 2012, Accepted: 15 January 2013, Published online in Wiley Online Library

(wileyonlinelibrary.com) DOI: 10.1002/cmmi.1534

Vascular changes after stroke in the rat: a longitudinal study using optimized magnetic resonance imaging

Philipp Boehm-Sturm[a†], Tracy D. Farr[a†], Joanna Adamczak[a], Jan F. Jikeli[a,b], Luam Mengler[a], Dirk Wiedermann[a], Therése Kallur[a], Valerij Kiselev[c] and Mathias Hoehn[a*]

During stroke, the reduction of blood flow leads to undersupply of oxygen and nutrients and, finally, to cell death, but also to upregulation of pro-angiogenic molecules and vascular remodeling. However, the temporal profile of vascular changes after stroke is still poorly understood. Here, we optimized steady-state contrast-enhanced magnetic resonance imaging (SSCE MRI) and followed the dynamic changes in vascular architecture for up to 4 weeks after transient middle cerebral artery occlusion (MCAO) in rats. Using MRI diffusion measurements and the changes of transversal relaxation rates ΔR_2 and ΔR_2^* after injection of a superparamagnetic contrast agent, SSCE MRI provided several hemodynamic parameters: relative cerebral blood volume (rCBV), rCBV in small vessels, microvascular density, and relative vessel size. Six rats underwent SSCE MRI before MCAO and at 7, 14, 21 and 28 days after surgery. 5-Bromo-2′deoxyuridine (BrdU) was injected between days 2 and 7 to label proliferating cells during this time. SSCE MRI depicted a decrease in microvessel density and an increase in vessel size in the ischemic striatum after stroke. A persistently decreased MRI vessel density was confirmed with histology at 28 days. BrdU + endothelial cells were found in regions close to the infarct indicating endothelial cell proliferation during the first week after MCAO; however, late-stage angiogenesis, as would be reflected by increased vessel density, was not detected. The optimized SSCE MRI protocol was used to follow spatio-temporal changes of important vessel characteristics, which may contribute to a better understanding of the role of angiogenesis at different stages after stroke. **Copyright © 2013 John Wiley & Sons, Ltd.**

Supporting information may be found in the online version of this paper

Keywords: steady-state contrast-enhanced MRI; vessel density imaging; vessel size imaging; middle cerebral artery occlusion; angiogenesis

1. INTRODUCTION

Stroke is characterized by a disturbance in blood supply to the brain. Reduction of blood flow results in widespread cell death, but also activation of several molecules and signaling pathways that are thought to promote angiogenesis, reviewed in (1–3). Proliferating endothelial cells were first observed more than a decade ago in human post mortem ischemic tissue (4), and vascular casting in rodent models of middle cerebral artery occlusion (MCAO) illustrated the formation of vascular buds, some of which appeared to anastomose with surrounding vessels (5). However, it is not clear whether or not these new vessels are functional, or whether they have the capacity to play a role in stroke outcome.

Magnetic resonance imaging (MRI) has long been used to observe alterations in cerebral blood supply following stroke. While resolution is currently lacking to detect formation of new microvessels directly, under the assumption that these vessels are functional, MRI can, however, depict cerebral blood volume (CBV) changes, which in turn can be used to noninvasively estimate microvessel density and size, as reviewed in Neeman *et al.* (6) and Seevinck *et al.* (7). Here, the term microvessel usually refers to capillaries (5–10 μm diameter) in contrast to large arteries and veins (~100 μm diameter). Although the vascular tree may more accurately be described by self-similar structures of a wide range of diameters, such simple categorization into small and large vessels is under defined conditions justified in the context of MRI signal from vasculature (8). Steady-state contrast-enhanced magnetic resonance imaging (SSCE MRI) provides measures of blood volume, vessel size, and vessel density by measuring relaxivity changes (ΔR_2 and ΔR_2^*) in

---

* Correspondence to: Mathias Hoehn, In-Vivo-NMR Laboratory, Max Planck Institute for Neurological Research, Cologne, Germany. Email: mathias@nf.mpg.de

† The first two authors contributed equally.

a P. Boehm-Sturm, T. D. Farr, J. Adamczak, J. F. Jikeli, L. Mengler, D. Wiedermann, T. Kallur, M. Hoehn
In-Vivo-NMR Laboratory, Max Planck Institute for Neurological Research, Cologne, Germany

b J. F. Jikeli
Molecular Sensory Systems Laboratory, Center for Advanced European Studies and Research, Bonn, Germany

c V. Kiselev
Medical Physics, Department of Diagnostic Radiology, University Hospital Freiburg, Freiburg, Germany

Copyright © 2013 John Wiley & Sons, Ltd.

tissue following injection of an intravascular superparamagnetic contrast agent (9–12).

Initial studies applying SSCE MRI in embolic stroke showed that the microvascular density in the lesion core and adjacent tissue decreased (13). However, another study reported an increase in relative cerebral blood volume (rCBV) and density of microvessels in cortical regions starting 14 days after permanent distal MCAO, interpreted as late-stage angiogenesis by those authors (14). Moreover, increased rCBV and vessel size were found in the ischemic territory of rats after MCAO and were interpreted as vasodilation in response to the stroke (15). Further work is required to better understand the optimal acquisition and analysis strategies for SSCE MRI in order to obtain deeper insight into biological processes. In the present study, we carefully refined the technique of SSCE MRI and applied it to the monitoring of vascular changes for up to 4 weeks after transient MCAO in the rat. The results were complemented with an assessment of endothelial cell proliferation during the first week after MCAO by histological means. Our ultimate aim was to elucidate the extent of angiogenesis after cerebral ischemia, which theoretically should be reflected by increased MRI-derived vessel density.

2. MATERIALS AND METHODS

2.1. Animals and experimental design

All animal experiments were conducted according to the guidelines laid out in the German Animal Welfare Act and approved by the authorities (Landesamt für Natur, Umwelt und Verbraucherschutz Nordrhein-Westfalen) under permission number 9.93.2.10.31.07.048 (dated 22 May 2007). Adult male Wistar rats (body weight 300–350 g, Harlan–Winkelmann GmbH, Borchen, Germany) were housed in cages under a 12 h light/12 h dark cycle with access to food and water *ad libitum*. During all surgical and scanning procedures animals were anesthetized and maintained with isoflurane in a 70:30 nitrous oxide–oxygen mixture, and core body temperature was maintained at $36.7 \pm 1.0\ ^{\circ}\mathrm{C}$ using in-house automated feedback systems and heat blankets (medres GmbH, Cologne, Germany). Animals were scanned with MRI 4–7 days before and on days 7, 14, 21 and 28 after MCAO, and were sacrificed for histology after the last experimental session. Additionally, rats received 5-bromo-2′deoxyuridine (BrdU, 50 mg kg^{-1} twice daily i.p., Sigma-Aldrich, Hamburg, Germany) between days 2 and 7 after MCAO to label proliferating cells.

2.2. Stroke induction

Stroke was induced by occlusion of the middle cerebral artery via intraluminal filament technique (16) with the following modifications. Rats were anesthetized and an incision was made in the right temporal muscle halfway between the eye and ear. The animals were subsequently placed in a supine position and a calibrated 1 mm diameter Laser probe was placed against the right skull to monitor cerebral blood flow changes in the sensorimotor cortex following filament placement with a laser doppler perfusion monitor (Perimed, Järfälla, Sweden). A midline incision was made in the neck, and the mandibular glands, pretrachial strap, and sternomastoid muscles were retracted. The carotid artery and external carotid artery were exposed and ligated with surgical sutures and a microclip was placed on the internal carotid artery. A small incision was made in the carotid artery below the external carotid artery and internal carotid artery bifurcation and a silicone coated monofilament (410 μm diameter, Doccol Corporation, Redlands, CA, USA) was inserted and advanced up the internal carotid artery until resistance was felt and a decrease in cerebral blood flow noted (approximately 17 mm). After 60 min the filament was withdrawn, the suture on the external carotid artery removed, muscles and glands guided back into place, wounds sutured and treated with local anesthetic. Animals received 2.5 ml of physiological saline s.c. daily and were provided with moistened food until weight stabilized. Exclusion criteria stipulated any animals with subarachnoid hemorrhage, incomplete MCAO (no observable T_2 changes during MRI 1 week after MCAO) were removed from the study. Six rats entered the study, four of which had a lesion restricted to the striatum, depicted as hyperintensities on T_2 maps; two animals exhibited cortical and striatal damage. One animal did not perform the SSCE MRI measurement 2 weeks post MCAO.

2.3. SSCE MRI

2.3.1. Theory

In order to analytically describe the changes in MRI signal owing to i.v. injection of a paramagnetic substance, the vessel network is modeled as a set of infinitely long, randomly distributed cylinders (17,18). Proton spins are assumed to be restricted to one of two compartments: either within vessels (intravascular) or within the tissue surrounding the vessels (extravascular). Further assumptions include a small blood volume fraction $\xi_0 << 1$ and a diffusion length much smaller than the size of a strongly dephased area around the vessel, that is, $\delta\omega \cdot \rho^2/D >> 1$ (8). D represents the water diffusivity in the extravascular compartment, ρ is the vessel radius, and $\delta\omega$ is the characteristic shift in Larmor frequency of a magnetized cylinder in an external magnetic field.

Under these assumptions, the change in MRI signal from before (S_{pre}) to after (S_{post}) the contrast agent injection can simply be described by shifts of the relaxation rates measured in a spin echo (SE) ($R_2 \to R_2 + \Delta R_2$) and gradient echo (GE) experiment ($R_2^* \to R_2^* + \Delta R_2^*$) (cgs units) (11):

$$\Delta R_2 = \frac{1}{TE} \ln\left(\frac{S_{\mathrm{pre,SE}}}{S_{\mathrm{post,SE}}}\right) \approx 0.694 \cdot \delta\omega^{2/3} D^{1/3} \xi_0 \rho^{-2/3} \qquad (1)$$

$$\Delta R_2^* = \frac{1}{TE} \ln\left(\frac{S_{\mathrm{pre,GE}}}{S_{\mathrm{post,GE}}}\right) \approx \frac{2}{3} \xi_0 \delta\omega \qquad (2)$$

Here, TE is the echo time.

In order to assess the important tissue parameters T_2 and ΔR_2 simultaneously, we decided to use a multi spin echo pulse sequence (MSME). This results in an effective reduction of the diffusion effect $D \to D/n^2$ depending on the number of refocusing pulses n (19,20). ΔR_2 is then determined with the MRI signal S_{MSME} of the nth echo of the MSME via the modified relationship:

$$\Delta R_2 = n^b \frac{1}{TE(n)} \ln\left(\frac{S_{\mathrm{pre,MSME}}(n)}{S_{\mathrm{post,MSME}}(n)}\right), b = \frac{2}{3} \qquad (3)$$

Neglecting the reduced diffusion effect leads to a high underestimation of ΔR_2 values. We found a lower exponent $b = 0.49$ in the experiment (Supporting Information, Fig. S1), which was used for all further analysis. The deviation from the theory will be subject to further studies.

Copyright © 2013 John Wiley & Sons, Ltd.

Equations (1) and (2) show that ΔR_2 is a measure of rCBV in small vessels whereas ΔR_2^* reflects the rCBV in all vessels. However, both still depend on the concentration C of the contrast agent in blood, which usually needs to be assessed invasively or with dynamic contrast-enhanced measurements (11). Therefore, Jensen and Chandra introduced the so-called Q -factor, which is largely independent of C and is a measure of microvessel density (10).

$$Q = \frac{\Delta R_2}{(\Delta R_2^*)^{2/3}} \tag{4}$$

Q relates to the number of vessels that punctuate a cross-section of tissue per unit area. Microvessel density N is counted in units of $[N] = 1\ \mathrm{mm}^{-2}$ and can be calculated when the presence of large macrovessels can be neglected and taking into account the water diffusivity in tissue (12):

$$N = 0.218\left(Q^3/D\right), [D] = \mathrm{mm}^2 s^{-1}, [Q] = s^{-1/3} \tag{5}$$

Furthermore it can be shown that the mean vessel size holds true (11):

$$\rho = 0.425\left(\frac{1}{\gamma \Delta\chi B_0}\right)^{1/2} \cdot (D)^{1/2} \left(\frac{\Delta R_2^*}{\Delta R_2}\right)^{3/2} \tag{6}$$

Owing to the lack of *in vivo* measurements of the contrast agent concentration and thus lack of $\Delta\chi$ values, we neglected the first term in eqn (6) and used a relative vessel size R (in arbitrary units) throughout the article, which is defined as:

$$R = \left(\frac{D}{D_{lit}}\right)^{1/2} \left(\frac{\Delta R_2^*}{\Delta R_2}\right)^{3/2} \tag{7}$$

Here, we accounted for local changes in diffusivity in the pathologic brain by multiplication with the square root of the quotient of measured diffusivity D and a known value for the healthy brain $D_{lit} = 6.64 \times 10^{-4}\ \mathrm{mm}^2\ \mathrm{s}^{-1}$ (21).

2.3.2. MRI acquisition

MRI was carried out on a 4.7 T animal scanner (Biospec47/30, Bruker BioSpin, Ettlingen, Germany) equipped with actively shielded gradient coils (BGA 12, 220 mT m^{-1}, 120 μs rise time, Bruker BioSpin). We used a custom-built surface radiofrequency coil 30 mm in diameter for reception and a Helmholtz coil for homogeneous transmission (medres GmbH, Cologne, Germany). Animals were fixed with tooth bar and ear bars in a custom-made animal holder (medres). Respiration rate was monitored with a pressure-sensitive pad under the thorax using DASYlab (Measurement Computing, Norton, USA) software.

The imaging protocol consisted of apparent diffusion coefficient (ADC) measurement [spin echo MRI, field of view = (2.56 cm)^2, eight contiguous 1 mm thick slices, matrix = 128×64, echo time/repetition time (TE/TR) = 40.66 ms/4 s, one diffusion direction medial-lateral in the animal coordinate system, $b_{\mathrm{eff}} = 0.26$, 600.26, and 1500.26 s mm^{-2}, Time of acquisition (TA) = 12:48 min], an MSME (TE/TR = 13.55 ms/4 s, 10 echoes, TA = 8:32 min) and a multigradient echo pulse sequence (MGE, TE/TR = 5 ms/2 s, eight equidistant echoes, flip angle = 60°, TA = 8:32 min). The geometries of the MSME and MGE were matched to the ADC measurement to allow voxel-wise calculation of vessel density, except that four additional slices were acquired in order to cover the whole forebrain in the T_2 and T_2^* images.

After initial measurements, superparamagnetic iron oxide particles (Endorem, Guerbet, Sulzbach, Germany, 11.2 mg Fe ml^{-1}) were injected in the tail vein at a dose of 30 mg Fe kg^{-1} without moving the animal. We allowed the contrast agent to distribute homogeneously over the blood pool for 3 min, and then identical post-contrast MSME and MGE images were acquired.

2.4. MRI data processing

The MRI data were processed with Interactive Data Language (IDL, ITT visual information solutions, Boulder, CO, USA) and FMRIB Software Library (FSL, http://www.fmrib.ox.ac.uk/fsl).

For T_2 maps, the MRI signal $S(TE)$ in MSME scans was fitted on a voxel-wise basis with a monoexponential decay $S(TE) = A\exp(-TE/T_2) + B$ with equilibrium signal A, relaxation time T_2, and an offset B to reduce bias introduced by the use of magnitude images (22). Accordingly, ADC maps were generated by fitting the MRI signal with $S(b) = A\exp(-b \cdot ADC) + B$. Maps were co-registered to a template rat brain (an average of 34 high-resolution T_2-weighted images from 28 rats, scaled to match the resolution of our scans) with FSL's linear registration tool.

For vessel size and density maps, the A_0 images ($b = 0.26\ \mathrm{s\ mm}^{-2}$) of the ADC scan and the first echo images of the pre- and post-contrast MSME and MGE scans were segmented with FSL's brain extraction tool. The segmented images were co-registered to the template brain with an affine transformation (12 degrees of freedom) with FSL. The determined transformation matrices were applied to the other ADC images, and the later echoes of the MSME and MGE datasets. Finally, the co-registered images were used for voxel-wise calculation of ΔR_2^*, ΔR_2, Q, N and R according to equations (2)–(5) and (7), respectively. ΔR_2 and ΔR_2^* were calculated from the second echo of the MSME and MGE images, respectively, in order to minimize error propagation in the data analysis scheme (Supporting Information, Fig. S2). Voxels with a signal to noise ratio < 5 in either the A_0 image of ADC measurements or in the first echo of the MSME or MGE were excluded from the analysis. Voxels with negative ΔR_2 or ΔR_2^* values, or those with $\Delta R_2 > \Delta R_2^*$ were also excluded.

Volume-of-interest (VOI) analysis was carried out with the freeware program ImageJ (http://rsbweb.nih.gov/ ij/). First, for anatomically selected VOIs, the intact and ischemic striatum was manually delineated in the coronal slices corresponding to −0.3 and −1.3 mm from bregma. Second, lesion-based VOIs were manually drawn in the same two slices for each animal on T_2 maps acquired 1 week post MCAO. The lesion-based VOIs encompassed voxels with increased T_2 values ($T_2 >$ mean + 2 standard deviations of contralateral striatum). Third, a VOI of the peri-infarct zone was drawn by extension of the lesion VOI by 0.4 mm in-plane (neglecting ventricles and areas outside the brain) and by subsequent subtraction of the lesion VOI. Mirroring of the lesion and peri-infarct VOIs at the midline with a custom ImageJ macro yielded the contralateral VOIs. Mean ΔR_2^*, ΔR_2, Q, N and R values were recorded and presented as a ratio of the ischemic to intact side.

The incidence maps were generated by normalization (voxel-wise division) of the post-MCAO parameter maps to the time point

Copyright © 2013 John Wiley & Sons, Ltd.

before surgery. An incidence in a voxel at a certain time point was counted when that voxel showed a significant increase/decrease, that is, with a normalized parameter of interest larger/smaller than the mean ± 2 standard deviations when compared with the contralateral striatum. For each SSCE MRI parameter increase/decrease, incidences of all animals were added voxel-wise. The resulting incidence map for the group of animals was smoothed (Gauss filtered, sigma = 0.2 mm) and overlaid on the template brain.

2.5. Immunohistochemistry

After the last MRI session, animals were deeply anesthetized and perfused transcardially with cooled saline followed by cooled 4% paraformaldehyde. Brains were post-fixed overnight and cryoprotected in 30% sucrose solution prior to coronal sectioning at 40 μm on a freezing microtome (Leica Microsystems, Wetzlar, Germany). Sections were kept at −20 °C in cryo-protective solution. For double-label immunofluorescence with BrdU, free-floating sections were denatured in 1 mol l^{-1} HCl for 10 min at 65 °C, followed by 20 min incubation at room temperature and pre-incubation in appropriate blocking solution: 5% normal sera and 0.25% Triton X-100 in potassium phosphate-buffered saline for 60 min at room temperature. Incubation with primary antisera was carried out overnight at +4 °C and the following primary antibodies were used: rat anti-BrdU (1:100, Abcam, Cambridge, MA, USA), and mouse anti-Rat Endothelial Cell Antigen (RECA; 1:400, AdB Serotec, Oxford, UK). Primary antibodies were detected using either standard diaminobenzidine (DAB) immunohistochemistry or appropriate fluorescent Cy3 (Jackson ImmunoResearch, West Grove, PA, USA) or biotin-conjugated (Vector Laboratories, Burlingame, CA, USA) secondary antibodies (1:200), the latter of which was detected with Alexa 488-conjugated streptavidin (1:200, Invitrogen, Carlsbad, CA, USA). Sections were mounted on poly L-lysine coated slides (Thermo Fisher Scientific, Waltham, MA, USA) and coverslipped with glycerol-based mounting medium.

Microscopic images were acquired and double-immunoreactivity verified with a confocal laser scanning microscope (Leica TCS SP5 X, Leica Microsystems). Microvessel density was semi-quantified across the entire intact and ischemic striatum from RECA DAB stained sections located approximately −0.3 mm from bregma (corresponding to the anterior commissure) (23) using the Stereo Investigator system (MicroBrightField Europe, E.K., Magdeburg, Germany) with a counting frame of 40 μm^2 at 20× magnification. Microvessel size was estimated by measuring the diameter at the thickest point of a counted vessel every 100 frames.

2.6. Statistical analysis

Data are expressed as group means ± standard deviation of the means. Statistical analysis was performed using SPSS version 17 software and a *p*-value < 0.05 was used as the significance level. VOI values in the striatum/lesion/peri-infarct zone were compared using one way repeated measures analysis of variance with time as the within-subject factor followed by *post-hoc* pairwise comparisons with the least significant difference test. For comparison of histology and MRI, microvessel densities in the intact and ischemic striatum were analyzed using paired Student's *t*-tests.

3. RESULTS

3.1. Impact of noise and echo times on SSCE MRI results

To determine the impact of noise on the most noise-sensitive parameter *N*, we performed simulation experiments in which white noise was added to artificial MRI datasets. In parallel we analyzed histograms in experimental MRI datasets from animals before MCAO. Our simulations also determined that suboptimal echo times result in non-Gaussian, widespread distribution of the resulting *N* values (Supporting Information, Fig. S2). From this, we anticipated that, in order to detect physiologically relevant changes in *N* (as a marker of microvessel density), the relative change must be in the order of magnitude of 20%.

3.2. Impact of tissue water diffusivity on interpretation of SSCE MRI results

In the chronic phase after MCAO, necrosis, phagocytosis and associated cystic formation in tissue are visualized by a steep increase in ADC values. In all animals with this cyst formation ($n = 3$) regions of elevated ΔR_2 were observed within or close to the lesion core (Fig. 1a). According to the theory, increases in ΔR_2 indicate an increase of rCBV in small vessels, but as is demonstrated by eqn (1), diffusivity also plays a role. Comparison of vessel density maps calculated under inclusion of a constant diffusion value from the literature (21) (Fig. 1b) with those vessel density maps for which the local diffusivity was taken into account on an experimentally recorded, voxel-wise basis (Fig. 1c, d), revealed that the dominant effect leading to the increased ΔR_2 was highly elevated water diffusivity in necrotic tissue. Vessel staining on histological sections confirmed that tissue in these regions was not intact at 4 weeks after MCAO and that the density of small vessels in adjacent regions was not higher compared with healthy tissue (Fig. 1e, f).

3.3. Vascular changes after stroke

3.3.1. *MRI Incidence maps*

Incidence maps revealed that decreases in ΔR_2 and Q and an increase in R were most frequent (Fig. 2, bottom three rows). All six animals were used for map calculations but the highest number of incidences found in all pixels for any of the SSCE MRI parameters was three, indicating a regionally and temporally variable pattern of vascular changes across the different animals. Other incidence maps did not show a specific trend.

3.3.2. *MRI VOI analysis*

Parameter maps from all animals are presented for all time points in Fig. 3. In all maps except T_2 and ADC we observed global image intensity fluctuations between animals and time points within the whole brain that followed no defined pattern and probably reflected differences in contrast agent concentration within the blood, which was not measured in this study. To account for this, quantitative analysis was carried out in the striatum (Fig. 4a), within the lesion (Fig. 4b) and within the peri-infarct areas (Fig. 4c), and values expressed as a percentage ratio of the ipsilateral (lesioned) to the contralateral (intact) hemisphere. Only a negligible number of voxels (<0.5 ‰) were excluded from the analysis owing to the imposed thresholds on signal to noise, ΔR_2 and ΔR_2^*.

Copyright © 2013 John Wiley & Sons, Ltd.

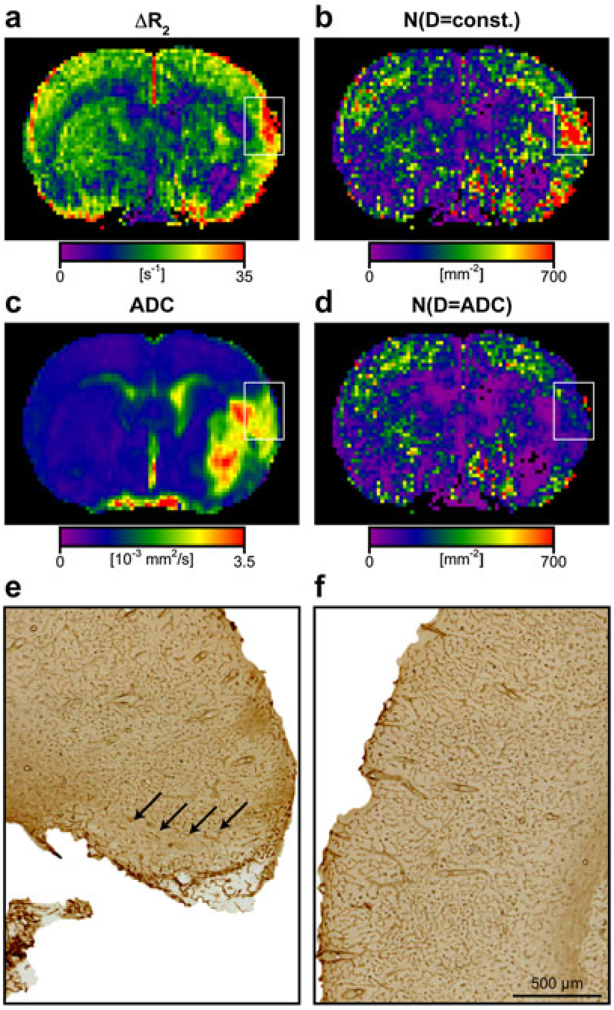

Figure 1. Impact of tissue diffusivity on MRI-derived blood volume and vessel density. All animals with cyst formation exhibited regions with highly elevated ΔR_2 close to or within the lesion core, which is usually interpreted as high rCBV in small vessels. Such an area is indicated by the box on the ΔR_2 map from a representative animal 4 weeks after MCAO (a). Assuming a constant diffusivity value for each voxel that is comparable to healthy tissue leads to high MRI-derived vessel densities (box in b). However, ADC values in this region were also elevated, which indicates necrosis and liquefaction of tissue (box in c). When we took local tissue diffusivity into account on a voxel-wise basis, the 'hot spots' in the MRI-derived vessel densities disappeared (box in d). Histology in the same region confirmed tissue necrosis (e) and a decrease in microvessel density (e, arrows) compared with the same region on the contralateral side (f). Thus, the high ΔR_2 was a result of high tissue diffusivity and not an indicator of increased rCBV in small vessels.

As expected, prior to MCAO the calculated MRI parameters were comparable between the ipsilateral and contralateral side: rCBV in small vessels ΔR_2 (striatum, 101.8 ± 1.3%; lesion, 101.6 ± 2.0%; peri-infarct, 98.5 ± 2.6%), rCBV ΔR_2^* (striatum, 100.5 ± 4.5%; lesion, 103.9 ± 8.2%; peri-infarct, 98.1 ± 4.3%), microvascular density index Q (striatum, 101.3 ± 3.3%; lesion, 99.1 ± 4.1%; peri-infarct, 99.7 ± 2.8%), vessel density N (striatum, 103.8 ± 9.0%; lesion, 98.3 ± 17.3%; peri-infarct, 97.3 ± 6.3%), and relative vessel size R (striatum, 97.1 ± 6.2%; lesion, 102.3 ± 11.4%; peri-infarct, 99.0 ± 9.3%) (Fig. 4). After stroke, the overall rCBV ΔR_2^* remained relatively constant over the course of the experiments. There was a significant effect of time in rCBV in small vessels ΔR_2 [striatum, $F(4,16)$ 3.890, $p = 0.022$; lesion, $F(4,16)$ 6.082, $p = 0.004$; peri-infarct, $F(4,16)$ 5.040, $p = 0.008$]. The percentage ratio of ΔR_2 decreased around 1 week after stroke with a trend towards subsequent increase by week 2, which was confirmed by *post-hoc* pairwise comparisons of values within the lesion before and 1 week post stroke ($p = 0.05$; Fig. 4b).

Significant effects of time were also observed for the microvascular density index Q [striatum, $F(4,16)$ 3.342, $p = 0.036$; lesion, $F(4,16)$ 6.861, $p = 0.002$; peri-infarct, $F(4,16)$ 3.339, $p = 0.036$], microvessel density N [striatum, $F(4,16)$ 3.586, $p = 0.029$; lesion, $F(4,16)$ 6.311, $p = 0.003$; peri-infarct, not significant], and relative vessel size R [striatum, $F(4,16)$ 3.259, $p = 0.039$; lesion, $F(4,16)$ 4.727, $p = 0.01$; peri-infarct, not significant]. In line with the decrease in rCBV in small vessels, Q and N ratios both decreased around 1 week after stroke, although *post-hoc* tests failed to reach significance. The decreases in N and Q at week 1 were accompanied by a dramatic increase in relative vessel size R. This persisted throughout the course of the experiments, although less pronounced for later times.

3.4. Immunohistochemistry

RECA staining clearly detected blood vessels in the brain sections 4 weeks after surgery. Photomicrographs from two representative animals indicate fewer visible vessels in the ischemic striatum (Fig. 5a and b). Histological microvessel density in the ischemic striatum was significantly lower than that of the intact striatum (585 ± 89 vs 827 ± 58 vessels mm^{-2}) [$t(5) = 4.679$, $p = 0.005$). This corresponded roughly to a ~29% decrease (Fig. 5c, right), which is within the detectability limits determined from our simulations. A similar, significant decrease of ~27% [$t(5) = 2.705$, $p = 0.043$) was observed in MRI-derived vessel density N from the VOI analysis at 4 weeks after MCAO, that is, (209 ± 81) mm^{-2} ipsilateral and (289 ± 75) mm^{-2} contralateral (Fig. 5c, left). The mean vessel diameter, and thus size, measured from brain sections in small vessels (<40 μm) were not significantly different between the ischemic (7.4 ± 1.0 μm) and the intact striatum (7.0 ± 1.0 μm; Fig. 5d, right). However, there was a ~50% increase in R in the ischemic striatum determined from the MRI VOI analysis, although this failed to reach significance [$t(5) = -2.037$, $p = 0.097$; Fig. 5d, left].

We systematically examined sections double-stained for BrdU and RECA. No double-labeled cells were observed in the hemisphere contralateral to the infarct, and green autofluorescence within the ischemic core did not permit analysis there. However, in peri-infarct regions we found occasional individual endothelial cells that also appeared to be BrdU + (Fig. 6). Overall, very few proliferating endothelial cells were detected.

4. DISCUSSION

The present study demonstrates that the temporal profile of vascular changes after stroke can be assessed noninvasively with SSCE MRI. However, our data indicate that it is crucial to optimize MRI acquisition in order to maximize sensitivity of the method. For the first time, we show that when cystic transformation occurs, inclusion of diffusion measurements on a voxel-wise basis is essential to prevent overestimation of SSCE MRI-derived

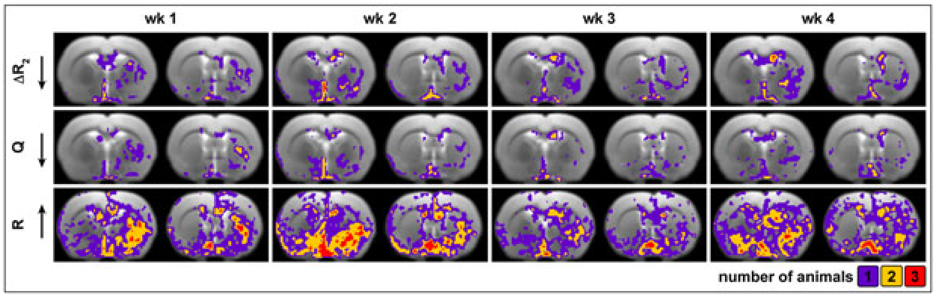
wk 1
wk 2
wk 3
wk 4
ΔR_2 ↓
Q ↓
R ↑
number of animals 1 2 3

Figure 2. Incidence maps for the MRI-derived parameters. Maps indicating, for each voxel, the number of animals that exhibited a decrease in ΔR_2 or *Q*, or an increase in *R* during the 4 weeks after MCAO. For each time point the two coronal slices shown are those that are most affected by the infarct: −1.3 (left) and −0.3 mm from bregma (right). A small trend towards the decrease of ΔR_2 and *Q* can be observed in the ischemic hemisphere, as well as an increase in *R* (bottom row) mostly in areas of the striatum. The striatum was therefore used for further quantitative volume-of-interest analysis. Other incidence maps did not show a specific trend. Although six animals entered the calculations, the maximum number of incidences found in any of the parameters was three, that is, within any region, a significant, simultaneous vascular change occurred only in a subgroup of animals.

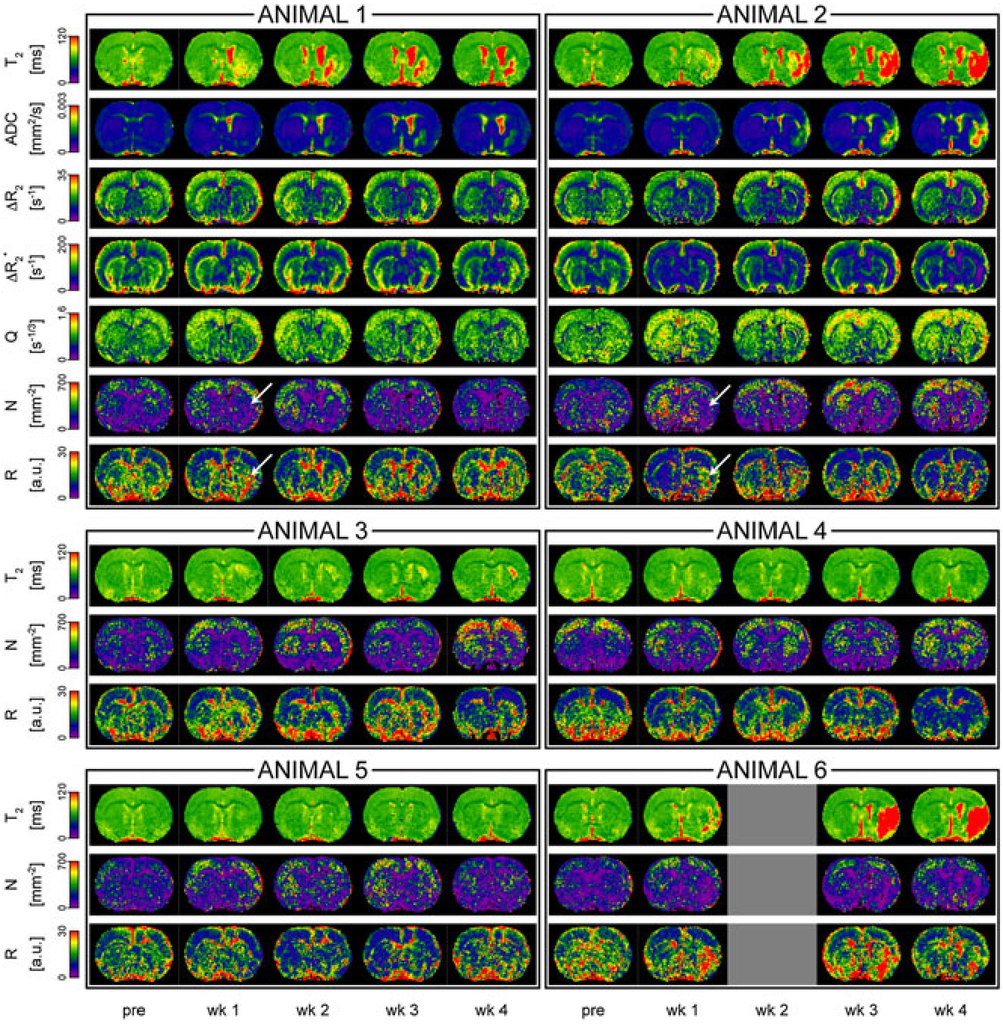
ANIMAL 1
ANIMAL 2
ANIMAL 3
ANIMAL 4
ANIMAL 5
ANIMAL 6
T_2 [ms]
ADC [mm²/s]
ΔR_2 [s⁻¹]
ΔR_2^* [s⁻¹]
Q [s⁻¹/³]
N [mm⁻²]
R [a.u.]
0
120
0.003
35
200
1.6
700
30
pre
wk 1
wk 2
wk 3
wk 4

Figure 3. Temporal profile of MRI-derived parameters. T_2, ADC, ΔR_2, ΔR_2^*, *Q*, *N* and *R* maps before and weekly after MCAO of an animal with a lesion restricted to the striatum (animal 1) and an animal with both, cortical and striatal damage (animal 2). Most relevant maps (T_2, *N* and *R*) are shown for all other animals. ΔR_2, *Q* and *N* decreased in the ischemic regions in all animals whereas there was an observable increase in relative vessel size *R*. The changes were most pronounced 1 week after surgery (arrows) but persisted also at the later time points. Animal 6 did not perform the SSCE MRI measurement at 2 weeks post stroke.

Copyright © 2013 John Wiley & Sons, Ltd.

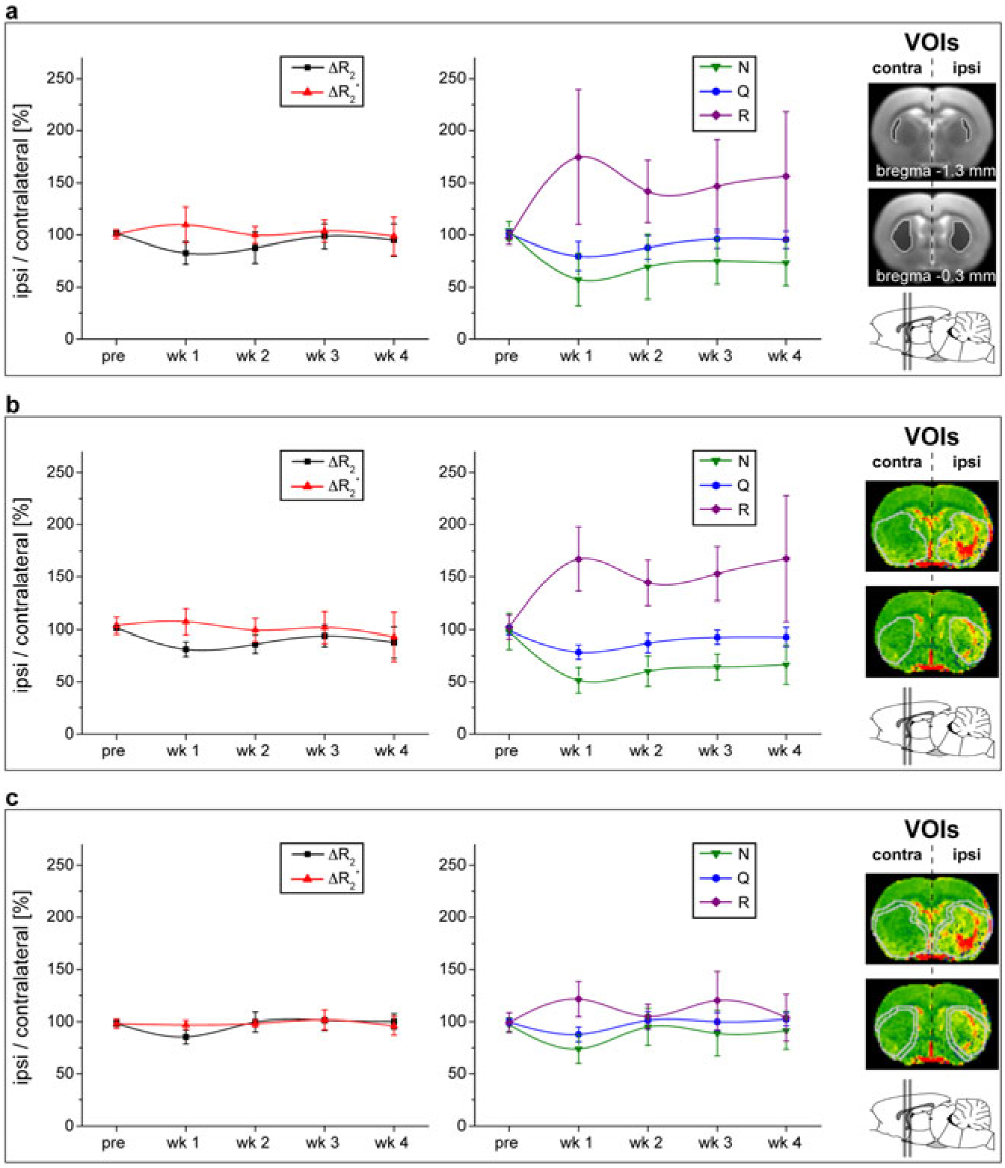

Figure 4. Quantification of MRI-derived parameters. Volume-of-interest analysis in the striatum (a), in the lesion (b), and peri-infarct zone (c) revealed a decrease in ΔR_2, Q and N and an increase in R in the ischemic striatum that was most pronounced 1 week after MCAO. These parameters normalized at the later time points (weeks 2–4). Values are expressed as a ratio of the ipsilateral to the contralateral side (group means ± standard deviation). The volumes of interest are indicated on coronal slices corresponding to −1.3 and −0.3 mm from bregma on a T_2-weighted template image (a) and a T_2-map (b, c) of animal 2. The two slices are illustrated in gray on a schematic sagittal view of the rat brain.

vessel densities. Our major finding was that there was a significant decrease in rCBV in small vessels, leading to a decrease in vessel density, which was accompanied by an increase in vessel size 1 week after MCAO in the ischemic striatum that persisted for several weeks. Microvessel density determination from histological brain sections confirmed that decreased vessel density was still present at 4 weeks after the initial insult. If large-scale angiogenesis occurred in response to stroke, this should have been reflected by an increase in vessel density. This was not the case, although the presence of sparse numbers of BrdU+/RECA + cells in the ischemic striatum indicated that some endothelial cell proliferation occurred during the first week after MCAO. Absence of double-labeled cells on the contralateral hemisphere indicated that the proliferation was induced by the stroke and not by natural turnover of endothelial cells.

4.1. SSCE MRI methodological considerations

When this method was first employed in a rodent model of stroke to measure changes in the vascular network (rCBV in small vessels, overall rCBV, vessel density and size) ΔR_2 was assessed with a turbo spin echo pulse sequence using multiple refocusing pulses to speed up the acquisition (14). Subsequent studies employed multi spin echo sequences in order to obtain measures of T_2 and ΔR_2 simultaneously and further included ADC measurements (13,24). This strategy is useful as both T_2 and ADC provide important

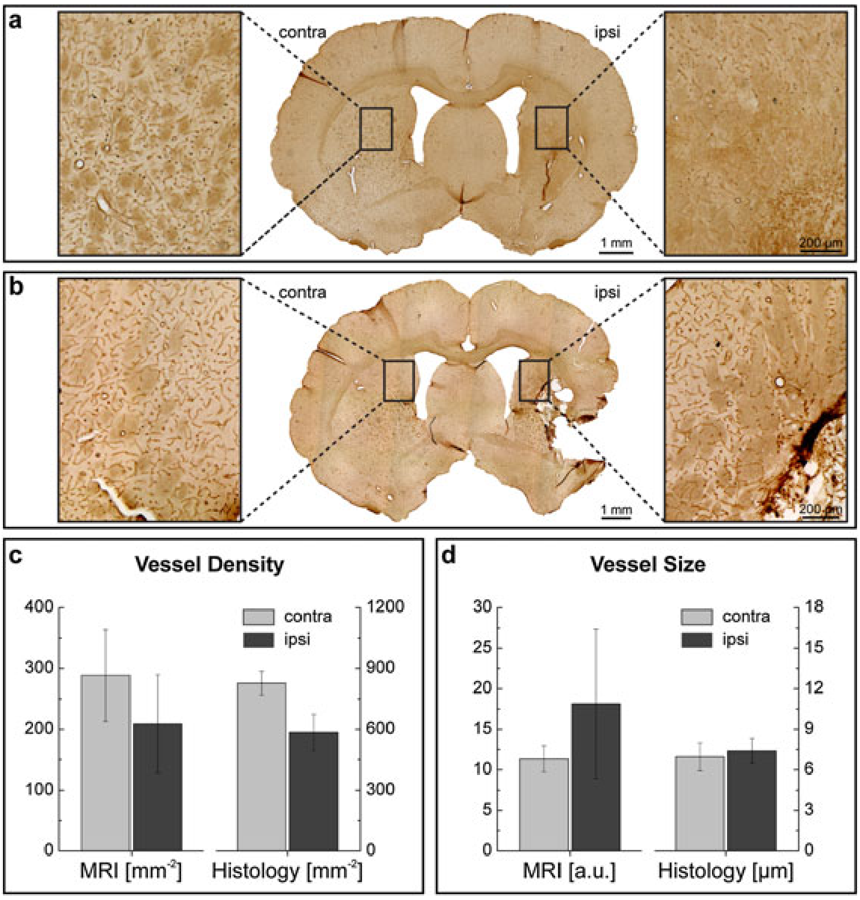

Figure 5. Comparison of MRI and histology. Tissue sections stained for vessels (RECA) of an animal with a small striatal lesion (a) and of a rat with a larger infarct (b). Semi-quantification on histological sections revealed a significant ipsilateral decrease in microvessel density (c, right) that corresponded well with the MRI results at 4 weeks after MCAO (c, left). Histological vessel diameter (of vessels <40 µm) showed only a small, nonsignificant increase in the ipsilateral striatum (d, right), whereas a highly elevated relative vessel size was found in the MRI analysis (d, left), although this failed to reach significance. For better visualization, MRI and histology data are scaled differently. Values are expressed as group means ± standard deviation.

information about the state of the ischemic tissue. However, neither of these studies performed any modification to the theory in order to account for the well-known reduction of the diffusion effect on MR transverse relaxation (19,20,25). Using the theory modification, however, leads to higher ΔR_2, Q and N values. In line with this, we found higher values of these parameters compared with the reports in which a theory correction was not applied. Furthermore, we also identified a major pitfall in the interpretation of SSCE MRI parameters when the tissue exhibits cystic transformation. In such cases, ΔR_2 is no longer a good measure of rCBV in small vessels, and neither is Q because of elevated tissue diffusivity. Our data indicate that it is essential to include local ADC values in the calculations, otherwise ΔR_2 'hot spots' may be misinterpreted as angiogenic activity.

Despite these improvements in MRI acquisition, our results show that SSCE MRI is prone to noise, especially for the vessel density estimate N. Even after optimization of acquisition parameters, the relative error in N values is on the order of ~20%. Although this is in accordance with the previous reports (13), it represents an inherent limitation of the technique. Further limitations come from the fact that the ischemic rodent brain probably violates some of the previously described assumptions that are made when applying the theory. For example, the mathematical model underlying SSCE MRI only holds for impermeable vessel walls, low blood volume fractions, and vasculature for which the microvessels can be modeled as rigid long cylinders (26). Therefore, the use of blood as an intravascular tracer through the blood oxygen level-dependent contrast seems to be an appealing alternative, e.g. to overcome problems of contrast agent leakage and heterogenous water diffusivity in peri-infarct area. Indeed, quantitative blood oxygen level-dependent approaches have been developed in order to map important parameters of oxygenation *in vivo* (27,28). Furthermore, the use of fast MR imaging during the first bolus (dynamic susceptibility MRI) or arterial spin labeling techniques could help to correlate SSCE MRI with perfusion and thus functionality of blood vessels.

4.2. Vascular changes after stroke

Using SSCE MRI we observed a decrease in microvessel density in the ischemic striatum at 1 week after stroke, a situation not surprising as this tissue has experienced widespread cell death by this time. Similar findings were reported as early as 1 day after ischemia in an embolic (13) and distal occlusion model (14). This decrease in microvessel density persisted for up to 2 weeks in the former study, which is also consistent with our results.

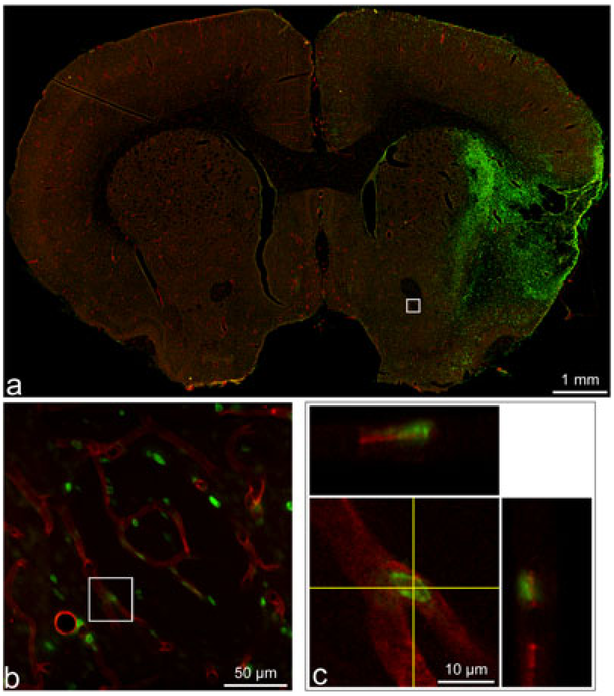

Figure 6. Confocal microscopy images of tissue sections stained for RECA (red) and BrdU (green) 4 weeks after MCAO. BrdU was administered between days 2–7 after MCAO. Overview (a) and higher magnification images (b, corresponds to the white box in a) revealed some red/green overlap and a confocal microscopy image (c, corresponds to the white box in b) confirmed this. Strong green ipsilateral staining in the lesion core (a) is due to ischemia-induced autofluorescence.

Despite the notion that the decrease in microvessel density observed in the ischemic region after stroke is persistent, the SSCE MRI study that employed the distal occlusion model noted a significant increase in microvessel density in the outer cortex of the ischemic region beginning after about 2 weeks that was attributed to angiogenesis (14). One potential reason for this discrepancy could be the choice of stroke model. However, our findings suggest that this effect could be artifactual in nature as we were able to observe a similar phenomenon in animals with cystic transformation when we employed, rather than the correct and necessary voxel-wise diffusion measurement, only a constant diffusion value to determine *N* maps. Indeed and in line with this, the authors of that study mentioned that this area of increased microvessel density was prone to cystic transformation.

In parallel to the decrease in microvessel density, we observed an increase in vessel size with SSCE MRI most pronounced at 7 days post stroke that was probably due to vasodilation of arterioles in an effort to maintain autoregulation. This phenomenon probably occurs earlier, and, indeed, Lin et al. (14) reported this observation within the first week of stroke (1–3 days), which was confirmed by an increase in the number of vessels with a diameter greater than 30 μm in tissue sections from the same time period. While that study reported a subsequent decline in vessel size, other groups suggested that this effect remains between days 7 and 21 (15) and even up to 6 weeks in the recovery region (24). In the present study, we only measured animals up to 28 days, and while *R* was still elevated at this time, this elevation was not as pronounced as during the first week. In accordance with these findings, we were also unable to observe an increase in the mean vessel diameter in the ipsilateral when compared with the contralateral striatum at 4 weeks post stroke. While it is possible that this could be an artifact of our sampling strategy, microvessel is a gross term that includes capillaries, venules and arterioles, which means that the size of vessels varies considerably even in the intact brain (29). Nevertheless, the mean vessel size estimated subcortically at 6 h post symptom onset was recently shown to be a good predictor of final infarct size at 6 days in a small cohort of patients that underwent a modified dynamic contrast-enhanced protocol similar to SSCE MRI (30). A follow-up study extended the same protocol to a larger patient cohort that presented a significant perfusion-diffusion mismatch around 24 h post symptom onset (31). Vessel size was found to be a poor predictor of infarct growth at 6 days, but microvessel density proved to be useful at discriminating infarcted from oligemic or healthy tissue. These studies highlight the utility of this technique to provide valuable information in the post-ischemic period.

4.3. Angiogenesis after stroke

Angiogenesis after ischemia is generally characterized at a cellular level by gene transcription leading to expression of pro-angiogenic molecules and finally to endothelial cell proliferation. We observed some endothelial cell proliferation during the first post-operative week, which is already well described (5), and another study observed increases in various pro-angiogenic compounds such as growth factors and endothelial nitric oxide synthase (14). While stabilization of vessel walls and formation of new networks have been reported (5), it is unclear if these processes can lead to truly functional new vasculature (7). Perfusion measurements could help to elucidate if proliferating, BrdU + endothelium belongs to functional vasculature. Unfortunately, as SSCE MRI is based on CBV measurements using an intravascular contrast agent, it is only capable of detecting perfused vessels. The evidence from the preclinical SSCE-MRI studies in stroke models consistently indicates that there is an overall decrease in microvessel density rather than a large-scale increase. The small number of animals in the present study renders general conclusions difficult. However, taken together, this implies that angiogenesis is not occurring at an advanced level and that new, functional vessel formation is limited. The histological evidence also supports this as measurements of microvessel density in tissue sections decrease corresponding to the same pattern in the MR images. From a translational point of view this may be discouraging. However, chronic hypoxia generally leads to angiogenesis and this has been shown for human stroke (4). Therefore, discrepancies owing to choice of species and model (transient ischemia in a specific rat strain versus human stroke) should further be addressed.

5. CONCLUSION

In conclusion, SSCE MRI is a useful technique to noninvasively estimate changes in the microvasculature after stroke. Our results indicate that optimization of the MR acquisition parameters is essential in order to allow robust conclusions. The focus of our study in experimental stroke has been to probe for evidence of angiogenesis in the chronic stages. Immunohistochemistry revealed endothelial cell proliferation only in peri-infarct regions, which is a sign for early angiogenesis, but newly formed endothelial cells failed to translate into higher vessel densities and functional vasculature.

6. SUPPORTING INFORMATION

Supporting information can be found in the online version of this article.

Acknowledgments

The authors thank Drs Philippe Robert and Claire Corot (Guerbet) for the generous supply of Endorem and Matthias Weigel from the Medical Physics group of the University Hospital of Freiburg for stimulating discussions. Melanie Nelles is acknowledged for technical support with histology, Ingo Przesdzing from the Department of Experimental Neurology at the Charité in Berlin with tissue section analysis, and Michael Diedenhofen for technical assistance with the data analysis. Financial support was provided from the EU-FP7 program (HEALTH-F5-2008-201842; ENCITE) and the EU-FP6 program (LSHB-CT-2006-037526; StemStroke). Funds from the German Federal Ministry of Education and Research (BMBF-0314104) and an Alexander von Humboldt fellowship for T.D.F. are gratefully acknowledged. The funders had no role in study design, data collection, analysis, the decision to publish or preparation of the manuscript.

REFERENCES

1. Beck H, Plate KH. Angiogenesis after cerebral ischemia. Acta Neuropathol 2009;117(5):481–496.
2. Hayashi T, Deguchi K, Nagotani S, Zhang H, Sehara Y, Tsuchiya A, Abe K. Cerebral ischemia and angiogenesis. Curr Neurovasc Res 2006;3(2):119–129.
3. Slevin M, Kumar P, Gaffney J, Kumar S, Krupinski J. Can angiogenesis be exploited to improve stroke outcome? Mechanisms and therapeutic potential. Clin Sci 2006;111(3):171–183.
4. Krupinski J, Kaluza J, Kumar P, Kumar S, Wang JM. Role of angiogenesis in patients with cerebral ischemic stroke. Stroke 1994;25(9):1794–1798.
5. Krupinski J, Stroemer P, Slevin M, Marti E, Kumar P, Rubio F. Three-dimensional structure and survival of newly formed blood vessels after focal cerebral. Neuroreport 2003;14(8):1171–1176.
6. Neeman M, Gilad AA, Dafni H, Cohen B. Molecular imaging of angiogenesis. J Magn Reson Imag 2007;25(1):1–12.
7. Seevinck P, Deddens L, Dijkhuizen R. Magnetic resonance imaging of brain angiogenesis after stroke. Angiogenesis 2010;13(2):101–111.
8. Kiselev VG. On the theoretical basis of perfusion measurements by dynamic susceptibility contrast MRI. Magn Reson Med 2001;46(6):1113–1122.
9. Dennie J, Mandeville JB, Boxerman JL, Packard SD, Rosen BR, Weisskoff RM. NMR imaging of changes in vascular morphology due to tumor angiogenesis. Magn Reson Med 1998;40(6):793–799.
10. Jensen JH, Chandra R. MR imaging of microvasculature. Magn Reson Med 2000;44(2):224–230.
11. Tropres I, Grimault S, Vaeth A, Grillon E, Julien C, Payen JF, Lamalle L, Decorps M. Vessel size imaging. Magn Reson Med 2001;45(3):397–408.
12. Wu EX, Tang HY, Jensen JH. High-resolution MR imaging of mouse brain microvasculature using the relaxation rate shift index Q. NMR Biomed 2004;17(7):507–512.
13. Bosomtwi A, Jiang Q, Ding GL, Zhang L, Zhang ZG, Lu M, Ewing JR, Chopp M. Quantitative evaluation of microvascular density after stroke in rats using MRI. J Cerebral Blood Flow Metab 2008;28(12):1978–1987.
14. Lin CY, Chang C, Cheung WM, Lin MH, Chen JJ, Hsu CY, Chen JH, Lin TN. Dynamic changes in vascular permeability, cerebral blood volume, vascular density, and size after transient focal cerebral ischemia in rats: evaluation with contrast-enhanced magnetic resonance imaging. J Cerebral Blood Flow Metab 2008;28(8):1491–1501.
15. Moisan A, Pannetier N, Grillon E, Richard M-J, Fraipont F, Rémy C, Barbier EL, Detante O. Intracerebral injection of human mesenchymal stem cells impacts cerebral microvasculature after experimental stroke: MRI study. NMR Biomed 2012;25(12):1340–1348.
16. Longa E, Weinstein P, Carlson S, Cummins R. Reversible middle cerebral artery occlusion without craniectomy in rats. Stroke 1989;20(1):84–91.
17. Kiselev VG, Posse S. Analytical model of susceptibility-induced MR signal dephasing: Effect of diffusion in a microvascular network. Magn Reson Med 1999;41(3):499–509.
18. Yablonskiy DA, Haacke EM. Theory of NMR Signal behavior in magnetically inhomogeneous tissues – the static dephasing regime. Magn Reson Med 1994;32(6):749–763.
19. Carr HY, Purcell EM. Effects of diffusion on free precession in nuclear magnetic resonance experiments. Phys Rev 1954;94(3):630–638.
20. Kiselev VG. Spin echo amplitude in biological tissue with implications for vessel size imaging. Joint Annual Meeting ISMRM-ESMRMB, Stockholm 2010;01-07052010(1):1792 (Proc.).
21. Hoehn-Berlage M, Eis M, Schmitz B. Regional and directional anisotropy of apparent diffusion coefficient in rat brain. NMR Biomed 1999;12(1):45–50.
22. Koay CG, Basser PJ. Analytically exact correction scheme for signal extraction from noisy magnitude MR signals. J Magn Reson 2006;179(2):317–322.
23. Paxinos G, Watson C. The Rat Brain in Stereotaxic Coordinates. Academic Press: San Diego, CA, 1998.
24. Bosomtwi A, Chopp M, Zhang L, Zhang ZG, Lu M, Jiang Q. Mean microvessel segment length and radius after embolic stroke: comparison of magnetic resonance imaging (MRI) and laser scanning confocal microscopy (LSCM). Brain Res 2011;1381(0):217–227.
25. Ullrich RT, Jikeli JF, Diedenhofen M, Böhm-Sturm P, Unruh M, Vollmar S, Hoehn M. In-vivo visualization of tumor microvessel density and response to anti-angiogenic treatment by high resolution MRI in mice. PLoS ONE 2011;6(5):e19592.
26. Neeman M, Dafni H. Structural, functional, and molecular MR imaging of the microvasculature. Annu Rev Biomed Eng 2003;5:29–56.
27. Grüne M, van Dorsten FA, Schwindt W, Oláh L, Hoehn M. Quantitative T*(2) and T′(2) maps during reversible focal cerebral ischemia in rats: separation of blood oxygenation from nonsusceptibility-based contributions. Magn Reson Med 1999;42(6):1027–1032.
28. He X, Yablonskiy DA. Quantitative BOLD: mapping of human cerebral deoxygenated blood volume and oxygen extraction fraction: default state. Magn Reson Med 2007;57(1):115–126.
29. Turner R. How much cortex can a vein drain? Downstream dilution of activation-related cerebral blood oxygenation changes. NeuroImage 2002;16(4):1062–1067.
30. Xu C, Schmidt WUH, Villringer K, Brunecker P, Kiselev V, Gall P, Fiebach JB. Vessel size imaging reveals pathological changes of microvessel density and size in acute ischemia. J Cerebral Blood Flow Metab 2011;31(8):1687–1695.
31. Xu C, Schmidt WUH, Galinovic I, Villringer K, Hotter B, Ostwaldt AC, Denisova N, Kellner E, Kiselev V, Fiebach JB. The potential of microvessel density in prediction of infarct growth: a two-month experimental study in vessel size imaging. Cerebrovasc Dis 2012;33(4):303–309.

Supplementary Figure 1

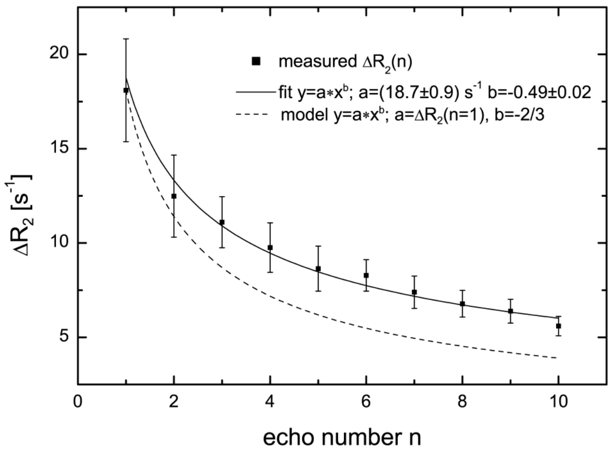

Supplementary Figure 2

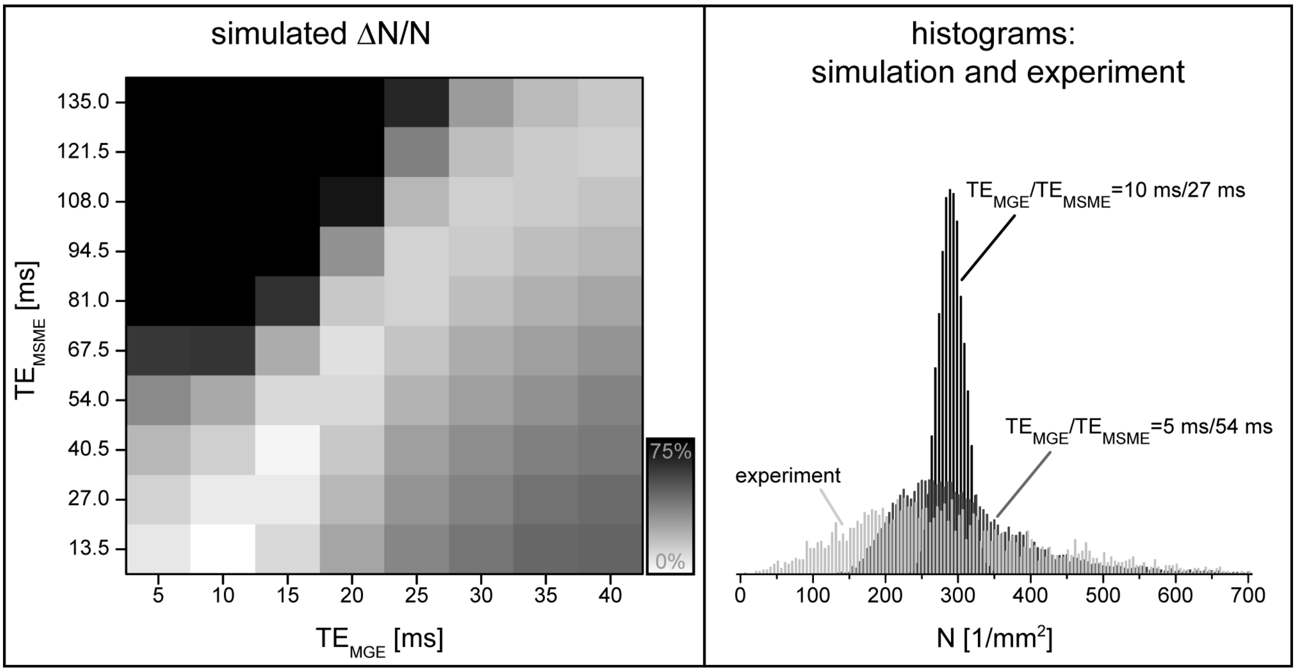

Supplementary Figure 1

Calculation of ΔR_2 values from multi spin echo pulse sequences. ΔR_2 values were calculated with equation [1] for each of the 10 echo images of the multi spin echo pulse sequences before and after injection of the superparamagnetic contrast agent. The resulting ΔR_2 values (mean ± standard deviation) in the striatum of six healthy rats are plotted (squares). The plot shows that using equation [1] leads to severe underestimation of ΔR_2, especially for later echoes (compared to the first echo). Therefore, a modification of the theory is necessary represented by equation [3]. The theoretical curve $\Delta R_2 \propto n^{-2/3}$ (dashed line) overestimates the decrease in ΔR_2 for echoes n>2. Instead, an empirical relationship $\Delta R_2 \propto n^{-0.49}$ was found (solid line). Since the use of the first echo images would lead to high noise (cf. Supplementary Fig. 2) we decided to use the 2nd echo image and to correct our data with the empirical model. A more complete theoretical description of these findings will be the subject of future studies.

Supplementary Figure 2

Optimization of acquisition and sensitivity of SSCE MRI. The parameter N is most affected by scanner noise. In order to optimize the acquisition to reduce noise propagation, signal intensities in the MSME and MGE sequences were simulated using a typical MRI-derived vessel density in the healthy striatum of rats $N = 300/mm^2$, relaxation times T_2/T_2^* (65 ms/45 ms) and changes in relaxivities $\Delta R_2/\Delta R_2^*$ (20 s^{-1}/95 s^{-1}) due to injection of iron oxide agent (30 mg Fe/kg) at 4.7 T. White noise was added to the signal intensities (10 000 simulation runs, noise level 5% of equilibrium MR signal at $TE = 0$) and N maps were calculated with the same analysis scheme used for the *in vivo* data. Left: The relative error of the mean of N was plotted as a function of echo times. Note that the relative error $\Delta N / N$ (standard deviation/mean) is highly dependent on the choice of echo time. Similar to the simulations, error propagation was minimized in the experiment at echo times of 10 and 27 ms for TE_{MGE} and TE_{MSME}, respectively. Right: Comparison of histograms of simulated N values for the optimized echo times against slightly varied echo times of TE_{MGE} / TE_{MSME} =5 ms/54 ms shows that the SSCE MRI method is very sensitive to noise and acquisition parameters. Choosing non-optimal echo times leads to a non-symmetric distribution of N values, including a shift of the expected mean. We compared the simulated histogram to what was obtained during the experiments (2800 data points from the striatum of six healthy rats) using the optimized echo times. The histogram from our experiments is normally distributed. However, additional physiological noise is introduced during our experiments, and simulations did not account for variation in vessel densities in the tissue. Therefore, we observed a relatively widespread (but still symmetric) distribution compared to the simulated data, for which we took only scanner/thermal noise into account. Given the width of the experimentally found distribution, we estimate that a change in vessel density needs to be on the order of ~20% to be detectable by SSCE MRI.

Spatio-temporal dynamics, differentiation and viability of human neural stem cells after implantation into neonatal rat brain

IV

EJN fens EUROPEAN JOURNAL OF NEUROSCIENCE

European Journal of Neuroscience, Vol. 34, pp. 382–393, 2011 doi:10.1111/j.1460-9568.2011.07759.x

MOLECULAR AND DEVELOPMENTAL NEUROSCIENCE

Spatio-temporal dynamics, differentiation and viability of human neural stem cells after implantation into neonatal rat brain

Therése Kallur,[1] Tracy D. Farr,[1] Philipp Böhm-Sturm,[1] Zaal Kokaia[2] and Mathias Hoehn[1]
[1]In-Vivo-NMR Laboratory, Max Planck Institute for Neurological Research, Gleuelerstrasse 50, D-50931 Cologne, Germany
[2]Laboratory of Neural Stem Cell Biology and Therapy, Department of Clinical Sciences, Stem Cell Center, Lund, Sweden

Keywords: cell tracking, human neural stem cell differentiation, implantation, magnetic resonance imaging, stem cell proliferation, superparamagnetic iron oxide nanoparticles

Abstract

Neural stem cells (NSCs) have attracted major research interest due to their potential use in cell replacement therapy. In patients, human cells are the preferred choice, one source of human NSCs being the brain of fetuses. The aims of the present study were to explore the long-term differentiation, mobility and viability of NSCs derived from the human fetal striatum in response to intracerebral implantation. To investigate long-term spatio-temporal and functional dynamics of grafts *in vivo* by magnetic resonance imaging, these cells were labeled with superparamagnetic iron oxide (SPIO) nanoparticles prior to implantation. SPIO-labeling of human NSCs left the quantitative profile of the proliferation, cell composition and differentiation capacity of the cells *in vitro* unaltered. Also after transplantation, the phenotypes after long-term cell differentiation were not significantly different from naïve cells. Upon transplantation, we detected a hypointensity corresponding to the striatal graft location in all animals and persisting for at least 4 months. The hypointense signal appeared visually similar both in location and in volume over time. However, quantitative volumetric analysis showed that the detectable, apparent graft volume decreased significantly from 3 to 16 weeks. Finally, the human NSCs were not proliferating after implantation, indicating lack of tumor formation. These cells are thus a promising candidate for translationally relevant investigations for stem cell-based regenerative therapies.

Introduction

Stem cell-based therapy aims to restore lost brain function after acute and chronic neurological conditions by exogenous delivery of stem cells. Neural transplantation of tissue, obtained from human embryos, has provided proof of successful restoration of lost brain function in the human brain (Lindvall & Kokaia, 2009). However, limited tissue availability and standardization make the use of fetal tissue problematic. Therefore, the discovery that embryo- and adult-derived neural cells could be expanded *in vitro* provided a promising route for cell replacement therapy (Reynolds & Weiss, 1992; Reynolds *et al.*, 1992). Stem cell research has demonstrated that cells in culture can generate a wide range of neural cells for this purpose. One source of human cells for use in cell therapy are neural stem cells (NSCs) of different origin (Guillaume *et al.*, 2008; Selden *et al.*, 2008; Koch *et al.*, 2009). Recently, NSCs derived from the fetal striatum have been expanded continuously *in vitro* for long periods of time, with maintained normal karyotype and high capacity to differentiate into cells with different neuronal phenotypes (Kallur *et al.*, 2006, 2008). Furthermore, when transplanted as neurospheres, the cells survive in the stroke-damaged rat striatum, migrate towards the injury and differentiate into mature neurons without tumor formation (Darsalia *et al.*, 2007). As such, these cells represent attractive candidates for cell replacement therapy. However, there are several unanswered questions, for which exploration is required before progression to full-scale clinical trials can be made feasible.

One fundamental issue is to determine the optimal proliferation, survival, differentiation and migration capacity of the grafted cells (Lindvall & Kokaia, 2010). This is especially important on a long-term basis and quantitatively. In the experimental setting, complete characterization of graft proliferation, survival, migration and differentiation capacity requires extensive work. Although immunohistochemistry remains fundamental in this regard, another strategy, allowing long-term monitoring of grafts non-invasively, is neuroimaging. Magnetic resonance imaging (MRI) offers the important advantage over other imaging modalities of high spatial resolution, and grafted stem cells have been successfully monitored *in vivo* when labeled with contrast agents, such as superparamagnetic iron oxide (SPIO) nanoparticles (Hoehn *et al.*, 2002; Bulte *et al.*, 2003; Stroh *et al.*, 2005; Guzman *et al.*, 2008). Some groups are also currently employing this approach *in vivo* to look at grafted human fetal-derived NSCs (Guzman *et al.*, 2007; Neri *et al.*, 2008). Even clinical Phase I application of human NSCs has been discussed for the treatment of

---

Correspondence: Professor M. Hoehn, as above.
E-mail: mathias@nf.mpg.de

Received 11 November 2010, revised 15 April 2011, accepted 11 May 2011

© 2011 The Authors. European Journal of Neuroscience © 2011 Federation of European Neuroscience Societies and Blackwell Publishing Ltd

neuronal ceroid lipofuscinosis. However, despite the popularity of iron oxide-based labels, most studies have examined whether these agents alter the specific characteristics of the stem cells only over short, subacute periods, rather than over chronic periods. There is also much debate as to the actual specificity of the signal observed in the magnetic resonance images, whether iron oxide particles are lost over time or whether the cells are removed by phagocytic activity.

The aims of the present study were: (i) to carefully assess the optimal labeling strategies with SPIO particles for minimization or exclusion of label influence on human striatal NSCs *in vitro*; (ii) to quantitatively analyse the long-term behavior of the cell phenotype and tolerance of the intracellular label *in vivo* after transplantation into rat brain; (iii) to observe the spatio-temporal and functional dynamics of the cells up to 4 months, using *in vivo* tracking by MRI of intrastriatally grafted human striatal NSCs; and (iv) to correlate MRI findings with standard post-mortem immunostainings and histological methods.

Materials and methods

Culturing of human NSCs

Striatal tissue was obtained from an 8-week-old aborted human fetus from Malmö/Lund University Hospitals, according to the guidelines approved by the Lund/Malmö Ethical Committee. The characterization of neurosphere-expanded NSCs from human fetal striatum has been described in detail elsewhere (Kallur *et al.*, 2006). Briefly, after microdissection and dissociation of the striatal tissue, cells were maintained at 37 °C in a humidified atmosphere with 5% CO_2. The expansion medium (DMEM/F-12; Gibco, Grand Island, NY, USA; L-glutamine, 2.92 g/100 mL; HEPES, 23.8 mg/100 mL; $NaHCO_3$, 7.5%; glucose, 0.6%; and heparin, 2%, all from Sigma-Aldrich, Hamburg, Germany) contained N-2 supplement (1%; Gibco), human leukemia inhibitory factor (10 ng/mL; Sigma-Aldrich), epidermal growth factor (20 ng/mL) and fibroblast growth factor (10 ng/mL (both from Peprotech, Hamburg, Germany).

Labeling cells with MRI contrast agent

SPIO nanoparticles (stock solution 11.2 mg Fe/mL; Endorem®; Guerbet, France) at a concentration of 56, 168, 280 or 560 μg Fe/mL (5, 15, 25 or 50 μL/mL; Endorem) of medium were added 4 days after the last passage directly to the NSC culture medium and incubated overnight. Subsequently, the cell suspension was spun down at 181 ***g*** for 5 min, the pellet was washed twice and finally resuspended in fresh medium. Labeled cells were either replated in culture flasks or kept on coated chamber slides.

Determination of detectability and dilution of contrast agent

To determine detectability limits with MRI, the SPIO-labeled neurospheres were spun down, washed in potassium phosphate-buffered saline (KPBS), fixed with 4% paraformaldehyde (PFA), washed again and resuspended in KPBS. The fixed, labeled neurospheres were injected at different cell concentrations into phantoms comprising 3% gelatin in small, custom-made 22-mm cups, and were subsequently scanned with MRI.

Dilution of the label through cell division was also examined. Labeled neurospheres were centrifuged, washed and replated in culture flasks for 1 week. Thereafter, the spheres were either prepared as phantoms and scanned, or plated on poly-L-lysine (PLL; Sigma)-coated eight-well chamber slides, immediately fixed with 4% PFA and stained with Prussian Blue (PB) for the presence of intracellular iron deposits. Additionally, dilution of label upon cell differentiation was examined by plating and differentiating SPIO-labeled neurospheres on coated chamber slides for 1 week.

Cell preparation for transmission electron microscopy

Cells were fixed in 3% glutaraldehyde in 0.1 M Soerensen's phosphate buffer for 22 h, washed with the same buffer overnight, embedded in 2% agarose, followed by 1 h in 1% OsO_4 in 17% sucrose buffer, rinsed with distilled water and dehydrated with increasing concentrations of ethanol. Finally, cell samples were embedded in Epon (Fluka; Sigma), polymerized for 8 h at 37 °C and 56 h at 60 °C, and cut into 70–100-nm-thick slices. The samples were analysed with a Philips EM 400 T (Philips) at 60 kV and photomicrographs were taken with a CCD camera (Olympus).

Assessment of label influence on cell survival, proliferation and differentiation

Cell viability was determined in culture by the trypan blue exclusion method before, shortly after and at 7 days after labeling with SPIOs. For determination of the cell phenotypes within the proliferating culture, SPIO-labeled neurospheres were plated on PLL-coated eight-well chamber slides, allowed to attach for 3 h, then fixed and processed for immunocytochemistry. For determination of cell differentiation capacity, growth factors were removed and 1% fetal bovine serum (Gibco) was added. Labeled cells were differentiated for up to 18 days, then fixed and subsequently stained. Medium was changed every third day during experiments.

Transplantation procedures

All animal experiments were conducted according to the guidelines laid out in the German Animal Welfare Act, in accordance with the European Communities Council Directive 86/609/EEC, and were approved by the local authorities.

Human NSC cultures (passage 21) were labeled with SPIOs as above. On the day of transplantation, SPIO-labeled neurospheres (diameter $\approx$100 μm) were centrifuged and resuspended in Hank's Balanced Salt Solution (Gibco). The neurosphere suspension had a concentration of approximately 100 000 viable cells/μL and was kept on ice during the entire transplantation procedure. To assess that the hypointensity in T2*-weighted MRI is due to the SPIO-labeled cells and not due to the implantation process itself, we performed one control experiment in which cells were treated identically, but labeled with a substance (CELSENSE 1000; Celsense, Pittsburgh, PA, USA) inert to T2*-weighted images.

Twenty-two neonatal (postnatal day 3) Sprague–Dawley rats (Janvier, France) were anesthetized by lowering body temperature to 1–3 °C and placed in a cooled Cunningham's stereotaxic frame with skull surface aligned in the horizontal plane. Using a Hamilton syringe, the neurosphere suspension (1 μL) was injected unilaterally into the right striatum at the following coordinates: 0.5 mm anterior and 2.1 mm lateral to bregma and 3.0 mm from the brain surface. After injection, the needle was kept in place for 5 min. The wound was closed and animals were resuscitated. Litters were kept together with the mother until weaning, and all animals were housed under a 12/12-h light–dark cycle with *ad libitum* access to food and water. The rats were perfused at 3 (n = 4), 6 (n = 8; one was control

© 2011 The Authors. European Journal of Neuroscience © 2011 Federation of European Neuroscience Societies and Blackwell Publishing Ltd

animal) and 16 ($n = 7$) weeks after transplantation. One animal received cells pre-labeled with a proton-non-sensitive label as sham control. This was performed to exclude T2*-weighted hypointensity caused by bleeding from the needle insertion or from air pockets generated in the course of the cell injection. No cyclosporine A (CsA) was applied as the immune system was not fully developed at the time of grafting. Furthermore, we decided against CsA treatment because we wanted to monitor the cell behavior in a naïve environment.

MRI acquisition

High-resolution magnetic resonance images were acquired on a Biospec 11.7-T/16-cm dedicated animal scanner system (Bruker BioSpin, Ettlingen, Germany) equipped with actively shielded gradient coils (BGA9S, 750 mT/m$^-$; Bruker). *In vitro* MRI was carried out with a 25-mm single-loop surface coil in transmit/receive mode and a three-dimensional (3D) gradient echo fast low-angle shot (FLASH) sequence: field of view (FOV) = 22 mm^2 × 0.88 mm, matrix = $512^2 \times 128$, TE/TR = 7 ms/200 ms, flip angle (FA) = 30°, number of averages = 2, with a total acquisition time (TA) of 7:17 h.

For *in vivo* MRI, animals were anesthetized and maintained with 1–2% isoflurane in a 70 : 30 nitrous oxide/oxygen mixture. Respiration rate was monitored using a pressure-sensitive pad placed under the thorax together with DASYLAB (Germany) software; body temperature was maintained by an in-house feedback control system. Animals were fixed with ear bars in standard animal holders (Bruker). Radiofrequency transmission was achieved with a birdcage quadrature resonator coil (72 mm diameter) and the signal was detected with quadrature mouse and rat brain surface coils (Bruker) depending on the size of the animals. The imaging protocol consisted of an isotropic 3D FLASH sequence: FOV = 19.2 mm^3, matrix = 96^3, TE/TR = 3.9 ms/100 ms, FA = 15°, TA = 15:21 min; a 2D multi-gradient echo (MGE) sequence: 20 contiguous 0.6-mm slices, FOV = 19.2 mm^2, matrix = 128^2, TE/TR = 3.5 ms/4000 ms, 32 echoes, FA = 30°, TA = 8:32 min; a 2D multi-slice multi spin echo (MSME) sequence: geometry and resolution identical to MGE, TE/TR = 10.25 ms/4000 ms, 16 echoes, TA = 8:32 min; and a 2D FLASH sequence: 16 contiguous 0.6-mm slices, FOV = 19.2 mm^2, matrix = 256^2, TE/TR = 6 ms/400 ms, FA = 30°, TA = 6:49 min.

Image postprocessing and data analysis

MR images were processed to calculate quantitative parameter maps with a home-written software program written in IDL (ITT Visual Information Solutions, Boulder, CO, USA). The MRI signal S(TE) in MSME/MGE scans was fitted on a voxel basis with a monoexponential decay $S(\mathrm{TE}) = A{*}\exp(-\mathrm{TE}/B) + C$ with equilibrium signal A, relaxation time $B = T_2$ (T_2^*) for the MSME (MGE) sequence, and an offset C to reduce bias introduced by the use of power images (Miller & Joseph, 1993).

Regions of interest (ROI) analysis of the quantitative maps was performed with the freeware program IMAGEJ (http://rsbweb.nih.gov/ij/). The slice exhibiting strongest T_2 and T_2^* effect was selected, and an area containing cells was segmented semi-automatically based on a T_2^* threshold of 10 ms. The resulting ROI was mirrored to the contralateral side, and the relative changes of mean T_2 and T_2^* in the ipsilateral ROI compared with the contralateral one were averaged over all animals. 3D reconstructions of the grafts were performed with the software package AMIRA (Mercury Computer Systems, Chelmsford, MA, USA) based on hypointensity in the 3D FLASH images. The FLASH 3D image was mirrored horizontally, registered to the original dataset with FMRIB Software Library (FSL; http://www.fmrib.ox.ac.uk/fsl/) and subtracted from the original. The image obtained, in which the contrast of labeled cells compared with the (mirrored) non-grafted contralateral side was expressed as a clear hyperintensity, was then used for manual segmentation.

Immunocytochemistry and histology

Cells were fixed in 4% PFA for 15 min at room temperature followed by three rinses in KPBS. For staining of tissue sections, animals were deeply anesthetized and perfused transcardially with saline followed by 4% PFA. Brains were post-fixed overnight and then kept in 20% sucrose solution until they sunk. Forty-micrometer-thick sections were cut in the coronal plane using a freezing microtome (Leica, Germany), and kept at −20 °C in cryo-protective solution. Before immunostaining, cells and tissue sections were pre-incubated in 5% normal serum, and 0.025 and 0.25% Triton X-100, respectively, in KPBS for 45 min at room temperature. Incubation in primary antiserum was carried out overnight at +4 °C and the following primary antibodies were used – mouse monoclonal anti-β-III tubulin (Cat. No. T8660; 1 : 333; Sigma-Aldrich, Lee & Pixley, 1994), mouse monoclonal anti-dextran (Cat. No. 01403; DX-1; 1 : 100; StemCell Technologies, Vancouver, BC, Canada, Guzman *et al.*, 2007), goat polyclonal anti-doublecortin (Cat. No. sc-8066; DCX; 1 : 400; Santa Cruz Biotechnologies, Santa Cruz, CA, USA, Rao & Shetty, 2004), mouse monoclonal anti-rat CD-68 (Cat. No. MCA341R; ED-1; 1 : 2000; AbD Serotec MorphoSys AbD, Düsseldorf, Germany, Graeber *et al.*, 1990), rabbit polyclonal anti-GFAP (Cat. No. Z0334; 1 : 500; DakoCytomation, Glostrup, Denmark), mouse monoclonal anti-GFAP (Cat. No. G6171; 1 : 400; Sigma-Aldrich, Reeves *et al.*, 1989), mouse monoclonal anti-human nucleus (Cat. No. MAB1281; HuNu; 1 : 100; Chemicon, Temecula, CA, USA, Vescovi *et al.*, 1999), rabbit polyclonal anti-Ki67 (Cat. No. ab15580; 1 : 500; Abcam, Cambridge, MA, USA, Scholzen & Gerdes, 2000) and rabbit polyclonal anti-human nestin (Cat. No. AB5922; 1 : 500; Chemicon; Hockfield & McKay, 1985). Primary antibodies were detected using appropriate fluorescent Cy3 (Jackson ImmunoResearch) or biotin-conjugated (Vector Laboratories) secondary antibodies (1 : 200), which were then detected with Alexa 488-conjugated streptavidin (1 : 200; Molecular Probes). To determine the specificity of the primary antibodies and the level of background generated from the secondary antibodies, in one well per *in vitro*-staining the primary antibodies were omitted as a negative control and *in vivo* a negatively stained control section was included. For double labeling, only one biotinylated secondary antibody was used at a time. For nuclear staining, Hoechst 33342 (1 : 1000; Molecular Probes) was added during final incubation with secondary antibodies. Sections were mounted on PLL-coated slides (Thermo Fisher Scientific, Germany) and slides coverslipped with glycerol-based mounting medium.

For PB staining, fixed cells and sections were washed with KPBS and incubated for 10 min in 10% potassium ferrocyanide [$K_4Fe(CN)_6$] solution and then for 20 min in 4% HCl and 4% $K_4Fe(CN)_6$ (2% Perl's solution). Following PB incubation, the fixed cells and sections were rinsed with water and coverslipped with Entellan (Merck, Darmstadt, Germany). For standard chromogenic visualization, endogenous peroxidase activity was quenched with KPBS containing 1% H_2O_2 and 10% methanol. After consecutive rinses, sections were incubated with primary antibodies overnight. The following day, sections were incubated with biotinylated secondary antibodies and, after subsequent rinses, were incubated with an avidin–biotin complex

© 2011 The Authors. European Journal of Neuroscience © 2011 Federation of European Neuroscience Societies and Blackwell Publishing Ltd

(Elite ABC kit; Vector), and developed by intensified reaction with diaminobenzidine (DAB; Sigma).

Cell quantification and statistical analysis

Quantification of grafted cells in the striatum was carried out in all brain slices with visible grafts under a 40× objective on a Leica TCS SP2 microscope equipped with a supplementary CCD camera (Leica Microsystems, Wetzlar, Germany). *In vitro* cell counting was performed on 20 randomly chosen fields, counting both total cell number and cells positive for the protein of interest. Each well was evaluated separately and at least eight wells per staining were counted. Double-immunoreactivity was verified with confocal laser scanning microscopy.

Differences between *in vitro* SPIO-labeled cells with different concentrations of Endorem and control cells were evaluated with one-way analysis of variance (ANOVA) followed by *post-hoc* pairwise comparison with a Bonferroni/Dunn correction for multiple comparisons. Analysis of the ROI data across all four time points was performed using a two-way repeated-measures ANOVA using both time and hemisphere (ipsilateral and contralateral to the graft) as the independent within-subject measures. Evaluation of the quantitative 3D reconstruction was performed by one-way repeated-measures ANOVA with a Greenhouse/Geisser correction if sphericity was violated. Differences between grafted cells at the early and late time point after transplantation were evaluated with Student's unpaired *t*-test. Data are expressed as means ± SEM and differences are considered significant at $P < 0.05$.

Results

Determination of contrast agent concentration, detectability and dilution in vitro

Human NSCs were readily labeled with both a low (5 μL Endorem/mL) and a high (50 μL Endorem/mL) concentration of SPIOs, without the need of lipofectant agents (Fig. 1A–D). The intracellular localization of the iron deposits was clearly visualized as electron-dense inclusions in the cytoplasm by transmission electron microscopy (Fig. 1E and F). To assess the detectability of the cells by MRI as a function of the number of cells, or of differences in the concentration of SPIOs in the culture medium, we scanned phantoms loaded with labeled, fixed human NSCs. Higher cell numbers were easily detected as they produced greater signal changes in the images. However, small changes in SPIO concentration within a constant number of cells did not appear to produce distinguishable differences in signal changes in the images (Fig. 2A). The detection limit *in vitro* was estimated from a dilution series using the same phantoms. These experiments, performed under ideal *in vitro* conditions, showed that as little as approximately 500 cells labeled with 50 μL/mL could be detected

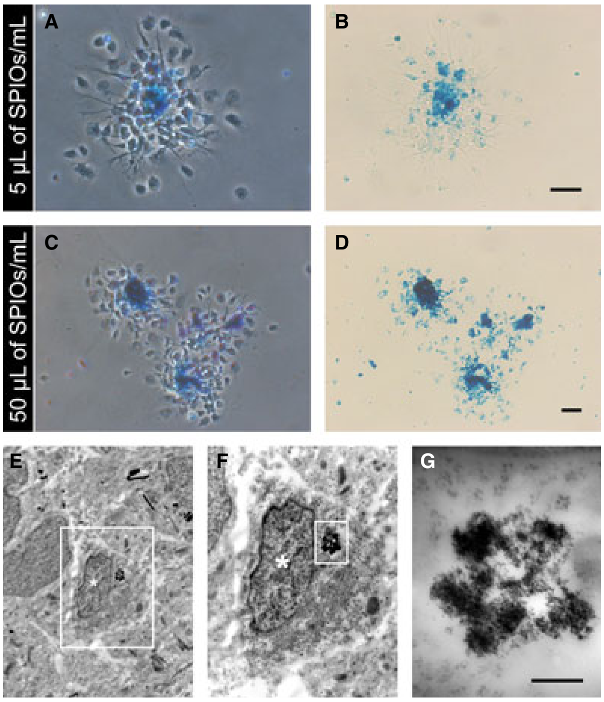

FIG. 1. Incorporation of SPIO nanoparticles by human striatal NSCs. Photomicrographs of Prussian Blue (PB)-stained human NSCs labeled either with 5 μL (A and B) of Endorem (56 μg Fe/mL) or 50 μL (C and D) of Endorem (560 μg Fe/mL). Images were acquired with phase contrast (A and C) and bright field (B and D) microscopy. The PB+ cells contain several punctate regions of blue deposits (B and D) that correspond to iron in endosomes as illustrated by transmission electron microscopy images (E–G). The boxed area in E depicts one SPIO-labeled human cell in F, and the boxed area in F shows cytosolic deposition of SPIO nanoparticles in G. White asterix indicates the nucleus. Scale bars in B and D = 50 μm and the scale bar (G) in E = 5 μm, F = 3 μm and G = 220 nm. For interpretation of color references in figure legend, please refer to the Web version of this article.

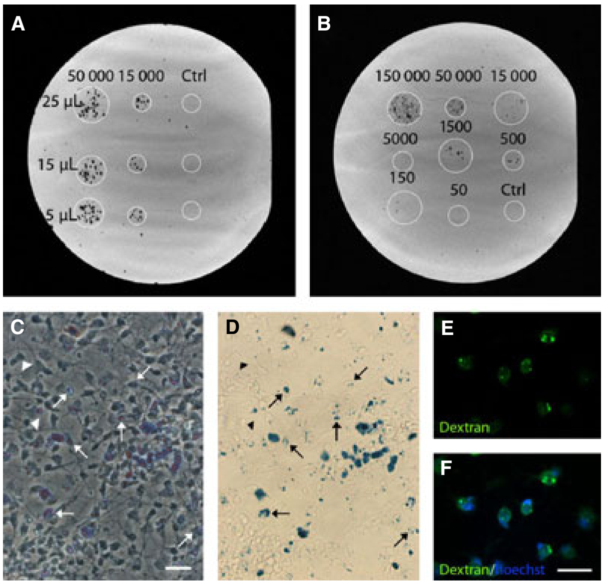

FIG. 2. (A) Detectability of SPIO-labeled NSCs. MR images of a phantom containing different amounts of NSCs (50 000 or 15 000) labeled with different concentrations of Endorem (25, 15 and 5 μL). Note – the amount of SPIO-labeled cells in the white circles was easily distinguished, but there appeared to be no differences in the signal intensities between the different doses of contrast agent employed. Cells without contrast agent (Ctrl) did not result in any hypointensity in the MR images (A). (B) Phantoms containing different amounts of cells labeled with 15 μL Endorem revealed that the detection limits of MRI was around 500 cells. Upon differentiation, the cells labeled with Endorem (15 μL) maintained the incorporated SPIO particles in the endosomes, as shown by PB (C and D), and anti-DX-1 (green) for the dextran coating of the SPIOs and Hoechst (blue) staining for cell nuclei (E and F). Arrows depict examples of PB-stained cells and arrowheads the few, non-stained cells. Scale bars = 50 μm. For interpretation of color references in figure legend, please refer to the Web version of this article.

© 2011 The Authors. European Journal of Neuroscience © 2011 Federation of European Neuroscience Societies and Blackwell Publishing Ltd

(Fig. 2B) and thus provided a lower threshold of cell number necessary for detectability (under ideal conditions).

Furthermore, to investigate whether differentiation of the cells resulted in loss of the SPIO-label, the human NSCs were allowed to differentiate for up to 6 days *in vitro*. After fixation and subsequent staining, in both cases it was clear that the label had remained within the cells, and the cells with SPIO particles were distributed evenly over the entire surface area in the chamber wells (Fig. 2C–F).

Effect of contrast agent-labeling in vitro

To determine whether the cellular phenotypes and the ratio of proliferating and apoptotic cells within the labeled cultures were influenced by incorporation of contrast agent or by the concentration of contrast agent, detailed quantifications of the immunostainings were performed. Quantification of the proliferating cultures revealed that, of the total number of cells, around 80% were nestin+ (Fig. 3A and B), 20–25% were GFAP+ (Fig. 3D and E) and 3% were β-III tubulin+ (Fig. 3G and H), and these percentages were not significantly different between the different concentrations of contrast agent nor from unlabeled control cell conditions. Moreover, the ratio of dead or dying cells exhibiting pyknotic or fragmented nuclei (as judged with Hoechst nuclear dye) was only around 5% (Fig. 3J and K) and the number of Ki67+ cells was 65% (Fig. 3M and N), irrespective of group.

In addition, cell viability was determined before and after labeling either directly or at 7 days and compared with unlabeled control cells, as a ratio of living cells out of the total number of living and dead cells

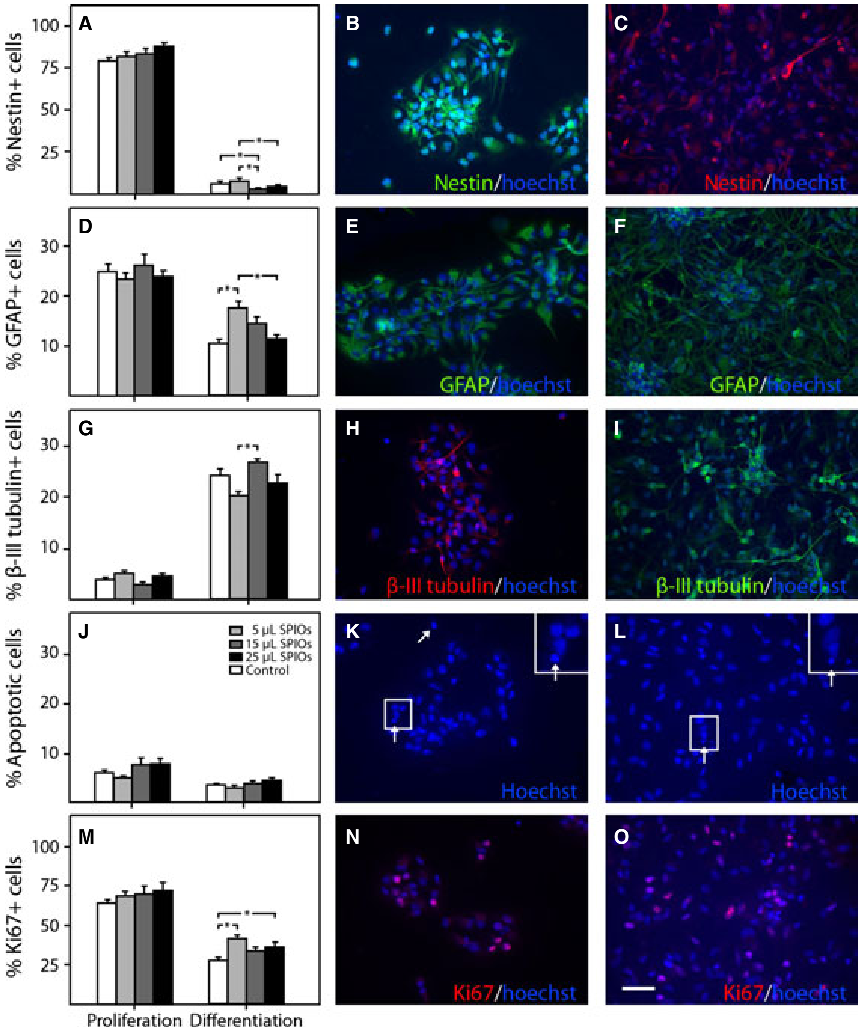
A
% Nestin+ cells
100
75
50
25
B
Nestin/hoechst
C
Nestin/hoechst
D
% GFAP+ cells
30
20
10
E
GFAP/hoechst
F
GFAP/hoechst
G
% β-III tubulin+ cells
30
20
10
H
β-III tubulin/hoechst
I
β-III tubulin/hoechst
J
% Apoptotic cells
30
20
10
5 µL SPIOs
15 µL SPIOs
25 µL SPIOs
Control
K
Hoechst
L
Hoechst
M
% Ki67+ cells
100
75
50
25
N
Ki67/hoechst
O
Ki67/hoechst
Proliferation
Differentiation

FIG. 3. Effect of label on cell phenotypes. Quantitative measurement of the cell phenotypes present in SPIO-labeled compared with non-labeled naïve human NSC cultures and neural phenotypes generated after *in vitro* differentiation of labeled and non-labeled cells (percentage of total number of cells ± SEM) (A–I) (light grey bars, 5 μL; gray bars, 15 μL; black bars, 25 μL Endorem; white bars, non-labeled control cells). Percentage of nestin+ (A), GFAP+ (D) and β-III tubulin+ (G) cells during proliferation and after 18 days of differentiation of the cultures. Photomicrographs of the labeled cells illustrate the nestin+, GFAP+ and β-III tubulin+ cells during proliferation (B, E and H) and after differentiation (C, F and I). The differentiated labeled neural cells, irrespective of label concentration, appeared morphologically similar to the non-labeled control cells. The percentage of cells with shrunken, rounded or fragmented nuclei (J) was similar overall, and is illustrated during proliferation (K) and after differentiation (L) with higher magnification insets in the respective images. The number of Ki67+ cells (M) and representative images acquired from proliferation (N) and after differentiation of the cells (O). Scale bar = 50 μm.

© 2011 The Authors. European Journal of Neuroscience © 2011 Federation of European Neuroscience Societies and Blackwell Publishing Ltd

counted by trypan blue exclusion. Prior to labeling the mean viability was 95.2 ± 2.4 and 93.0 ± 1.5% of the control batch and of the batch for later labeling, respectively. Immediately after labeling it was 92.9 ± 3.8% for the control and 85.6 ± 3.1% for the labeled batch. At 7 days post-labeling, we observed 87.0 ± 0.4 and 88.0 ± 0.8% of viable cells for non-labeled control and SPIO-labeled cultures, respectively.

To investigate if the differentiation capacity of the human NSCs incubated with contrast agent was affected, quantification of the neural phenotypes generated after 18 days of differentiation was performed. As expected, the number of nestin+ cells was dramatically decreased from 80% in all SPIO-labeled differentiated groups to around 4% following differentiation. However, cultures labeled with 15 μL Endorem contained significantly less nestin+ cells than the unlabeled control cells ($F_{3,39} = 6.38$, $P = 0.0013$; Fig. 3A and C). The number of GFAP+ cells decreased (from approximately 25%) to around 15% in all groups, and the group labeled with 5 μL Endorem had significantly more GFAP+ cells than the unlabeled control group ($F_{3,35} = 9.07$, $P = 0.0001$; Fig. 3D and F). In comparison, after differentiation there were high numbers of β-III tubulin+ cells, approximately 20–25%, in all groups compared with the proliferation experiments (< 10%), with more generated in the group labeled with 15 μL Endorem (Fig. 3G and I). The proportion of dead or dying cells was similar to what was observed in the proliferation experiments (Fig. 3J and L). The number of Ki67+ cells in all differentiated groups decreased (from approximately 65%) to around 30% (Fig. 3M and O). However, despite the overall decrease of Ki67+ cells, the only group with a comparable proportion of Ki67+ cells to the unlabeled control group was the cells labeled with 15 μL Endorem. The other two groups contained significantly more Ki67+ cells after differentiation compared with the control group ($F_{3,35} = 9.86$, $P < 0.0001$).

Altogether, the contrast agent did not seem to severely alter the *in vitro* character of the human striatal NSCs. However, due to the smaller proportion of nestin+ and Ki67+ and larger proportion of β-III tubulin+ cells generated after differentiation, the following *in vivo* experiments were conducted with a cell labeling concentration of 15 μL Endorem/mL culture medium.

Qualitative and quantitative longitudinal MRI of transplanted human neural stem cells

To monitor long-term dynamics of labeled human NSCs *in vivo*, we transplanted the cells homotopically into the striatum of neonatal rats and imaged the animals repetitively at 3, 6, 12 and 16 weeks post-transplantation. At all time points and in all animals scanned, a hypointense signal in the striatum was observed at the cell injection site (Fig. 4). In comparison, when grafting an animal with human NSCs labeled with a non-proton-based contrast agent, no hypointense signal at the site of implantation was detected (Fig. 4; bottom), thus confirming that the observed signal change in the striatum was produced from the SPIO label and was not an artifact introduced by the transplantation procedure itself.

Both T_2- and T_2^*-maps were calculated at all time points (Fig. 5A–D). ROI selection and subsequent analysis revealed a significant effect of time ($F_{3,18} = 210$, $P < 0.0001$) and hemisphere ($F_{1,6} = 244$, $P > 1.0001$) in the T_2-images. T_2 values decreased over time both ipsi- and contralateral to the graft, specifically between 3 and 6 weeks post-transplantation (Fig. 5E). This is considered as due to changes in relaxivity of the brain during development (Prayer *et al.*, 1997). T_2 values were also consistently lower in ROIs in the ipsilateral vs. contralateral hemisphere. No effect of time was detected in the T_2^* values ($F_{3,18} = 2.46$, $P = 0.096$; Fig. 5E and F). However, the susceptibility sensitive T_2* effects of the iron oxide nanoparticles produced a substantial decrease in T_2* relaxivity in the ipsilateral hemisphere; a significant effect was observed ($F_{1,6} = 7200$, $P < 0.0001$; Fig. 5F).

By visual examination of the hypointense areas on the MR images, we could not detect any substantial migration of the grafted human cells at the four time points. To estimate eventual migration or movement of the grafted human NSCs into the naïve brains, we co-registered the 3D-FLASH datasets from all time points (Fig. 6A–D). First visual inspection revealed that not only was the volume and location of the graft similar at 3 (Fig. 6E), 6 (Fig. 6F), 12 (Fig. 6G) and 16 (Fig. 6H) weeks, but the size of the graft in relation to the overall volume of the brain appeared comparable (Fig. 6I). In contrast,

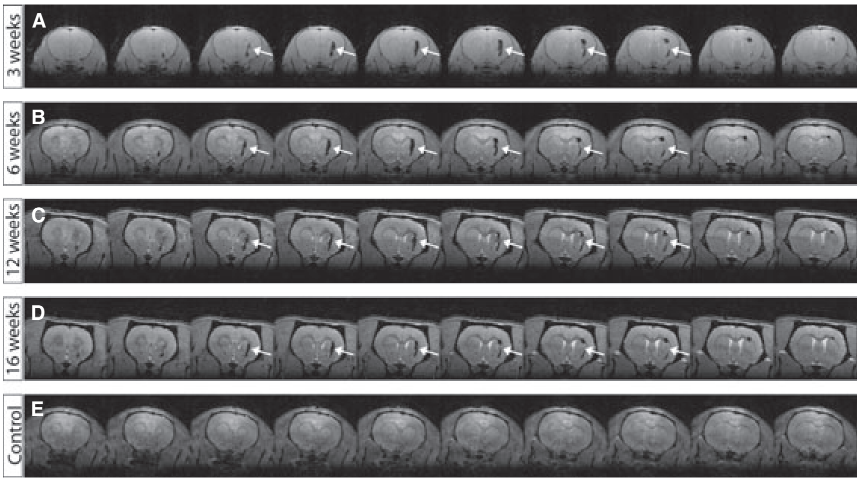

FIG. 4. Imaging time course of the human cell grafts. FLASH 3D images showing one representative animal grafted with SPIO-labeled human NSCs and scanned at 3 (A), 6 (B), 12 (C) and 16 (D) weeks. The montage for each time point consists of ten consecutive 200-μm-thick slices that were judged to contain the majority of the hypointense area in the right striatum. Arrows identify the areas in six slices at all four time points. An animal transplanted with human NSCs labeled with a non-proton-based contrast agent was scanned at 6 weeks (E). No hypointensity was detected at the site of implantation. Note – at 3 weeks post-transplantation a mouse surface coil was used which has lower penetration depth (and thus the signal-to-noise ratio is much higher dorsal than ventral) than the larger rat surface coil used at the other time points.

© 2011 The Authors. European Journal of Neuroscience © 2011 Federation of European Neuroscience Societies and Blackwell Publishing Ltd

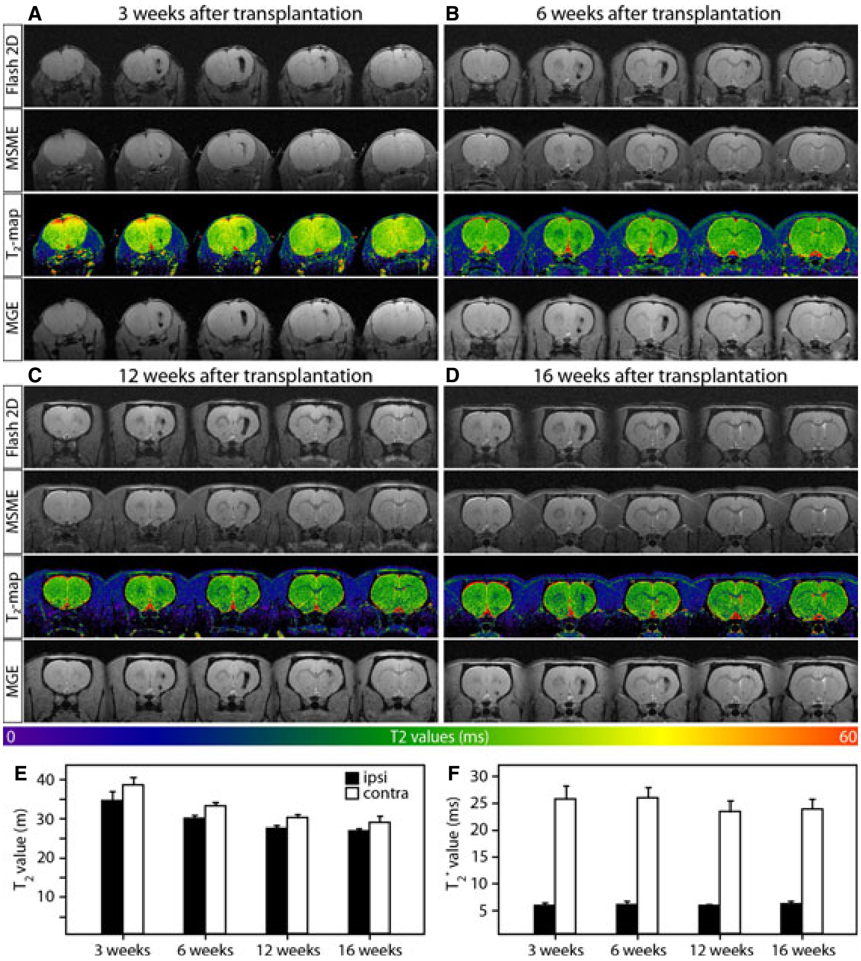

FIG. 5. Sensitivity of the different sequences to the grafted human cells. Montages of images acquired with a high-resolution FLASH 2D, MSME (and corresponding quantitative T_2 maps) and MGE sequences of an animal at 3 (A), 6 (B), 12 (C) and 16 (D) weeks after transplantation of SPIO-labeled human NSCs. T_2 values (ms) for the T_2 maps are indicated in the color scale bar below the images. The montages at each time point consist of five consecutive 600-μm-thick slices, with the slice containing the largest region of hypointensity as the center image. Quantitative T_2 (E) and T_2* (F) values obtained from the ROI analysis in the ipsilateral (black bars) and contralateral (clear bars) hemispheres across all time points. There was a significant effect in the T_2 images of time ($P < 0.0001$) and hemisphere ($P > 1.0001$).

quantitative analysis of the 3D reconstructions at the four time points revealed that the absolute volume of the grafts decreased gradually over time from 3.8 mm^3 at 3 weeks to 2.2 mm^3 at 16 weeks post-transplantation ($F_{1.3,7.7} = 9.30$, $P = 0.014$) (Fig. 6J and K). At the same time, the brains all increased in volume, especially between 3 and 6 weeks (from 659 to 899 mm^3), due to rat brain development, and continued to increase further to 925 mm^3 at 16 weeks ($F_{3,18} = 60.7$, $P < 0.0001$; Fig. 6K). After correction for the increasing brain volume it was evident that the relative graft to brain volume therefore also decreased over time, from 5.79‰ at 3 weeks to 2.41‰ at 16 weeks ($F_{1.2,7.2} = 20.4$, $P = 0.002$; Fig. 6K).

Survival and fate of SPIO-labeled human NSCs after transplantation

To investigate the survival and fate of the transplanted SPIO-labeled human NSCs, animals were killed at 3 and 6 weeks (early; data were pooled), and 16 weeks (late) after transplantation. Thereafter, double immunofluorescence labeling was performed with anti-HuNu, for all grafted human cells, in combination with neural- and proliferation-specific markers. Quantification of the total number of HuNu+ cells revealed that survival of the grafted cells was 14.1 ± 2.6 and 6.8 ± 2.8% at the early and late time points after transplantation, respectively. The difference in survival between both time points was not statistically significant ($t_{14} = 1.9$, $P = 0.08$). At all time points, PB staining was present around the site of injection in all the animals (Fig. 7B, E, I and G), corresponding both to the hypointense regions detected by MRI (Fig. 7A, D and H) and to the location of the HuNu+ grafted cells (Fig. 7C, F and J). Furthermore, iron deposits stained with PB were always found within the cytoplasm of cells and never appeared to be non-specifically located in the brain parenchyma (Fig. 7G). These results indicated that the hypointense areas seen by MRI were an effect produced by intracellularly located SPIO nanoparticles.

To investigate the potential contribution of rat host cells to the intracellularly located contrast agent, we performed additional stainings for ED1+-activated microglia ⁄ macrophages. Overall activation was low (Fig. 7K, M and O), but both early (3 weeks) and late

© 2011 The Authors. European Journal of Neuroscience © 2011 Federation of European Neuroscience Societies and Blackwell Publishing Ltd

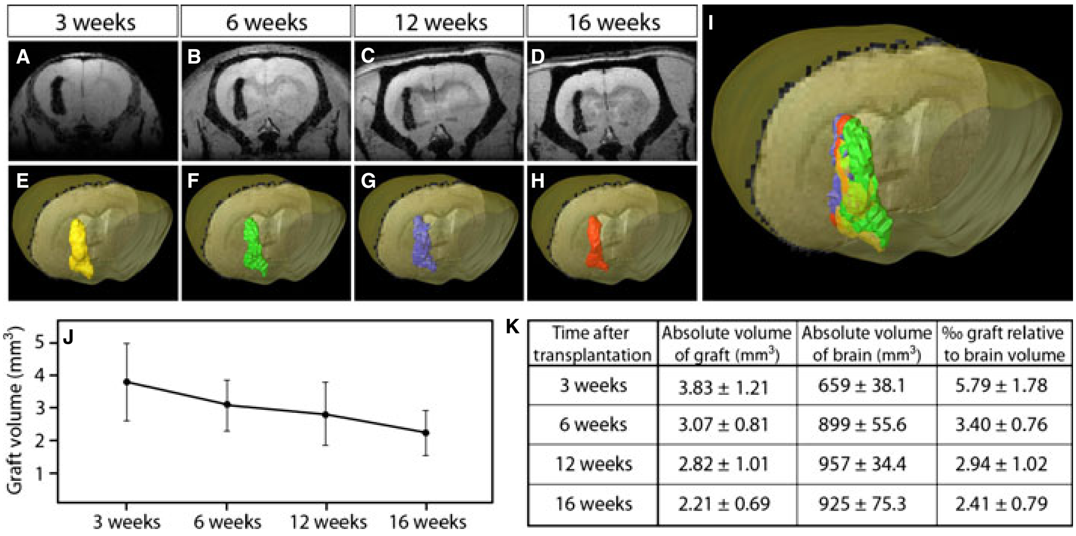

Time after transplantation	Absolute volume of graft (mm^3)	Absolute volume of brain (mm^3)	‰ graft relative to brain volume
3 weeks	3.83 ± 1.21	659 ± 38.1	5.79 ± 1.78
6 weeks	3.07 ± 0.81	899 ± 55.6	3.40 ± 0.76
12 weeks	2.82 ± 1.01	957 ± 34.4	2.94 ± 1.02
16 weeks	2.21 ± 0.69	925 ± 75.3	2.41 ± 0.79

FIG. 6. Estimated volume of human cell grafts over time. Coronal FLASH 3D images (A–D) of a representative animal illustrating the grafted human NSCs and corresponding 3D reconstruction and surface rendering from high-resolution FLASH 3D images at 3 (E; yellow), 6 (F; green), 12 (G; blue) and 16 (H; red) weeks after transplantation. (I) A compilation of the grafted cells at all four time points with respective color code maintained. Note the similar volume and shape of the grafts from 3 to 16 weeks. (J) Quantitative analysis of all animals across the four time points (n = 7) shows a gradual decrease in the absolute graft volume over time (P = 0.014). (K) Absolute values for both graft and brain volume and the relative size of the graft as per mille (‰) of the brain volume at 3, 6, 12 and 16 weeks after grafting. Note the decrease of both absolute and relative graft volume over time, and the substantial increase in brain volume especially between 3 and 6 weeks after transplantation. For interpretation of color references in figure legend, please refer to the Web version of this article.

(16 weeks) after transplantation there were slightly more ED1+ cells in the grafted than the non-grafted hemisphere (Fig. 7L, N and P). Around the injection tract there were a few ED1+ cells with amoeboid morphology (Fig. 7M and O) and only one or two of these were somewhat close to PB+ deposits (Fig. 7Q). The majority of the ED1+ cells were located adjacent to the graft location in or around blood vessels (Fig. 7L, N and P). No cells were observed that were both HuNu+ and ED1+. By contrast, HuNu+ cells were consistently in close proximity to PB+ blue deposits (Fig. 7R).

At the early time point after engraftment, of the total number of HuNu+ cells, approximately 14% were nestin+ (Fig. 8A–D), 13% were GFAP+ (Fig. 8E–H) and 12% were DCX+ (Fig. 8I–L). At the late time point after transplantation, the percentage of grafted nestin+ and GFAP+ cells remained at similar levels, around 16 and 11%, respectively (Fig. 8A–H). By contrast, the proportion of DCX+ grafted human cells significantly decreased over time to approximately 6% (t_{14} = 2.6, P = 0.0224; Fig. 8I–L). To determine whether the SPIO-labeled human cells continued to proliferate after engraftment, the sections were double-stained for HuNu and Ki67. Only approximately 0.5% of the grafted human cells were positive for Ki67, irrespective of early or late after transplantation.

Discussion

The present investigation is the first to have comprehensively both determined the influence of SPIO-labeling on human striatal NSCs both *in vitro* and *in vivo* on a long-term basis, and characterized graft evolution with quantitative MRI post-processing tools. The results from this comprehensive investigation are of interest because human NSCs are considered the ideal source for cell replacement therapy of cerebral lesions. Potential applications span from neurodegeneration and stroke (Lindvall & Kokaia, 2006; Darsalia *et al.*, 2011) to neural ceroid lipfuscinosis (Guillaume *et al.*, 2008; Selden *et al.*, 2008). For all such applications, the profile of the long-term viability and cell characteristics is essential to assess whether the cells can perform their expected role in network re-formation or as a supportive role through protein secretion. For this purpose, we show here that quantitatively the labeling of human striatal NSCs with SPIO particles does not influence the short-term proliferation, survival or differentiation capacities of the human cells *in vitro*. Second, we can easily detect a hypointense area in the intact rat striatum up to 4 months after intrastriatal transplantation, and quantitative measures imply that both degree of hypointensity as well as volume change over time. Third, we have correlated our MRI findings with histology, thus confirming that the MRI hypointensity is indeed produced by cells containing iron oxide particles and not by free particles within the parenchyma. In addition, we performed extensive double immunostainings to determine not only cell viability, but also the proportion of grafted SPIO-labeled cells that differentiated into various neural lineages at an early and late time point after transplantation. The methods described here are important tools for non-invasive, longitudinal evaluation of graft survival and migration, while the results provide the essential prerequisite information for further transplantation studies in animals with neurological lesions.

Effect of MRI label on cell characteristics

The ability to follow the status and location of grafted human cells in animal models of disease with MRI is important for the future application of stem cell-based therapies. To visualize the cells, they need to be labeled with an MRI contrast agent. Although there are many available contrast agents with different chemical compositions and magnetic properties (Geraldes & Laurent, 2009), the most popular choice for *ex vivo* cell labeling followed by *in vivo* detection are SPIO nanoparticles (Hoehn *et al.*, 2002; Bulte *et al.*, 2003; Magnitsky *et al.*, 2005; Stroh *et al.*, 2005; Guzman *et al.*, 2008; Li *et al.*, 2010). However, the vast majority of these studies have been performed on rodent-derived stem cells, which is a disadvan-

© 2011 The Authors. European Journal of Neuroscience © 2011 Federation of European Neuroscience Societies and Blackwell Publishing Ltd

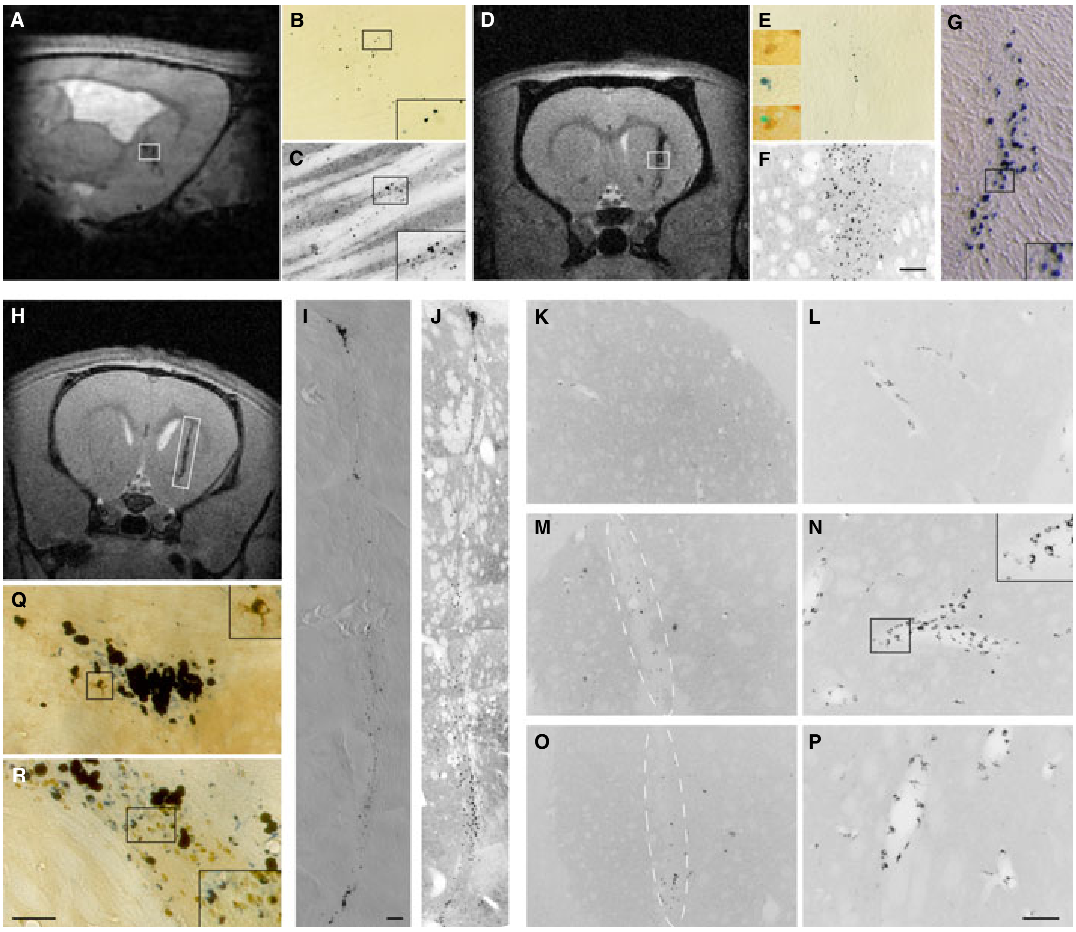

FIG. 7. Location of grafted human cells and iron deposits analysed on post-mortem tissue sections correspond to the hypointensity observed at all time points by MRI. MR images obtained at 3 weeks (A; sagittal view), 16 weeks (D) and 6 weeks (H) after cell implantation with corresponding PB (B, E and I) and HuNu (C, F and J) stainings on tissue sections. B and C are photomicrographs acquired in the boxed area in A, E and F in D, and I and J (whole graft; images merged) in H. Iron is deposited in the cytoplasm of cells and not scattered freely in the parenchyma (G) and insets in E show a closer examinated HuNu+ cell (brown) containing iron as detected with PB (blue/green). Microglia activation/macrophage infiltration analysed by ED1 staining (K–P) early (K–N) and late (O and P) after transplantation. In the contralateral hemisphere (K and L) almost no ED1+ cells can be detected, whereas more can be found in the implanted hemisphere (M–P), in which the needle tract is indicated by a dotted line. (Q) ED1+ cell (inset) in close proximity to PB-stained iron deposits. Note – almost no ED1+ cells were found to contain or were close to blue stained deposits. By contrast, almost all HuNu+ cells were found to be near PB staining (R). All black lined corner boxes correspond to higher magnification insets of the delineated area within the same image. Scale bar (E) in B, C, E and F = 100 μm and in G = 50 μm; scale bar (R) in Q and R = 50 μm; scale bar (I) in J and I = 100 μm; and scale bar (P) in K, M and O = 200 μm and in L, N and P = 100 μm. For interpretation of color references in figure legend, please refer to the Web version of this article.

tage given that human stem cells are the most clinically relevant source for cell replacement therapy. Furthermore, many studies lack thorough analysis of the effects of the labeling on the properties and fate of the cells as well as the MRI data obtained. Even though the SPIO nanoparticles are composed of biodegradable iron that can, theoretically, be recycled by the normal biochemical pathways for iron metabolism (Arbab *et al.*, 2003; Pawelczyk *et al.*, 2006), there have been reports of incorporated SPIO particles affecting the biology of mesenchymal stem cells (Kostura *et al.*, 2004). Our *in vitro* analysis of the labeled human cells revealed that compared with the non-labeled control cells, there were no differences in the general biological characteristics of the cells during proliferation irrespective of the amount of Endorem used for labeling. These results concur with previous reports showing that incorporation of SPIO particles does not affect short-term survival, proliferation, and multipotency or differentiation capacity of NSCs (Guzman *et al.*, 2007; Neri *et al.*, 2008). However, after long-term (18 days) *in vitro* differentiation, some changes appeared in both the proportion of neural phenotypes generated as well as in the number of proliferating cells in some of the labeled cultures as compared with non-labeled control cell cultures. This could be caused by a delayed toxicity due to iron overloading, which leads to cellular stress responses that may have effects on cell characteristics (Glei *et al.*, 2002; Knobel *et al.*, 2006), manifested only after longer experimental times. Therefore, for the continued *in vivo* experiments we chose the labeling concentration that, under our experimental conditions, introduced almost no changes compared with the control.

Profile of the graft over time

After transplantation of the SPIO-labeled human NSCs into the non-neurogenic striatum of naïve neonatal rats, we performed repetitive MRI for up to 4 months. Detailed quantitative analysis of the 3D

© 2011 The Authors. European Journal of Neuroscience © 2011 Federation of European Neuroscience Societies and Blackwell Publishing Ltd

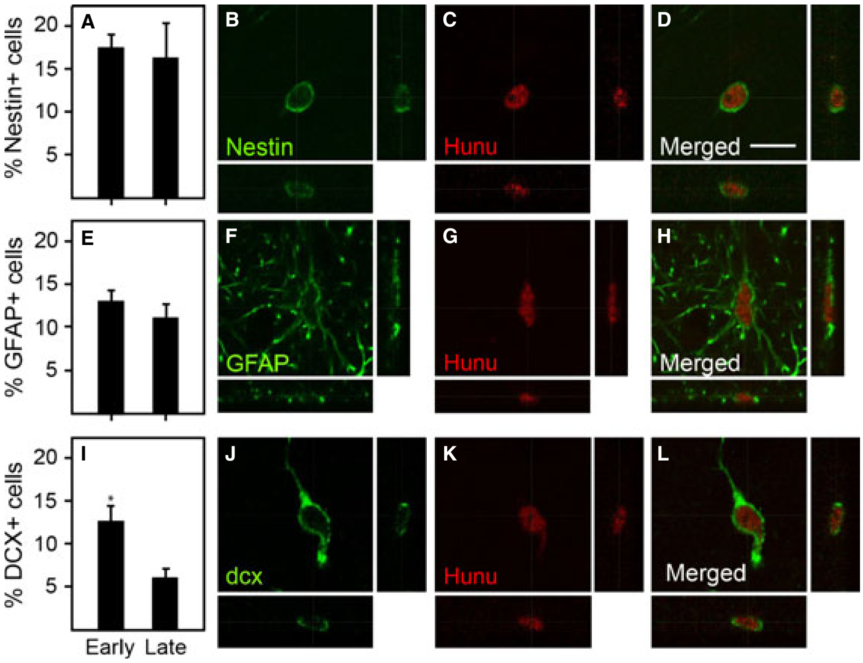

FIG. 8. Cell fate following transplantation of SPIO-labeled human cells into the neonatal rat brain. Percentage of nestin+ (A), GFAP+ (E) and DCX+ (I) grafted human cells early (3 and 6 weeks) and late (16 weeks) after transplantation. Photomicrographs (B–D, F–H and J–L) of confocal images with orthogonal reconstruction of grafted human HuHu+ cells (C, G and K), which are double-immunostained with antibodies for nestin (B and D), GFAP (F and H) and DCX (J and L) at 16 weeks post-transplantation. Scale bar = 10 μm. * indicates significant difference between early and late time points ($P < 0.05$).

reconstructions of the overall graft volume revealed that the absolute volume of the grafts decreased over time (from 3.8 to 2.2 mm^3), which was not discernible by simple visual examination of the 3D FLASH images. As the brains of the developing animals also increased significantly in volume during this time (from 660 to 930 mm^3), calculation of the relative graft to brain volume revealed a decrease of around 50% at 16 weeks as compared with at 3 weeks. This is supported by quantification of numbers of HuNu+ cells in tissue sections. Early (up to 6 weeks) and late (16 weeks) after transplantation revealed that approximately 14 and 7%, respectively, of the grafted cells had survived. The overall number of surviving cells is in agreement with previous studies with same or similar cells (Englund *et al.*, 2002; Parmar *et al.*, 2003; Kallur *et al.*, 2006) and is consistent with an earlier study showing 6–10% survival of cells at 4 months after grafting (Kallur *et al.*, 2006). The observed, slight decrease in numbers of HuNu+ cells from the early to late time point after transplantation is also completely within the range of cell survival reported earlier for these unlabeled cells under otherwise same conditions (Kallur *et al.*, 2006). Thus, it can safely be excluded that the decrease in both signal intensity and volume of the grafts was caused by compromised survival of the SPIO-labeled grafted human NSCs over time after implantation, although iron-overload has been shown to induce a stress response that is known to increase the formation of reactive oxygen species (Glei *et al.*, 2002; Knobel *et al.*, 2006), thus affecting the survival of cells when challenged long term under *in vivo* conditions.

In addition to the overall shrinkage of the graft volume in the MR images and tissue sections, we found that there was a significant decrease in the T_2 values within the ROI corresponding to the graft with time after transplantation. Several possibilities exist to explain this. As a similar trend in T_2 decrease was observed in the contralateral hemisphere, this response must be due to overall changes in relaxivity that occur as a consequence of brain development, as has been reported during the initial weeks after birth (Prayer *et al.*, 1997; Heiland *et al.*, 2002; Bockhorst *et al.*, 2008). Alternatively, cells may have lost the label passively to the surrounding brain parenchyma, or the label was diluted through cell proliferation or migration (Arbab *et al.*, 2003; Guzman *et al.*, 2007). Our analysis of post-mortem tissue sections showed that almost none of the grafted human cells was proliferating after engraftment and therefore it is not plausible that the decline in T_2 values was due to loss of label through cell division. It is conceivable that some cells may have migrated out from the graft core. Although no obvious hypointensities were observed in other regions of the brain, if migration occurred it was below the detection limits of the MRI, as our phantom experiments suggested that the detection limit was around 500 labeled cells under ideal *in vitro* conditions (Bulte & Kraitchman, 2004; Heyn *et al.*, 2005). *In vivo* cell cluster size for detectability will be even substantially larger. Thus, we cannot exclude that a certain fraction of cells evades inclusion in the graft volume as the cell density at the outer margin of the graft volume may decrease below detectability threshold due to partial volume effect. To clarify this aspect, we have decided to speak of an ‘apparent graft volume’ because of potential lack of cell detection at the outer rim. However, using microscopy of immunostained tissue sections, we did not observe many cells that had migrated to areas outside the graft site. Thus, migration of grafted cells also represents an unlikely explanation for the decline of T_2. In conclusion, we believe that the T_2 decrease over time observed from 3 to 16 weeks can be assigned to development-dependent changes during growth. This is in line with our relaxometry studies as a function of rat brain age, showing a relationship between T_2 decrease in early life and cortical cell density (L. Mengler, personal communication).

Of great concern is the notion that activated microglia and macrophages will engulf dead, labeled cells or iron nanoparticles

© 2011 The Authors. European Journal of Neuroscience © 2011 Federation of European Neuroscience Societies and Blackwell Publishing Ltd

dispersed freely in the brain parenchyma, and thus contribute to the MRI signal (Pawelczyk *et al.*, 2008). At the time points analysed by immunohistochemistry, we found that there were relatively few, scattered ED1+ cells overall, although more were located in the grafted hemisphere and almost exclusively associated with blood vessels. Some were located close to the needle tract, but almost none was in direct connection to PB+ iron deposits and none was positive for HuNu. Although we cannot exclude that some of the PB+ cells were inflammatory, the overall low levels of ED1+ cells in general suggests that the inflammatory cells were not a major contributor to the graft-induced hypointensity in the MRI images at all times (Guzman *et al.*, 2007; Arbab *et al.*, 2008).

Detection of cell death caused by, for example, graft rejection and clearance of grafted cells by activated, resident microglia or blood macrophages will always be a major issue when MRI is applied in future clinical cell transplantation studies. The recipient animals (postnatal day 3) used in this xenotransplantation study were not immunosuppressed, as the immune system is not fully developed by this time (Lund *et al.*, 1987). However, we cannot completely exclude some rejection of the grafted cells, especially from 18 days and onwards when the immune system is mature (Lund *et al.*, 1988; Marion *et al.*, 1990; Kelly *et al.*, 2009). We performed our first MRI scans and tissue slices from animals that were around 24 days old (3 weeks after transplantation) and therefore the loss of cells in the initial phase may have evaded us.

Fate of grafted cells

Quantification of the fate of the grafted human cells showed that both early and late after transplantation around 20% of the cells were nestin+ and 10% were GFAP+, whereas the number of DCX+ cells decreased three-fold over time after transplantation. This is in agreement with previous studies using these cells *in vivo* (Kallur *et al.*, 2006, 2008). Thus, no major changes in the phenotypes generated *in vivo* at up to 4 months after transplantation was detected in response to cell labeling. Importantly, at all the time points analysed, only a very small fraction of the grafted human cells (around 0.5%) were positive for the proliferative marker Ki67. Proliferative activity within grafts is always a concern due to risk of tumor formation, which is unacceptable for the clinical use of stem cell replacement therapy (Lindvall & Kokaia, 2010).

Conclusions

The semi-quantitative and quantitative tools presented here are more accurate for the assessment of survival and migration of implanted cells by MRI than simple visual inspection of MR images. Using these quantitation tools, the decreasing number of vital cells of the graft, determined by quantitative immunohistochemistry, is reflected in the MRI-derived graft volume change. Thus, essential information about the human cell graft dynamics can be monitored over long periods of time.

Our study evaluates the long-term effect of SPIO-labeling on the biology of human NSCs, derived from the fetal striatum, both *in vitro* and *in vivo*. We have carefully determined the optimal choice of contrast agent amount with the goal not only to optimize short-term viability of the cells but also to minimize long-term alterations in phenotypes of labeled cells. Our study suggests that there are only minor long-term effects of the label on the biology of the cells and that the labeled cells show a long-term behavior after grafting, comparable with naïve cells.

Finally, the observed lack of proliferation, detected by a lack of graft volume increase and confirmed by quantitative immunohistochemistry, is an essential prerequisite for implantation of cells for therapeutic purposes as it indicates that they do not have the tendency to form tumors after cerebral engraftment.

Acknowledgements

We thank M. Diedenhofen and M. Nelles for excellent technical support, S. Schwarz and Dr J. Bornemann, Electron Microscopic Facility, RWTH Aachen University, and for the generous supply of Endorem by Drs C. Corot and P. Robert (Guerbet, France) and of CELSENSE by C. O'Hanlon (Celsense, USA). This work was funded by EU projects LSHB-CT-2006-037526 (STEMSTROKE) and HEALTH-F5-2008-201842 (ENCITE), and an Alexander von Humboldt Research Fellowship to T.D.F.

Abbreviations

ANOVA, analysis of variance; CsA, cyclosporine A; DCX, doublecortin; DX, dextran; FA, flip angle; FLASH, fast low-angle shot; FOV, field of view; KPBS, potassium phosphate-buffered saline; MGE, multi-gradient echo; MRI, magnetic resonance imaging; MSME, multi-slice multi spin echo; NSCs, neural stem cells; PB, Prussian Blue; PFA, paraformaldehyde; PLL, poly-L-lysine; ROI, region of interest; SPIO, superparamagnetic iron oxide.

References

Arbab, A.S., Bashaw, L.A., Miller, B.R., Jordan, E.K., Lewis, B.K., Kalish, H. & Frank, J.A. (2003) Characterization of biophysical and metabolic properties of cells labeled with superparamagnetic iron oxide nanoparticles and transfection agent for cellular MR imaging. *Radiology*, **229**, 838–846.

Arbab, A.S., Janic, B., Knight, R.A., Anderson, S.A., Pawelczyk, E., Rad, A.M., Read, E.J., Pandit, S.D. & Frank, J.A. (2008) Detection of migration of locally implanted AC133+ stem cells by cellular magnetic resonance imaging with histological findings. *FASEB J.*, **22**, 3234–3246.

Bockhorst, K.H., Narayana, P.A., Liu, R., Ahobila-Vijjula, P., Ramu, J., Kamel, M., Wosik, J., Bockhorst, T., Hahn, K., Hasan, K.M. & Perez-Polo, J.R. (2008) Early postnatal development of rat brain: in vivo diffusion tensor imaging. *J. Neurosci. Res.*, **86**, 1520–1528.

Bulte, J.W. & Kraitchman, D.L. (2004) Iron oxide MR contrast agents for molecular and cellular imaging. *NMR Biomed.*, **17**, 484–499.

Bulte, J.W., Ben-Hur, T., Miller, B.R., Mizrachi-Kol, R., Einstein, O., Reinhartz, E., Zywicke, H.A., Douglas, T. & Frank, J.A. (2003) MR microscopy of magnetically labeled neurospheres transplanted into the Lewis EAE rat brain. *Magn. Reson. Med.*, **50**, 201–205.

Darsalia, V., Kallur, T. & Kokaia, Z. (2007) Survival, migration and neuronal differentiation of human fetal striatal and cortical neural stem cells grafted in stroke-damaged rat striatum. *Eur. J. Neurosci.*, **26**, 605–614.

Darsalia, V., Allison, S.J., Cusulin, C., Monni, E., Kuzdas, D., Kallur, T., Lindvall, O. & Kokaia, Z. (2011) Cell number and timing of transplantation determine survival of human neural stem cell grafts in stroke-damaged rat brain. *J. Cereb. Blood Flow Metab.*, **31**, 235–242.

Englund, U., Fricker-Gates, R.A., Lundberg, C., Bjorklund, A. & Wictorin, K. (2002) Transplantation of human neural progenitor cells into the neonatal rat brain: extensive migration and differentiation with long-distance axonal projections. *Exp. Neurol.*, **173**, 1–21.

Geraldes, C.F. & Laurent, S. (2009) Classification and basic properties of contrast agents for magnetic resonance imaging. *Contrast Media Mol. Imaging*, **4**, 1–23.

Glei, M., Latunde-Dada, G.O., Klinder, A., Becker, T.W., Hermann, U., Voigt, K. & Pool-Zobel, B.L. (2002) Iron-overload induces oxidative DNA damage in the human colon carcinoma cell line HT29 clone 19A. *Mutat. Res.*, **519**, 151–161.

Graeber, M.B., Streit, W.J., Kiefer, R., Schoen, S.W. & Kreutzberg, G.W. (1990) New expression of myelomonocytic antigens by microglia and perivascular cells following lethal motor neuron injury. *J. Neuroimmunol.*, **27**, 121–132.

Guillaume, D.J., Huhn, S.L., Selden, N.R. & Steiner, R.D. (2008) Cellular therapy for childhood neurodegenerative disease. Part I: rationale and preclinical studies. *Neurosurg. Focus*, **24**, E21.

© 2011 The Authors. European Journal of Neuroscience © 2011 Federation of European Neuroscience Societies and Blackwell Publishing Ltd

Guzman, R., Uchida, N., Bliss, T.M., He, D., Christopherson, K.K., Stellwagen, D., Capela, A., Greve, J., Malenka, R.C., Moseley, M.E., Palmer, T.D. & Steinberg, G.K. (2007) Long-term monitoring of transplanted human neural stem cells in developmental and pathological contexts with MRI. *Proc. Natl. Acad. Sci. USA*, **104**, 10211–10216.

Guzman, R., Bliss, T., De Los Angeles, A., Moseley, M., Palmer, T. & Steinberg, G. (2008) Neural progenitor cells transplanted into the uninjured brain undergo targeted migration after stroke onset. *J. Neurosci. Res.*, **86**, 873–882.

Heiland, S., Sartor, K., Martin, E., Bardenheuer, H.J. & Plaschke, K. (2002) In vivo monitoring of age-related changes in rat brain using quantitative diffusion magnetic resonance imaging and magnetic resonance relaxometry. *Neurosci. Lett.*, **334**, 157–160.

Heyn, C., Bowen, C.V., Rutt, B.K. & Foster, P.J. (2005) Detection threshold of single SPIO-labeled cells with FIESTA. *Magn. Reson. Med.*, **53**, 312–320.

Hockfield, S. & McKay, R.D. (1985) Identification of major cell classes in the developing mammalian nervous system. *J. Neurosci.*, **5**, 3310–3328.

Hoehn, M., Kustermann, E., Blunk, J., Wiedermann, D., Trapp, T., Wecker, S., Focking, M., Arnold, H., Hescheler, J., Fleischmann, B.K., Schwindt, W. & Buhrle, C. (2002) Monitoring of implanted stem cell migration in vivo: a highly resolved in vivo magnetic resonance imaging investigation of experimental stroke in rat. *Proc. Natl. Acad. Sci. USA*, **99**, 16267–16272.

Kallur, T., Darsalia, V., Lindvall, O. & Kokaia, Z. (2006) Human fetal cortical and striatal neural stem cells generate region-specific neurons in vitro and differentiate extensively to neurons after intrastriatal transplantation in neonatal rats. *J. Neurosci. Res.*, **84**, 1630–1644.

Kallur, T., Gisler, R., Lindvall, O. & Kokaia, Z. (2008) Pax6 promotes neurogenesis in human neural stem cells. *Mol. Cell. Neurosci.*, **38**, 616–628.

Kelly, C.M., Precious, S.V., Scherf, C., Penketh, R., Amso, N.N., Battersby, A., Allen, N.D., Dunnett, S.B. & Rosser, A.E. (2009) Neonatal desensitization allows long-term survival of neural xenotransplants without immunosuppression. *Nat. Methods*, **6**, 271–273.

Knobel, Y., Glei, M., Osswald, K. & Pool-Zobel, B.L. (2006) Ferric iron increases ROS formation, modulates cell growth and enhances genotoxic damage by 4-hydroxynonenal in human colon tumor cells. *Toxicol. In Vitro*, **20**, 793–800.

Koch, P., Kokaia, Z., Lindvall, O. & Brustle, O. (2009) Emerging concepts in neural stem cell research: autologous repair and cell-based disease modelling. *Lancet Neurol.*, **8**, 819–829.

Kostura, L., Kraitchman, D.L., Mackay, A.M., Pittenger, M.F. & Bulte, J.W. (2004) Feridex labeling of mesenchymal stem cells inhibits chondrogenesis but not adipogenesis or osteogenesis. *NMR Biomed.*, **17**, 513–517.

Lee, V.M. & Pixley, S.K. (1994) Age and differentiation-related differences in neuron-specific tubulin immunostaining of olfactory sensory neurons. *Brain Res. Dev. Brain Res.*, **83**, 209–215.

Li, L., Jiang, Q., Ding, G., Zhang, L., Zhang, Z.G., Li, Q., Panda, S., Lu, M., Ewing, J.R. & Chopp, M. (2010) Effects of administration route on migration and distribution of neural progenitor cells transplanted into rats with focal cerebral ischemia, an MRI study. *J. Cereb. Blood Flow Metab.*, **30**, 653–662.

Lindvall, O. & Kokaia, Z. (2006) Stem cells for the treatment of neurological disorders. *Nature*, **441**, 1094–1096.

Lindvall, O. & Kokaia, Z. (2009) Prospects of stem cell therapy for replacing dopamine neurons in Parkinson's disease. *Trends Pharmacol. Sci.*, **30**, 260–267.

Lindvall, O. & Kokaia, Z. (2010) Stem cells in human neurodegenerative disorders – time for clinical translation? *J. Clin. Invest.*, **120**, 29–40.

Lund, R.D., Rao, K., Hankin, M.H., Kunz, H.W. & Gill, T.J. 3rd (1987) Immunogenetic aspects of neural transplantation. *Transplant. Proc.*, **19**, 1128–1129.

Lund, R.D., Rao, K., Kunz, H.W. & Gill, T.J. 3rd (1988) Instability of neural xenografts placed in neonatal rat brains. *Transplantation*, **46**, 216–223.

Magnitsky, S., Watson, D.J., Walton, R.M., Pickup, S., Bulte, J.W., Wolfe, J.H. & Poptani, H. (2005) In vivo and ex vivo MRI detection of localized and disseminated neural stem cell grafts in the mouse brain. *Neuroimage*, **26**, 744–754.

Marion, D.W., Pollack, I.F. & Lund, R.D. (1990) Patterns of immune rejection of mouse neocortex transplanted into neonatal rat brain, and effects of host immunosuppression. *Brain Res.*, **519**, 133–143.

Miller, A.J. & Joseph, P.M. (1993) The use of power images to perform quantitative analysis on low SNR MR images. *Magn. Reson. Imaging*, **11**, 1051–1056.

Neri, M., Maderna, C., Cavazzin, C., Deidda-Vigoriti, V., Politi, L.S., Scotti, G., Marzola, P., Sbarbati, A., Vescovi, A.L. & Gritti, A. (2008) Efficient in vitro labeling of human neural precursor cells with superparamagnetic iron oxide particles: relevance for in vivo cell tracking. *Stem Cells*, **26**, 505–516.

Parmar, M., Skogh, C. & Englund, U. (2003) A transplantation study of expanded human embryonic forebrain precursors: evidence for selection of a specific progenitor population. *Mol. Cell. Neurosci.*, **23**, 531–543.

Pawelczyk, E., Arbab, A.S., Pandit, S., Hu, E. & Frank, J.A. (2006) Expression of transferrin receptor and ferritin following ferumoxides-protamine sulfate labeling of cells: implications for cellular magnetic resonance imaging. *NMR Biomed.*, **19**, 581–592.

Pawelczyk, E., Arbab, A.S., Chaudhry, A., Balakumaran, A., Robey, P.G. & Frank, J.A. (2008) In vitro model of bromodeoxyuridine or iron oxide nanoparticle uptake by activated macrophages from labeled stem cells: implications for cellular therapy. *Stem Cells*, **26**, 1366–1375.

Prayer, D., Roberts, T., Barkovich, A.J., Prayer, L., Kucharczyk, J., Moseley, M. & Arieff, A. (1997) Diffusion-weighted MRI of myelination in the rat brain following treatment with gonadal hormones. *Neuroradiology*, **39**, 320–325.

Rao, M.S. & Shetty, A.K. (2004) Efficacy of doublecortin as a marker to analyse the absolute number and dendritic growth of newly generated neurons in the adult dentate gyrus. *Eur. J. Neurosci.*, **19**, 234–246.

Reeves, S.A., Helman, L.J., Allison, A. & Israel, M.A. (1989) Molecular cloning and primary structure of human glial fibrillary acidic protein. *Proc. Natl. Acad. Sci. USA*, **86**, 5178–5182.

Reynolds, B.A. & Weiss, S. (1992) Generation of neurons and astrocytes from isolated cells of the adult mammalian central nervous system. *Science*, **255**, 1707–1710.

Reynolds, B.A., Tetzlaff, W. & Weiss, S. (1992) A multipotent EGF-responsive striatal embryonic progenitor cell produces neurons and astrocytes. *J. Neurosci.*, **12**, 4565–4574.

Scholzen, T. & Gerdes, J. (2000) The Ki-67 protein: from the known and the unknown. *J. Cell. Physiol.*, **182**, 311–322.

Selden, N.R., Guillaume, D.J., Steiner, R.D. & Huhn, S.L. (2008) Cellular therapy for childhood neurodegenerative disease. Part II: clinical trial design and implementation. *Neurosurg. Focus*, **24**, E22.

Stroh, A., Faber, C., Neuberger, T., Lorenz, P., Sieland, K., Jakob, P.M., Webb, A., Pilgrimm, H., Schober, R., Pohl, E.E. & Zimmer, C. (2005) In vivo detection limits of magnetically labeled embryonic stem cells in the rat brain using high-field (17.6 T) magnetic resonance imaging. *Neuroimage*, **24**, 635–645.

Vescovi, A.L., Parati, E.A., Gritti, A., Poulin, P., Ferrario, M., Wanke, E., Frolichsthal-Schoeller, P., Cova, L., Arcellana-Panlilio, M., Colombo, A. & Galli, R. (1999) Isolation and cloning of multipotential stem cells from the embryonic human CNS and establishment of transplantable human neural stem cell lines by epigenetic stimulation. *Exp. Neurol.*, **156**, 71–83.

© 2011 The Authors. European Journal of Neuroscience © 2011 Federation of European Neuroscience Societies and Blackwell Publishing Ltd

In Vivo Tracking of Human Neural Stem Cells with ^{19}F Magnetic Resonance Imaging

V

In Vivo Tracking of Human Neural Stem Cells with ^{19}F Magnetic Resonance Imaging

Philipp Boehm-Sturm[1], Luam Mengler[1], Stefan Wecker[2], Mathias Hoehn[1]*, Therése Kallur[1]

1 In-Vivo-NMR Laboratory, Max Planck Institute for Neurological Research, Cologne, Germany, 2 Medres – Medical Research GmbH, Cologne, Germany

Abstract

Background: Magnetic resonance imaging (MRI) is a promising tool for monitoring stem cell-based therapy. Conventionally, cells loaded with ironoxide nanoparticles appear hypointense on MR images. However, the contrast generated by ironoxide labeled cells is neither specific due to ambiguous background nor quantitative. A strategy to overcome these drawbacks is ^{19}F MRI of cells labeled with perfluorocarbons. We show here for the first time that human neural stem cells (NSCs), a promising candidate for clinical translation of stem cell-based therapy of the brain, can be labeled with ^{19}F as well as detected and quantified *in vitro* and after brain implantation.

Methodology/Principal Findings: Human NSCs were labeled with perfluoropolyether (PFPE). Labeling efficacy was assessed with ^{19}F MR spectroscopy, influence of the label on cell phenotypes studied by immunocytochemistry. For *in vitro* MRI, NSCs were suspended in gelatin at varying densities. For *in vivo* experiments, labeled NSCs were implanted into the striatum of mice. A decrease of cell viability was observed directly after incubation with PFPE, which re-normalized after 7 days in culture of the replated cells. No label-related changes in the numbers of Ki67, nestin, GFAP, or βIII-tubulin+ cells were detected, both *in vitro* and on histological sections. We found that 1,000 NSCs were needed to accumulate in one image voxel to generate significant signal-to-noise ratio *in vitro*. A detection limit of ~10,000 cells was found *in vivo*. The location and density of human cells (hunu+) on histological sections correlated well with observations in the ^{19}F MR images.

Conclusion/Significance: Our results show that NSCs can be efficiently labeled with ^{19}F with little effects on viability or proliferation and differentiation capacity. We show for the first time that ^{19}F MRI can be utilized for tracking human NSCs in brain implantation studies, which ultimately aim for restoring loss of function after acute and neurodegenerative disorders.

Citation: Boehm-Sturm P, Mengler L, Wecker S, Hoehn M, Kallur T (2011) *In Vivo* Tracking of Human Neural Stem Cells with ^{19}F Magnetic Resonance Imaging. PLoS ONE 6(12): e29040. doi:10.1371/journal.pone.0029040

Editor: Christoph Kleinschnitz, Julius-Maximilians-Universität Würzburg, Germany

Received June 30, 2011; **Accepted** November 18, 2011; **Published** December 28, 2011

Copyright: © 2011 Boehm-Sturm et al. This is an open-access article distributed under the terms of the Creative Commons Attribution License, which permits unrestricted use, distribution, and reproduction in any medium, provided the original author and source are credited.

Funding: Financial support from the EU grants HEALTH-F5-2008-201842 (ENCITE) and LSHBCT-2006-037526 (StemStroke), and by funds from the German Federal Ministry of Education and Research (BMBF-0314104) are gratefully acknowledged. The funders had no role in study design, data collection and analysis, decision to publish, or preparation of the manuscript.

Competing Interests: The authors have declared that no competing interests exist.

* E-mail: mathias@nf.mpg.de

Introduction

To achieve translation of experimental stem cell-based therapy into the clinic, non-invasive imaging modalities are necessary tools. One such modality, magnetic resonance imaging (MRI), provides true three-dimensional data at high spatial resolution, enabling good detection of even small cell numbers in the living, intact individual. Commonly, contrast is achieved through *in vitro* labeling of cells with superparamagnetic iron oxide (SPIO) nanoparticles [1,2,3]. Although even single cells can be detected [4] with this procedure, the contrast generated by iron oxide labeled cells can easily be confounded with other sources such as bleedings or blood vessels [5]. Furthermore, since contrast is achieved indirectly through disturbances of the local magnetic field experienced by surrounding hydrogen nuclei, quantification of the number of cells *in vivo* is questionable [6].

A rapidly emerging field to overcome these drawbacks of ambiguity of contrast assignment and cell quantification is cell labeling with perfluorocarbon (PFC) nano-emulsions, which can be detected with ^{19}F MRI [7,8,9]. The ^{19}F nucleus is particularly suitable for labeling as its relative MR sensitivity is only 17% less than that of ^{1}H. Furthermore, the signal intensity is directly proportional to the number of accumulated ^{19}F, hence, allowing *in vivo* quantification of ^{19}F labeled cells [10]. In addition, since the level of background ^{19}F signal in host tissue is virtually absent [10], overlaying the ^{19}F image on an anatomical ^{1}H image allows for unambiguous, quantitative tracking of labeled cells *in vivo*. However, compared to labeling and tracking with metal-based contrast agents the technique is considerably less sensitive requiring a large amount of ^{19}F to accumulate in order to generate sufficient signal-to-noise ratio (SNR).

The strategy of ^{19}F cell labeling has already been applied to monitor cells during pathological conditions, e.g. umbilical cord blood cell localization in tumor-bearing mice [11], T-cell migration in murine models of diabetes [12], and local inflammation [13]. More recently, PFCs have proven useful in ^{19}F MRI studies of inflammatory response to cerebral and cardiac ischemia [14] and *in vivo* measurements of intracellular pO_2 of glioblastoma cells in response to chemotherapy [15].

In experimental models of human neurodegenerative diseases cell therapies have shown that neuronal replacement and partial repair of damaged brain circuitry is possible [16]. For a successful clinical translation, only cells of human origin will be needed, and one source of human cells are neural stem cells (NSCs) [17]. NSCs derived from the human fetal striatum have been expanded with both maintained normal karyotype and high capacity to generate different neuronal phenotypes for a long time *in vitro* [18,19]. Upon implantation, these cells survived in the stroke-damaged rat striatum, migrated towards the injury, and differentiated into mature neurons without tumor formation [18].

Since these cells represent a relevant cell source for clinical translation, the purpose of the present study was to establish a platform to visualize NSCs *in vivo* after intracerebral implantation with ^{19}F MRI. Monitoring the spatio-temporal dynamics of NSCs grafted into the brain requires the ability to detect even low cell numbers with high spatial resolution, since pathology-related migration processes of interest may take place on a small scale, the graft size may be diluted due to these processes or be initially relatively small. A first report has already indicated that it is feasible to detect fluorine labeled, immortalized, murine neural progenitor cells in the healthy mouse brain with ^{19}F MRI [20]. The current study is the first to show that these results can be extended to the tracking of human NSCs. Novelties of our experiments compared to the previous studies on ^{19}F MRI of stem cells [11,20] include i) the use of a clinically relevant source of neural stem cells and detection with *in vivo* ^{19}F MRI in a proof-of-concept, ii) a conservative estimate of cell detection limits for preclinical ^{19}F MRI studies of neural stem cell implantation, and iii) a careful assessment of potential adverse effects of the ^{19}F marker on cell viability and function both *in vitro* and *in vivo* over a period of at least one week. We show that under optimized preclinical conditions low numbers of cells can be detected *in vivo* at good resolution and within acceptable scan time. Our results suggest that ^{19}F MRI may prove useful in monitoring implanted cells in models of neurodegeneration, thus allowing the optimization of preclinical protocols of graft induced brain repair.

Materials and Methods

Culturing of human neural stem cells

NSCs were obtained from the ganglionic eminences of an 8-week old aborted human fetus from Malmö/Lund University Hospitals, according to the guidelines approved by the Lund/Malmö Ethical Committee. The full characterization of these NSCs, derived from the human fetal striatum, has previously been described in detail [19]. Briefly, after microdissection and dissociation of the striatal tissue, cells were maintained at 37°C in a humidified atmosphere with 5% CO_2. The neurosphere expansion medium (DMEM/F-12, Gibco, Grand Island, USA; L-glutamine, 2.92 g/100 mL; HEPES, 23.8 mg/100 mL; $NaHCO_3$, 7.5%; glucose, 0.6%; and heparin, 2%, all from Sigma–Aldrich, Hamburg, Germany) contained N-2 supplement (1%, Gibco), human leukemia inhibitory factor (10 ng/mL, Sigma–Aldrich), epidermal growth factor, 20 ng/mL and fibroblast growth factor, 10 ng/mL (both from Peprotech, Hamburg, Germany).

Labeling cells with ^{19}F marker and determination of intracellular ^{19}F content

A few hours prior to labeling, the small neurospheres were transferred to a Poly(2-hydroxyethyl methacrylate) (Poly-HEMA, Sigma-Aldrich) coated culture flask, in order to avoid strong attachment of the cells as a consequence of the label. We incubated cells with 5 µL, 15 µL, 50 µL, 100 µL, and 150 µL of a perfluoropolyether (PFPE) nano-emulsion (CELSENSE 1000, Celsense, Pittsburg, USA, 120 mg PFPE/ml, experimentally determined concentration of magnetically equivalent ^{19}F c = 3.11 M)/mL culture medium to determine the optimal concentration in terms of fluorine uptake. In the end the emulsion was added at the empirically determined optimal (see Results) concentration of 100 µl/mL medium 3 days after the last passage directly to the NSC culture medium and cells were incubated for 36 hours. Subsequently, the cell suspension was spun down at 184× g for 5 min, the pellet was washed twice and finally resuspended in either fresh medium or potassium phosphate-buffered saline (KPBS) or Hank's Balanced Salt Solution (HBSS), depending on the application.

In order to determine the amount of intracellular ^{19}F, 10 µl of a solution containing 10 mg KF/mL H_2O (i.e. $1.04*10^{18}$ ^{19}F spins) was added as an internal fluorine reference to the sample, which was then scanned with magnetic resonance spectroscopy (MRS, see below). The amount of fluorine was determined by comparing the integrated area of the PFPE main peak and the KF reference peak in the ^{19}F MR spectra.

Determination of in vitro cell detectability

To determine the limits of *in vitro* detectability with MRI, the ^{19}F labeled, small neurospheres were spun down, washed in KPBS, fixed with 4% paraformaldehyde (PFA), washed again and resuspended in KPBS. The fixed, labeled neurospheres were either transferred to small tubes or injected at different cell concentrations into phantoms made of 2% gelatin in small, custom-made cups 22 mm in diameter for subsequent scans with MRI.

Assessment of label influence on cell viability, proliferation and differentiation

Cell viability was determined in culture by trypan blue exclusion method before, shortly after, and at 7 days after labeling, and compared to unlabeled control cultures. Experiments were performed in triplicates. For determination of the cell phenotypes within the proliferating culture, ^{19}F labeled neurospheres were plated on PLL coated 8-well chamber slides, allowed to attach for 3 h, then fixed and processed for immunocytochemistry. For determination of cell differentiation capacity, growth factors were removed and 1% fetal bovine serum (Gibco) was added. Labeled cells were differentiated for 9 days, then fixed and subsequently stained. Medium was changed every third day during experiments.

Animal experiments

All experiments were conducted according to the guidelines laid out in the German Animal Welfare Act and approved by the local authorities (Landesamt für Natur, Umwelt und Verbraucherschutz Nordrhein-Westfalen) under permission number 9.93.2.10. 31.07.048 (dated 22 May 2007). Four adult male CD 1 mice (bodyweight 37–42 g, Janvier, Le Genest Saint Isle, France) were used for the cell implantation and ^{19}F MRI investigations. All experiments were performed under anesthesia. Animals were housed in cages under a 12 h light/12 h darkness cycle with access to food and water *ad libitum*.

Implantation procedures

Human NSC cultures (passage 14) were labeled with ^{19}F marker as stated above. At the day of implantation, ^{19}F labeled neurospheres (diameter≈100 µm) were centrifuged and resuspended in HBSS (Gibco). The neurosphere suspension had a concentration of approximately 100,000 viable cells/µL and was kept on ice during the whole procedure. Mice were anesthetized with 1–2% isoflurane in a 70/30 nitrous oxide/oxygen mixture and placed in a stereotaxic frame. A feedback controlled system maintained the body temperature at 37°C (medres, Cologne, Germany). The non-labeled and ^{19}F labeled neurosphere suspensions were injected using a Hamilton syringe into two deposits per hemisphere into the striatum (1.5 µL i.e. 150,000 cells per deposit) in two animals. Two further animals were injected bilaterally with two deposits of ^{19}F labeled cells on the left and one deposit on the right hemisphere. The following coordinates were used: AP, +1.0, ML, ±2.0 mm from bregma, and DV, −3.0 and −2.0 mm from the brain surface. After each deposit, the needle was kept in place for 5 min before slow withdrawal. The wound was closed with suture and animals were allowed to recover in their cages. To suppress an immune reaction, animals received a subcutaneous injection of 20 mg/kg Cyclosporine A (Sigma-Aldrich) every second day starting 2 days before implantation.

MRI acquisition

MRI and MRS were carried out on a Biospec 11.7 T/16 cm dedicated animal scanner system (Bruker BioSpin, Ettlingen, Germany) equipped with actively shielded gradient coils (BGA9S, 750 mT m^{-1}, Bruker BioSpin). For radiofrequency transmission and reception, we used custom-built, inductively coupled, single-loop surface coils of 9 mm diameter for *in vitro* MRS, 25 mm diameter for *in vitro* MRI, and 20 mm diameter for *in vivo* MRI, all tunable from 470 MHz for the ^{19}F resonance frequency up to 500 MHz for ^{1}H imaging.

In vitro ^{19}F MRS: For the *in vitro* quantification of ^{19}F content with MRS, we used a spin-density weighted pulse-acquire spectroscopic sequence with short acquisition delay of 0.05 µs, and with long repetition time (TR) of 20 s to assure full relaxation recovery (90° rectangular hard pulse, duration/bandwidth (BW) = 0.01 ms/128 kHz, 163.8 ms acquisition window, spectral points/BW = 8192/50 kHz). We chose the number of averages (NA) dependent on the strength of PFPE signal, with typically NA = 30, leading to an acquisition time (TA) = 10 min. All measured ^{19}F concentrations are presented with respect to the main PFPE frequency (−93.2 ppm), i.e. the chemical shift signal originating from the end group of the PFPE molecule was not taken into account.

Determination of relaxation times: To optimize sequence parameters, the relaxation times were measured with the 9 mm coil on a tube containing either the pure PFPE marker or the labeled cells. The temperature was kept at 37° throughout the experiment with a feedback controlled water system (medres). T_1 was measured with a pulse-acquire saturation-recovery sequence (20 experiments, TR = 90.3 ms up to 20 s, pulse identical to *in vitro*, 66.7 ms acquisition window, spectral points/BW = 1000/15 kHz), T_2 with a multi spin echo sequence (TR = 4 s, echo spacing 20 ms, field of view (FOV) = 16×16×2.5 mm^3, 32×32 matrix, 15 echoes, NA = 4 (PFPE)/100 (cells), TA = 4 min/3:33 h). The spectral peak area or the signal in the multi-echo images S were then fitted with the software Origin (OriginLab Corporation, Northhampton, USA) to the function $S = S_0(1-\exp(-TR/T_1))$ for T_1 or $S = S_0\exp(-TE/T_2)$ for T_2, with the equilibrium signal S_0.

In vivo ^{19}F MRS: MRS was performed to determine the exact PFPE frequency *in vivo* using a pulse-acquire sequence identical to the *in vitro* experiments but with shorter TR (30° pulse, TR = 200 ms, NA = 3,000, TA = 10 min).

In vitro and *in vivo* ^{1}H/^{19}F imaging: Anatomical ^{1}H imaging was performed with a turbo spin echo sequence (TR/effective echo time (TE_{eff}) = 2200 ms/42.8 ms, 8 echoes per excitation, NA = 2, 10 consecutive, 1 mm thick slices, FOV = 1.92×1.92 cm^2, 128×128 matrix, i.e. a resolution of 150×150×1000 µm^3, TA = 1 min, BW = 50 kHz, linear phase encoding scheme) [21]. ^{19}F images were acquired with the same sequence and matching geometry, but at lower in-plane resolution and lower BW (NA = 256, 48×48 matrix, i.e. a resolution of 400×400×1000 µm^3, TA = 57 min, BW = 10 kHz). The transmission power needed for a 90° pulse was determined on the ^{1}H channel on a 1 mm thick slice parallel to the coil through the ^{19}F labeled cells and the same power was used after switching to the ^{19}F frequency. Approximately the same power is needed for the ^{1}H and the ^{19}F 90° pulse, which we tested on a combined ^{1}H/^{19}F standard (diluted Trifluoroaceticacid, data not shown).

In vivo measurement protocol: *In vivo* ^{19}F and ^{1}H imaging was carried out 2 d after implantation for those mice that received non-labeled control cells, and 2 d and 6 d after implantation for the animals that were injected with labeled cells in both hemispheres. Mice were anesthetized with an intraperitoneal injection of a ketamine (120 mg/kg) and xylazine (8 mg/kg) mixture to avoid background signal from fluorinated inhalation of anesthesia gases. Anesthesia time was prolonged by subcutaneous administration of 30–60 mg/kg ketamine at 1 h after induction. Respiration rate was monitored using a pressure sensitive pad placed under the thorax, together with DASYlab (Measurement Computing, Norton, USA) software and body temperature was maintained at 37°C with an in-house feedback controlled system. Animals were fixed with ear bars in standard animal holders (Bruker BioSpin) and scanned with ^{1}H MRI, ^{19}F MRS, and ^{19}F MRI. The total time of the imaging session did not exceed 1.5 h.

Immunocytochemistry/immunohistochemistry

After the last MRI session, animals were deeply anesthetized and perfused transcardially with saline followed by 4% PFA. Brains were post-fixed overnight and then kept in 20% sucrose solution until they sunk. Thirty micrometer thick sections were cut in the coronal plane using a freezing microtome (Leica Microsystems, Wetzlar, Germany), and kept at −20°C in cryo-protective solution. Cells were fixed in 4% PFA for 15 min at room temperature followed by three rinses in KPBS. Before immunostaining, cells and tissue sections were pre-incubated in 5% normal serum, and 0.025% and 0.25% Triton X-100, respectively, in KPBS for 45 min at room temperature. Incubation in primary antiserum was carried out overnight at +4°C and the following primary antibodies were used: mouse anti-β-III tubulin (1:333, Sigma-Aldrich), goat anti-doublecortin (DCX, 1:400, Santa Cruz Biotechnologies, Santa Cruz, USA), mouse anti-rat CD-68 (ED-1, 1:200, AbD Serotec MorphoSys AbD, Düsseldorf, Germany), rabbit anti-GFAP (1:500, DakoCytomation, Glostrup, Denmark), mouse anti-GFAP (1:400, Sigma-Aldrich), mouse anti-human nucleus (HuNu, 1:100, Chemicon, Temecula, USA), rabbit anti-Ki67 (1:500, Abcam, Cambridge, USA), rabbit anti-human nestin (1:500, Chemicon). Primary antibodies were detected using appropriate fluorescent Cy3 (Jackson ImmunoResearch Laboratories, West Grove, USA) or biotin-conjugated (Vector Laboratories, Burlingame, USA) secondary antibodies (1:200), which were then detected with Alexa 488-conjugated streptavidin (1:200, Molecular Probes). In order to determine the specificity of the primary antibodies and the level of background generated from the secondary antibodies, in one well per *in vitro*-staining the primary antibodies were omitted as negative control. For double labeling, only one biotinylated secondary antibody was used at a time. For nuclear staining Hoechst 33342 (1:1000, Invitrogen, Carlsbad, USA) was added during final incubation with secondary antibodies. Sections were mounted on PLL-coated slides (Thermo Fisher Scientific, Waltham, USA) and slides were coverslipped with glycerol-based mounting medium. Immunostainings were controlled, microscopic images acquired and double-immunoreactivities verified with a confocal laser scanning (Leica TCS SP2, Leica Microsystems) microscope equipped with a supplementary CCD camera (Leica Microsystems).

MRI data processing and statistical analysis

All MR images were processed with the program ImageJ (http://rsbweb.nih.gov/ij/).

For SNR analysis of the ^{19}F signal, the measured signal and noise in the raw ^{19}F images were corrected voxel-wise for non-Gaussian noise distribution due to the low SNR [22]. Only voxels with a corrected SNR above 3.5 were considered significant and included in the analysis.

For display purposes of the merged ^{1}H/^{19}F images, the fluorine SNR datasets were resized to a 128×128 matrix with bilinear interpolation, grey-levels were converted to transparency levels of red, and overlaid on the ^{1}H image.

To estimate the minimum number of cells (N_{min}) per voxel to generate a detectable SNR of 3.5, we assumed a linear correlation between number of cells and SNR. Knowing the summed SNR of all voxels (SNR_{total}) with significant ^{19}F signal and the overall number of cells (N_{total}) within this volume the detection limit was then calculated with the simple relationship $N_{min} = N_{total} \times 3.5/SNR_{total}$, similar to a method described previously [11].

Differences between *in vitro* labeled and non-labeled cells were evaluated with Student's unpaired t-test. Data are expressed as mean±SEM and differences considered significant at $p<0.05$.

Results

Labeling of NSCs

NSCs readily took up the PFPE emulsion without the aid of transfection agents. The intracellular ^{19}F content was maximized for 100 µL of the ^{19}F marker substance per mL medium as confirmed with MRS (Fig. 1, A–C). With this protocol labeled cells contained on average $3.70 \pm 0.78 * 10^{12}$ (n = 3 biological replicates) ^{19}F spins.

In order to analyze if the cells keep the fluorine marker over time, we took out 1/3 of the cells (i.e. 1/3 of the internalized ^{19}F) directly after the labeling procedure and determined the amount of intracellular ^{19}F with MRS. The remaining 2/3 of the cells were replated for another 7 days. The incorporated ^{19}F was then again measured and 2.10±0.54 times (n = 4 technical replicates) the amount of the first sample was found, which is in good agreement with the expected value of 2 in case there was no significant loss of label.

The measured relaxation times were $T_1/T_2 = (280 \pm 20)$ ms/(153 ± 4) ms for the free PFPE marker and $T_1/T_2 = (380 \pm 4)$ ms/(68 ± 3) ms for the labeled cells.

Detectability and quantification in vitro

MRI of a dilution series of labeled NSCs (20,000, 10,000, 5,000 labeled and 65,000 non-labeled cells for control) suspended in gelatin clearly detected spots with 20,000 down to 10,000 cells, while there was no background ^{19}F signal from non-labeled cells.

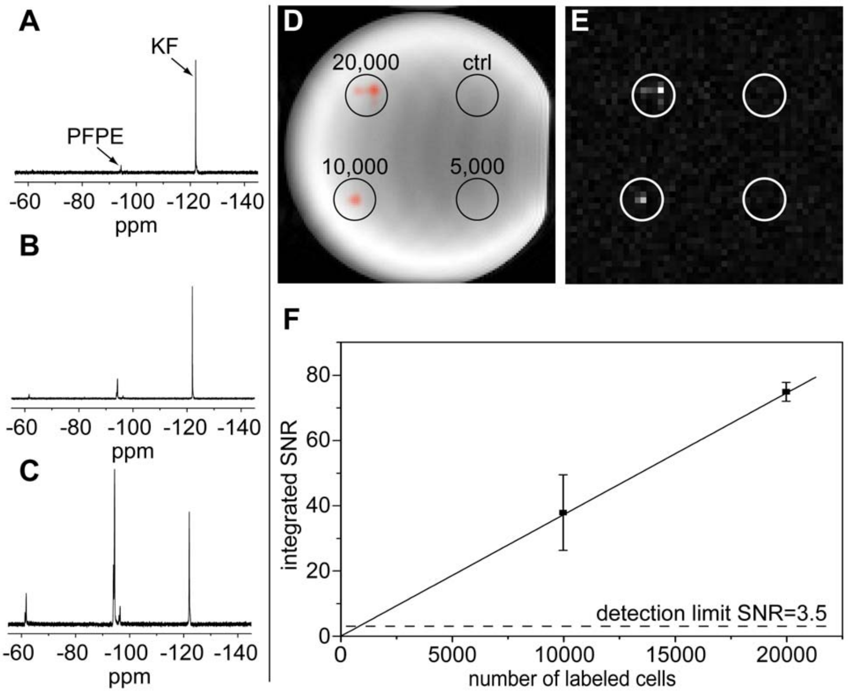

Figure 1. Optimization of labeling and *in vitro* detection limits. A–C: ^{19}F MRS of NSCs incubated with 15 µL (A), 50 µL (B), and 100 µL (C) PFPE emulsion per mL medium together with a KF solution as an internal standard, KF frequency set to −120.9 ppm, main PFPE peak at −93.2 ppm, signal intensity in arbitrary units. The cell signal was maximized at a concentration of 100 µL/mL. D–F: MRI of 20,000, 10,000, and 5,000 labeled, and 65,000 control cells plated in gelatin, D shows the merged ^{1}H and ^{19}F, E the ^{19}F image only. The 20,000 and 10,000 cells spots were clearly detectable, whereas a significant signal was not detected for the 5,000 cells, probably due to cells spreading over many voxels, thus not exceeding the critical detection limit. From the summed SNR of the two spots with ^{19}F signal we estimate that approximately 1,000 cells need to accumulate in one image voxel to overcome the detection limit, as indicated by the crossing of the linear fit in F with the dashed line illustrating an SNR of 3.5. For the fit we assumed 0 SNR for 0 cells. Error bars in F are over n = 3 technical replicates. Note: The surface coil was adjusted parallel to the paper plane.
doi:10.1371/journal.pone.0029040.g001

Spots with 5,000 cells could not be detected by *in vitro* MRI. From the SNR of the two cell clusters with significant signal ($SNR_{total} = 112 \pm 14$, n = 3 technical replicates) we estimate that the minimum number of cells, which need to accumulate in one image voxel in order to generate significant signal *in vitro*, is approximately $N_{min} \approx 1{,}000$ cells (Fig. 1, D–F). This finding was supported by ^{19}F MRI of a dilution series of the ^{19}F marker (supplementary Fig. S1). Although the 5,000 cell spot is clearly above the estimated detectable number of cells, it was most likely not discovered because cells were spread over too many image voxels.

Effect of the ^{19}F marker in vitro

The labeling procedure had only very minor effects on the cells' viability and no significant effects on their proliferation (Fig. 2, A–H) and differentiation (Fig. 2, I–P) capacity. Furthermore, carefully analyzing both the proportion and morphology of nestin+, GFAP+ and β-III tubulin+ cells, we did not detect any significant changes compared to the non-labeled control cells. Also, no differences in the numbers of Ki67+ cells were found either during proliferation (37.7±3.2%; directly after the labeling) or after 7 days of differentiation (27.2±1.0%) *in vitro* compared to non-labeled control cells (44.1±2.4% for non-differentiated and 29.2±1.7% for differentiated cells, n = 3 technical replicates) (Fig. 2, Q).

The percentage of living cells was equal compared to controls before labeling (95.2±4.2% and 94.7±5.0%) but significantly decreased directly after incubation with the ^{19}F marker (83.1±3.7% compared to 92.9±6.6% for unlabeled cells, $p < 0.05$). However, this value normalized again after replating and subsequent culturing of the cells for 7 days (87.0±5.6% for the labeled cells and 88.9±3.2% for controls, n = 3 biological replicates, Fig. 2, R).

^{19}F signal detectability in vivo

In order to assess whether ^{19}F MRI is a useful tool for the longitudinal tracking of implanted cells in the brain, we injected PFPE labeled NSCs and non-labeled control cells into the striatum of mice and scanned the animals a few days later. We detected significant ^{19}F signal from the grafts with labeled cells in all animals, while there was no signal from implanted non-labeled control cells (Fig. 3, A). Presence of Hoechst+/hunu+ cells allowed definite assignment of NSC aggregations on histological sections (Fig. 3, B, D, and F). These cell spots corresponded well, both in intensity and location, to regions exhibiting significant ^{19}F signal. In the two mice with labeled cells grafted on both hemispheres, the ^{19}F signal persisted at least 6 days after implantation (Fig. 3, C and E). Quantitative SNR analysis of these animals revealed that total ^{19}F SNR decreased by ≈20% from day 2 to day 6.

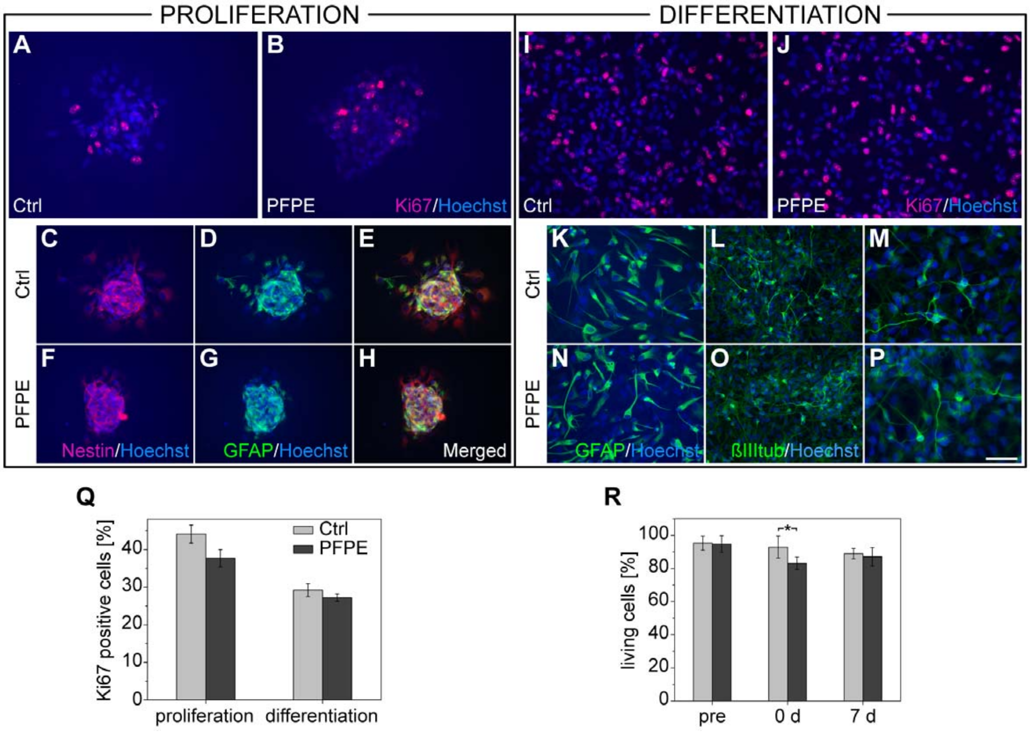

Figure 2. Effect of the labeling on cell viability, proliferation, and differentiation capacity. Photomicrographs of *in vitro* samples stained for Ki67 (A, B, I and J), nestin (C, F E and H), GFAP (D, E G, H, K and N), and βIII-tubulin (L, M, O and P). There were no major qualitative differences in the viability or proliferation and differentiation capacity of the labeled (B, F, G, H, J, N, O and P) versus non-labeled control cells (A, C, D, E, I, K, L and M), both during proliferation (A–H), i.e. directly after the labeling procedure, and after 9 days of differentiation (I–P). The percentage of proliferating Ki67+ cells during proliferation or after differentiation was not significantly altered by the labeling (Q). Quantification of the number of living cells before, 0 days after, and 7 days after incubation with the ^{19}F marker revealed that the viability was significantly decreased compared to controls at 0 days but normalized at 7 days after labeling (R). The scale bar represents 25 μm for M and P, 50 μm for all others.
doi:10.1371/journal.pone.0029040.g002

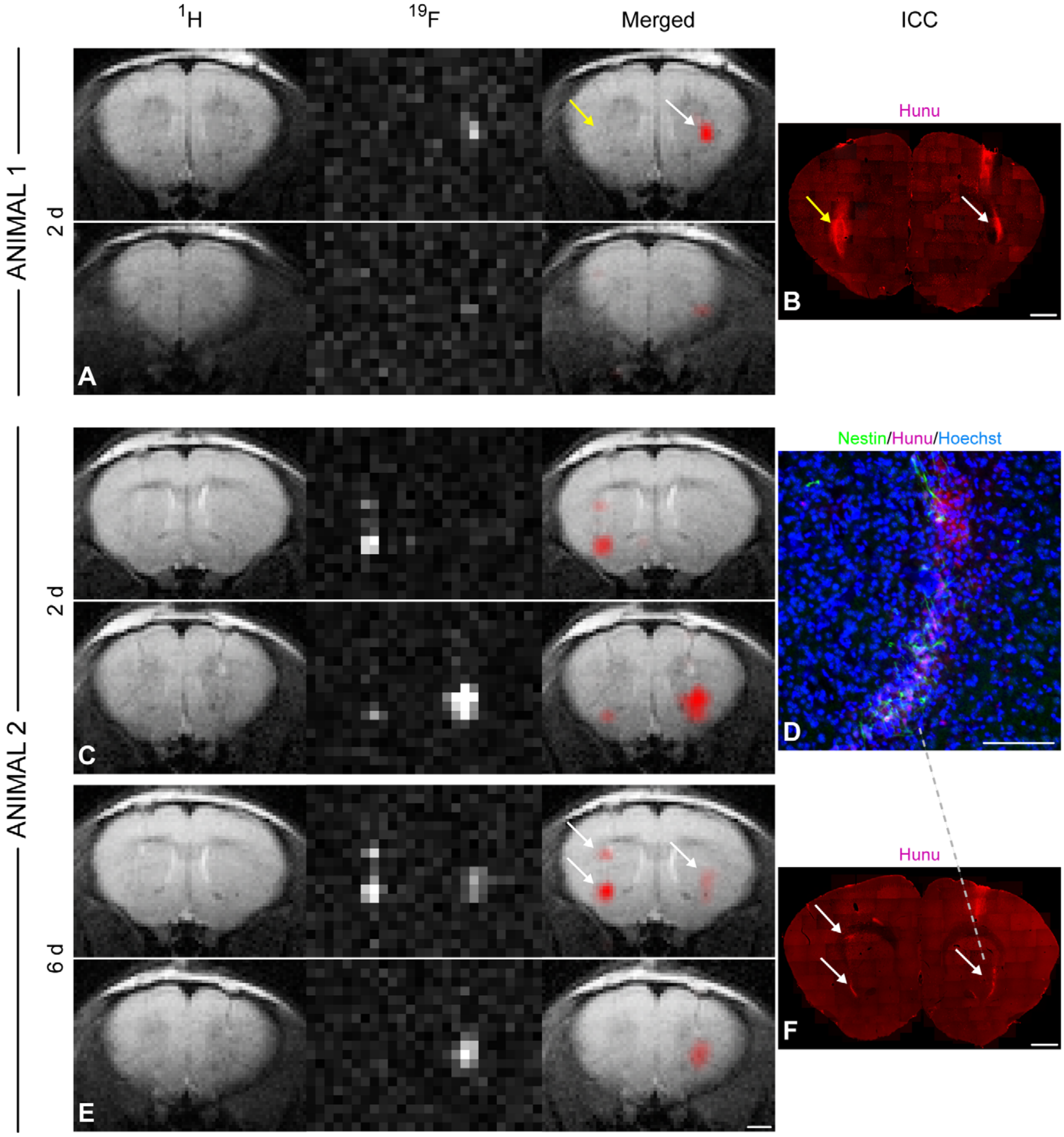

Figure 3. *In vivo* ^{19}F MRI and correlation with immunohistochemistry. ^{1}H, ^{19}F, and merged MR images of a mouse (Animal 1), which had been injected with non-labeled control cells into the left striatum and labeled NSCs into the right hemisphere (A). Only the labeled cells generated a ^{19}F signal whereas hunu staining confirmed the presence of cell grafts on both sides as indicated by the arrows (B). MRI of another mouse (Animal 2) 2 days (C) and 6 days (E) after grafting showed no major signal loss in the ^{19}F images over time. This animal had received two deposits of labeled cells in the left striatum and one deposit in the right striatum. The location and intensity of ^{19}F signal from cell clusters, marked with white arrows, correlated well with hunu staining on histological sections. Note that the ^{19}F resolution allows the distinction of the two clusters on the left hemisphere (B, F). Only cells that were clearly immunoreactive to both hoechst and hunu were considered as grafted human NSCs (D). Scale bars are 50 µm for D, 1 mm for all others.
doi:10.1371/journal.pone.0029040.g003

To estimate the *in vivo* detection limit N_{min} at 2 days after surgery, the overall ^{19}F SNR in all animals was determined ($SNR_{total} = 612.5$) and used together with the known number of transplanted cells ($N_{total} = 1.5$ million) to calculate the minimum number of detectable cells at an $SNR = 3.5$ ($N_{min} \approx 9{,}000$).

Effect of the ^{19}F marker in vivo

At the end of the ^{19}F MRI *in vivo* measurements, the animals were sacrificed and the brains were processed for immunohistochemistry to study implanted cell phenotypes. Qualitative analysis of brain sections stained for nestin, GFAP and DCX showed that the vast majority of the implanted NSCs were nestin+ and GFAP+ cells (Fig. 4 A–D). We also detected a portion of the implanted cells that had already differentiated into DCX+ neuroblasts (Fig. 4 E and F). Overall, these images revealed that the fraction of cells of each cell phenotype studied was similar for ^{19}F labeled and non-labeled cell grafts.

Discussion

We show that efficient labeling of NSCs with a PFC-based marker is possible without impairment of their naïve cell behavior and thus, in consequence, their therapeutic potential. We have successfully demonstrated detectability of these human neural stem cells with high sensitivity after implantation into mouse brain and the usefulness of this imaging approach for monitoring the cell dynamics longitudinally because the graft was followed with ^{19}F MRI for a week, being most likely detectable even much longer.

Efficacy and effects of labeling NSCs with ^{19}F

PFC nano-emulsions are particularly suitable agents for stem cell tracking because of the excellent MR properties for imaging and the high biocompatibility [10,23]. Important for a possible clinical translation, PFCs are chemically stable, biologically inert, and related compounds have already been evaluated in preclinical and clinical trials as blood-substitutes [23,24,25].

Our labeling procedure with PFPE lead to an uptake of $3.7*10^{12}$ spins/cell, similar to reports on other cell types. For experimental studies, ^{19}F uptake could potentially be further

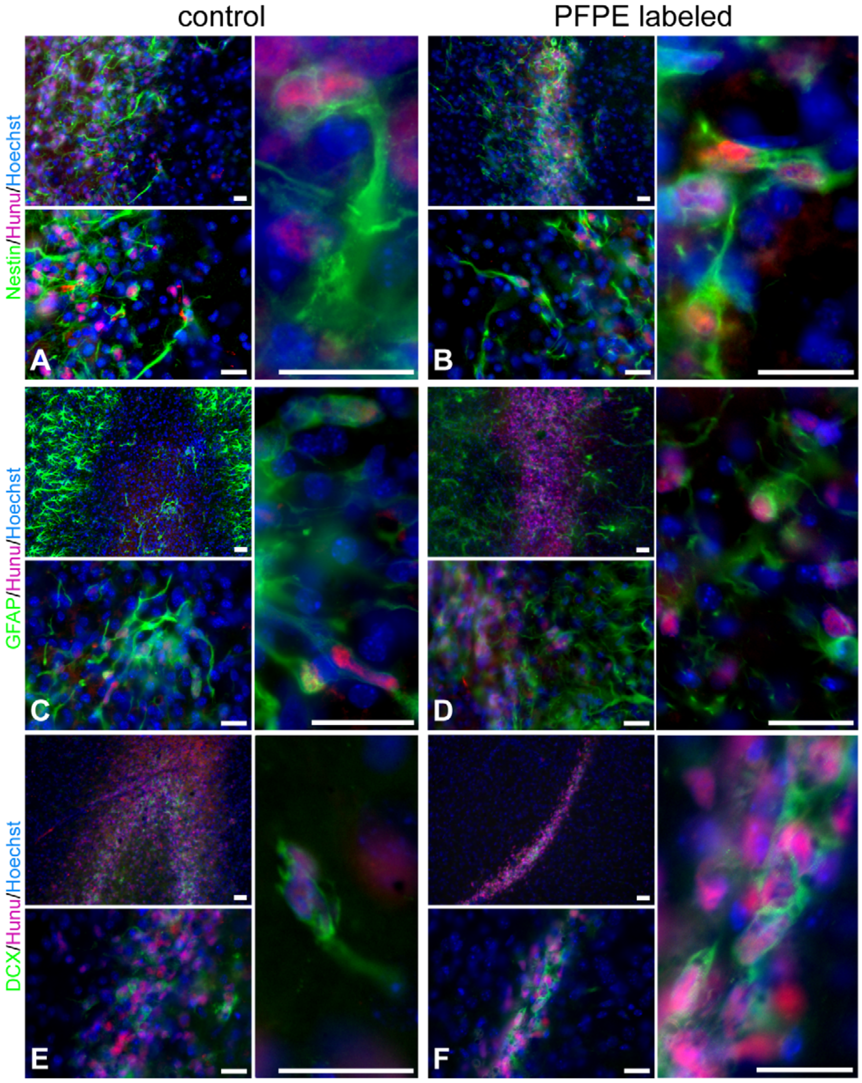

Figure 4. Effect of the ^{19}F marker on cell phenotypes *in vivo*. Photomicrographs of non-labeled control (A, C, E) and PFPE labeled NSCs (B, D, F) on tissue sections from transplanted animals. The majority of the implanted cells were, at this early time point after injection, still neural stem and progenitor cells as confirmed by nestin/hunu and GFAP/hunu stainings (A–D). Presence of DCX+/hunu+ (E, F) neuroblasts showed that NSCs were capable of neuronal differentiation. By qualitative analysis we did not detect major differences in the PFPE labeled cell population compared to control cells. Scale bars are 20 µm.
doi:10.1371/journal.pone.0029040.g004

increased through the use of transfection agents, however, most of these are not approved for use in the clinic [10]. We found a high T_2/T_1 ratio both for the free PFPE tracer and for the labeled cells. This indicates that the MR properties of the tracer are in deed optimal in terms of maximizing the SNR particularly when using turbo spin echo sequences. We note however, that the reported relaxation times may not be universal, e.g. due to slice thinning or excitation/refocusing flip angle imperfections and echo train signal variations.

Careful assessment of important immunohistochemical markers revealed that the label has only minor effects on viability, differentiation capacity, and proliferation *in vitro* and *in vivo*. In other reports the viability of PFC labeled stem cells was not different from non-labeled controls [11,20] whereas we observed a decrease in viability directly after incubation. This could either be a specific feature of the human NSCs or be due to the relatively high concentration of ^{19}F marker in the medium compared to those other studies. We observed a decrease in viability over time, although non-significant, also in the non-labeled control cells. This suggests that the impairment in viability may rather be related to other factors such as the PolyHEMA coating of flasks.

The use of a fluorescent agent, attached to the PFPE, could provide a more direct proof that the agent is internalized, analyzing localization by fluorescence microscopy. However, most fluorophores are not suitable for clinical use and, therefore, we used an emulsion without fluorescent tag. We included thorough washing steps in all procedures in order to remove excessive ^{19}F marker particles. Moreover, a study with a similar, fluorescent PFC emulsion showed localization of the ^{19}F marker in the cytosol of murine neural progenitor cells and persistence of ^{19}F MRI signal over 2 weeks [20]. Importantly, we did not detect a decrease in MRS-determined ^{19}F content from labeled, replated cells over a period of one week. *In vivo* the ^{19}F SNR only slightly decreased between day 2 and day 6 after implantation. Overall, there is strong evidence that NSCs retain the label over time and can be tracked longitudinally, even for longer periods than the time span of this study. This feature of long-term tracking of cells was not provided employing alternative fluorine markers such as Poly-L-lysine CF_3, for which labeled cells lost half the ^{19}F signal within 7 days [26,27]. However, thorough long-term evaluations of both effects of PFCs on grafted stem cells and efficacy of the labeled cells in the pathological brain e.g. stroke models are needed in the future.

Cell quantification and detection limits

The ^{19}F MR signal is proportional to the amount of magnetically equivalent fluorine nuclei within a certain voxel. This allows quantification of the number of cells. If the total number of implanted cells is known, one strategy is to link this number to the sum total of SNR and to assume linear correlation between both. This way each SNR can be assigned a cell number. We employed this for the determination of detection limits by extrapolation of the number of cells generating an SNR of 3.5. However, the strategy works only under the assumption that cells are labeled homogeneously, do not lose the label, and do not proliferate as this leads to a dilution of ^{19}F content/cell, and that partial volume effects can be neglected. The assumption of a homogeneous labeling is reasonable when fluorine content per cell is averaged over a few hundred cells. Further, we have shown containment of the ^{19}F marker within NSCs over one week under *in vitro* conditions. The dilution of label through cell division is a potential threat to our strategy, since injected cells can divide after transplantation. However, the cells used here cease to proliferate shortly after implantation. The previously reported time span of 2 days for proliferation *in vivo* is rather short considering a doubling time of approximately 72 hours under ideal *in vitro* conditions [18,19,28,29].

With the small graft sizes used in brain implantation studies, an image voxel is typically only partly filled by labeled cells. This becomes particularly severe with ^{19}F MRI as one strategy to enhance sensitivity is to measure with rather low spatial resolution [10]. As a consequence, quantification in regions with cell densities below the detection limit leads to underestimated cell numbers, graft borders are only inaccurately defined on ^{19}F MR images, and migratory processes on a small scale cannot be monitored. A post-processing scheme to ease the problem has been applied in models of T-cell homing to the pancreas or lymph node by dilation of regions of interest by one-half voxel [12,13]. This scheme could potentially be included in future MRI studies of ^{19}F labeled NSCs depending on expected cell distribution. In order to minimize these partial volume effects in the first place, we used a relatively high *in vivo* resolution (160 nL voxel size in the present report compared to for example 305 nL used before in the mouse brain [20]). To our knowledge there is only one *in vivo* study with a higher resolution, but in mouse hind limb (15.6 nL voxel size [30]). To compensate the loss of sensitivity at the higher resolution, we decided for the use of surface radiofrequency coils with inhomogeneous field profile and T_2-weighted turbo spin echo pulse sequences. Thus the measured ^{19}F signal from a certain region depended not only on the amount of fluorine contained therein but also on ^{19}F relaxation times and the region's distance from the coil. The use of time-consuming, purely spin-density weighted pulse sequences can improve quantification only at the cost of SNR per unit time. A volume coil with more uniform magnetic field profile may be better suited for quantification. However, the coil is often larger and less sensitive compared to a surface coil. To minimize the problem we adjusted the setup in a way that the cell spots were placed within the same distance from the coil for the *in vitro* experiments. For the *in vivo* experiments cells were spread over a slightly larger region and further away from the coil, thereby leading to loss of signal. This may partly explain the order of magnitude difference of *in vitro* and *in vivo* detection limits. In conclusion, coil design and choice of pulse sequence must be carefully adapted to the specific application in future studies employing ^{19}F MRI for cell tracking.

Using a ^{19}F marker with high spin density, using optimized radiofrequency coils and a very high field of 11.7 T we show detection of small numbers of cells in a preclinical setting. Our data indicates that within $\sim$1 h acquisition time *in vitro* detection of $\sim$1,000 cells/voxel is feasible corresponding to less than 10^{16} fluorine spins/voxel. *In vivo* we estimate a detection limit in the order of $\sim$10,000 cells/voxel. The limits are in agreement with earlier studies [11,12,14]. These numbers are usually sufficient for imaging the graft core and possibly even for larger cell clusters migrating away from injection sites in the brain.

Potential of ^{19}F MRI of NSCs in cell replacement therapy

The usefulness of cell tracking with ^{19}F MRI mainly depends on its sensitivity. Although the ^{19}F marker and MRI methods used in this study are likely to be safe for clinical translation, detection sensitivity will be orders of magnitude lower in a clinical setting due to lower field strengths, larger radiofrequency coils, and shorter acquisition times [31]. Still, ^{19}F MRI of NSCs may become clinically relevant in the near future as a result of further advances in MRI hardware and pulse sequence development.

However, before stem cell based therapy of neurological disorders can be used in human patients the action of these cells needs to be further investigated in animal models [16]. ^{19}F labeling may prove superior to labeling with magnetic iron oxide nanoparticles in such preclinical investigations particularly when the pathology induces changes in ^{1}H relaxation times that make distinction between diseased tissue and labeled cells difficult. Possible scenarios include vasogenic edema after ischemic stroke or lesions involving bleedings, in which heterogeneous background T_1, T_2, and T_2* impose major challenges in unambiguous detection of magnetically labeled cells with ^{1}H MRI. As ^{19}F MRI allows quantification of cell numbers it may also help to optimize efficacy of stem cell therapy e.g. in terms of injection sites, monitoring graft size changes [29] and routes of migration.

Conclusion

In future clinical applications, NSCs are one of the most potential and attractive cell sources for stem cell based treatment of diseases affecting the central nervous system. However, for the successful translation of cell therapy additional live imaging tools such as MRI are a prerequisite. ^{19}F MRI is a promising, quantitative, and non-invasive technique to monitor NSC grafts after implantation. We have shown that labeling NSCs with a PFC marker, potentially suitable for clinical use, does not significantly impair cell function both *in vitro* and *in vivo*. Our high detection sensitivity and resolution have allowed for the first time true *in vivo* tracking of small groups of human NSCs. This is particularly interesting for studies of brain cell replacement therapy, in which the graft can initially be small and may become further diluted through lesion-induced cell migration.

Supporting Information

Figure S1 Dilution series of ^{19}F marker. ^{19}F MRI of six tubes containing different concentrations of the PFPE agent (1, 2, 3, 4, 5, and 6 times 31.1 mM corresponding to multiples of $3*10^{15}$ ^{19}F spins/voxel). The tube with $3*10^{15}$ spins/voxel can clearly be depicted (SNR~6). Assuming a labeling efficacy of $3–4*10^{12}$ spins/cell this would translate to detection of less than 1,000 cells/voxel in agreement with the results obtained with our quantification strategy (Fig. 1). Pulse sequence parameters were chosen identical to the cell dilution series in Fig. 1. Note: The surface coil was oriented parallel to the paper plane.
(TIF)

Acknowledgments

We thank C. O'Hanlon for the generous supply of CELSENSE.

Author Contributions

Conceived and designed the experiments: PBS TK MH SW. Performed the experiments: PBS TK LM. Analyzed the data: PBS TK LM. Contributed reagents/materials/analysis tools: PBS TK LM. Wrote the paper: PBS TK MH.

References

1. Guzman R, Uchida N, Bliss TM, He DP, Christopherson KK, et al. (2007) Long-term monitoring of transplanted human neural stem cells in developmental and pathological contexts with MRI. Proceedings of the National Academy of Sciences of the United States of America 104: 10211–10216.
2. Hoehn M, Kustermann E, Blunk J, Wiedermann D, Trapp T, et al. (2002) Monitoring of implanted stem cell migration in vivo: A highly resolved in vivo magnetic resonance imaging investigation of experimental stroke in rat. Proceedings of the National Academy of Sciences of the United States of America 99: 16267–16272.
3. Modo M, Mellodew K, Cash D, Fraser SE, Meade TJ, et al. (2004) Mapping transplanted stem cell migration after a stroke: a serial, in vivo magnetic resonance imaging study. Neuroimage 21: 311–317.
4. Shapiro EM, Sharer K, Skrtic S, Koretsky AP (2006) In vivo detection of single cells by MRI. Magnetic Resonance in Medicine 55: 242–249.
5. Himmelreich U, Weber R, Ramos-Cabrer P, Wegener S, Kandal K, et al. (2005) Improved Stem Cell MR Detectability in Animal Models by Modification of the Inhalation Gas. Molecular Imaging 4: 104–109.
6. Himmelreich U, Dresselaers T (2009) Cell labeling and tracking for experimental models using Magnetic Resonance Imaging. Methods 48: 112–124.
7. Ahrens ET, Flores R, Xu H, Morel PA (2005) In vivo imaging platform for tracking immunotherapeutic cells. Nat Biotech 23: 983–987.
8. Helfer BM, Balducci A, Nelson AD, Janjic JM, Gil RR, et al. (2010) Functional assessment of human dendritic cells labeled for in vivo F-19 magnetic resonance imaging cell tracking. Cytotherapy 12: 238–250.
9. Janjic JM, Ahrens ET (2009) Fluorine-containing nanoemulsions for MRI cell tracking. Wiley Interdisciplinary Reviews: Nanomedicine and Nanobiotechnology 1: 492–501.
10. Srinivas M, Heerschap A, Ahrens ET, Figdor CG, Vries IJMd (2010) 19F MRI for quantitative in vivo cell tracking. Trends in Biotechnology 28: 363–370.
11. Partlow KC, Chen JJ, Brant JA, Neubauer AM, Meyerrose TE, et al. (2007) F-19 magnetic resonance imaging for stem/progenitor cell tracking with multiple unique perfluorocarbon nanobeacons. Faseb Journal 21: 1647–1654.
12. Srinivas M, Morel PA, Ernst LA, Laidlaw DH, Ahrens ET (2007) Fluorine-19 MRI for visualization and quantification of cell migration in a diabetes model. Magnetic Resonance in Medicine 58: 725–734.
13. Srinivas M, Turner MS, Janjic JM, Morel PA, Laidlaw DH, et al. (2009) In Vivo Cytometry of Antigen-Specific T Cells Using F-19 MRI. Magnetic Resonance in Medicine 62: 747–753.
14. Flogel U, Ding Z, Hardung H, Jander S, Reichmann G, et al. (2008) In vivo monitoring of inflammation after cardiac and cerebral ischemia by fluorine magnetic resonance imaging. Circulation 118: 140–148.
15. Kadayakkara DKK, Janjic JM, Pusateri LK, Young W-B, Ahrens ET (2010) In vivo observation of intracellular oximetry in perfluorocarbon-labeled glioma cells and chemotherapeutic response in the CNS using fluorine-19 MRI. Magnetic Resonance in Medicine 64: 1252–1259.
16. Lindvall O, Kokaia Z (2006) Stem cells for the treatment of neurological disorders. Nature 441: 1094–1096.
17. Koch P, Kokaia Z, Lindvall O, Brustle O (2009) Emerging concepts in neural stem cell research: autologous repair and cell-based disease modelling. Lancet Neurol 8: 819–829.
18. Darsalia V, Kallur T, Kokaia Z (2007) Survival, migration and neuronal differentiation of human fetal striatal and cortical neural stem cells grafted in stroke-damaged rat striatum. European Journal of Neuroscience 26: 605–614.
19. Kallur T, Darsalia V, Lindvall O, Kokaia Z (2006) Human fetal cortical and striatal neural stem cells generate region-specific neurons in vitro and differentiate extensively to neurons after intrastriatal transplantation in neonatal rats. Journal of Neuroscience Research 84: 1630–1644.
20. Ruiz-Cabello J, Walczak P, Kedziorek DA, Chacko VP, Schmieder AH, et al. (2008) In Vivo "Hot Spot" MR Imaging of Neural Stem Cells Using Fluorinated Nanoparticles. Magnetic Resonance in Medicine 60: 1506–1511.
21. Hennig J, Nauerth A, Friedburg H (1986) RARE imaging: A fast imaging method for clinical MR. Magnetic Resonance in Medicine 3: 823–833.
22. Gudbjartsson H, Patz S (1995) The Rician distribution of noisy MRI data. Magnetic Resonance in Medicine 34: 910–914.
23. Bulte JWM (2005) Hot spot MRI emerges from the background. Nature Biotechnology 23: 945–946.
24. Castro CI, Briceno JC (2010) Perfluorocarbon-Based Oxygen Carriers: Review of Products and Trials. Artificial Organs 34: 622–634.
25. Ruiz-Cabello J, Barnett BP, Bottomley PA, Bulte JWM (2011) Fluorine (19F) MRS and MRI in biomedicine. NMR in Biomedicine 24: 114–129.
26. Maki J, Masuda C, Morikawa S, Morita M, Inubushi T, et al. (2007) The MR tracking of transplanted ATDC5 cells using fluorinated poly L-lysine-CF3. Biomaterials 28: 434–440.
27. Masuda C, Maki Z, Morikawa S, Morita M, Inubushi T, et al. (2006) MR tracking of transplanted glial cells using poly-L-lysine-CF3. Neuroscience Research 56: 224–228.
28. Darsalia V, Allison SJ, Cusulin C, Monni E, Kuzdas D, et al. (2011) Cell number and timing of transplantation determine survival of human neural stem cell grafts in stroke-damaged rat brain. J Cereb Blood Flow Metab 31: 235–242.
29. Kallur T, Farr TD, Böhm-Sturm P, Kokaia Z, Hoehn M (2011) Spatio-temporal dynamics, differentiation and viability of human neural stem cells after implantation into neonatal rat brain. European Journal of Neuroscience 34: 382–393.
30. Waiczies H, Lepore S, Janitzek N, Hagen U, Seifert F, et al. (2011) Perfluorocarbon Particle Size Influences Magnetic Resonance Signal and Immunological Properties of Dendritic Cells. PLoS ONE 6: e21981.
31. Bonetto F, Srinivas M, Heerschap A, Mailliard R, Ahrens ET, et al. (2010) A novel 19F agent for detection and quantification of human dendritic cells using magnetic resonance imaging. International Journal of Cancer 129: 365–373.

Supplementary Figure 1

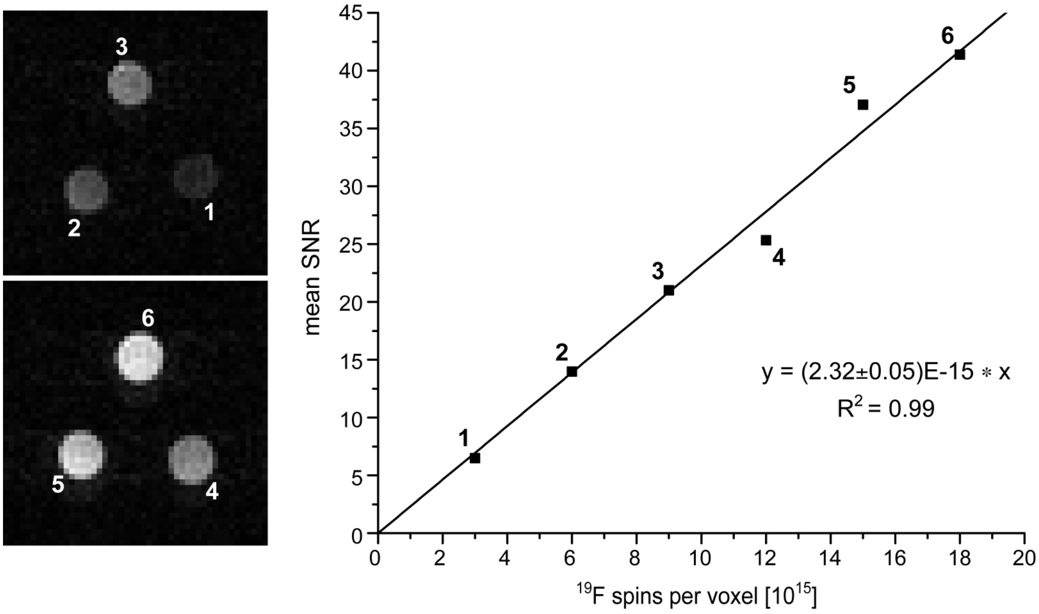

Labeling cells for in vivo cell tracking with ^{19}F MRI VI

Biomaterials 33 (2012) 8830–8840

Contents lists available at SciVerse ScienceDirect

Biomaterials

journal homepage: www.elsevier.com/locate/biomaterials

Review

Labeling cells for in vivo tracking using ^{19}F MRI

Mangala Srinivas [a,*], Philipp Boehm-Sturm [b], Carl G. Figdor [a], I. Jolanda de Vries [a], Mathias Hoehn [b]

[a] Department of Tumor Immunology, Nijmegen Center for Molecular Life Sciences, Radboud University Nijmegen Medical Center, Postbox 9101, 6500HB Nijmegen, The Netherlands
[b] In-Vivo-NMR Laboratory, Max-Planck-Institute for Neurological Research, Cologne, Germany

ARTICLE INFO

Article history:
Received 8 August 2012
Accepted 22 August 2012
Available online 6 September 2012

Keywords:
^{19}F MRI
Cell tracking
Cell therapy
In vivo imaging
Perfluorocarbons

ABSTRACT

Noninvasive in vivo cell tracking is crucial to fully understand the function of mobile and/or transplanted cells, particularly immune cells and cellular therapeutics. ^{19}F MRI for cell tracking has several advantages; chief among them are its noninvasive nature which allows longitudinal data acquisition, use of a stable, non-radioactive isotope permitting long-term tracking, the absence of confounding endogenous signal, and the ability to quantify cell numbers from image data. However, generation of sufficient signal i.e. ^{19}F cell loading is a key challenge, particularly with non-phagocytic cells such as lymphocytes and stem cells. A range of ^{19}F cell labels have been developed, including emulsions, particles, polymers, and agents for clinical use. Various animal and primary human cells, such as dendritic cells, lymphocytes and phagocytes have been successfully labeled and studied in models of autoimmune disease, inflammation and transplant rejection. Primary human cells, particularly dendritic cells as used in vaccine therapy have been tested for imminent clinical application. Here, we summarize current cell loading strategies and sensitivity of in vivo cell imaging with ^{19}F MRI, and discuss the processing of image data for accurate quantification of cell numbers. This novel technology is uniquely applicable to the longitudinal and quantitative tracking of cells in vivo.

© 2012 Elsevier Ltd. All rights reserved.

1. Introduction

Perfluorocarbons (PFCs) are C-F polymers with unique properties: These compounds are extremely inert and stable, even at high temperatures and pressures, and are singularly immiscible with both lipophilic and hydrophilic solvents. For example, Teflon is a PFC well-known for its "non-stick" property. The high stability of PFCs has made them useful as a wide range of products including as lubricants in spacecraft. Their high density has made them useful in eye surgery, to hold the retina in place. Due to their ability to dissolve gases, PFCs have been used to formulate artificial blood substitutes and are still used in partial liquid ventilation in premature infants. Thus, PFCs have a long history of varied use, both in industry and in the clinic.

More recently, the increasingly widespread use of cellular therapeutics has generated a new role for fluorocarbons as labels for cell tracking using ^{19}F MRI [1]. MR imaging allows for high resolution anatomic and functional images, with intrinsic contrast even in soft tissues. MRI is noninvasive and does not use ionizing radiation. However, relevant cells must be labeled to distinguish them from background cells. ^{19}F compounds are excellent labels for in vivo MRI, as the ^{19}F nucleus is extremely sensitive for MR imaging, several orders of magnitude higher than ^{13}C or ^{23}Na and comparable to the ^{1}H nucleus, and there is no detectable background in vivo [2]. The signal received is directly proportional to the amount of ^{19}F present. This allows for quantification of cell numbers from the in vivo images, when the average ^{19}F cell loading is known. Furthermore, the T_1 relaxation parameters of some ^{19}F compounds can vary with oxygen content; this allows for ^{19}F MRI-based measurement of oxygen levels in vivo, although this T_1 variability can also complicate quantification.

In order to carry out ^{19}F MRI-based cell tracking, the cells must be loaded with sufficient ^{19}F for imaging within a reasonable length of time. This requires the formulation of appropriate labels and the development of suitable labeling techniques to load the relevant cells, whether ex vivo or in vivo. A typical outline of the entire procedure is shown in Fig. 1. In this article, we review the different types of cell labels developed and the labeling procedures used. We also discuss the selection of a specific label for a cell type, as well as strategies to improve sensitivity during imaging. Finally, we discuss potential new technologies that may transfer successfully to ^{19}F MRI in the near future. ^{19}F MRI and NMR have been applied to tumor oximetry, localizing inflammation and other applications, but here we will focus specifically on ^{19}F MRI for in vivo cell tracking.

---

* Corresponding author. Tel.: +31 (0)624892288; fax: +31 24 3540339.
E-mail addresses: mangala.srinivas@gmail.com, M.Srinivas@ncmls.ru.nl (M. Srinivas).

0142-9612/$ – see front matter © 2012 Elsevier Ltd. All rights reserved.
http://dx.doi.org/10.1016/j.biomaterials.2012.08.048

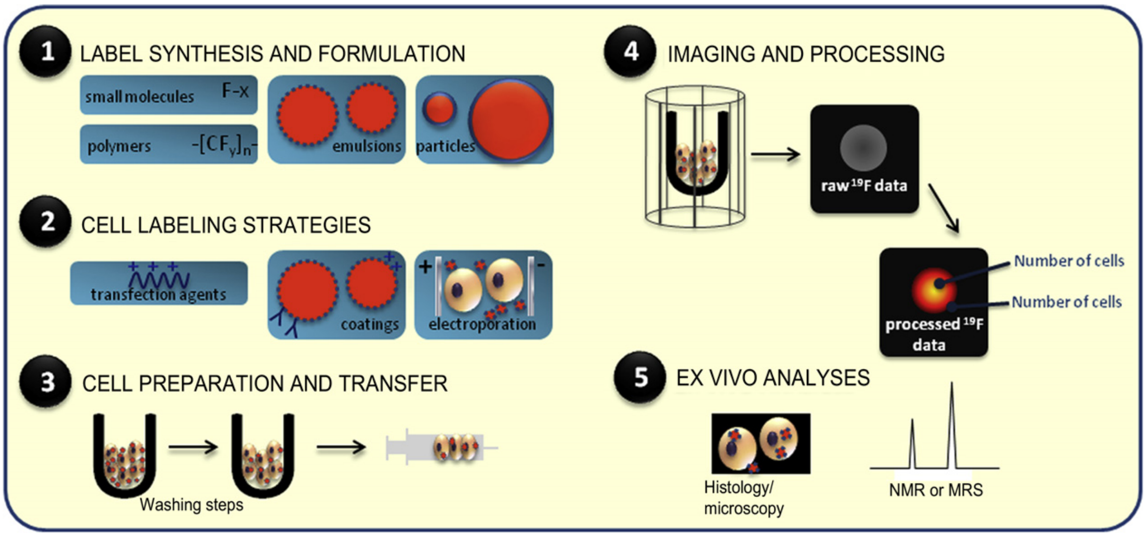

Fig. 1. Key steps in cell labeling for ^{19}F MRI. The figure shows the most commonly used protocols for each step; variations proposed in the literature are discussed in the text. Appropriate selection of label and labeling protocol is crucial for success of the experiment (*Step 1*). Cell labeling (*Step 2*), may require enhancement through the use of coatings or transfection agents. After suitable preparation (*Step 3*) the cells can be imaged. Post-processing leads to quantification (*Step 4*). Finally, various ex vivo analysis can be carried out (*Step 5*) to corroborate the in vivo data.

2. Types of ^{19}F cell labels and their effect on cells

The main purpose of a ^{19}F cell label is to render the relevant cells detectable by loading with sufficient ^{19}F for detection. Thus, these labels are typically large fluorocarbons or aggregates of fluorocarbons. General requirements for ^{19}F cell labels are described elsewhere [2]; chiefly, these include a sufficiently large number of ^{19}F atoms for detection, nontoxicity to the cell and a single (overall) resonance frequency. In general, labels consist of the fluorinated molecule and a component to stabilize the fluorocarbon in the cell environment or make it more accessible for cell uptake. Thus, the most common labels consist of a perfluorocarbon coated with a lipid surfactant. Additional components, such as fluorescent dyes, drugs or targeting moieties can be added to these complexes. These and other types of labels are discussed in the following sections. Examples of cell labels are shown in Fig. 2, together with corresponding in vitro or in vivo images.

2.1. Emulsions

The majority of cell labels used thus far have been emulsions, due to their high content of PFC per droplet and the ease of formulation. Emulsions are droplets of an immiscible compound surrounded by a surfactant that stabilizes the droplet in the continuous phase, typically water. Fluorinated compounds, especially the large PFCs used in cell labels, are not miscible with water and these must be coated with a suitable surfactant in order to remain dispersed. Otherwise, the PFC will settle out of the solvent as a separate layer, analogous to oil and vinegar. The emulsion droplet therefore consists of a large payload of ^{19}F surrounded by a lipid coat. Emulsions can be formulated by simple mixing of the components, or more sophisticated processes such as microfluidization (MF), which yields more homogeneous droplets. Perfluorocarbons used for labeling thus far include perfluorooctyl bromide (PFOB), perfluoro-15-crown-5 ether (PFCE) and linear perfluoropolyethers (PFPE). PFOB, in particular, has previously been used in clinical blood substitutes. The surfactants used most frequently are lipids such as phospholipids and poloxamers. These data are summarized in Table 1. The biological effects of poloxamers are described elsewhere [3]. Poloxamers are in active research for drug delivery, and are known to affect cell membrane properties, among others. Phospholipids are major components of cell membranes and are generally considered safe for use.

PFC emulsions have been used for decades as blood substitutes, although with limited success. Indeed, it was the instability of these emulsions that hindered their use in the clinic and in other applications. However, in a preclinical setting, emulsions are still convenient, as they can be made in smaller batches when necessary. One must keep in mind that any extra moieties added to an emulsion, such as a dye or an antibody, are more likely to blend with the surfactant than the PFC and may become separated from the PFC in vivo or in the cell. Recently, we proposed an alternative to emulsions to overcome these issues, consisting of polymer-encapsulated PFC [4]. Here, any dyes or other compounds can be covalently bound to the particle surface or encapsulated within, and the particles can be frozen for easy storage. In general, both types of label result in cell loading in the order of 10^{11}-10^{13} ^{19}F atoms/cell. Fluorescent, fluorinated micelles have also been developed, although these have not been applied to cell labeling [5]. Finally, an expected benefit on cell viability may occur if the ^{19}F agent can improve oxygenation, as has been shown with some cell types [6].

2.2. Other types of label

The ^{19}F cellular labels used thus far are summarized in Table 1. Over two thirds of these studies used PFC emulsions due to their high content of ^{19}F. Other options include fluorinated peptides or polymers or fluorinated small molecules, such as sugars; these often result in much lower cell loading, and thus much lower detection sensitivity. Fluorinated drugs have been studied using ^{19}F, even in the clinic. While these drugs were not designed specifically to label cells, cellular uptake occurs and it may be possible to modify these compounds for cell tracking in vivo. However, ^{19}F is highly reactive and electronegative, and its incorporation in a compound can significantly alter its chemistry. For cell labels, especially when used in vivo, any metabolism of the compound must also be considered.

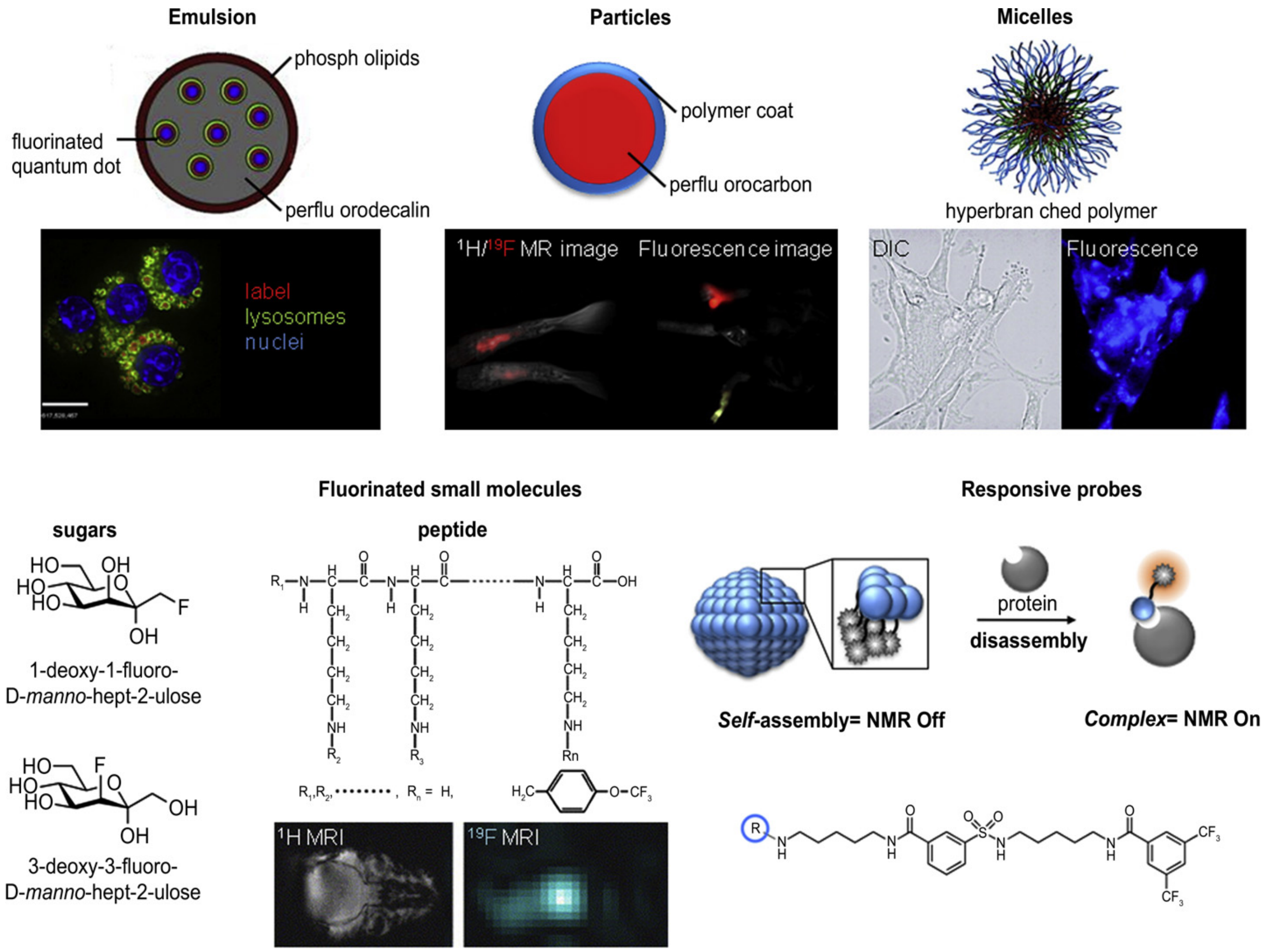
Emulsion
phosph olipids
fluorinated quantum dot
perflu orodecalin
label
lysosomes
nuclei
Particles
polymer coat
perflu orocarbon
¹H/¹⁹F MR image
Fluorescence image
Micelles
hyperbran ched polymer
DIC
Fluorescence
Fluorinated small molecules
sugars
1-deoxy-1-fluoro-D-manno-hept-2-ulose
3-deoxy-3-fluoro-D-manno-hept-2-ulose
peptide
R₁,R₂,……, Rₙ = H,
¹H MRI
¹⁹F MRI
Responsive probes
protein
disassembly
Self-assembly= NMR Off
Complex= NMR On
R

Fig. 2. Types of ^{19}F cell labels. The main types of cell labels, listed in Table 1, are shown here. *Emulsions* consist of droplets of fluorocarbon with a lipid bilayer coating; additional components such as dyes or quantum dots can be added [86]; the inset shows a micrograph of labeled cells with the quantum dots in red, lysosomes in green, nuclei in blue and scale bar of 10 μm. *Particles* consist of a perfluorocarbon core with a polymer coat, to which additional components can be covalently added [4]. The inset shows in vivo MRI (left) and fluorescence images (right) of the particles injected in the footpads of a mouse. *Micelles* typically consist of a polymer in a conformation that only exposes hydrophilic regions, in this case with the fluorine groups on the inside [5]; the inset shows micrographs of labeled cells with a diffusion interference contrast (DIC) image on the left and a fluorescence image on the right, where the micelles are blue. Other labels that have been developed include *fluorinated small molecules* such as sugars [85] or fluorinated peptides [47]; inset shows in vivo ^{1}H (left) and ^{19}F MR images of labeled cells implanted in the cranial bone of mice. *Responsive probes* only become detectable upon binding to a specific protein; *R* represents different side groups [9]. Ref. [86] reprinted from Biomaterials, copyright 2010 [4]; from Biomaterials, copyright 2010 [85]; from Arch Biochem Biophys, copyright 2012 [47]; from Biomaterials, copyright 2007; all with permission from Elsevier. Ref. [5] reprinted with permission from Bioconjug Chem, copyright 2008, American chemical Society. Ref. [9] reprinted from Nat Chem, copyright 2009, with permission from Macmillan Publishers Ltd. (For interpretation of the references to color in this figure legend, the reader is referred to the web version of this article.)

The main advantage of smaller labels over emulsions, despite their lower ^{19}F content, is that they can be adapted to study (or manipulate) a specific aspect of cell functionality. Probes have been developed that are switched on or off by specific enzyme activity [7], gene expression [8] and protein binding [9]. Although promising, these labels tend to have insufficient sensitivity for in vivo use. Finally, some cell labels applied to ^{1}H MRI may be relatively easy to adapt for ^{19}F MRI. For example, rationally designed multistage nanovectors [10], dendrimers [11], and even gadolinium loaded nanoparticles [12].

3. Cell loading strategies

Cell loading is influenced by the fluorinated compound, the method of delivery, and cell uptake, which is dependent on the cell type and status. For purposes of quantification, it is important that average cell uptake is reproducible for a given set of labeling conditions. Variables in ex vivo labeling conditions include the point of time at which the label is added, the labeling medium, surface chemistry of cell culture flasks, length of incubation with the label, label concentration and washing steps. Non-phagocytic cells in particular may need extra enhancement to take up sufficient label. This can be achieved with positive lipids, typically transfection agents, or antibodies (see Table 2).

Phagocytic cells such as dendritic cells and macrophages have been labeled most often, both due to their biological significance and the relative ease of labeling. Furthermore, these cells are migratory and thus are relevant for cell tracking studies. In particular, macrophages have been labeled through simple intravenous administration of PFC emulsions (see Table 1). The use of ^{19}F MRI to study inflammation, primarily through tracking macrophages, has recently been reviewed [13,14]. These labeled

Table 1
Current cell labels. The table lists ^{19}F cell tracking studies carried out thus far, with information on the type of label, its formulation, any additives used, the cell type and the average loading achieved (where indicated in the publication). All cells are cell lines unless indicated as primary; "lipids" include compounds such as phospholipids; poloxamers are listed separately. Note that the fluorinated reporter probes are typically assessed using spectroscopy.

Major ^{19}F component	Main surfactant	Formulation	Additives	Hydrodynamic diameter (nm)	Cell type	Average cell loading ($\times 10^{12}$ ^{19}F atoms/cell)	Ref
Cell tracking: Ex vivo labeling							
Various PFCs	PLGA	Nanoparticles	Dye	200–300	Primary human DCs	30	[4]
PFCE	Lipids	MF		233	Primary human stem/progenitor cells	20	[82]
PFOB	Lipids			224		0.5	
PFCE	Lipids	MF		100	Murine DCs	20	[81]
PFPE	Poloxamer	Sonication	Dye	120	Primary murine T cells	20	[62]
PFPE	Lipids	MF			Primary human DCs	20	[24]
PFPE	Lipids	MF		180	Human neural stem cells	4	[16]
PFCE	Poloxamer	Sonication		130, 245, 365, 560	Primary murine DCs	2	[21]
PFPE	Lipids	MF	Dye	180	Human neural stem cells	2	[15]
PFPE	Poloxamer	MF	Dye	180	Primary murine T cells	0.3	[83]
PFPE	Poloxamer	MF		180	Primary murine T cells	0.3	[84]
PFCE	Poloxamer	Sonication	Dye		Rodent glioma	0.2	[68]
Fluorinated sugars	n/a	n/a		n/a	Primary rodent hepatocytes	0.03–0.1	[85]
Perfluorodecalin	Lipids	Sonication & MF	Quantum dots	250	Human NK and leukemia cell lines		[86]
PFOB	Lipids	MF	Drug targeting agent	250	Primary porcine aortic smooth muscle cells		[87]
PFOB	Lipids	Sonication & MF	Drug	225	Primary human umbilical cord smooth muscle cells		[88]
Various PFCs	Fluorinated \surfactants	MF	Fluorinated quantum dots	200	Murine macrophage; human carcinoma		[89]
PFCE	Lipids	MF	Targeting peptide	170	Human umbilical cord vein endothelial cells		[69]
PFOB	Lipids	Sonication	Dye	80	Harvested human pancreatic islets		[90]
PFCE	Lipids	Sonication		170			
Various PFCs	Lipids	Sonication & MF	Quantum dots		Murine macrophage and DC cell lines; and primary murine DCs and T cells		[91]
PFOB	Lipids		Targeting antibody transfection agent		Human cancer cell lines		[92] [93]
Fluorinated poly-L-lysine			Dye	n/a	Glial cells	n/a	[48]
Fluorinated poly-L-lysine			Dye	n/a	Bone/cartilage stem cells	n/a	[47]
Cell tracking: In vivo labeling							
PFCE	Lipid	MF	Dye	130	Monocyte/macrophages	9 (macrophage cell line labeled ex vivo)	[61]
PFCE	Lipids	Sonication and MF	Targeting agent and fluorescent dye	245	Endothelial cells		[54]
PFCE	Lipids	MF		145	Macrophages		[94]
PFCE	Lipids	MF		145	Macrophages		[37]
PFCE	Lipids	MF			Monocytes/macrophages		[95]
PFCE	Lipids				Monocytes/macrophages		[96]
PFOB	Lipids	Imagent/ Perflurobron	Dye		Macrophages (rabbit)		[97]
PFCE	Lipids	MF	Dye	145	Macrophages		[98]
Other							
Hyperbranched fluorinated polymer	Specific polymers (micelles)		Drug	20-30	Human glioblastoma cell line	0.0005	[5]
Fluorinated colchicine derivatives	n/a	n/a	n/a	n/a	Human leukemia cell line		[99]
Fluorinated nitroimidizole	n/a	n/a	n/a	n/a	Tumor retention (humans)		[100,101]
Trifluoronitroimidazole					Primary murine tumor cells		[102]
Fluorinated reporter molecules	n/a	n/a	n/a	n/a	Various, including bacteria and human cancer cell lines		[103-107] [76,108] [8] [109]
On-off probes	n/a	n/a	n/a	n/a	Red blood cells		[9]
Fluorinated prodrug					Human cancer cell lines		[110]
Fluorouracil					Tumor (human trial)		[45] [111]

Table 2
Improvement of cell loading. The effect of transfection agents or targeting peptides on increasing cell loading is summarized here, including the fold-increase in cellular ^{19}F content.

Label	Loading strategy	Cell type	Cell loading improvement (fold increase)	Ref
Emulsion	Transfection agent	Murine DCs	26	[81]
Emulsion	RGD-peptide	Primary human umbilical cord vein endothelial cells	6	[69]
Emulsion	Transfection agent	Primary murine T cells	5	[62]
Emulsion	Targeting antibody	Primary porcine aortic smooth muscle	2	[87]
Emulsion	Transfection agent	Human breast cancer cell line	~1.2	[93]
Emulsion	Integrin targeting	In vivo binding to vascular endothelium		[54]

macrophages accumulate in loci of inflammation and can be imaged. Non-phagocytic cells that have been labeled for ^{19}F MRI include T cells, stem cells, and smooth muscle cells. In many of these cases, label uptake was enhanced with transfection agents used to stimulate DNA uptake in cells (see Table 2). To avoid stickiness of label or the labeled cells to cell culture dishes, precoating of dishes or addition of serum to culture medium was necessary in some studies [15–17]. Electroporation has been used to stimulate uptake with contrast agents (for example [18],). This is a relatively harsh technique where a transient electric pulse is used to open cell membrane channels to stimulate uptake. Techniques for improving cell loading are similar to those used for contrast agents, and have been reviewed in more detail [19]. In all cases, labels that are taken up by cells without further interference are preferred, as viability tends to improve (for example [20],). However, for some cell types and labels, addition of a transfection agent or other aid is crucial, resulting in up to a 20-fold increase in uptake (Table 2).

Finally, it is interesting that most of the (emulsion) labels used thus far tend to be around 200 nm in diameter, although one study with dendritic cells found that increasing size to 560 nm resulted in better loading [21]. With non-phagocytic T cells, it has been shown that uptake of iron oxide particles was also affected by particle size, with optimal uptake at 200–300 nm and further enhancement by the use of a positively-charged coating [22]. These studies suggest that the majority of labels used thus far may be improved simply by slightly increasing their size. However, increasing the size of emulsion droplets also increases their density; this can make it more difficult to remove excess label from labeled cells by techniques such as centrifugation.

4. Labeling optimization

In vivo, targeted labeling with high specificity and efficiency would generally be ideal; although currently unachievable for most cell types. The main issues to consider are whether the expected ^{19}F/voxel will be sufficient for detection, and whether the relevant cells can be labeled without significant toxicity and phenotype change. An outline of the overall procedure is shown in Fig. 1. Steps 1–3 in particular must be optimized for each cell type and label combination. Step 4 is dependent on the NMR properties of the ^{19}F agent, and the available hardware and imaging sequences. The final step may or may not be necessary, dependent on the aims of the study.

In all studies thus far, the labeled cells are typically assayed for viability, using trypan blue exclusion or other assays, and for functionality, such as the expression of typical membrane markers. These data are compared to those from non-labeled controls. One aspect that is often overlooked is the effect of the label on cell migration, as the PFCs are very dense and cells can become completely engorged with PFC droplets. Migration is vital to the functionality of cells such as macrophages, and thus should be assayed in vitro. This can easily be done using microscopy-based or transwell migration assays. It is now known that cell migration can be seriously affected by iron oxide loading [23]. In our studies, we found no significant effect of PFC labeling on the migration of primary human dendritic cells [24]. In the case of PLGA particles used for cell labeling [4], a vast body of literature already exists on the engineering of PLGA particles for specific applications [25,26]. The amount of label taken up by a cell may influence its intracellular fate and phenotype or functionality of the cell. Iron oxide labels have been used for cell tracking extensively, but their effect on the cell and in vivo is only now being uncovered. In particular, these agents can impact migration [23], proliferation, and the intracellular redox state [27].

Finally, cell labeling conditions that result in nonhomogeneous cell uptake may show mixed or inconsistent results in functionality assays dependent on the cell loading [28]. Cell functionality can also vary with differences in particle size [21]. Thus, several interdependent factors must be studied and manipulated for optimal cell labeling.

5. In vivo effects and clearance of perfluorocarbons

Cell labels themselves have not been studied in terms of their long-term fate and clearance in vivo. The tiny concentrations of PFC used as cell labels, typically nano- or picogram amounts, are usually undetectable after loss from the cells. However, much work has been done on the clearance of PFCs used as blood substitutes in the 1970's and 80's. In particular, research focused on Fluosol-DA, which was FDA-approved for use as a clinical blood substitute in early 1980. It was used in 40,000 patients, but its use was limited due to problems with stability and storage of the emulsion. The emulsion consisted primarily of perfluorodecalin, emulsified with poloxamer F-68 in saline. In general, the emulsion was well tolerated with the main side effects being minor flu-like symptoms [29], when administered to healthy volunteers at up to 1.2 g PFC/kg. In rodents, the functioning of the liver and spleen can be decreased temporarily [30,31]. The emulsion itself is removed from circulation primarily by macrophages in the spleen and liver. In general, the emulsion causes depression of the mononuclear phagocyte system, which results in temporarily increased susceptibility to infection [32]. It was later shown that this side effect of Fluosol-DA was mainly caused by the poloxamer surfactant [33,34] which reduced neutrophil migration to infection loci, thus resulting in higher mortality due to infection.

It is known that all side effects of PFC emulsions are strongly dose-dependent [35], and hence may not be applicable to cell tracking studies with their tiny doses of PFC. Furthermore, all the side effects are thought to be due to the effect of macrophage stimulation and are fully reversible. In terms of clearance from circulation, PFCs are taken up by macrophages, first in the liver and spleen, and then eventually exhaled in the lungs. The half-life is influenced by chain length, with heavier PFCs lingering longer [36]. In all cases, there is no metabolism of the PFCs in vivo. A study in rats found that an emulsion of 30% w/v PFCE with an average diameter of 145 nm had a circulatory half-life of about 9.5 h after intravenous transfer [37].

A recent study using PLGA-encapsulated PFOB particles administered intravenously also found uptake primarily in the liver and spleen. However, circulation time could be increased by using a PEG coating to make the particles "stealthy" [38]. This allowed for accumulation at tumor sites within 7 h post-administration.

Finally, the effect of the surfactants or other components on a systemic level should also be considered. Typical surfactants, such as phosphotidylcholine, are generally considered as safe. Poloxamers and PLGA both have been tested in humans, generally without major safety concerns.

6. Implementation of in vivo ^{19}F MRI

For most MRI systems an upgrade for in vivo ^{19}F MRI is available at reasonable cost since the resonance frequency of the ^{19}F nucleus is very close to that of ^{1}H and most of the existing hardware for ^{1}H MRI can be used. For true dual nuclei detection or for ^{1}H/^{19}F decoupling experiments, an upgrade would comprise ^{19}F transmitter and receiver units, combiner and splitter for ^{1}H/^{19}F signals, and a dual-resonant radiofrequency (RF) coil [39]. These components are commercially available, however most research groups rely on custom designed RF coils to accommodate their specific needs. With the first ^{19}F agent for in vivo cell tracking being FDA-approved (press release, Celsense Inc., Pittsburgh, USA) implementation of ^{19}F MRI of labeled cells at clinical systems will become relevant. Here, lessons can be learnt from studies on gastrointestinal transit in humans with ^{19}F capsules [40,41], ^{19}F MRI of lung ventilation in large animals using fluorinated gases [42], and pharmacokinetic studies of fluorinated anesthetics or drugs in patients (reviewed e.g. in [43]). For the latter, the first MRS study was reported over two decades ago [44]. Since then hardware and acquisition strategies have greatly improved allowing spatially-resolved MRS imaging of these drugs in the liver of patients despite low in vivo concentrations (for example [45],).

7. Sensitivity of ^{19}F MRI of labeled cells

Once cellular uptake of a ^{19}F agent has been optimized, the sensitivity of ^{19}F MRI of labeled cells mainly depends on 1) MR properties of the ^{19}F agent, i.e. spin density, relaxation times, NMR spectrum (single/multiple peaks) 2) the MRI system (field strength and RF coil being the most critical components) 3) MRI acquisition, i.e. RF pulse sequence and 4) post-processing strategies. It is essential to optimize these since direct detection of nuclear spins with MRI is inherently insensitive due to low energies between different spin states when compared to thermal fluctuations in the electronics and sample. If needed, such optimization must be carried out under the constraint that accurate quantification of ^{19}F concentrations is still possible. The SNR achievable in ^{19}F MR spectroscopy of fluorinated compounds has recently been reviewed extensively [46]. In agreement, sensitivity of cellular ^{19}F MR imaging is at the order of $\sim 10^{16}$ ^{19}F spins/voxel for small animal systems and imaging time of 1 h. For typical voxel sizes of $(1\ \text{mm})^3$ this translates to ^{19}F concentrations in the mM range and a detection threshold down to the order of ~1000 cells in vitro depending on average ^{19}F content per cell (Table 3).

7.1. Enhancing sensitivity: MR properties of ^{19}F agent

So far, PFCs have been used for in vivo ^{19}F MRI almost exclusively, except for two studies using poly-L-lysine-CF_3 [47,48]. This is due to the very high density of ^{19}F in PFCs and relatively high T_2/T_1 ratio for some of these (~0.5 for the linear PFPE). Interestingly, we observed an order of magnitude lower T_2^* (<10 ms, unpublished) than T_2 (~150 ms, [16]) for a PFPE emulsion, which decreases sensitivity in gradient echo experiments. The large difference could be explained by local susceptibilities at the PFC/water surfaces and longer T_2^* might be achievable with susceptibility-matching of the PFC core with its surrounding.

The main focus to further enhance MR sensitivity from the chemical synthesis side has been towards manipulation of relaxation time T_1 by adding paramagnetic ions such as Gd^{3+}, which would allow shorter measurement times or higher SNR at identical scan time. Since PFCs are neither hydrophilic nor lipophilic incorporation of Gd is not straightforward. Direct incorporation of Gd in the lipid monolayer of PFC emulsions has been shown to efficiently decrease ^{19}F T_1, which translated to ~125% increased SNR at 1.5 T [49]. However, only ^{19}F close to the emulsion droplet surface will exhibit the short-range T_1 reduction. Furthermore, the shortening in T_2 induced by the paramagnetic ion can annihilate the gain in sensitivity, thus fine-tuning of the ion-^{19}F interaction is essential [50].

7.2. Enhancing sensitivity: MRI system

The trend towards high and ultra-high magnetic field strengths has certainly contributed to the increasing impact of ^{19}F MRI since this is a straightforward (but financially costly) way to increase SNR due to enhanced equilibrium magnetization. An alternative way to boost the magnetization is hyperpolarization which has been shown to enhance SNR by a factor of 60 in vitro [51]. However, the decay of enhanced signal in this study was on the order of 1 min; thus, this technique may only have an impact on in vivo studies of early metabolites of ^{19}F compounds or lung imaging after inhalation of hyperpolarized ^{19}F gases, but not for long-term cell tracking. At fixed field strength, the RF coil is certainly the most critical component of the MRI system that determines sensitivity. Sensitivity of the coil mostly depends on the filling factor, which is higher when the coil is close to the sample and of small size. In this context, arrays of small surface coils have revolutionized sensitivity and sped of ^{1}H MRI in combination with parallel imaging techniques. First reports exist using custom-made ^{19}F array coils for cell imaging [52] but broader application to ^{19}F MRI is still missing. Another emerging technology to improve SNR in small animal MRI are cryogenically cooled RF coils since these coils are now commercially available (see review [53]). For in vivo ^{1}H MRI of the mouse brain a factor 2.4 gain in sensitivity has been reported and similar improvements would be expected for a ^{19}F cryo-coil, which may become available with increasing demand. Importantly, the gain in SNR is higher for lower magnetic field strengths due to their higher coil-dominant noise, which can be reduced by cooling. Thus, the cryo-technology may also greatly improve sensitivity of ^{19}F MRI at clinical systems.

7.3. Enhancing sensitivity: MRI acquisition

One of the main advantages of MRI is the flexibility of acquisition and resulting contrast in the image, e.g. generation of spin density-, T_1-, T_2-, T_2^*-, and diffusion-weighted images. For example, introduction of diffusion weighting in a conventional ^{19}F MRS pulse sequence was used to selectively image nanoparticles bound to a molecular target whereas the signal from moving nanoparticles in the blood stream was eliminated by the diffusion weighting [54]. Finding the right pulse sequence for an in vivo application may become very complex and will not be discussed here. However, for ^{19}F MRI the task is usually simpler: Find a pulse sequence that maximizes SNR efficiency (SNR divided by square root of acquisition time) at the given relaxation times of a ^{19}F compound. This generally narrows down the choice to fast pulse sequences, such as fast gradient echo, fast spin echo or steady-state-free-precession sequences. For example, a framework to overcome the problems of extremely short T_2/T_2^* relaxation of paramagnetic ^{19}F complexes by using fast ultrashort echo time (UTE) and zero echo time (ZTE) pulse sequences was recently presented [55]. The authors were

Table 3
Reported detection limits of ^{19}F MRI-based cell tracking. Reported detection limits of ^{19}F labeled cells in dependency of ^{19}F compound and relaxation times, cellular uptake of ^{19}F, MRI system and MR acquisition.

^{19}F label	Cell type	Average cell loading [$\times 10^{12}$ ^{19}F's/cell]	Field strength (T)	T_1/T_2 [ms][a]	RF coil (diameter)	Pulse sequence	Imaging time [min]	Reported detection limit	Detection limit [$\times 10^{16}$ ^{19}F's/voxel][b]	SNR	Estimated detection limit (SNR=5) at 9.4 T within 1 h [$\times 10^{16}$ ^{19}F's/voxel][c]	Reference
PLGA-PFCE nanoparticles	Human dendritic cells	25	7	n/a	Surface coil (10 mm)	TSE	n/a	<30,000 cells	n/a	n/a	n/a	[4]
PFPE emulsion	Murine T-cells	22	11.7	n/a	Birdcage volume resonator	TSE	68	7500 cells in vitro/30,000 cells in vivo	17	2.5	44	[62]
PFPE emulsion	Human dendritic cells	17	7	350/40	Surface coil (10 mm)	Spin echo	82	2000 cells	3.4	3	4.9	[24]
PLGA-PFCE nanoparticles	Human dendritic cells	7	7	950/50	Solenoid (15 mm)	MRSI	60	5000 cells	3.5	3	4.3	[112]
PFCE emulsion	Primary human stem/progenitor cells	6.2	11.7	800/-	Solenoid (5 mm)	FLASH	7	6100 cells in vitro	3.8	3	2.7	[82]
PFPE emulsion	Human neural stem cells	3.70	11.7	380/70	Single loop surface Tx/Rx (25 mm)	TSE	57	1000 cells in vitro/10,000 cells in vivo	0.37	3.5	0.64	[16]
PFPE emulsion	Human neural stem cells	2	7	425/82	Quadrature volume coil	TSE	60	17,000 cells in vitro	3.3	1.25	9.9	[15]
PFCE emulsion	Murine dendritic cells	1.66	9.4	n/a	4-turn solenoid	FLASH	106	10^6 cells	170	n/a	n/a	[21]
PFCE emulsion	Murine macrophages	0.44	9.4	n/a	Birdcage volume resonator (30 mm)	TSE	19	200 cells	0.18	3	0.17	[61]
avb3-targeted Gd/PFCE emulsion	Human umbilical vein-derived endothelial cells		6.3	800/ varying with [Gd]	Solenoid Tx/Rx (5 mm)	FLASH	10	200 mM cell-internalized ^{19}F	0.59	5	0.16	[69]
PFCE emulsion	Murine neural stem cells		11.7	580/540	Slotted tube volume resonator	TSE	8	30 mM ^{19}F agent at 20 μL voxel		n/a	n/a	[17]
PFPE emulsion	Human pancreatic islets		9.4	n/a	Solenoid Tx/Rx	TSE	37	10 islets/∼ 20000 cells	n/a	n/a	n/a	[90]

[a] Intracellular T_1/T_2 times when available.

[b] If minimum detectable ^{19}F concentration $c^{19}F_{,min}$ was reported we used $c^{19}F_{,min} \times$ voxel size, if minimum number of detectable cells $n_{cells,min}$ was reported we used $n_{cells,min} \times (^{19}F/cell)$.

[c] For better comparison of detection limits, the minimum detectable ^{19}F/voxel at 9.4 T and 1 h imaging time and an SNR = 5 is stated assuming SNR linear with ^{19}F concentration, a linear SNR increase with field strength (sample dominant noise) and inverse square root dependency on imaging time.

able to synthesize lanthanide ^{19}F compounds with T_2^*/T_1 ratio up to the maximum of ∼1, which boosted SNR by a factor of 27 compared to non-paramagnetic compound using these special sequences, whereas the SNR gain in conventional fast gradient echo MRI was only 11.

For compounds with ^1H-^{19}F coupling, SNR can further be improved by using the Nuclear Overhauser Effect and proton decoupling, although this has not been exploited yet for in vivo ^{19}F MRI [56].

7.4. Data reconstruction and post-processing

Many ^{19}F compounds such as linear PFC molecules have more than one resonance frequency due to chemical shift or coupling to other ^{19}F or ^1H atoms in the same molecule. Conventionally, for MRI only the signal of one of the peaks is used by frequency-selective RF pulses for excitation of the desired peak, by saturation of undesired peaks [57] or by choosing an echo time at which J-modulation annihilates signal from undesired peaks [58]. This leads to either decrease of SNR since not all ^{19}F signal can be exploited or to chemical shift artifacts if more than one peak contributes to the signal. Chemical shift imaging records for each voxel a whole NMR spectrum and thus avoids the artifact but it presents an SNR-inefficient alternative. Early studies have shown that deconvolution techniques can potentially remove these artifacts and improve SNR although finding a post-processing method which is robust against noise is challenging [59].

A problem in the in vivo situation, especially when imaging the abdomen, is the presence of motion over the long ^{19}F MR imaging times, which leads to blurring, motion artifacts, and decreased SNR. Respiratory gating is an SNR-inefficient solution due to the dead time during parts of the respiratory cycle. In a study using a setup for simultaneous $^1H/^{19}F$ MRI, the motion could be measured on low resolution ^1H images reconstructed for different time points during ^{19}F MRI acquisition and this information could be used to retrospectively correct the acquired data [39].

Recently, for the first time the potential of compressed sensing has been investigated for ^{19}F MRI and applied to speed up in vivo ^{19}F MRI of PFC accumulation in a brain lesion in the mouse [60]. Under defined conditions, compressed sensing allows reconstruction of MR images from undersampled data, i.e. within shorter acquisition times. It has had an immense impact on anatomical and functional ^1H MRI, e.g. MR angiography. Despite significant reduction of imaging times at comparable image quality, the authors remained skeptical of the profit for ^{19}F MRI in situations of low SNR. Sufficient signal is one of the prerequisites for a successful reconstruction. Thus, it is questionable if cell tracking with ^{19}F MRI can profit from compressed sensing.

7.5. Cell quantification

The signal in a voxel of a ^{19}F MR image is proportional to the amount of ^{19}F therein. This linear relation can then be used to quantify signal on in vivo images by an in vitro calibration curve acquired in a separate experiment [61] or by placing a reference tube with defined ^{19}F concentration in the field of view [62]. If the ^{19}F content per cell is known, signal in ^{19}F MR images can be used to calculate cell number (reviewed in [2]). A small coil that is inductively coupled to the signal-receiving RF coil can be used to "inject" an artificial reference signal alternatively to using a reference tube [63]. Before quantification, ^{19}F image data should be pre-processed to account for non-linear noise at low signal intensities either by an analytical correction scheme [64] or by simulated calibration curves [62]. Unfortunately, accurate cell quantification becomes challenging for low SNR due to partial volume effects which cannot easily be corrected for. For example, if the number of cells within a voxel is just below the detection limit this information will under certain circumstances be completely lost. We estimated the resulting variability in ^{19}F signal to be up to ~30% by measuring the signal in ^{19}F MR images of a phantom containing a small pellet of ^{19}F labeled neural stem cells after stepwise displacement of the imaging slices in a 2D pulse sequence. However, localized ^{19}F MRS in the whole volume of interest could be used to overcome partial volume effects at the cost of spatial resolution [65].

The extensive use of surface coils for quantification of ^{19}F concentration is problematic. For superficial tissue these coils are superior in sensitivity over larger volume coils and they are relatively easy to design. However, due to the inhomogeneous magnetic field profile (B_1 profile) the ^{19}F MR image intensity depends not only on ^{19}F concentration but also on the distance from the coil. The bias could be corrected by spatially mapping the B_1 on the ^{19}F channel, although this is very time-consuming at low ^{19}F concentrations and hence not applicable in vivo. We have recently presented a workflow to correct in vivo ^{19}F MR images of neural stem cell grafts acquired with a ^{1}H/^{19}F surface coil by mapping the B_1 on the ^{1}H channel, which allowed to spatially resolve cell densities in vivo [66]. The strategy is easily implemented if a coil is used with identical B_1 profile for ^{1}H and ^{19}F and if sufficient ^{1}H background signal is provided in regions of the cell implant. Fast B_1 mapping methods developed in the context of parallel imaging could further improve quantitative in vivo ^{19}F MRI with double-tuned surface coils [67].

8. Future of cellular ^{19}F MRI: molecular and multimodal imaging strategies

One of the main advantages of ^{19}F MRI is the lack of endogenous ^{19}F. On the other hand, the signal on ^{19}F MR images needs to be generated by an exogenously delivered ^{19}F agent and is only an indirect marker of the cells. A single ^{19}F MRI experiment of ex vivo labeled cells using a non-targeted ^{19}F marker provides cell anatomical location and possibly density but information on cell function such as gene expression or viability is missing. However, these parameters are crucial for a successful action of cells delivered for a therapeutic purpose. If the agent is contained within cells over longer times, changes in signal location over time can be linked to migratory capacity, which is an indicator of viability at least for the migrating fraction of cells. Furthermore, when using PFC nanoemulsions intracellular pO_2 can be exploited as another marker of cell function in vivo [68].

To make ^{19}F MRI more specific to a certain cell population, molecular process, or micro-environment two major strategies exist in the literature 1) the functionalization of ^{19}F agents with surface molecules to promote cell/molecule specific accumulation of ^{19}F and 2) the generation of "smart" ^{19}F agents or "reporter molecules" that change chemical properties upon interaction with a molecular target.

Functionalizing PFC emulsions with an antibody against the integrin $\alpha v\beta 3$ has been used to specifically enhance uptake by endothelial cells [69] and to detect angiogenesis [70]. Other molecular targets included VCAM-1 [71] and fibrin [72] for detection and quantification by ^{19}F MRS. Importantly, these nanoparticles can be loaded with drugs, which allows simultaneous monitoring and mediation of therapy (reviewed in [73]). Binding of the agent to a surface molecule is, however, limited, i.e. accumulation ^{19}F above detection limits for in vivo MRI is challenging, although improved MRI acquisition allowed the true in vivo detection of targeted agents in preliminary studies [74,75]. A wide range of ^{19}F reporter molecules, so-called "smart" or responsive agents, have been developed for ^{19}F MRS including markers of gene activity, hypoxia, pH, metal ions, temperature, diffusion and more (reviewed in [76]). In vivo proof-of-concepts were shown for ^{19}F MRS detection of lacZ gene expression in transgenic tumor cells [77,78]. However, many of these compounds are not easily taken up by cells and detailed toxicity and biocompatibility profiles are unknown. Moreover, lack of sensitivity has hampered the use of responsive agents for in vivo ^{19}F MRI but this may soon be feasible with improvements in MRI hardware and acquisition.

An alternative strategy to assess cell function in vivo is the combination of ^{19}F MRI with other modalities that can be more sensitive, such as ^{1}H MRI, X-ray imaging, fluorescence imaging (FLI), bioluminescence imaging (BLI) or positron emission tomography (PET). ^{19}F agents containing Gd^{3+}, fluorophores, emulsified PFC core, or bromide have been synthesized for in vivo multimodal detection with ^{1}H MRI, optical imaging, ultrasound or CT respectively. Multimodal nanoparticles are useful to confirm ^{19}F MRI results and to visualize the ^{19}F agent for immunohistochemistry, although the in vivo information from other imaging modalities again provides only indirect measures of cell function. In a different approach, we have recently shown efficient ^{19}F labeling of neural stem cells transduced with luciferase for BLI detection ([79], Fig. 2). Since the transgene is only expressed in vital cells and the light reaction is ATP-dependent, the BLI signal is a marker of cell viability. Bimodal in vivo detection of the transgenic, ^{19}F labeled cells with ^{19}F MRI and BLI was possible after implantation in the mouse brain, which allowed noninvasive assessment of cell graft location, density, and viability under normal conditions and after stroke.

Interestingly, and perhaps distressingly, we found that the ^{19}F signal persisted even after the BLI signal was lost at 28 days, indicating that the ^{19}F data was of either dead cells or of label that was no longer within the relevant cells. This is a key issue that must be resolved before ^{19}F MRI can mature as an in vivo cell tracking technique. Some attempts in this direction have been made, for example through the addition of a fluorescent dye for histology at late time points to localize the ^{19}F agent precisely [80]. This is especially necessary for cell tracking studies that stretch over longer periods of time - one of the unique advantages of ^{19}F MRI.

9. Conclusion

It has been just over 5 years since the introduction of ^{19}F MRI for in vivo cell tracking [81]. The explosion in label developments and advances in MRI technology have allowed ^{19}F MRI to become established in this short time. Although sensitivity remains a key hurdle, probes such as reporter molecules and other responsive probes are very promising. As a final point, it is necessary to keep in mind that comprehensive validation is crucial both in vitro (for example, cell functionality, fluorescence microscopy) and in vivo (post-mortem histology and multimodal imaging).

Acknowledgments

The authors would like to thank the participants of an ENCITE-internal workshop on “In vivo ^{19}F MRI” held in Cologne, Germany 2011 for fruitful discussions. We are grateful to the authors of the publications listed in the legend of Fig. 2 for permission to adapt their figures. This work was financially supported by the European Union EU-FP7 ENCITE (HEALTH-F5-2008-201842) grant. MS is supported by Netherlands Organization for Scientific Research (NWO) VENI 700.10.409, and JdV by NWO-Vidi 917.76.363 and Netherlands Institute for Regenerative Medicine (NIRM) FES0908.

References

[1] Srinivas M, Aarntzen EH, Bulte JW, Oyen WJ, Heerschap A, de Vries IJ, et al. Imaging of cellular therapies. Adv Drug Deliv Rev 2010;62(11):1080–93.

[2] Srinivas M, Heerschap A, Ahrens ET, Figdor CG, de Vries IJ. ^{19}F MRI for quantitative in vivo cell tracking. Trends Biotechnol 2010;28(7):363–70.

[3] Batrakova EV, Kabanov AV. Pluronic block copolymers: evolution of drug delivery concept from inert nanocarriers to biological response modifiers. J Control Release 2008;130(2):98–106.

[4] Srinivas M, Cruz LJ, Bonetto F, Heerschap A, Figdor CG, de Vries IJ. Customizable, multi-functional fluorocarbon nanoparticles for quantitative in vivo imaging using 19F MRI and optical imaging. Biomaterials 2010;31(27):7070–7.

[5] Du W, Xu Z, Nystrom AM, Zhang K, Leonard JR, Wooley KL. 19F- and fluorescently labeled micelles as nanoscopic assemblies for chemotherapeutic delivery. Bioconjug Chem 2008;19(12):2492–8.

[6] Maillard E, Juszczak MT, Langlois A, Kleiss C, Sencier M, Bietiger W, et al. Perfluorocarbon emulsions prevent hypoxia of pancreatic beta cells. Cell Transplant, in press.

[7] Mizukami S, Takikawa R, Sugihara F, Hori Y, Tochio H, Walchli M, et al. Paramagnetic relaxation-based 19f MRI probe to detect protease activity. J Am Chem Soc 2008;130(3):794–5.

[8] Yu J, Ma Z, Li Y, Koeneman KS, Liu L, Mason RP. Synthesis and evaluation of a novel gene reporter molecule: detection of beta-galactosidase activity using 19F NMR of a fluorinated vitamin B6 conjugate+. Med Chem 2005;1(3):255–62.

[9] Takaoka Y, Sakamoto T, Tsukiji S, Narazaki M, Matsuda T, Tochio H, et al. Self-assembling nanoprobes that display off/on 19F nuclear magnetic resonance signals for protein detection and imaging. Nat Chem 2009;1(7):557–61.

[10] Godin B, Tasciotti E, Liu X, Serda RE, Ferrari M. Multistage nanovectors: from concept to novel imaging contrast agents and therapeutics. Acc Chem Res 2011;44(10):979–89.

[11] Bulte JW, Douglas T, Witwer B, Zhang SC, Strable E, Lewis BK, et al. Magnetodendrimers allow endosomal magnetic labeling and in vivo tracking of stem cells. Nat Biotechnol 2001;19(12):1141–7.

[12] Liu Y, Zhang N. Gadolinium loaded nanoparticles in theranostic magnetic resonance imaging. Biomaterials 2012;33(21):5363–75.

[13] Temme S, Bonner F, Schrader J, Flogel U. 19F magnetic resonance imaging of endogenous macrophages in inflammation. Wiley Interdiscip Rev Nanomed Nanobiotechnol 2012;4(3):329–43.

[14] Stoll G, Basse-Lüsebrink T, Weise G, Jakob P. Visualization of inflammation using (19) F-magnetic resonance imaging and perfluorocarbons. Wiley Interdiscip Rev Nanomed Nanobiotechnol 2012;4(4):438–47.

[15] Bible E, Dell'acqua F, Solanky B, Balducci A, Crapo PM, Badylak SF, et al. Non-invasive imaging of transplanted human neural stem cells and ECM scaffold remodeling in the stroke-damaged rat brain by (19)F- and diffusion-MRI. Biomaterials 2012;33(10):2858–71.

[16] Boehm-Sturm P, Mengler L, Wecker S, Hoehn M, Kallur T. In vivo tracking of human neural stem cells with 19F magnetic resonance imaging. PLoS One 2011;6(12):e29040.

[17] Ruiz-Cabello J, Walczak P, Kedziorek DA, Chacko VP, Schmieder AH, Wickline SA, et al. In vivo “hot spot” MR imaging of neural stem cells using fluorinated nanoparticles. Magn Reson Med 2008;60(6):1506–11.

[18] Kim T, Momin E, Choi J, Yuan K, Zaidi H, Kim J, et al. Mesoporous silica-coated hollow manganese oxide nanoparticles as positive T1 contrast agents for labeling and MRI tracking of adipose-derived mesenchymal stem cells. J Am Chem Soc 2011;133(9):2955–61.

[19] Cromer Berman SM, Walczak P, Bulte JW. Tracking stem cells using magnetic nanoparticles. Wiley Interdiscip Rev Nanomed Nanobiotechnol 2011;3(4):343–55.

[20] Liu L, Ye Q, Wu Y, Hsieh WY, Chen CL, Shen HH, et al. Tracking T-cells in vivo with a new nano-sized MRI contrast agent. Nanomedicine, in press.

[21] Waiczies H, Lepore S, Janitzek N, Hagen U, Seifert F, Ittermann B, et al. Perfluorocarbon particle size influences magnetic resonance signal and immunological properties of dendritic cells. PLoS One 2011;6(7):e21981.

[22] Thorek DL, Tsourkas A. Size, charge and concentration dependent uptake of iron oxide particles by non-phagocytic cells. Biomaterials 2008;29(26):3583–90.

[23] Cromer Berman SM, Kshitiz, Wang CJ, Orukari I, Levchenko A, Bulte JW, et al. Cell motility of neural stem cells is reduced after SPIO-labeling, which is mitigated after exocytosis. Magn Reson Med, in press.

[24] Bonetto F, Srinivas M, Heerschap A, Mailliard R, Ahrens ET, Figdor CG, et al. A novel (19)F agent for detection and quantification of human dendritic cells using magnetic resonance imaging. Int J Cancer 2011;129(2):365–73.

[25] Jain AK, Das M, Swarnakar NK, Jain S. Engineered PLGA nanoparticles: an emerging delivery tool in cancer therapeutics. Crit Rev Ther Drug Carrier Syst 2011;28(1):1–45.

[26] Luo R, Neu B, Venkatraman SS. Surface functionalization of nanoparticles to control cell interactions and drug release. Small 2012;8(16):2585–94.

[27] Huang DM, Hsiao JK, Chen YC, Chien LY, Yao M, Chen YK, et al. The promotion of human mesenchymal stem cell proliferation by superparamagnetic iron oxide nanoparticles. Biomaterials 2009;30(22):3645–51.

[28] Mant A, Chinnery F, Elliott T, Williams AP. The pathway of cross-presentation is influenced by the particle size of phagocytosed antigen. Immunology 2012;136(2):163–75.

[29] Noveck RJ, Shannon EJ, Leese PT, Shorr JS, Flaim KE, Keipert PE, et al. Randomized safety studies of intravenous perflubron emulsion. II. Effects on immune function in healthy volunteers. Anesth Analg 2000;91(4):812–22.

[30] Castro O, Nesbitt AE, Lyles D. Effect of a perfluorocarbon emulsion (Fluosol-DA) on reticuloendothelial system clearance function. Am J Hematol 1984;16(1):15–21.

[31] Lutz J. Studies on RES function in rats and mice after different doses of fluosol. Prog Clin Biol Res 1983;122:197–208.

[32] Lutz J, Barthel U, Metzenauer P. Variation in toxicity of Escherichia coli endotoxin after treatment with perfluorated blood substitutes in mice. Circ Shock 1982;9(2):99–106.

[33] Lane TA, Lamkin GE. Paralysis of phagocyte migration due to an artificial blood substitute. Blood 1984;64(2):400–5.

[34] Lane TA, Lamkin GE. Increased infection mortality and decreased neutrophil migration due to a component of an artificial blood substitute. Blood 1986;68(2):351–4.

[35] Lutz J, Kettemann M, Racz I, Noth U. Several methods utilized for the assessment of biocompatibility of perfluorochemicals. Artif Cells Blood Substit Immobil Biotechnol 1995;23(3):407–15.

[36] Flaim SF. Pharmacokinetics and side effects of perfluorocarbon-based blood substitutes. Artif Cells Blood Substit Immobil Biotechnol 1994;22(4):1043–54.

[37] Hitchens TK, Ye Q, Eytan DF, Janjic JM, Ahrens ET, Ho C. 19F MRI detection of acute allograft rejection with in vivo perfluorocarbon labeling of immune cells. Magn Reson Med 2011;65(4):1144–53.

[38] Diou O, Tsapis N, Giraudeau C, Valette J, Gueutin C, Bourasset F, et al. Long-circulating perfluorooctyl bromide nanocapsules for tumor imaging by (19) FMRI. Biomaterials 2012;33(22):5593–602.

[39] Keupp J, Rahmer J, Grasslin I, Mazurkewitz PC, Schaeffter T, Lanza GM, et al. Simultaneous dual-nuclei imaging for motion corrected detection and quantification of 19F imaging agents. Magn Reson Med 2011;66(4):1116–22.

[40] Hahn T, Kozerke S, Schwizer W, Fried M, Boesiger P, Steingoetter A. Visualization and quantification of intestinal transit and motor function by real-time tracking of 19F labeled capsules in humans. Magn Reson Med 2011;66(3):812–20.

[41] Schwarz R, Kaspar A, Seelig J, Kunnecke B. Gastrointestinal transit times in mice and humans measured with 27Al and 19F nuclear magnetic resonance. Magn Reson Med 2002;48(2):255–61.

[42] Schreiber WG, Markstaller K, Weiler N, Eberle B, Laukemper-Ostendorf S, Scholz A, et al. 19F-MRT of pulmonary ventilation in the breath-hold technic using SF6 gas. Rofo 2000;172(6):500–3.

[43] Wolf W, Presant CA, Waluch V. 19F-MRS studies of fluorinated drugs in humans. Adv Drug Deliv Rev 2000;41(1):55–74.

[44] Wolf W, Albright MJ, Silver MS, Weber H, Reichardt U, Sauer R. Fluorine-19 NMR spectroscopic studies of the metabolism of 5-fluorouracil in the liver of patients undergoing chemotherapy. Magn Reson Imaging 1987;5(3):165–9.

[45] van Laarhoven HW, Klomp DW, Rijpkema M, Kamm YL, Wagener DJ, Barentsz JO, et al. Prediction of chemotherapeutic response of colorectal liver metastases with dynamic gadolinium-DTPA-enhanced MRI and localized 19F MRS pharmacokinetic studies of 5-fluorouracil. NMR Biomed 2007;20(2):128–40.

[46] Ruiz-Cabello J, Barnett BP, Bottomley PA, Bulte JW. Fluorine (19F) MRS and MRI in biomedicine. NMR Biomed 2011;24(2):114–29.

[47] Maki J, Masuda C, Morikawa S, Morita M, Inubushi T, Matsusue Y, et al. The MR tracking of transplanted ATDC5 cells using fluorinated poly L-lysine-CF3. Biomaterials 2007;28(3):434–40.

[48] Masuda C, Maki Z, Morikawa S, Morita M, Inubushi T, Matsusue Y, et al. MR tracking of transplanted glial cells using poly-L-lysine-CF3. Neurosci Res 2006;56(2):224–8.

[49] Neubauer AM, Myerson J, Caruthers SD, Hockett FD, Winter PM, Chen J, et al. Gadolinium-modulated 19F signals from perfluorocarbon nanoparticles as a new strategy for molecular imaging. Magn Reson Med 2008;60(5):1066–72.

[50] Chalmers KH, Botta M, Parker D. Strategies to enhance signal intensity with paramagnetic fluorine-labelled lanthanide complexes as probes for 19F magnetic resonance. Dalton Trans 2011;40(4):904–13.

[51] Bommerich U, Trantzschel T, Mulla-Osman S, Buntkowsky G, Bargon J, Bernarding J. Hyperpolarized 19F-MRI: parahydrogen-induced polarization and field variation enable 19F-MRI at low spin density. Phys Chem Chem Phys 2010;12(35):10309–12.

[52] Barnett BP, Ruiz-Cabello J, Hota P, Liddell R, Walczak P, Howland V, et al. Fluorocapsules for improved function, immunoprotection, and visualization of cellular therapeutics with MR, US, and CT imaging. Radiology 2011; 258(1):182–91.

[53] Doty FD, Entzminger G, Kulkarni J, Pamarthy K, Staab JP. Radio frequency coil technology for small-animal MRI. NMR Biomed 2007;20(3):304–25.

[54] Waters EA, Chen J, Yang X, Zhang H, Neumann R, Santeford A, et al. Detection of targeted perfluorocarbon nanoparticle binding using 19F diffusion weighted MR spectroscopy. Magn Reson Med 2008;60(5):1232–6.

[55] Schmid F, Holtke C, Parker D, Faber C. Boosting. (19)F MRI-SNR efficient detection of paramagnetic contrast agents using ultrafast sequences. Magn Reson Med, in press.

[56] Krems B, Bachert P, Zabel HJ, Lorenz WJ. F-19-(H-1) nuclear Overhauser effect and proton decoupling of 5-fluorouracil and alpha-fluoro-beta-alanine. J Magn Reson B 1995;108(2):155–64.

[57] Noth U, Jager LJ, Lutz J, Haase A. Fast 19F-NMR imaging in vivo using FLASH-MRI. Magn Reson Imaging 1994;12(1):149–53.

[58] Mason RP, Bansal N, Babcock EE, Nunnally RL, Antich PP. A novel editing technique for 19F MRI: molecule-specific imaging. Magn Reson Imaging 1990;8(6):729–36.

[59] Busse LJ, Pratt RG, Thomas SR. Deconvolution of chemical shift spectra in two- or three-dimensional [19F] MR Imaging. J Comput Assist Tomogr 1988; 12(5):824–35.

[60] Kampf T, Fischer a, Basse-Lüsebrink TC, Ladewig G, Breuer F, Stoll G, et al. Application of compressed sensing to in vivo 3D -19F CSI. J Magn Reson 2010;207(2):262–73.

[61] Flogel U, Ding Z, Hardung H, Jander S, Reichmann G, Jacoby C, et al. In vivo monitoring of inflammation after cardiac and cerebral ischemia by fluorine magnetic resonance imaging. Circulation 2008;118(2):140–8.

[62] Srinivas M, Morel PA, Ernst LA, Laidlaw DH, Ahrens ET. Fluorine-19 MRI for visualization and quantification of cell migration in a diabetes model. Magn Reson Med 2007;58(4):725–34.

[63] Lee D, Marro K, Shankland E, Mathis M. Quantitative 19F imaging using inductively coupled reference signal injection. Magn Reson Med 2010;63(3):570–3.

[64] Koay CG, Basser PJ. Analytically exact correction scheme for signal extraction from noisy magnitude MR signals. J Magn Reson 2006;179(2):317–22.

[65] Waiczies H, Lepore S, Millward JM, Purfürst B, Niendorf T, Waiczies S. 19F/1H MRI of brain inflammation in experimental autoimmune encephalomyelitis. International Society for Magnetic Resonance in Medicine, 20th Annual Meeting and Exhibition; Melbourne, Australia; 2012.

[66] Boehm-Sturm P, Pracht ED, Aswendt M, Henn N, Hoehn M. B1 correction for quantitative in vivo 19F magnetic resonance imaging with surface coils. International Society for Magnetic Resonance in Medicine, 20th Annual Meeting and Exhibition; Melbourne, Australia; 2012.

[67] Basse-Lüsebrink TC, Sturm VJF, Vilter A, Kampf T, Behr VC, Jakob PM. Fast, Indirect assessment of the 19F B1 profile by 1H Bloch-Siegert B1 mapping using double-resonant 1H/19F Coils. International Society for Magnetic Resonance in Medicine, 20th Annual Meeting and Exhibition; Melbourne, Australia; 2012.

[68] Kadayakkara DK, Janjic JM, Pusateri LK, Young WB, Ahrens ET. In vivo observation of intracellular oximetry in perfluorocarbon-labeled glioma cells and chemotherapeutic response in the CNS using fluorine-19 MRI. Magn Reson Med 2010;64(5):1252–9.

[69] Kok MB, de Vries A, Abdurrachim D, Prompers JJ, Grull H, Nicolay K, et al. Quantitative (1)H MRI, (19)F MRI, and (19)F MRS of cell-internalized perfluorocarbon paramagnetic nanoparticles. Contrast Media Mol Imaging 2011;6(1):19–27.

[70] Waters EA, Chen JJ, Allen JS, Zhang HY, Lanza GM, Wickline SA. Detection and quantification of angiogenesis in experimental valve disease with integrin-targeted nanoparticles and 19-fluorine MRI/MRS. J Cardiovasc Magn Reson 2008;10(1):43.

[71] Southworth R, Kaneda M, Chen J, Zhang L, Zhang H, Yang X, et al. Renal vascular inflammation induced by Western diet in ApoE-null mice quantified by 19F NMR of VCAM-1 targeted nanobeacons. Nanomedicine 2009;5(3): 359–67.

[72] Morawski AM, Winter PM, Yu X, Fuhrhop RW, Scott MJ, Hockett F, et al. Quantitative "magnetic resonance immunohistochemistry" with ligand-targeted (19)F nanoparticles. Magn Reson Med 2004;52(6):1255–62.

[73] Kaneda MM, Caruthers S, Lanza GM, Wickline SA. Perfluorocarbon nanoemulsions for quantitative molecular imaging and targeted therapeutics. Ann Biomed Eng 2009;37(10):1922–33.

[74] Keupp J, Schmieder AH, Williams TA, Allen JS, Wickline SA, Lanza GM, et al. Ultra-short echo time 19F/1H Imaging of gadolinium-free perfluoro-carbon nanoparticles: A robust method for in vivo angiogenesis imaging. International Society for Magnetic Resonance in Medicine, 19th Annual Meeting and Exhibition; Montreal, Canada; 2011.

[75] Goette MJ, Schmieder AH, Williams TA, Allen JS, Keupp J, Lanza G, et al. In vivo quantitative imaging of angiogenesis- targeted PFOB nanoparticles in a hypercholesterol rabbit model using 19 F-MRI with ultra-short echo time balanced SSFP. Proceedings of the Society for Cardiovascular Magnetic Resonance, 15th Annual Meeting; Nice, France 2012;14(Suppl. 1):1–2.

[76] Yu JX, Kodibagkar VD, Cui W, Mason RP. 19F: a versatile reporter for non-invasive physiology and pharmacology using magnetic resonance. Curr Med Chem 2005;12(7):819–48.

[77] Yu J-X, Kodibagkar VD, Hallac RR, Liu L, Mason RP. Dual 19F/1H MR gene reporter molecules for in vivo detection of beta-galactosidase. Bioconjug Chem 2012;23(3):596–603.

[78] Yu JX, Kodibagkar VD, Liu L, Mason RP. A 19F-NMR approach using reporter molecule pairs to assess beta-galactosidase in human xenograft tumors in vivo. NMR Biomed 2008;21(7):704–12.

[79] Boehm-Sturm P, Aswendt M, Breucker L, Henn N, Mengler L, Adamczak J, et al. Imaging structure and function of stem cell grafts in the mouse brain by combining 19F magnetic resonance imaging with bioluminescence imaging. International Society for Magnetic Resonance in Medicine, 20th Annual Meeting and Exhibition; Melbourne, Australia; 2012.

[80] Srinivas M, Turner MS, Janjic JM, Morel PA, Laidlaw DH, Ahrens ET. In vivo cytometry of antigen-specific t cells using (19)F MRI. Magn Reson Med 2009; 62(3):747–53.

[81] Ahrens ET, Flores R, Xu H, Morel PA. In vivo imaging platform for tracking immunotherapeutic cells. Nat Biotechnol 2005;23(8):983–7.

[82] Partlow KC, Chen J, Brant JA, Neubauer AM, Meyerrose TE, Creer MH, et al. 19F magnetic resonance imaging for stem/progenitor cell tracking with multiple unique perfluorocarbon nanobeacons. FASEB J 2007;21(8):1647–54.

[83] Janjic JM, Srinivas M, Kadayakkara DK, Ahrens ET. Self-delivering nanoemulsions for dual fluorine-19 MRI and fluorescence detection. J Am Chem Soc 2008;130(9):2832–41.

[84] Morel PA, Srinivas M, Turner MS, Fuschiotti P, Munshi R, Bahar I, et al. Gene expression analysis of dendritic cells that prevent diabetes in NOD mice: analysis of chemokines and costimulatory molecules. J Leukoc Biol 2011; 90(3):539–50.

[85] Malaisse WJ, Zhang Y, Louchami K, Sharma S, Dresselaers T, Himmelreich U, et al. (19)F-heptuloses as tools for the non-invasive imaging of GLUT2-expressing cells. Arch Biochem Biophys 2012;517(2):138–43.

[86] Lim YT, Cho MY, Kang JH, Noh YW, Cho JH, Hong KS, et al. Perfluorodecalin/[InGaP/ZnS quantum dots] nanoemulsions as 19F MR/optical imaging nanoprobes for the labeling of phagocytic and nonphagocytic immune cells. Biomaterials 2010;31(18):4964–71.

[87] Lanza GM, Yu X, Winter PM, Abendschein DR, Karukstis KK, Scott MJ, et al. Targeted antiproliferative drug delivery to vascular smooth muscle cells with a magnetic resonance imaging nanoparticle contrast agent: implications for rational therapy of restenosis. Circulation 2002;106(22):2842–7.

[88] Zhou ZX, Zhang BG, Zhang H, Huang XZ, Hu YL, Sun L, et al. Drug packaging and delivery using perfluorocarbon nanoparticles for targeted inhibition of vascular smooth muscle cells. Acta Pharmacol Sin 2009;30(11):1577–84.

[89] Gorelikov I, Martin AL, Seo M, Matsuura N. Silica-coated quantum dots for optical evaluation of perfluorocarbon droplet interactions with cells. Langmuir 2011;27(24):15024–33.

[90] Barnett BP, Ruiz-Cabello J, Hota P, Ouwerkerk R, Shamblott MJ, Lauzon C, et al. Use of perfluorocarbon nanoparticles for non-invasive multimodal cell tracking of human pancreatic islets. Contrast Media Mol Imaging 2011;6(4):251–9.

[91] Lim YT, Noh YW, Cho JH, Han JH, Choi BS, Kwon J, et al. Multiplexed imaging of therapeutic cells with multispectrally encoded magnetofluorescent nanocomposite emulsions. J Am Chem Soc 2009;131(47):17145–54.

[92] Bartusik D, Tomanek B. Detection of fluorine labeled herceptin using cellular (19)F MRI ex vivo. J Pharm Biomed Anal 2010;51(4):894–900.

[93] Bartusik D, Tomanek B. Application of 19F magnetic resonance to study the efficacy of fluorine labeled drugs in the three-dimensional cultured breast cancer cells. Arch Biochem Biophys 2010;493(2):234–41.

[94] Ahrens ET, Young WB, Xu H, Pusateri LK. Rapid quantification of inflammation in tissue samples using perfluorocarbon emulsion and fluorine-19 nuclear magnetic resonance. Biotechniques 2011;50(4):229–34.

[95] Ebner B, Behm P, Jacoby C, Burghoff S, French BA, Schrader J, et al. Early assessment of pulmonary inflammation by 19F MRI in vivo. Circ Cardiovasc Imaging 2010;3(2):202–10.

[96] Noth U, Morrissey SP, Deichmann R, Jung S, Adolf H, Haase A, et al. Perfluoro-15-crown-5-ether labelled macrophages in adoptive transfer experimental allergic encephalomyelitis. Artif Cells Blood Substit Immobil Biotechnol 1997;25(3):243–54.

[97] Ikomi F, Hanna G, Schmid-Schonbein GW. Intracellular and extracellular transport of perfluoro carbon emulsion from subcutaneous tissue to regional lymphatics. Artif Cells Blood Substit Immobil Biotechnol 1994;22(4):1441–7.

[98] Kadayakkara DK, Ranganathan S, Young WB, Ahrens ET. Assaying macrophage activity in a murine model of inflammatory bowel disease using fluorine-19 MRI. Lab Invest 2012;92(4):636–45.

[99] Bartusik D, Tomanek B, Lattova E, Perreault H, Tuszynski J, Fallone G. The efficacy of new colchicine derivatives and viability of the T-Lymphoblastoid cells in three-dimensional culture using 19F MRI and HPLC-UV ex vivo. Bioorg Chem 2009;37(6):193–201.

[100] Lee CP, Payne GS, Oregioni A, Ruddle R, Tan S, Raynaud FI, et al. A phase I study of the nitroimidazole hypoxia marker SR4554 using 19F magnetic resonance spectroscopy. Br J Cancer 2009;101(11):1860–8.

[101] Seddon BM, Payne GS, Simmons L, Ruddle R, Grimshaw R, Tan S, et al. A phase I study of SR-4554 via intravenous administration for noninvasive

investigation of tumor hypoxia by magnetic resonance spectroscopy in patients with malignancy. Clin Cancer Res 2003;9(14):5101–12.
[102] Procissi D, Claus F, Burgman P, Koziorowski J, Chapman JD, Thakur SB, et al. In vivo 19F magnetic resonance spectroscopy and chemical shift imaging of tri-fluoro-nitroimidazole as a potential hypoxia reporter in solid tumors. Clin Cancer Res 2007;13(12):3738–47.
[103] Cui W, Otten P, Li Y, Koeneman KS, Yu J, Mason RP. Novel NMR approach to assessing gene transfection: 4-fluoro-2-nitrophenyl-beta-D-galactopyranoside as a prototype reporter molecule for beta-galactosidase. Magn Reson Med 2004;51(3):616–20.
[104] Dingman S, Snyder-Leiby T, Mack DJ, Thomas R, Guo C. Enzymatic assay for perfluoro-tagged metabolites of l-DOPA using crude lysate from *E. coli* transformed with pKKAADCII. Appl Microbiol Biotechnol 2004;64(4):556–9.
[105] Hamstra DA, Lee KC, Tychewicz JM, Schepkin VD, Moffat BA, Chen M, et al. The use of 19F spectroscopy and diffusion-weighted MRI to evaluate differences in gene-dependent enzyme prodrug therapies. Mol Ther 2004; 10(5):916–28.
[106] Kodibagkar VD, Yu J, Liu L, Hetherington HP, Mason RP. Imaging beta-galactosidase activity using 19F chemical shift imaging of lacZ gene-reporter molecule 2-fluoro-4-nitrophenol-beta-D-galactopyranoside. Magn Reson Imaging 2006;24(7):959–62.
[107] Yu J, Mason RP. Synthesis and characterization of novel lacZ gene reporter molecules: detection of beta-galactosidase activity by 19F nuclear magnetic resonance of polyglycosylated fluorinated vitamin B6. J Med Chem 2006; 49(6):1991–9.
[108] Liu L, Kodibagkar VD, Yu JX, Mason RP. 19F-NMR detection of lacZ gene expression via the enzymic hydrolysis of 2-fluoro-4-nitrophenyl beta-D-galactopyranoside in vivo in PC3 prostate tumor xenografts in the mouse. FASEB J 2007;21(9):2014–9.
[109] Matsushita H, Mizukami S, Mori Y, Sugihara F, Shirakawa M, Yoshioka Y, et al. (19) F MRI monitoring of gene expression in living cells through cell-surface beta-lactamase activity. Chembiochem 2012;13(11):1579–83.
[110] Mancini L, Davies L, Friedlos F, Falck-Miniotis M, Dzik-Jurasz AS, Springer CJ, et al. A novel technique to monitor carboxypeptidase G2 expression in suicide gene therapy using 19F magnetic resonance spectroscopy. NMR Biomed 2009;22(5):561–6.
[111] Presant CA, Jacobson J, Wolf W, Waluch V, Weitz IC, Macdonald JS. Does leucovorin alter the intratumoral pharmacokinetics of 5-fluorouracil (5-FU)? A Southwest Oncology Group study. Invest New Drugs 2002;20(4):369–76.
[112] Bonetto F, Srinivas M, Weigelin B, Cruz LJ, Heerschap A, Friedl P, et al. A large-scale (19) F MRI-based cell migration assay to optimize cell therapy. NMR Biomed 2012;25(9):1095–103.

3 Discussion and outlook

The topics of papers underlying this dissertation can be categorized in two relatively self-contained major topics, MRI of angiogenesis and MRI of stem cell implantations. Therefore, these topics will first be discussed individually. Implications for biology and regenerative medicine and perspectives for methodological improvements will be discussed including presentation of data not contained in the papers of this dissertation. Finally, there is significant overlap in these topics and suggestions will be made on noninvasive imaging of stem cell interaction with the vasculature.

3.1 MRI of angiogenesis

3.1.1 Biological aspects

Temporal profile of vascular changes in tumors

As the temporal continuity of information is an exclusive advantage of noninvasive imaging, one of the main goals of this dissertation was to identify relevant time frames during which vascular changes occur in tumor and after stroke.

In the subcutaneous lung tumor model, microvessel density peaked at around 8 days post implantation of the tumor cells but increased vessel densities at the tumor rim could be found as early as one day post implantation (paper I). An effect of anti-angiogenic treatment was observed within the first week after PTK787 injections. For the glioblastoma model, the relevant time frame for important vascular changes seems to be longer (paper II). Small signs of angiogenesis could first be detected 3 weeks post implantation of tumor cells via an increase in blood volume in small vessels but extensively increased blood volume was only observed at 6 weeks post implantation although – in contrast to paper I - mainly in large vessels. The differences are certainly due to genetic differences of tumor types but may also be due to the differences in microenvironment (skin vs. brain) since it is known that host cells, e.g. fibroblasts, play a major role in tumoral angiogenesis [81].

Anti-angiogenic treatment of tumors

Interestingly, it seems to be a common feature of both models (paper I+II) that anti-angiogenic treatment efficiently decreases the number of small vessels and induces a shift towards large vessels. These findings are in agreement with other studies on squamous cell carcinoma [82], renal cell carcinoma [83], and melanoma [84]. However, the formation of abnormally large vessels is distressing for the widely propagated concept of vascular normalization under anti-angiogenic therapy [85]. This concept states, that inhibition of pro-angiogenic molecules in angiogenic tumors leads to a normalization of tumor vasculature towards less leaky and less dilated vessels. This is beneficial for patients undergoing chemotherapy and radiotherapy in parallel to anti-angiogenic treatment due to better delivery of drugs through functional vasculature. In the light of our findings and those of other groups [82–84], it must be considered, however, that there is no general concept that can describe the response to anti-angiogenic therapy for all tumor types.

Temporal profile of vascular changes after stroke

There is much debate on the extent of stroke-induced angiogenesis and relevant time frames. Focusing on the subacute period up to 4 weeks after the infarct, we found very few signs of early angiogenesis (endothelial cell proliferation) but no signs of late-stage angiogenesis as would be reflected in increased vessel density (paper III). A decrease in blood volume in small vessels was most pronounced 1 week after stroke and there seemed to be very little change from 2-4 weeks in all SSCE MRI derived parameters. This indicates that most changes in vascular architecture are to be expected during the first two weeks after stroke in agreement with an earlier study [86]. Importance of early time frames is supported by reports on strong hyperperfusion of ischemic tissue [86] and even of the contralateral cortex [87] within the first week after stroke, which correlated with higher microvessel densities. This was interpreted as a result of angiogenesis. A few studies, however, showed changes in vasculature and signs of angiogenesis up to 30 days [87] or even 3 months [88] after focal cerebral ischemia.

In summary, results from different groups are very variable, which possibly can be attributed to differences in stroke models and lesion type. Indeed, whether or not cyst formation and immune cell infiltration were present was shown to be correlated with increases in microvessel densities in rats [87]. The variability raises the important question to what extent results from rodent stroke models can be translated to the human situation. Initial MRI results of clinical studies confirm increased vessel diameters and decreased vessel densities in stroke patients [89], [90] in agreement with our study (paper III) as well as others' using the filament model of transient middle cerebral artery occlusion [91], [92]. Noninvasive imaging of vessel size and density in the clinic requires, however, improvements in MRI methodology. These will be discussed in the next section.

3.1.2 Methodological aspects

SSCE MRI in humans

For SSCE MRI in animals, usually very high concentrations of contrast agent are used. This is due to two reasons. First, the effect on the signal is small compared to noise especially for the spin echo experiment. As the change in relaxation rate scales with $\Delta R_2 \sim c^{2/3}$, increasing concentration is efficient to increase effect-to-noise ratio. Second, the analytical description of the signal holds only for the static dephasing regime (see next section). The system is in this regime when the average distance from the vessel for which spins are completely dephased is much larger than the average diffusion length $l_D / \rho << 1$ [24]. ρ can be interpreted as an effective vessel radius. This distance scales with $\rho \sim c^{1/2}$ for the gradient echo and $\rho \sim c^{1/3}$ for the spin echo. Thus an increase of concentration pushes the spin system into the static dephasing regime. For lower concentrations, vessel size would be over-estimated [93].

However, the typical doses used in animal experiments (30 mg Fe/kg) are around 100 times higher than approved for human use. Kiselev et al. have therefore proposed a different experimental strategy for vessel size imaging in patients [30]. A bolus of the clinically approved paramagnetic contrast agent Gd-DTPA is injected intravenously. Once the agent has spread homogeneously over the blood pool, the paramagnetic effect is too small to perform vessel size imaging for the reasons above. However, the first pass of the bolus through the vessel system is highly concentrated. A special echo planar imaging (EPI) pulse sequence is used to quickly acquire both gradient echo and spin echo MR images during the bolus. Fitting of the dynamic data can then be used to calculate vessel size or density in the healthy brain [94] or under pathological conditions [30], [89], [90]. Although the quality of EPI images is much lower compared to human data such fast imaging approaches could be very helpful for vessel size imaging in small animals in future studies. Obviously, faster imaging times reduce anesthesia time thus stress for the animal. Dynamic data allows absolute quantification of blood volume fraction, i.e. of vessel size and density, without the need to withdraw blood samples. Furthermore, uptake of contrast agent by host cells is small during the fast image acquisition. This uptake, e.g. by cells in liver and spleen (see next section) leads to decreasing concentration of contrast agent in the blood and accumulation of contrast agent in these organs. For long acquisition times, this is a problem since it may violate the assumption that the agent is in a steady state over the MR experiment.

Limitations of vessel size imaging using the cylinder model

Despite its success and wide application, mainly in brain research of tumor and stroke, it should be remembered that the cylinder model is based on very distinct assumptions that may be justified in normal brain tissue but are violated under pathological conditions or for other parts of the body. One of the main restrictions is for example a low blood volume fraction. To tackle these problems, I made two research visits during my doctoral thesis at the “MRI of angiogenesis” group of Prof. Michal Neeman at the Weizmann Institute of Science (Rehovot, Israel). The goal of these visits was to develop a model for the MR signal in tissues with non-cylindrical vessels and high blood volumes. Main foci of the Weizmann group are vascular changes during fetal development, pregnancy, and in tumor.

All assumptions underlying vessel size imaging, the rationale behind them, and justification in different tissues are summarized in Table 1. Six different tissue types are discussed: brain, skeletal muscle, spleen, liver, placenta, ischemic brain, and tumor.

assumption	rationale	justification
infintely long cylinders, i.e. average branching length>>vessel radius	magnetic field can be analytically calculated	brain (+); muscle (++); liver/spleen (-); placenta (--); stroke brain (+); tumor (0)
number of vessels per voxel>>1; size of substructures within voxel (e.g. vessels)<<voxel size; random distribution of vessels	statistical averaging possible	brain (+); muscle (+); liver/spleen (+); placenta (+); stroke brain (+); tumor (0)
blood volume<<1	theory interaction-free, i.e. spins in extravascular compartment on average experience only field of one cylinder	brain (++); muscle (+); liver/spleen (-); placenta (--); stroke brain (++); tumor (0)
contrast agent intravascular (no leakage)	otherwise vessel geometry ≠ geometric distribution of contrast agent	brain (++); muscle (++); liver/spleen (-); placenta (++); stroke brain (+); tumor (-)
contrast agent concentration constant over the experiment	steady-state condition	depends on duration of the MR experiment; relevant tissue features are leakage and uptake by organ cells; brain (++); muscle (+); liver/spleen (--); placenta (n/a); stroke brain (+); tumor (0)
vessel walls impermeable for water molecules	two compartment model, avoid exchange terms	brain (+); muscle (+); liver/spleen (+); placenta (+); stroke brain (+); tumor (-)
distance around vessel for which spins are effectively dephased>>diffusion length	justifies analytical description in static dephasing regime	depends on good adjustment of MRI parameters (mainly echo time); relevant tissue parameters are average vessel diameter and water diffusivity; brain (+); muscle (+); liver/kidney (0); placenta (0); stroke brain (+); tumor (0)
isotropic, free diffusion	diffusion effect can be analytically calculated	brain (0); muscle (+); liver/spleen (++); placenta (++); stroke brain (0); tumor (++)

Table 1: Assumptions underlying the cylinder model of the vasculature, their rationale and justification in different tissues. Categories range from very well justified (++) to highly violated (--). Note that for stroke and especially for tumor tissue, categories may very much depend on exact type and progression of the disease.

Brain vasculature mainly consists of small capillaries and the blood brain barrier is impermeable for most contrast agent particles. Water diffusion in brain tissue is not isotropic [95], especially in white matter, but most other requirements are met. Skeletal muscle vasculature, e.g. back muscle, mainly consists of small, parallel capillaries. Liver and spleen vessels have non-cylindrical, sinusoidal vessels and generally much higher blood volume fraction than brain and muscle [96], [97]. Contrast agent particles accumulate in cells of these organs (Kupffer cells in the liver and monocytes in the spleen) since they act as blood filters [97], [98]. The main part of the placenta consists of the sponge-like labyrinth, with cup-shaped pools of blood [99]. Direct leakage of contrast agent injected in the maternal blood pool is impossible for healthy placenta due to the placental barrier. Crossing of contrast agent particles from maternal to fetal blood pool may only be possible through cellular uptake, which - to my knowledge - has not been characterized yet. Fig. 8 shows fluorescence microscopy images of histological sections from back muscle, liver, and placenta of pregnant mice to illustrate the differences in vascular geometry of different tissues. Tissue was excised after i.v.

injection of the fluorescent dye FITC-Dextran. The agent was used to visualize perfused vessels for histology. The data was acquired in experiments at the Weizmann Institute of Science. For comparison, images of brain vasculature can be found in figures of paper II and III.

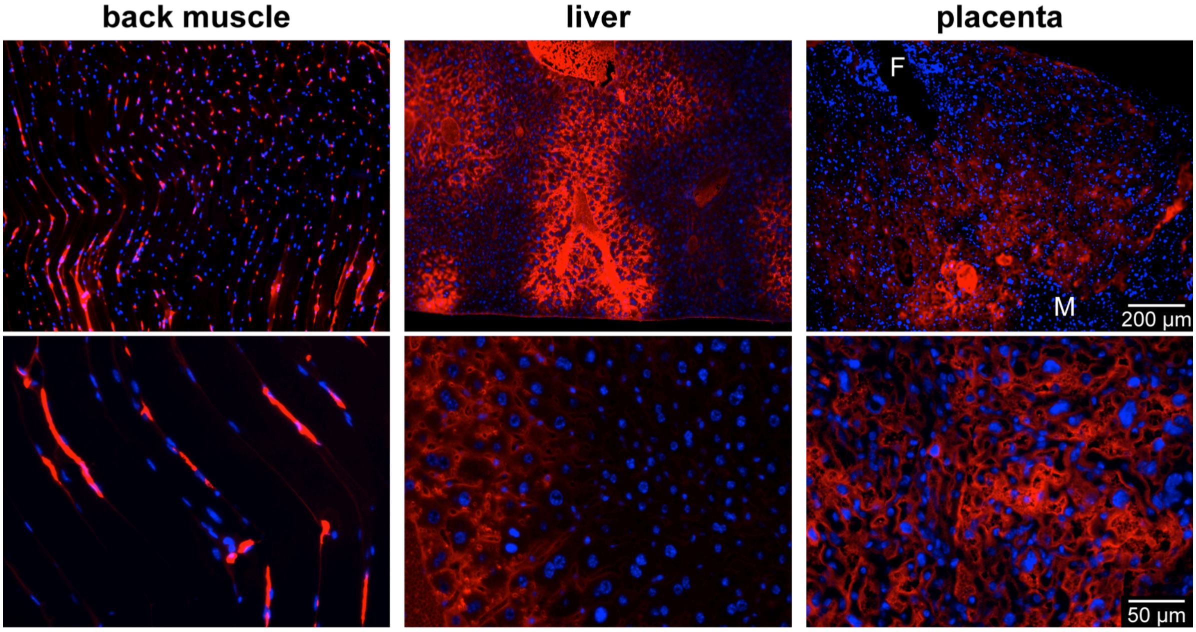

Figure 8: Fluorescence microscopy to illustrate differences in vascular structure of back muscle, liver, and placenta. Top panels show 10x magnified, lower panels 40x magnified images of tissue excised ~10 min after i.v. injection of FITC-Dextran (red) into a living pregnant mouse (embryonic day 17.5). Cell nuclei are stained with Hoechst (blue). Muscle vessels are homogeneous, long, and cylindrically shaped and occupy a low fraction of tissue volume. Liver vasculature is more heterogeneous and characterized by much higher blood volume fraction and presence of non-cylindrical vessels. The labyrinth of the placenta consists of a network of non-cylindrical, sinusoidal spaces occupying very high blood volume fraction. Note that FITC-Dextran cannot cross the placental barrier, thus only the maternal vessels are stained red and very little staining is seen at the far end towards the fetus (marked with F) compared to the maternal side (M).

Brain vasculature does not change significantly (with respect to the cylinder model restrictions) after stroke except for blood-brain barrier opening during the first hours/days and permeability during early angiogenesis [15], [100]. Tumors, however, can have very large, leaky, non-cylindrically shaped vessels depending on tumor type and progression [81].

Perspective: vessel size imaging beyond the cylinder model

Improved models of the vasculature would be of great benefit for many fields in MRI, for which the contrast or signal of interest originates from blood. Examples are MRI of perfusion, flow, functional MRI, or any MRI method that uses intravascular tracers. Today, powerful MRI simulators exist and can be combined with tissue models to predict MRI signal in magnetically heterogeneous tissue for any given MRI pulse sequence. Such strategy was recently shown for quantification of the BOLD effect in functional MRI with spin echo sequences [101], [102]. However, vasculature in these studies was also modeled as infinitely long cylinders. A conceptionally different approach is the use of fractal geometry. Instead of using traditional, simple geometric objects, e.g. spheres or cylinders of certain diameter and length, the vascular tree is assumed to consist of self-similar, irregular objects of many different sizes. This can be used to find better parameters, e.g. fractal dimension, to describe the irregular tumor vasculature [103] and to better describe MRI signal from flowing water in porous media

[104]. In the following, preliminary data of a more experimental approach will be presented, which we developed at the Weizmann Institute of Science.

To model sponge-like vasculature in vitro, e.g. the labyrinth of the murine placenta, tubes filled with the cross-linked dextran gel Sephadex (Sigma-Aldrich, Hamburg, Germany) and agarose gel were doped with different concentrations of SPIO particles (Endorem). Iron concentrations were chosen equidistantly from 0-1 mM Fe, which corresponds to 0-55.8 mg/kg. R_1, R_2, and R_2^* relaxation rates of these tubes were measured at a 9.4 T MRI vertical bore scanner (Bruker BioSpin, Ettlingen, Germany). When the Sephadex powder beads are saturated with water, they form spheres. The pore size of the beads is well below the diameter of SPIO particles (<<200 nm) thus contrast agent particles are restricted to the space between beads. The tube therefore consists of two compartments. The beads represent the extravascular compartment (no contrast agent) and the spaces between the beads represent the intravascular compartment (doped with contrast agent). Different Sephadex bead sizes are commercially available: coarse (100-300 µm), medium (50-150 µm), fine (20-80 µm), and superfine (20-50 µm). These can be used to probe MRI relaxation rate dependency on bead or "vessel" size. Water-saturated beads were packed as densely as possible. Then the volume between the beads (the "blood volume fraction") is 26% of total volume. This number is well-known from dense sphere packing. More agarose was added to end up with a 50% volume of inter-bead space in order to model tissue with very high blood volume. A Sephadex tube is schematically illustrated in Fig. 9 next to light microscopy images of the water-saturated beads of different sizes.

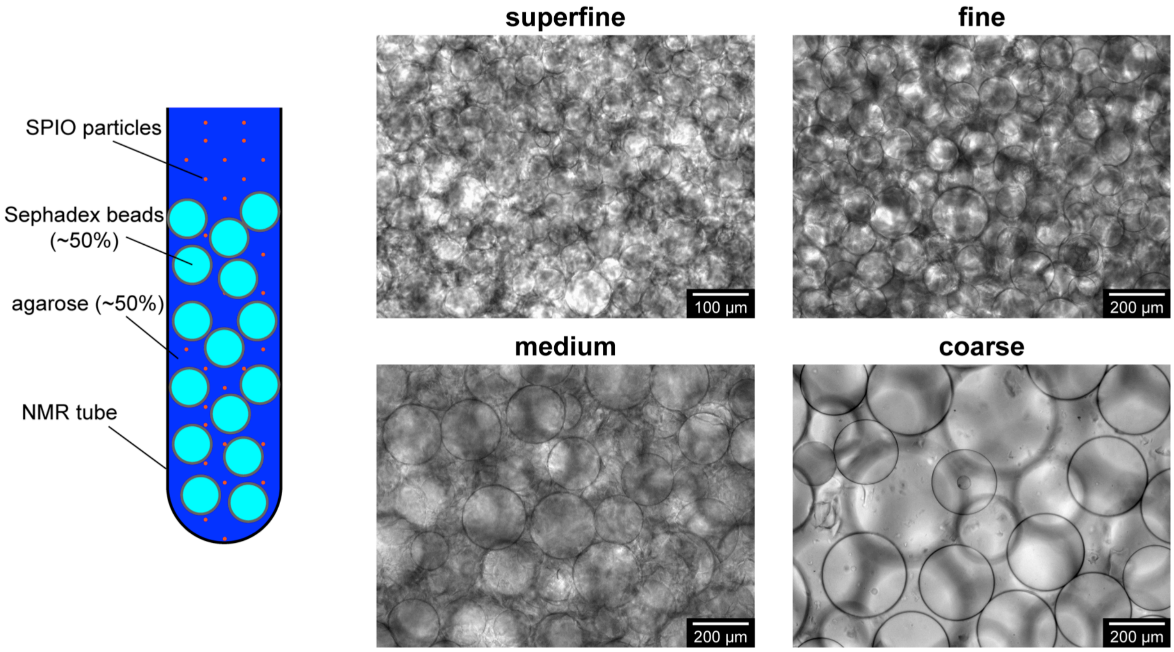

Figure 9: Schematic illustration of the Sephadex model of sponge-like vasculature (left) and microscopy images of hydrated Sephadex beads of different sizes (right). Sephadex beads represent the extravascular compartment, the space in between beads represents the intravascular compartment and can be doped with MR contrast agents. Image of superfine Sephadex shown in 20x magnification, all others 10x.

For the cylinder model, the most intriguing finding is a vessel size dependency of ΔR_2 on average vessel radius R due to the diffusion effect in the extravascular compartment. This leads to a non-trivial relation $\Delta R_2 \sim c^{2/3} R^{-2/3}$ compared to the expected trivial proportionality to iron oxide concentration seen for $\Delta R_2^* \sim c$. Thus it was interesting whether or not a non-trivial relation between ΔR_2, iron concentration, and bead size would be found in the Sephadex model. Fig. 10 shows R_1, R_2, and R_2^* over iron concentration (note that differences ΔR_1, ΔR_2, and ΔR_2^* would be obtained by subtracting the 0 mM value). Indeed, a very strong dependency of R_2 on bead size was found and an increase less than linear with concentration. Interestingly, R_1 was also significantly different for different bead sizes. In contrast, R_2^* grew approximately linearly with concentration. As expected, all relaxation rates grew linearly with concentration in control tubes containing only the SPIO-doped agarose without Sephadex beads. Thus it was truly the microstructure, i.e. the compartmentalization, which induced the deviation from a linear relation. These data indicate that vessel size imaging could also be feasible in tissue with sponge-like vasculature and very high blood volume.

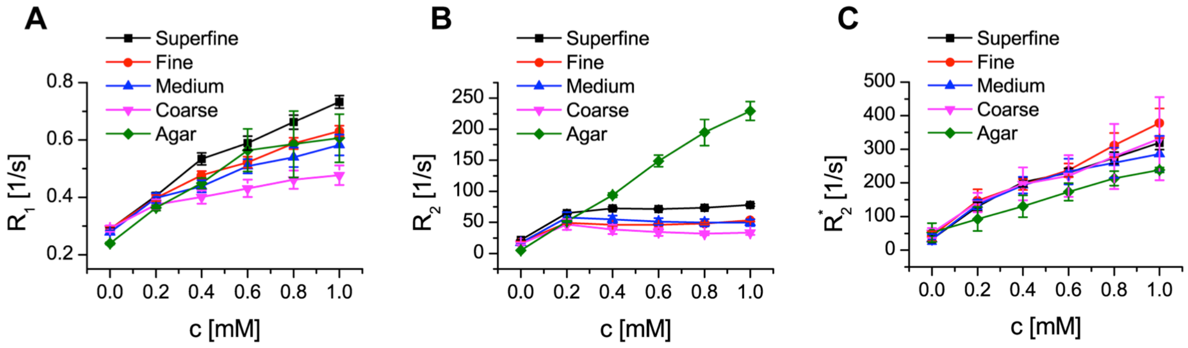

Figure 10: Relaxation rates R_1 (A), R_2 (B), and R_2^* (C) in Sephadex phantoms. Tubes were doped with varying amounts of SPIOs, concentrations are given in iron molarities. Different bead sizes were used and agarose without Sephadex served as a control. R_2 curves strongly deviate from trivial linear increase seen for media without microstructure, e.g. the agarose. For both R_1 and R_2 differences were found for the various bead sizes. Highest relaxation rate was found for the smallest beads and lowest relaxation rate for coarse beads. This indicates that distinguishing different vessel radii in sponge-like vasculature may be possible in analogy to the cylinder model-based vessel size imaging.

To test whether or not the Sephadex model reflects the in vivo situation, pregnant mice (ICR strain, n=7, n=63 placentas, embryonic day 17.5) were scanned with MRI at a 9.4 T (Bruker BioSpin). SPIO particles were injected i.v. in 3 accumulating doses (1.5 mg/kg Fe each, i.e. up to 4.5 mg/kg). R_2 and R_2^* were recorded before and after injection (Fig. 11). The curves seem to resemble the in vitro situation but these trends are not statistically significant due to high variability in the data. High blood volume of placenta and liver lead to very high relaxation rates thus signal decays extremely fast. Accuracy of R_2 / R_2^* measurements is therefore low using conventional spin echo and gradient echo pulse sequences, which can be seen by the large error bars. Furthermore, since SPIOs accumulate fast in cells of the liver, data from there is not reliably acquired in a steady-state. Future studies need to validate the in vitro findings with computer simulations or new analytical models. Furthermore, animal studies with improved MRI methodology, e.g. ultra-short or steady state pulse sequences, are proposed to sample the fast decay of signal in placenta and liver. This will help to further explore if the in vitro findings really reflect the in vivo situation or if they are only artificial.

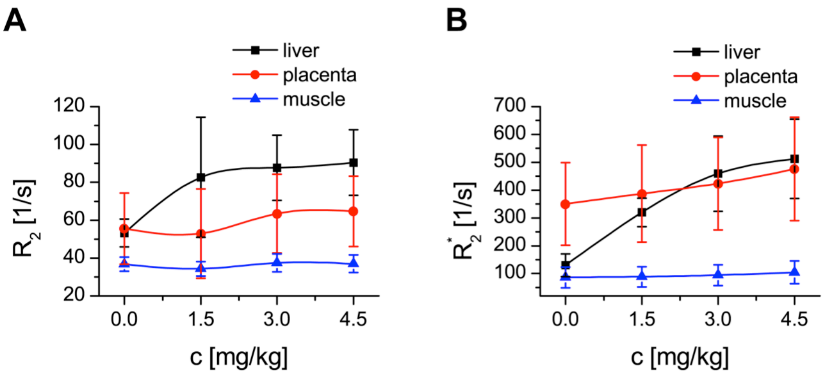

Figure 11: Relaxation rates R_2 *(A) and* R_2^* *(B) in liver, placenta, and muscle of pregnant mice after i.v. injection of SPIO particles. Concentrations are given in mg iron per kg body weight.* R_2 *in liver and placenta seems to increase less than linearly whereas* R_2^* *increases linearly. However, signal decays so fast in these tissues that measurements are challenging, which leads to the large error bars. For muscle, blood volume and iron oxide doses are too low to see a strong effect.*

3.2 MRI of stem cell implantations

3.2.1 Biological aspects

Although treatment of neurological diseases with stem cells has proven beneficial in many animal studies there is a wide variety of parameters that need to be optimized before stem cells can be used in patients. Certainly, optimal parameters depend on the individual pathology, e.g. lesion type, and the patient's biological and even psychological status. Nevertheless, detailed standard protocols need to be defined to ensure safety and maximum benefit for the patient. The most important parameters are the source of stem cells, stem cell fate, route of delivery, dose, timing and site of transplantation, immune suppression to prevent graft rejection, and ethical considerations. In the following, the results of this dissertation will be discussed with respect to these parameters focusing on stroke.

The source of stem cells for therapy is a critical factor for successful action of these cells in vivo and raises ethical questions. To prevent host immune response, cells originating from the same species as the host are tolerated best, i.e. for human use cells of human origin are most promising [37]. For large-scale use, expansion of cells in culture should be possible since the use of primary cells from large numbers of human embryos or fetuses is ethically unacceptable. Under these premises, the human NSCs used in this dissertation are a suitable source for therapy since they can be expanded in neurosphere culture for long times. IPS cells, derived for example from a patient's skin cell, would be an optimal source since they promise unlimited access to stem cells, ethical issues would be practically solved and problems with immune rejection would be minimized, but the field is still young.

A homogeneous cell population in terms of differentiation status is of utmost importance. Pluripotent embryonic stem cells need to be sufficiently pre-differentiated towards the neuronal type before implantation as too immature cells can proliferate in an uncontrolled manner and form a tumor [105], [106]. To ensure homogeneity, cells either need to be selected, e.g. by differences in expression of surface markers, through co-culturing with cells that release factors, or through addition of factors to culture medium that drive the heterogeneous population of cells into a more similar state [107].

The human NSCs used for this dissertation ceased to proliferate shortly after implantation in all studies and did not form tumors. However, they likely consist of a heterogeneous population of both neural stem cells and less potent neural progenitor cells using strict definitions of these terms [46]. Cells can alternatively be genetically modified to express markers that force the population in a defined state. For example, to yield more cells of neuronal phenotype, the human NSCs of this dissertation can be modified to overexpress the factor Pax6 [43].

For stroke, there is much debate on the optimal dose, timing, and site of implantation and no general answer exists. In perspective of clinical practice, early intervention would only help those who come to the hospital quick enough and would thus exclude a large patient population. However, it has been hypothesized that implantation within the first days would maximize beneficial effect for host tissue at risk through release of trophic factors by the grafted cells [46], [108]. Subacute implantation (>1 week) is most likely optimal to stimulate endogenous repair mechanisms such as neurogenesis and angiogenesis, whereas optimal cell survival was hypothesized for later times when the initial immune response to the stroke has declined [108]. However, a recent study showed better survival due to less stroke-induced immune response for early implantation at 48 h compared to 6 weeks [45]. For this reason, in follow-up studies of this dissertation, NSCs were implanted 48 h after stroke surgery (see last paragraph of section 3.2.2).

Studies that showed stem cell-mediated recovery after stroke used intracerebral, intravascular, or intraventricular route of delivery and each route has its distinct advantages (reviewed in [60], [108]). The highest delivery of cells to the brain is given by intracerebral implantation and this route was therefore chosen for the present studies. However, large intracerebral implants can damage healthy tissue, and lacking supply of oxygen and nutrients to implanted cells can severely lower graft survival. Indeed, we saw a rim of glial (GFAP positive) cells aligning the graft (Fig. 4 of paper V), which is a sign for glial scar in response to the implantation procedure. Darsalia et al. speculated about existence of a maximum threshold, beyond which higher implanted cell number would not lead to higher number of surviving cells [45]. Such threshold is, for rodents, probably in the hundred thousands range.

For intracerebral implantation after stroke, the most optimal implantation site is probably intact tissue adjacent to the lesion in order to avoid the hostile environment of the lesion core whilst assuring maximum infiltration of damaged tissue by the cells [46]. For follow-up studies in ischemic mice we therefore implanted cells in this region (see last paragraph of section 3.2.2). Cells can also be implanted directly into the lesion cavity in the chronic stage of stroke. However, since the cavity is filled with fluid, structural support of the cells needs to be provided. This can be achieved by embedding them in extracellular matrix proteins and implanting a mixture of cells and such scaffold proteins [52], [109], [110]. This is an appealing strategy as intact tissue is minimally affected, much higher number of cells can be implanted, and the scaffold can be doped with drugs, e.g. VEGF to facilitate growth of supporting vasculature for the graft [52].

3.2.2 Methodological aspects

Cell quantification

Accurate cell quantification in vivo with MRI would facilitate finding optimal parameters as discussed in the previous section, especially to find optimal dosage. Invasive studies face two major problems. First, the exact number of cells is usually derived from cell countings of the suspension before implantation. However, cells can be lost when transferred from one tube to another, they can get stuck in the syringe used for implantation, or cells can be pushed back through the injection canal. When animals are sacrificed days or weeks later and much less cells are found, it is unknown whether they were lost before implantation due to imperfect preparation/surgery or after implantation due to some biological process of interest. Quantitative MRI would allow controlling the number of cells that truly reached their target in the brain directly after surgery. Second, cells are packed very closely in intracerebral grafts. From our experience, counting the cells on histological sections is labor-intensive, can become very inaccurate on dense cell spots, and requires very good, sensitive cell markers for histology and excellent microscopy image quality. Thus, noninvasive cell quantification could, less labor-intensively, yield more accurate results.

For SPIO labels, our semi-quantification of gradient echo images provided graft volume (paper IV), however, absolute cell number could not be assessed due to complete signal dropout in regions of the graft. Since iron oxide labels are widely used, several improvements in MRI acquisition and data post-processing have been proposed for more specific and quantifiable contrast generated by labeled cells. In order to quantify relaxation rate R_2^* in densely packed cell grafts, ultrashort echo time sequences can be used [111]. Cell number is yielded assuming a linear proportionality of R_2^* and cell density. In another study, a theoretical model was derived and confirmed in vitro. Cell quantification was possible using balanced steady-state free precession pulse sequences but validation in vivo was missing [112]. The utility of R_2^* for cell quantification is questionable due to large macroscopic magnetic inhomogeneities, which lead to very heterogeneous background R_2^*. Strong inhomogeneities are present for example around tissue to air interfaces [113]. Therefore, other groups have used spin-echo derived R_2 for quantification [114]. However, for the reasons stated in the introduction (section 1.4.2), the signal also depends on cell distribution and graft shape in a complex manner and it is questionable to assume a linear relation between cell density and relaxation rate. This is particularly true for R_2. To enhance specificity of cell contrast, the shift in Larmor frequency around iron oxide particles can be visualized by suppressing the basic frequency of water signal, which leads to bright spots on MR images in regions of iron oxides. This is referred to as “positive contrast” MRI of cells [113], [115]. To summarize the literature, cell quantification seems possible in vitro but the mechanisms of contrast generation using magnetic labels limits the usefulness for in vivo quantification.

To date, ^{19}F MRI of fluorine labeled cells is the only modality that promises cell localization and quantification in deep tissues over long times. Detailed experimental workflows to quantify transplanted cells in vivo have been reviewed elsewhere [73] and in paper VI of this dissertation. Furthermore, we think that we have solved one of the pending problems of quantitative in vivo ^{19}F MRI. For sensitive detection of ^{19}F MR signal, small surface coils are extensively used. In contrast to a (less sensitive) volume coil with homogeneous magnetic field profile, the intensity on a ^{19}F image from a surface coil depends on the distance of labeled cells from the coil. For example, if cells migrated to deeper regions in the brain further away from the coil, this would lead to a loss of signal, which could be misinterpreted as a decrease in cell number. For this reason, the detection limits of 1,000 cells/voxel in vitro and 10,000 cells/voxel in vivo reported in paper V give only a rough order-of-magnitude. We therefore further improved our cell quantification strategies. In the following, I will present our experimental workflow to correct image data for the coil profile by mapping the RF pulse flip angle on ^{1}H images [116].

The magnitude of magnetic field produced by the coil is proportional to the flip angle $B_1(\vec{r}) \sim FA(\vec{r})$. A ^{1}H flip angle map is acquired using the double flip angle method [117]. We usually use a turbo spin echo sequence with centric encoding and repetition time TR>>T$_1$. Detailed MRI parameters can be found in [116]. For these pulse sequences the spin echo signal can be calculated [118]. As a result of imperfect RF excitation (Tx), the image intensity is attenuated by a factor

$$att_{Tx}(\vec{r}) = \sin^3\left(FA(\vec{r})\right) \tag{5}$$

Due to Faraday's principle of reciprocity, image intensity is additionally attenuated during signal reception (Rx) by a factor proportional to the B_1 thus FA:

$$att_{Rx}(\vec{r}) = {FA(\vec{r})}\Big/{90°} \tag{6}$$

Note that both factors are normalized so that in case of perfect 90° flip angle, the overall attenuation $att_{19F} = att_{Tx} \cdot att_{Rx} = 1$. Consequently the ^{19}F signal at $\vec{r}$ depends not only on ^{19}F concentration but also on the flip angle

$$S_{19F}(\vec{r}) = A \cdot c_{19F}(\vec{r}) \cdot att_{19F}(\vec{r}), \quad A = const. \tag{7}$$

i.e. division of the ^{19}F image by att_{19F} yields a B_1 corrected image with signal intensities $S_{19F,corr}(\vec{r})$, which only depend on ^{19}F concentrations. The concentration of ^{19}F in cells m ($[m] = mol/cell$) can be experimentally determined by ^{19}F MR spectroscopy (Fig. 1 of paper V). A is circumvented by normalizing the image intensity to a reference tube with known ^{19}F concentration $c_{19F,ref}$, which is placed in the field of view together with the animal. Finally, the number of cells in the voxel at $\vec{r}$ is determined via

$$n(\vec{r}) = S_{19F,corr}(\vec{r}) \cdot \frac{c_{19F,ref}}{S_{19F,corr,ref} \cdot m} \tag{8}$$

This workflow was implemented in custom scripts written in Matlab (The Mathworks, Natick, MA, USA) and validated in vitro on a dilution series of perfluoropolyether (PFPE) emulsion (Fig. 12). Furthermore, the scheme was applied in vivo in order to absolutely quantitate NSC densities after intracerebral implantation (Fig. 13).

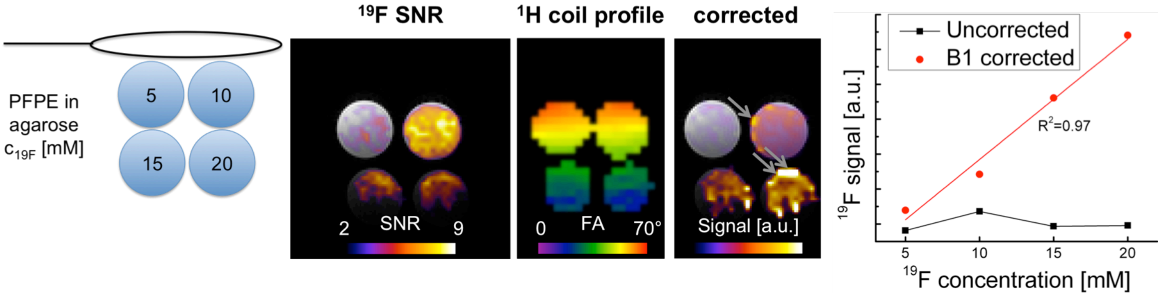

Figure 12: Validation of B_1 correction scheme in vitro at very low ^{19}F signal-to-noise ratio (SNR). Tubes with different concentrations of perfluoropolyether emulsion in agarose were imaged with ^{19}F MRI. The ^{19}F SNR map (color) overlaid on a ^1H image (grayscale) was corrected for B_1 inhomogeneities by mapping the coil profile on the ^1H and by using equations (5) and (6). The corrected ^{19}F image has some artifacts at the edges of tubes due to partial volume effects (gray arrows). After removal of artifacts by taking a trimmed mean (mean neglecting 25% of highest and lowest values) a linear relation of ^{19}F concentration and signal was shown (red line). ^{19}F signal was not proportional to concentration before correction due to attenuation for tubes further away from the coil (black curve).

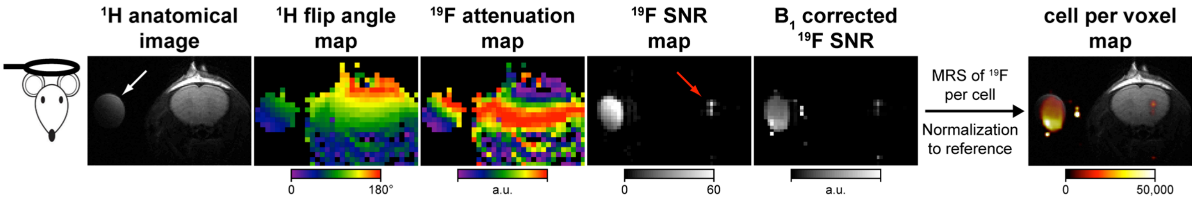

Figure 13: Quantitative in vivo ^{19}F MRI with surface coils. After implantation of ^{19}F labeled cells, a mouse is imaged with anatomical ^1H MRI together with a reference tube containing 200 mM ^{19}F in agarose (white arrow). The surface coil is placed at the top of the head. A ^1H flip angle map is acquired and a ^{19}F attenuation map can be calculated, in this case for a turbo spin echo pulse sequence. The uncorrected ^{19}F SNR map shows signal from the reference and the cell graft (red arrow). ^{19}F SNR divided by the attenuation map yields the B1 corrected ^{19}F image. MR spectroscopy of ^{19}F per cell and normalization of the ^{19}F image intensity to the mean in the reference tube allow calculation of a quantitative cell density map. The cell density map is color-coded and overlaid on the anatomical image to localize and quantify cells in vivo. Note the artifacts at edges of the reference tube after B1 correction (bright spots). These need to be removed in analogy to the procedure outlined in Fig. 12.

Limitations of external MRI labels

External MRI labels, e.g. SPIO particles for cell detection with ^1H MRI or PFC emulsions for detection with ^{19}F MRI, can have a negative effect on cell function, e.g. viability, differentiation or migratory capacity. This is particularly true for NSCs since these cells are very sensitive to their microenvironment. Despite the extensive use of SPIO particles for over a decade, these “side effects” are only now being investigated in detail. Recent studies showed reduced viability and motility of stem cells after SPIO labeling and these reports suggest an optimization of intracellular SPIO dose to minimize these effects [119], [120]. Usually, stem cell function is assessed through standard in vitro tests, e.g. trypan blue exclusion assay to assess viability or scratch assay to test for migratory capacity. These and similar tests were used for studies of this dissertation and we found minimal effects on cell function for both SPIO labels (paper IV) and PFC labels (paper V). However, the tests are generally carried out on cells in 2 dimensional cultures, e.g. adherent cultures, which do not reflect the 3D environment the cells face in vivo. Development of novel 3D cell cultures that better simulate the in vivo situation is therefore of importance [121], [122].

On the other hand, external labels can have adverse effect on the host. From studies using PFC emulsions as blood substitutes, it is known that PFCs are well tolerated by the human body (paper VI). In rare cases, superparamagnetic iron oxides can cause cardiovascular adverse events and back pain, which is known from studies using large i.v. injections for liver imaging [123]. However, most negative effects are dose-dependent and the amount of contrast agent/^{19}F agent is low when used for cell tracking. Still, biocompatibility, degradation and clearance of free particles by host cells are important issues for rightful interpretation of imaging data. When an implanted cell dies, the label will be released and still be detectable by MRI. Directly after cell death, the signal will likely be indistinguishable from signal of live cells. It is important to know whether or not the released agent will be removed by the host and on what time scale these clearance processes occur. Much is known about clearance of nanoparticles from the blood system (paper VI, [124]). However, few studies have investigated clearance after intracerebral implantation. SPIO particles in the interstitial space of the brain are taken up by host phagocytes and subsequently removed through the reticuloendothelial system. The time scale depends on particle size and surface coating [125]. For example, complete clearance of free USPIOs from the brain after infusion in the striatum was shown to occur over approximately 2 weeks [126]. For PFC emulsions no reports exist for clearance after intracerebral implantation. We therefore injected a PFPE emulsion (CS-green, Celsense, Pittsburgh, USA) stereotactically in the striatum of healthy mice (n=3, NuNu strain). Animals were sacrificed for histology at 24 h, one week, and four weeks. Additionally, we performed ^{19}F MRI 24 h and weekly after injection. In the animal that survived longest, ~50% of the initial ^{19}F signal was still detectable by ^{19}F MRI four weeks after implantation (Fig. 14). Histology would clarify whether the remaining agent is free in the interstitial space or taken up by host cells but this is still work in progress. However, the persistence of ^{19}F signal already indicates that free PFCs can reside for long times in the brain and that removal of ^{19}F agent is very slow. Thus false positive ^{19}F MRI signal is expected should PFPE labeled cells die after implantation.

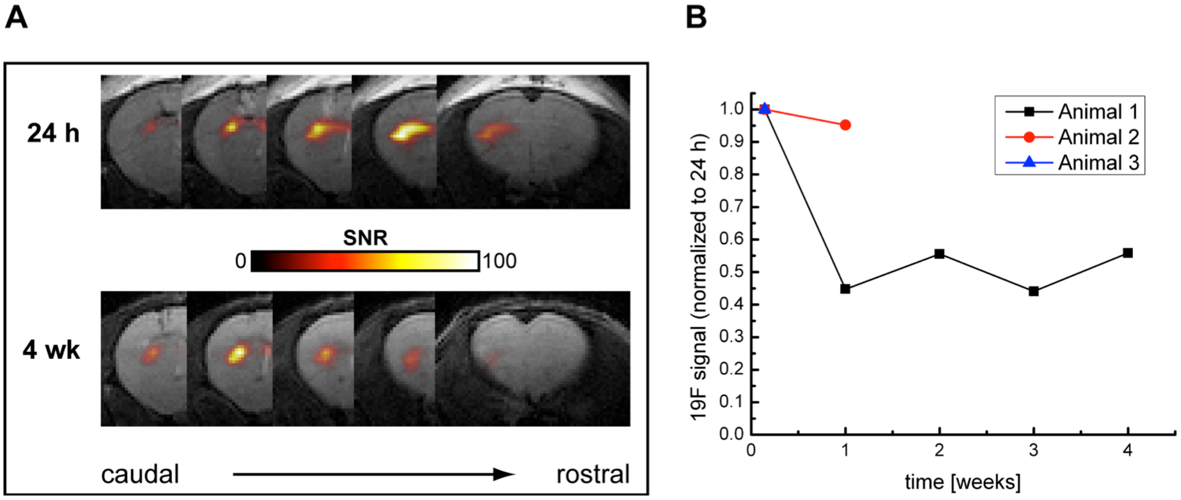

Figure 14: Clearance of PFPE emulsion from the mouse brain. Three mice received an implant (2 µL) of the pure emulsion (125 mg/mL PFPE) and were sacrificed for histology at different time points. ^{19}F MRI revealed persistence of strong ^{19}F MRI signal up to four weeks in animal #1 (A). All coronal brain slices with significant ^{19}F signal are shown from caudal to rostral at 24 h and 4 weeks after implantation. The colorcoded ^{19}F SNR map is overlaid on an anatomical ^{1}H MR image shown in grayscale. Quantification of ^{19}F SNR confirmed presence of 90% signal for animal #2 after one week and ~50% for animal #1 after 4 weeks compared to the 24 h time point (B). Animal #3 was scanned with ^{19}F MRI only once to confirm successful implantation and sacrificed for histology at the first time point.

External MRI labels thus fail in two situations that can occur in vivo. First, cells can proliferate and this is not reflected by changes in MR signal since the amount of label does not double when cell number is doubled. Second, when cells die MRI signal can persist or decrease with a long delay. The delay is dependent on clearance of the released label. However, both proliferation and viability are very important parameters for the risk of tumor formation and for successful action of implanted cells. Therefore, we developed a multimodal imaging approach that combines the strengths of MRI using external labels and optical imaging using genetic labels in order to image localization, quantity, and function of implanted cells [127]. This will be presented in the next section.

Perspective: multimodal imaging of stem cell location, number, and function after stroke

As stated in section 1.2.1 of the introduction, reporter genes are suitable to noninvasively assess cell function. When cells genetically modified to express a reporter gene divide, the signal accordingly increases since each clone of the mother cell produces its own reporter molecules. If a cell dies, gene transcription ceases and the signal is turned off, usually with little delay since reporter molecules are degraded fast. This is particularly true for Bioluminescence imaging (BLI). Here, transplanted cells are genetically modified to express a luciferase. After implantation, the cells constantly produce the enzyme. Upon injection of the substrate luciferin, luciferin is converted via enzymatic reaction with the luciferase to oxyluciferin under emission of light (Fig. 15). This light can be detected with an optical CCD camera. Since the reaction is ATP dependent, the light reaction exclusively occurs in cells that have both normal gene expression and metabolism, i.e. in truly viable cells. When care is taken, the detected light can be used to quantify the number of viable cells via linear relation to number of photons per second per cm^2 per steradian [128–130]. However in deep tissues, scattering and absorption of light in tissue hinder absolute quantification of cell number. Furthermore, scattering and absorption usually lead to low resolution, 2D (projection image) data. Since ^{19}F labels promise quantification and 3D localization of cells with good resolution (< 1 mm) in deep tissues, we decided to combine the strengths of both ^{19}F MRI and BLI by using genetic luciferase labeling with external ^{19}F labeling of NSCs.

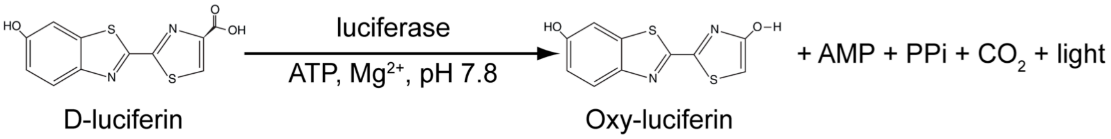

Figure 15: Schematic illustration of the luciferase reaction. Modified from [128].

Neural stem cells were derived from murine embryonic stem cells with the protocol described in [40] and transduced to express the click beetle luciferase (CBG99) for BLI detection. To label the cells for histology, we incubated them with the red fluorescent marker Cell Tracker Orange (Invitrogen). For ^{19}F MRI detection, cells were labeled with the PFPE agent used for paper V (CS-1000, Celsense, Pittsburgh, USA). The labeling procedure was optimized using NMR spectroscopy to yield maximum ^{19}F content per cell in analogy to paper V. These experiments resulted in an optimal dose of 25 µL agent per mL medium and incubation time of 36 h. For some experiments we used a fluorescent PFPE agent (CS-green, Celsense) for detection of the agent on histological sections via fluorescence microscopy. Cells were implanted in healthy and in ischemic NuNu mice that received 30 min middle cerebral artery occlusion as described in [131]. For ischemic mice we performed T$_2$ weighted MRI 24 h after surgery to identify the lesion and implanted the cells in tissue adjacent to the lesion 48 h post stroke. Animals were scanned repetitively with BLI and ^{19}F MRI up to 4 weeks after implantation.

Detailed MRI parameters can be found in [116], [127]. The procedure and all reporter systems are illustrated in Fig. 16.

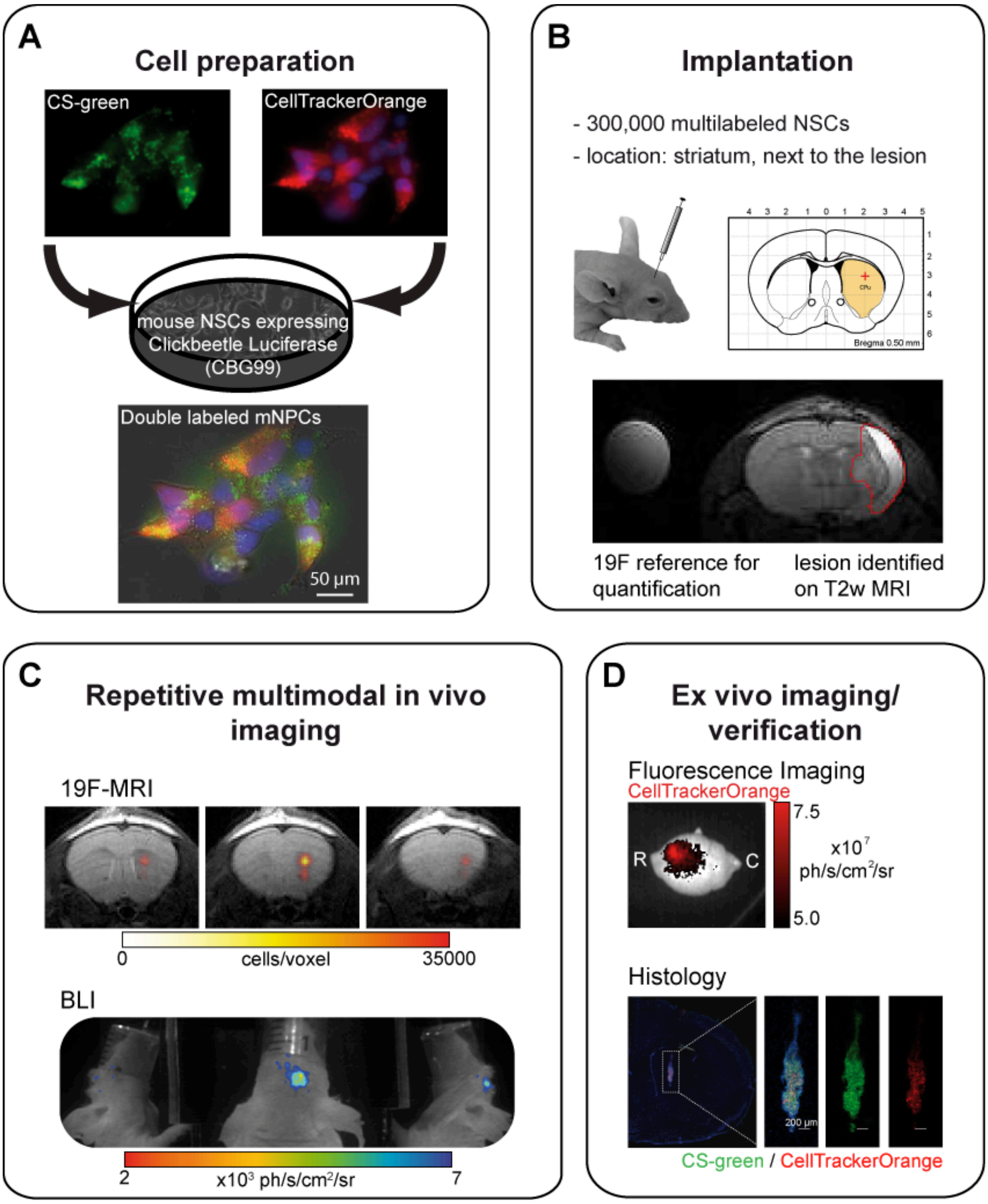
A
Cell preparation
CS-green
CellTrackerOrange
mouse NSCs expressing Clickbeetle Luciferase (CBG99)
Double labeled mNPCs
50 µm
B
Implantation
- 300,000 multilabeled NSCs
- location: striatum, next to the lesion
Bregma 0.50 mm
19F reference for quantification
lesion identified on T2w MRI
C
Repetitive multimodal in vivo imaging
19F-MRI
0
cells/voxel
35000
BLI
2
x10³ ph/s/cm²/sr
7
D
Ex vivo imaging/ verification
Fluorescence Imaging
CellTrackerOrange
R
C
7.5
x10⁷ ph/s/cm²/sr
5.0
Histology
200 µm
CS-green / CellTrackerOrange

Figure 16: Multimodal imaging of NSC graft location, density, and function. Murine NSCs were genetically modified to express the click beetle luciferase and labeled with a green fluorescent ^{19}F agent. For later identification on histological sections, NSCs were additionally labeled with the red fluorescent marker Cell Tracker Orange. Fluorescence microscopy of NSCs after labeling confirmed high intracellular accumulation of ^{19}F agent (A). Cells were implanted in the striatum of healthy and stroke NuNu mice. For ischemic mice the lesion was localized on T_2-weighted MRI scans 24 h after surgery and stereotactic coordinates adjusted for peri-infarct implantation 48 h post surgery. A ^{19}F reference tube was used for all MRI scans in order to quantify cell densities with the protocol presented in Fig. 13 (B). Repetitive ^{19}F MRI and BLI was carried out in order to assess location, density, and viability of NSCs up to four weeks. Images of a healthy mouse 24 h after implantation are shown. BLI signal colorcoded and overlaid on a photograph of the mouse inside the camera taken from top view. For better visualization of depth of signal origin, two side mirrors were placed next to the animal (C). After in vivo experiments, fluorescent markers allowed to identify cells with fluorescence imaging on the excised brain (top view). Fluorescence microscopy on coronal histological sections was used to identify cells (red) and ^{19}F agent (green) (D). R/C: rostral/caudal. Hoechst fluorescence staining of cell nuclei shown in blue for A and D.

We saw a massive decrease in cell viability (BLI signal) over time for grafted NSCs. Interestingly, this was independent of whether we implanted into the healthy or pathological brain. For one animal we saw an increase in BLI signal, which indicated cell proliferation but confirmation by histology is still pending. We detected no signs of cell migration using ^{19}F MRI. Although ~70% of the cells died over 4 weeks, ^{19}F MRI signal persisted for healthy animals, which can be explained by limited clearance of ^{19}F label once released from dead cells in agreement with the results of implantation of pure agent (Fig. 14). Thus ^{19}F MRI alone would have lead to the wrong conclusion that all NSCs are still present at 4 weeks. This stresses the importance of combining external MRI label approaches with other modalities in order to rightfully interpret biological processes. We speculate that immune reaction as a response to the implanted cells is the key factor that leads to the decrease in viability. Indeed, we do see signs of microglial activation, however thorough analysis of histological sections is still in progress.

The massive reduction in the number of viable cells was observed also in paper IV of this dissertation, by other groups [45], and even in studies, in which a recovery of brain function was observed many weeks after implantation [62]. The number of surviving implanted cells in all those studies was orders of magnitude lower than the number of cells lost during an infarct. This supports the hypothesis that stem cell mediated functional recovery is not a result of direct tissue replacement but rather due to indirect, paracrine effects of implanted cells.

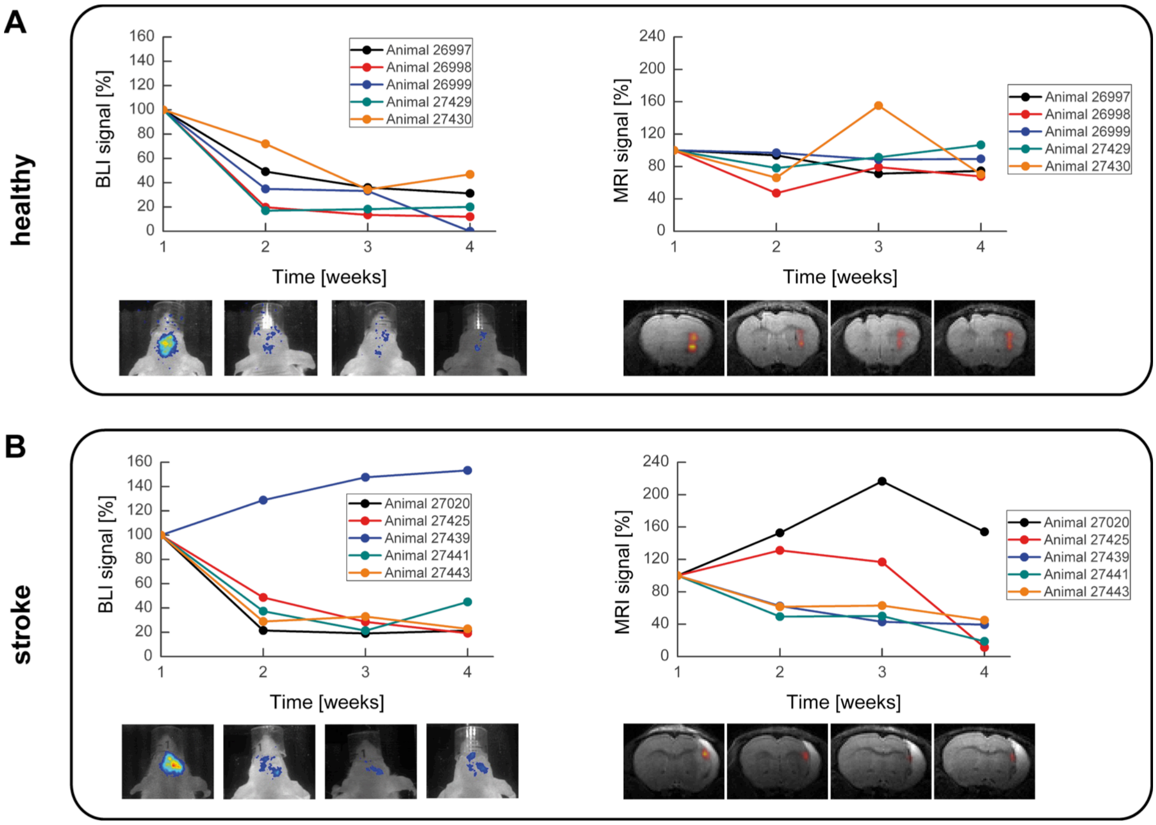

Figure 17: Cell graft location, density, and viability after implantation in healthy and stroke mice. In healthy animals BLI signal (viability) dropped to ~30% over 4 weeks whereas ^{19}F SNR (location, density) remained relatively constant. The persisting ^{19}F signal may be explained by limited clearance of ^{19}F label when cells die. The decrease in cell viability was most pronounced between week one and two (A). A similar trend was observed in stroke animals although one animal showed an increase in BLI signal indicating cell proliferation. ^{19}F MRI signal decreased in all stroke animals except for animal 27020, which exhibited large scatter in values due to very low signal (B). For each graph, representative images of one animal are shown at different time points. For ^{19}F MR images, the slice through the brain with highest ^{19}F SNR is shown.

3.3 Interactions of angiogenesis and stem cells after cerebral lesions

Remarkably, VEGF-A and some other angiogenic molecules have shown neuroprotective properties and strong interaction with neurogenesis, i.e. formation of new neurons from endogenous neural progenitor cells [132]. Migration of neuroblasts that are newly generated in the subventricular zone of rats after stroke was shown to occur along blood vessels [133]. Migration of endothelial cells follows along the gradient of VEGF [5] and one can speculate that molecules involved in angiogenesis also play a role in migration of other cell types. These findings highlight the importance of angiogenesis after an ischemic insult and exemplify the tight link of angiogenesis with other stroke-induced endogenous repair mechanisms.

On the other hand, angiogenesis is important in order to provide blood supply for transplanted cells. Graft vascularization was shown to occur very slowly in rats implanted with human NSCs [134]. Delivery of stem cells could help to facilitate vascularization through expression of factors. Indeed, delivery of VEGF overexpressing NSCs and CD34 positive hematopoietic stem cells was shown to induce angiogenesis, enhance graft survival, and improve animal behavior after stroke [135], [136]. Recently, a study showed delayed vasodilation after stroke in rats as a result of human mesenchymal stem cell transplantation [137].

The imaging methods developed in this dissertation could help to further elucidate interactions between grafted cells and the vasculature. Here, ^{19}F labeling presents a very attractive way to visualize cells, since these labels do not generate contrast on ^{1}H MR images as seen in the control animal of Fig. 4 of paper IV, in all anatomical ^{1}H MR images shown in paper V, and those shown in section 3.2.2 of this dissertation. Therefore, the signal of ^{1}H MR contrast-based methods, e.g. mapping of relaxation time, diffusion imaging, BOLD MRI, fMRI, dynamic or SSCE MRI would be untouched. Combination of the presented cellular ^{19}F MRI and BLI with these ^{1}H MRI methods could help to answer pending important questions: Is a suitable vascular microenvironment inevitable for good graft acceptance? What is the contribution of angiogenesis – or of cell-vasculature interactions in general - for functional recovery in models of stem cell therapy of the damaged brain?

3.4 Conclusion

Undoubtedly, the rapid advances in angiogenesis and stem cell research have had and will have a major impact on our understanding of neurological disease and treatment. However, the initial excitement has partly been replaced by the realization of how complex molecular and cellular processes underlying the disease are and how difficult it is to manipulate these for therapy. Noninvasive imaging can spatially and temporally resolve some of the biological processes underlying the pathology and mechanisms of therapy and therefore provide the needed complexity of information. In this dissertation, SSCE MRI to image angiogenesis in tumor and stroke was optimized and proved useful to monitor vascular changes and response to therapy in rodents. For the first time, the importance of diffusion measurements for rightful interpretation of SSCE MRI data was specifically assessed. The impact of noise was minimized through optimization of MRI parameters. A novel modification of the theory for multi spin echo signal from a vascular network was developed in collaboration with theorists. An in vitro model for tissues with non-cylindrical vessels and high blood volume was evaluated and promises feasibility of vessel size imaging beyond the cylinder model of the vasculature. The spatio-temporal dynamics of human NSCs were followed over long time with ^{1}H MRI using SPIO labels. To improve cellular MRI, a novel, comprehensive framework for neural stem cell tracking by ^{19}F MRI and optical imaging has been established. This allowed for the first time to noninvasively assess grafted NSC location, density, and viability. Combination of the innovations of this dissertation with established imaging methods will help to better understand the indirect mechanisms, that lead to stem cell-mediated functional recovery after stroke, e.g. interactions of grafted NSCs with the vasculature.

4 References

[1] P. Fraisl, M. Mazzone, T. Schmidt, and P. Carmeliet, “Regulation of angiogenesis by oxygen and metabolism.,” *Developmental cell*, vol. 16, no. 2, pp. 167–79, Feb. 2009.

[2] P. Carmeliet and R. K. Jain, “Angiogenesis in cancer and other diseases.,” *Nature*, vol. 407, no. 6801, pp. 249–57, Sep. 2000.

[3] P. Carmeliet, “Angiogenesis in life, disease and medicine.,” *Nature*, vol. 438, no. 7070, pp. 932–6, Dec. 2005.

[4] H. Beck and K. H. Plate, “Angiogenesis after cerebral ischemia,” *Acta Neuropathologica*, vol. 117, no. 5, pp. 481–496, 2009.

[5] P. Carmeliet, F. De Smet, S. Loges, and M. Mazzone, “Branching morphogenesis and antiangiogenesis candidates: tip cells lead the way,” *Nature Reviews Clinical Oncology*, vol. 6, no. 6, pp. 315–326, 2009.

[6] J. Folkman, “Angiogenesis in cancer, vascular, rheumatoid and other disease.,” *Nature medicine*, vol. 1, no. 1, pp. 27–31, Jan. 1995.

[7] G. Bergers and L. E. Benjamin, “Tumorigenesis and the angiogenic switch.,” *Nature reviews. Cancer*, vol. 3, no. 6, pp. 401–10, Jun. 2003.

[8] J. Folkman, “Angiogenesis: an organizing principle for drug discovery?,” *Nature reviews. Drug discovery*, vol. 6, no. 4, pp. 273–86, Apr. 2007.

[9] L. M. Ellis and D. J. Hicklin, “VEGF-targeted therapy: mechanisms of anti-tumour activity.,” *Nature reviews. Cancer*, vol. 8, no. 8, pp. 579–91, Aug. 2008.

[10] J. M. L. Ebos and R. S. Kerbel, “Antiangiogenic therapy: impact on invasion, disease progression, and metastasis.,” *Nature reviews. Clinical oncology*, vol. 8, no. 4, pp. 210–21, Apr. 2011.

[11] J. J. C. Verhoeff, O. van Tellingen, A. Claes, L. J. A. Stalpers, M. E. van Linde, D. J. Richel, W. P. J. Leenders, and W. R. van Furth, “Concerns about anti-angiogenic treatment in patients with glioblastoma multiforme.,” *BMC cancer*, vol. 9, p. 444, Jan. 2009.

[12] D. M. Hermann and A. Zechariah, “Implications of vascular endothelial growth factor for postischemic neurovascular remodeling,” *Journal of Cerebral Blood Flow and Metabolism*, vol. 29, no. 10, pp. 1620–1643, 2009.

[13] J. Krupinski, J. Kaluza, P. Kumar, S. Kumar, and J. M. Wang, “Role of Angiogenesis in Patients with Cerebral Ischemic Stroke,” *Stroke*, vol. 25, no. 9, pp. 1794–1798, Sep. 1994.

[14] J. Krupinski, P. Stroemer, M. Slevin, E. Marti, P. Kumar, and F. Rubio, “Three-dimensional structure and survival of newly formed blood vessels after focal cerebral ischemia,” *Neuroreport*, vol. 14, no. 8, pp. 1171–1176, Jun. 2003.

[15] M. Slevin, P. Kumar, J. Gaffney, S. Kumar, and J. Krupinski, “Can angiogenesis be exploited to improve stroke outcome? Mechanisms and therapeutic potential,” *Clinical Science*, vol. 111, no. 3, pp. 171–183, 2006.

[16] D. Navaratna, S. Guo, K. Arai, and E. H. Lo, “Mechanisms and targets for angiogenic therapy after stroke,” *Cell adhesion & migration*, vol. 3, no. 2, pp. 216–223, 2009.

[17] M. Neeman, A. A. Gilad, H. Dafni, and B. Cohen, “Molecular imaging of angiogenesis,” *Journal of Magnetic Resonance Imaging*, vol. 25, no. 1, pp. 1–12, 2007.

[18] D. M. McDonald and P. L. Choyke, “Imaging of angiogenesis: from microscope to clinic.,” *Nature medicine*, vol. 9, no. 6, pp. 713–25, Jun. 2003.

[19] T. Jeswani and A. R. Padhani, “Imaging tumour angiogenesis.,” *Cancer imaging : the official publication of the International Cancer Imaging Society*, vol. 5, pp. 131–8, Jan. 2005.

[20] P. Seevinck, L. Deddens, and R. Dijkhuizen, “Magnetic resonance imaging of brain angiogenesis after stroke,” *Angiogenesis*, vol. 13, no. 2, pp. 101–111, 2010.

[21] D. A. Yablonskiy and E. M. Haacke, “Theory of NMR Signal Behavior in Magnetically Inhomogeneous Tissues - The Static Dephasing Regime,” *Magnetic Resonance in Medicine*, vol. 32, no. 6, pp. 749–763, 1994.

[22] V. G. Kiselev and S. Posse, “Analytical model of susceptibility-induced MR signal dephasing: Effect of diffusion in a microvascular network,” *Magnetic Resonance in Medicine*, vol. 41, no. 3, pp. 499–509, Mar. 1999.

[23] V. G. Kiselev and S. Posse, “Analytical theory of susceptibility induced NMR signal dephasing in a cerebrovascular network,” *Physical Review Letters*, vol. 81, no. 25, pp. 5696–5699, 1998.

[24] V. G. Kiselev, “On the theoretical basis of perfusion measurements by dynamic susceptibility contrast MRI,” *Magnetic Resonance in Medicine*, vol. 46, no. 6, pp. 1113–1122, 2001.

[25] J. L. Boxerman, L. M. Hamberg, B. R. Rosen, and R. M. Weisskoff, “MR contrast due to intravascular magnetic-susceptibility perturbations,” *Magnetic Resonance in Medicine*, vol. 34, no. 4, pp. 555–566, 1995.

[26] J. Dennie, J. B. Mandeville, J. L. Boxerman, S. D. Packard, B. R. Rosen, and R. M. Weisskoff, “NMR imaging of changes in vascular morphology due to tumor angiogenesis,” *Magnetic Resonance in Medicine*, vol. 40, no. 6, pp. 793–799, 1998.

[27] I. Tropres, S. Grimault, A. Vaeth, E. Grillon, C. Julien, J. F. Payen, L. Lamalle, and M. Decorps, “Vessel size imaging,” *Magnetic Resonance in Medicine*, vol. 45, no. 3, pp. 397–408, 2001.

[28] E. X. Wu, H. Y. Tang, and J. H. Jensen, “High-resolution MR imaging of mouse brain microvasculature using the relaxation rate shift index Q,” *Nmr in Biomedicine*, vol. 17, no. 7, pp. 507–512, 2004.

[29] J. H. Jensen and R. Chandra, “MR imaging of microvasculature,” *Magnetic Resonance in Medicine*, vol. 44, no. 2, pp. 224–230, 2000.

[30] V. G. Kiselev, R. Strecker, S. Ziyeh, O. Speck, and J. Hennig, “Vessel size imaging in humans,” *Magnetic Resonance in Medicine*, vol. 53, no. 3, pp. 553–563, 2005.

[31] S. Temple, “The development of neural stem cells.,” *Nature*, vol. 414, no. 6859, pp. 112–7, Nov. 2001.

[32] F. H. Gage, “Mammalian neural stem cells.,” *Science (New York, N.Y.)*, vol. 287, no. 5457, pp. 1433–8, Feb. 2000.

[33] A. Alvarez-Buylla and J. M. Garcia-Verdugo, “Neurogenesis in adult subventricular zone.,” *The Journal of neuroscience : the official journal of the Society for Neuroscience*, vol. 22, no. 3, pp. 629–34, Feb. 2002.

[34] F. H. Gage, “Neurogenesis in the adult brain.,” *The Journal of neuroscience : the official journal of the Society for Neuroscience*, vol. 22, no. 3, pp. 612–3, Feb. 2002.

[35] G. Kempermann, “Why new neurons? Possible functions for adult hippocampal neurogenesis.,” *The Journal of neuroscience : the official journal of the Society for Neuroscience*, vol. 22, no. 3, pp. 635–8, Feb. 2002.

[36] A. Bjorklund and O. Lindvall, “Cell replacement therapies for central nervous system disorders,” *Nature Neuroscience*, vol. 3, no. 6, pp. 537–544, 2000.

[37] O. Lindvall and Z. Kokaia, “Stem cells for the treatment of neurological disorders,” *Nature*, vol. 441, no. 7097, pp. 1094–1096, 2006.

[38] B. A. Reynolds and S. Weiss, “Generation of neurons and astrocytes from isolated cells of the adult mammalian central nervous system.,” *Science (New York, N.Y.)*, vol. 255, no. 5052, pp. 1707–10, Mar. 1992.

[39] M. H. Buc-Caron, “Neuroepithelial progenitor cells explanted from human fetal brain proliferate and differentiate in vitro.,” *Neurobiology of disease*, vol. 2, no. 1, pp. 37–47, Feb. 1995.

[40] L. Conti, S. M. Pollard, T. Gorba, E. Reitano, M. Toselli, G. Biella, Y. Sun, S. Sanzone, Q.-L. Ying, E. Cattaneo, and A. Smith, “Niche-independent symmetrical self-renewal of a mammalian tissue stem cell.,” *PLoS biology*, vol. 3, no. 9, p. e283, Sep. 2005.

[41] M. B. Jensen, H. Yan, R. Krishnaney-Davison, A. Al Sawaf, and S.-C. Zhang, “Survival and Differentiation of Transplanted Neural Stem Cells Derived from Human Induced Pluripotent Stem Cells in A Rat Stroke Model.,” *Journal of stroke and cerebrovascular diseases : the official journal of National Stroke Association*, Nov. 2011.

[42] D. A. Robinton and G. Q. Daley, “The promise of induced pluripotent stem cells in research and therapy.,” *Nature*, vol. 481, no. 7381, pp. 295–305, Jan. 2012.

[43] T. Kallur, R. Gisler, O. Lindvall, and Z. Kokaia, “Pax6 promotes neurogenesis in human neural stem cells,” *Molecular and Cellular Neuroscience*, vol. 38, no. 4, pp. 616–628, 2008.

[44] V. Darsalia, T. Kallur, and Z. Kokaia, “Survival, migration and neuronal differentiation of human fetal striatal and cortical neural stem cells grafted in stroke-damaged rat striatum,” *European Journal of Neuroscience*, vol. 26, no. 3, pp. 605–614, 2007.

[45] V. Darsalia, S. J. Allison, C. Cusulin, E. Monni, D. Kuzdas, T. Kallur, O. Lindvall, and Z. Kokaia, “Cell number and timing of transplantation determine survival of human neural stem cell grafts in stroke-damaged rat brain,” *J Cereb Blood Flow Metab*, vol. 31, no. 1, pp. 235–242, 2011.

[46] T. Kallur, “Human neural stem cells - region specific properties and prospects for cell therapy,” Lund University, 2008.

[47] T. Kallur, V. Darsalia, O. Lindvall, and Z. Kokaia, “Human fetal cortical and striatal neural stem cells generate region-specific neurons in vitro and differentiate extensively to neurons after intrastriatal transplantation in neonatal rats,” *Journal of Neuroscience Research*, vol. 84, no. 8, pp. 1630–1644, 2006.

[48] R. D. Lund, K. Rao, M. H. Hankin, H. W. Kunz, and T. J. Gill, “Transplantation of retina and visual cortex to rat brains of different ages. Maturation, connection patterns, and immunological consequences.,” *Annals of the New York Academy of Sciences*, vol. 495, pp. 227–41, Jan. 1987.

[49] M. Olsson, C. Bentlage, K. Wictorin, K. Campbell, and A. Björklund, “Extensive migration and target innervation by striatal precursors after grafting into the neonatal striatum.,” *Neuroscience*, vol. 79, no. 1, pp. 57–78, Jul. 1997.

[50] R. A. Barker and H. Widner, “Immune problems in central nervous system cell therapy.,” *NeuroRx : the journal of the American Society for Experimental NeuroTherapeutics*, vol. 1, no. 4, pp. 472–81, Oct. 2004.

[51] R. H. Andres, N. Horie, W. Slikker, H. Keren-Gill, K. Zhan, G. Sun, N. C. Manley, M. P. Pereira, L. a Sheikh, E. L. McMillan, B. T. Schaar, C. N. Svendsen, T. M. Bliss, and G. K. Steinberg, “Human neural stem cells enhance structural plasticity and axonal transport in the ischaemic brain.,” *Brain*, vol. 134, no. Pt 6, pp. 1777–89, Jun. 2011.

[52] E. Bible, O. Qutachi, D. Y. S. Chau, M. R. Alexander, K. M. Shakesheff, and M. Modo, "Neo-vascularization of the stroke cavity by implantation of human neural stem cells on VEGF-releasing PLGA microparticles.," *Biomaterials*, vol. 33, no. 30, pp. 7435–46, Oct. 2012.

[53] L. Rota Nodari, D. Ferrari, F. Giani, M. Bossi, V. Rodriguez-Menendez, G. Tredici, D. Delia, A. L. Vescovi, and L. De Filippis, "Long-term survival of human neural stem cells in the ischemic rat brain upon transient immunosuppression.," *PloS one*, vol. 5, no. 11, p. e14035, Jan. 2010.

[54] E. J. Smith, R. P. Stroemer, N. Gorenkova, M. Nakajima, W. R. Crum, E. Tang, L. Stevanato, J. D. Sinden, and M. Modo, "Implantation site and lesion topology determine efficacy of a human neural stem cell line in a rat model of chronic stroke.," *Stem cells (Dayton, Ohio)*, vol. 30, no. 4, pp. 785–96, May 2012.

[55] H. J. Lee, K. S. Kim, E. J. Kim, H. B. Choi, K. H. Lee, I. H. Park, Y. Ko, S. W. Jeong, and S. U. Kim, "Brain transplantation of immortalized human neural stem cells promotes functional recovery in mouse intracerebral hemorrhage stroke model.," *Stem cells (Dayton, Ohio)*, vol. 25, no. 5, pp. 1204–12, May 2007.

[56] S. Ishibashi, M. Sakaguchi, T. Kuroiwa, M. Yamasaki, Y. Kanemura, I. Shizuko, T. Shimazaki, M. Onodera, H. Okano, and H. Mizusawa, "Human neural stem/progenitor cells, expanded in long-term neurosphere culture, promote functional recovery after focal ischemia in Mongolian gerbils," *Journal of Neuroscience Research*, vol. 78, no. 2, pp. 215–223, 2004.

[57] B. Z. Roitberg, E. Mangubat, E.-Y. Chen, K. Sugaya, K. R. Thulborn, J. H. Kordower, A. Pawar, T. Konecny, and M. E. Emborg, "Survival and early differentiation of human neural stem cells transplanted in a nonhuman primate model of stroke.," *Journal of neurosurgery*, vol. 105, no. 1, pp. 96–102, Jul. 2006.

[58] S. Kelly, T. M. Bliss, A. K. Shah, G. H. Sun, M. Ma, W. C. Foo, J. Masel, M. A. Yenari, I. L. Weissman, N. Uchida, T. Palmer, and G. K. Steinberg, "Transplanted human fetal neural stem cells survive, migrate, and differentiate in ischemic rat cerebral cortex," *Proceedings of the National Academy of Sciences of the United States of America*, vol. 101, no. 32, pp. 11839–11844, 2004.

[59] F. Locatelli, A. Bersano, E. Ballabio, S. Lanfranconi, D. Papadimitriou, S. Strazzer, N. Bresolin, G. P. Comi, and S. Corti, "Stem cell therapy in stroke.," *Cellular and molecular life sciences : CMLS*, vol. 66, no. 5, pp. 757–72, Mar. 2009.

[60] T. Bliss, R. Guzman, M. Daadi, and G. K. Steinberg, "Cell Transplantation Therapy for Stroke," *Stroke*, vol. 38, no. 2, pp. 817–826, Feb. 2007.

[61] P. Ramos-Cabrer and M. Hoehn, "MRI Stem Cell Tracking for Therapy in Experimental Cerebral Ischemia," *Translational Stroke Research*, vol. 3, no. 1, pp. 22–35, Mar. 2012.

[62] P. Ramos-Cabrer, C. Justicia, D. Wiedermann, and M. Hoehn, “Stem Cell Mediation of Functional Recovery after Stroke in the Rat,” *PLoS One*, vol. 5, no. 9, p. e12779, Jan. 2010.

[63] E. Gu, W.-Y. Chen, J. Gu, P. Burridge, and J. C. Wu, “Molecular imaging of stem cells: tracking survival, biodistribution, tumorigenicity, and immunogenicity.,” *Theranostics*, vol. 2, no. 4, pp. 335–45, Jan. 2012.

[64] M. Rodriguez-Porcel, J. C. Wu, and S. S. Gambhir., “Molecular imaging of stem cells,” in *Stem Book (http://www.ncbi.nlm.nih.gov/books/NBK27079/)*, Harvard Stem Cell Institute, 2009.

[65] T. Schroeder, “Imaging stem-cell-driven regeneration in mammals.,” *Nature*, vol. 453, no. 7193, pp. 345–51, May 2008.

[66] A. A. Gilad, K. Ziv, M. T. McMahon, P. C. M. van Zijl, M. Neeman, and J. W. M. Bulte, “MRI reporter genes.,” *Journal of nuclear medicine : official publication, Society of Nuclear Medicine*, vol. 49, no. 12, pp. 1905–8, Dec. 2008.

[67] M. Hoehn, E. Kustermann, J. Blunk, D. Wiedermann, T. Trapp, S. Wecker, M. Focking, H. Arnold, J. Hescheler, B. K. Fleischmann, W. Schwindt, and C. Buhrle, “Monitoring of implanted stem cell migration in vivo: A highly resolved in vivo magnetic resonance imaging investigation of experimental stroke in rat,” *Proceedings of the National Academy of Sciences of the United States of America*, vol. 99, no. 25, pp. 16267–16272, 2002.

[68] R. Guzman, N. Uchida, T. M. Bliss, D. P. He, K. K. Christopherson, D. Stellwagen, A. Capela, J. Greve, R. C. Malenka, M. E. Moseley, T. D. Palmer, and G. K. Steinberg, “Long-term monitoring of transplanted human neural stem cells in developmental and pathological contexts with MRI,” *Proceedings of the National Academy of Sciences of the United States of America*, vol. 104, no. 24, pp. 10211–10216, 2007.

[69] J. S. Weinstein, C. G. Varallyay, E. Dosa, S. Gahramanov, B. Hamilton, W. D. Rooney, L. L. Muldoon, and E. A. Neuwelt, “Superparamagnetic iron oxide nanoparticles: diagnostic magnetic resonance imaging and potential therapeutic applications in neurooncology and central nervous system inflammatory pathologies, a review.,” *Journal of cerebral blood flow and metabolism : official journal of the International Society of Cerebral Blood Flow and Metabolism*, vol. 30, no. 1, pp. 15–35, Jan. 2010.

[70] E. T. Ahrens, R. Flores, H. Xu, and P. A. Morel, “In vivo imaging platform for tracking immunotherapeutic cells,” *Nature Biotechnology*, vol. 23, no. 8, pp. 983–987, 2005.

[71] J. M. Janjic and E. T. Ahrens, “Fluorine-containing nanoemulsions for MRI cell tracking,” *Wiley Interdisciplinary Reviews: Nanomedicine and Nanobiotechnology*, vol. 1, no. 5, pp. 492–501, 2009.

[72] J. Ruiz-Cabello, B. P. Barnett, P. A. Bottomley, and J. W. M. Bulte, “Fluorine (19F) MRS and MRI in biomedicine,” *NMR in Biomedicine*, vol. 24, no. 2, pp. 114–129, 2011.

[73] M. Srinivas, A. Heerschap, E. T. Ahrens, C. G. Figdor, and I. J. M. de Vries, “19F MRI for quantitative in vivo cell tracking,” *Trends in Biotechnology*, vol. 28, no. 7, pp. 363–370, 2010.

[74] B. M. Helfer, A. Balducci, A. D. Nelson, J. M. Janjic, R. R. Gil, P. Kalinski, I. J. M. De Vries, E. T. Ahrens, and R. B. Mailliard, “Functional assessment of human dendritic cells labeled for in vivo F-19 magnetic resonance imaging cell tracking,” *Cytotherapy*, vol. 12, no. 2, pp. 238–250, 2010.

[75] F. Bonetto, M. Srinivas, A. Heerschap, R. Mailliard, E. T. Ahrens, C. G. Figdor, and I. J. M. De Vries, “A novel (19)F agent for detection and quantification of human dendritic cells using magnetic resonance imaging.,” *International journal of cancer Journal international du cancer*, vol. 129, no. 2, pp. 365–373, 2011.

[76] M. Srinivas, L. J. Cruz, F. Bonetto, A. Heerschap, C. G. Figdor, and I. J. M. de Vries, “Customizable, multi-functional fluorocarbon nanoparticles for quantitative in vivo imaging using 19F MRI and optical imaging.,” *Biomaterials*, vol. 31, no. 27, pp. 7070–7, Sep. 2010.

[77] H. Waiczies, S. Lepore, N. Janitzek, U. Hagen, F. Seifert, B. Ittermann, B. Purf√ºrst, A. Pezzutto, F. Paul, T. Niendorf, and S. Waiczies, “Perfluorocarbon Particle Size Influences Magnetic Resonance Signal and Immunological Properties of Dendritic Cells,” *PLoS ONE*, vol. 6, no. 7, p. e21981, 2011.

[78] M. Srinivas, P. A. Morel, L. A. Ernst, D. H. Laidlaw, and E. T. Ahrens, “Fluorine-19 MRI for visualization and quantification of cell migration in a diabetes model,” *Magnetic Resonance in Medicine*, vol. 58, no. 4, pp. 725–734, 2007.

[79] M. Srinivas, M. S. Turner, J. M. Janjic, P. A. Morel, D. H. Laidlaw, and E. T. Ahrens, “In Vivo Cytometry of Antigen-Specific T Cells Using F-19 MRI,” *Magnetic Resonance in Medicine*, vol. 62, no. 3, pp. 747–753, 2009.

[80] J. Ruiz-Cabello, P. Walczak, D. A. Kedziorek, V. P. Chacko, A. H. Schmieder, S. A. Wickline, G. M. Lanza, and J. W. M. Bulte, “In Vivo ‘Hot Spot’ MR Imaging of Neural Stem Cells Using Fluorinated Nanoparticles,” *Magnetic Resonance in Medicine*, vol. 60, no. 6, pp. 1506–1511, 2008.

[81] D. Fukumura and R. K. Jain, “Tumor microvasculature and microenvironment: targets for anti-angiogenesis and normalization.,” *Microvascular research*, vol. 74, no. 2–3, pp. 72–84, 2007.

[82] S. Zwick, R. Strecker, V. Kiselev, P. Gall, J. Huppert, M. Palmowski, W. Lederle, E. C. Woenne, A. Hengerer, M. Taupitz, W. Semmler, and F. Kiessling, “Assessment of vascular remodeling under antiangiogenic therapy using DCE-MRI and vessel size imaging.,” *Journal of magnetic resonance imaging*, vol. 29, no. 5, pp. 1125–33, May 2009.

[83] J. Drevs, R. Müller-Driver, C. Wittig, S. Fuxius, N. Esser, H. Hugenschmidt, M. A. Konerding, P. R. Allegrini, J. Wood, J. Hennig, C. Unger, and D. Marmé, “PTK787/ZK 222584, a specific vascular endothelial growth factor-receptor tyrosine kinase

inhibitor, affects the anatomy of the tumor vascular bed and the functional vascular properties as detected by dynamic enhanced magnetic resonance imaging.," *Cancer research*, vol. 62, no. 14, pp. 4015–22, Jul. 2002.

[84] I. Helfrich, I. Scheffrahn, S. Bartling, J. Weis, V. von Felbert, M. Middleton, M. Kato, S. Ergün, and D. Schadendorf, "Resistance to antiangiogenic therapy is directed by vascular phenotype, vessel stabilization, and maturation in malignant melanoma.," *The Journal of experimental medicine*, vol. 207, no. 3, pp. 491–503, Mar. 2010.

[85] R. K. Jain, "Normalization of tumor vasculature: an emerging concept in antiangiogenic therapy.," *Science (New York, N.Y.)*, vol. 307, no. 5706, pp. 58–62, Jan. 2005.

[86] C. Y. Lin, C. Chang, W. M. Cheung, M. H. Lin, J. J. Chen, C. Y. Hsu, J. H. Chen, and T. N. Lin, "Dynamic changes in vascular permeability, cerebral blood volume, vascular density, and size after transient focal cerebral ischemia in rats: evaluation with contrast-enhanced magnetic resonance imaging," *Journal of Cerebral Blood Flow and Metabolism*, vol. 28, no. 8, pp. 1491–1501, 2008.

[87] P. S. Manoonkitiwongsa, C. Jackson-Friedman, P. J. McMillan, R. L. Schultz, and P. D. Lyden, "Angiogenesis after stroke is correlated with increased numbers of macrophages; the clean-up hypothesis," *J Cereb Blood Flow Metab*, vol. 21, no. 10, pp. 1223–1231, 2001.

[88] N. M. E. A. Hayward, P. Yanev, A. Haapasalo, R. Miettinen, M. Hiltunen, O. Grohn, and J. Jolkkonen, "Chronic hyperperfusion and angiogenesis follow subacute hypoperfusion in the thalamus of rats with focal cerebral ischemia," *J Cereb Blood Flow Metab*, vol. 31, no. 4, pp. 1119–1132, Apr. 2011.

[89] C. Xu, W. U. H. Schmidt, K. Villringer, P. Brunecker, V. Kiselev, P. Gall, and J. B. Fiebach, "Vessel size imaging reveals pathological changes of microvessel density and size in acute ischemia," *Journal of Cerebral Blood Flow and Metabolism*, vol. 31, no. 8, pp. 1687–1695, Aug. 2011.

[90] C. Xu, W. U. H. Schmidt, I. Galinovic, K. Villringer, B. Hotter, A.-C. Ostwaldt, N. Denisova, E. Kellner, V. Kiselev, and J. B. Fiebach, "The Potential of Microvessel Density in Prediction of Infarct Growth: A Two-Month Experimental Study in Vessel Size Imaging.," *Cerebrovascular diseases (Basel, Switzerland)*, vol. 33, no. 4, pp. 303–309, Feb. 2012.

[91] A. Bosomtwi, Q. Jiang, G. L. Ding, L. Zhang, Z. G. Zhang, M. Lu, J. R. Ewing, and M. Chopp, "Quantitative evaluation of microvascular density after stroke in rats using MRI," *Journal of Cerebral Blood Flow and Metabolism*, vol. 28, no. 12, pp. 1978–1987, 2008.

[92] A. Bosomtwi, M. Chopp, L. Zhang, Z. G. Zhang, M. Lu, and Q. Jiang, "Mean microvessel segment length and radius after embolic stroke: Comparison of magnetic resonance imaging (MRI) and laser scanning confocal microscopy (LSCM)," *Brain Research*, vol. 1381, no. 0, pp. 217–227, 2011.

[93] I. Tropres, L. Lamalle, R. Farion, C. Segebarth, and C. Remy, “Vessel size imaging using low intravascular contrast agent concentrations,” *Magnetic Resonance Materials in Physics Biology and Medicine*, vol. 17, no. 3–6, pp. 313–316, 2004.

[94] J. H. Jensen, H. Lu, and M. Inglese, “Microvessel density estimation in the human brain by means of dynamic contrast-enhanced echo-planar imaging,” *Magnetic Resonance in Medicine*, vol. 56, no. 5, pp. 1145–1150, 2006.

[95] C. Beaulieu, “The basis of anisotropic water diffusion in the nervous system - a technical review.,” *NMR in biomedicine*, vol. 15, no. 7–8, pp. 435–55, 2002.

[96] W. E. Burkel and F. N. Low, “The fine structure of rat liver sinusoids, space of Dissé and associated tissue space.,” *The American journal of anatomy*, vol. 118, no. 3, pp. 769–83, May 1966.

[97] R. E. Mebius and G. Kraal, “Structure and function of the spleen.,” *Nature reviews. Immunology*, vol. 5, no. 8, pp. 606–16, Aug. 2005.

[98] S. Saini, D. D. Stark, P. F. Hahn, J. Wittenberg, T. J. Brady, and J. T. Ferrucci, “Ferrite particles: a superparamagnetic MR contrast agent for the reticuloendothelial system.,” *Radiology*, vol. 162, no. 1 Pt 1, pp. 211–6, Jan. 1987.

[99] S. Adamson, Y. Lu, K. Whiteley, D. Holmyard, M. Hemberger, C. Pfarrer, and J. Cross, “Interactions between Trophoblast Cells and the Maternal and Fetal Circulation in the Mouse Placenta,” *Developmental Biology*, vol. 250, no. 2, pp. 358–373, Oct. 2002.

[100] K. E. Sandoval and K. A. Witt, “Blood-brain barrier tight junction permeability and ischemic stroke.,” *Neurobiology of disease*, vol. 32, no. 2, pp. 200–19, Nov. 2008.

[101] T. Stöcker, K. Vahedipour, D. Pflugfelder, and N. J. Shah, “High-performance computing MRI simulations.,” *Magnetic resonance in medicine : official journal of the Society of Magnetic Resonance in Medicine / Society of Magnetic Resonance in Medicine*, vol. 64, no. 1, pp. 186–93, Jul. 2010.

[102] D. Pflugfelder, K. Vahedipour, K. Uludağ, N. J. Shah, and T. Stöcker, “On the numerically predicted spatial BOLD fMRI specificity for spin echo sequences.,” *Magnetic resonance imaging*, vol. 29, no. 9, pp. 1195–204, Nov. 2011.

[103] J. W. Baish and R. K. Jain, “Fractals and cancer.,” *Cancer research*, vol. 60, no. 14, pp. 3683–8, Jul. 2000.

[104] R. Kimmich, “Strange kinetics, porous media, and NMR,” *Chemical Physics*, vol. 284, no. 1–2, pp. 253–285, Nov. 2002.

[105] A. Brederlau, A. S. Correia, S. V. Anisimov, M. Elmi, G. Paul, L. Roybon, A. Morizane, F. Bergquist, I. Riebe, U. Nannmark, M. Carta, E. Hanse, J. Takahashi, Y. Sasai, K. Funa, P. Brundin, P. S. Eriksson, and J.-Y. Li, “Transplantation of human embryonic stem cell-derived cells to a rat model of Parkinson’s disease: effect of in vitro

differentiation on graft survival and teratoma formation.," *Stem cells (Dayton, Ohio)*, vol. 24, no. 6, pp. 1433–40, Jun. 2006.

[106] F. Erdö, C. Bührle, J. Blunk, M. Hoehn, Y. Xia, B. Fleischmann, M. Föcking, E. Küstermann, E. Kolossov, J. Hescheler, K.-A. Hossmann, and T. Trapp, "Host-dependent tumorigenesis of embryonic stem cell transplantation in experimental stroke.," *Journal of cerebral blood flow and metabolism : official journal of the International Society of Cerebral Blood Flow and Metabolism*, vol. 23, no. 7, pp. 780–5, Jul. 2003.

[107] A. Benchoua and B. Onteniente, "Intracerebral transplantation for neurological disorders. Lessons from developmental, experimental, and clinical studies.," *Frontiers in cellular neuroscience*, vol. 6, p. 2, Jan. 2011.

[108] T. M. Bliss, R. H. Andres, and G. K. Steinberg, "Optimizing the success of cell transplantation therapy for stroke.," *Neurobiology of disease*, vol. 37, no. 2, pp. 275–83, Feb. 2010.

[109] E. Bible, F. Dell'acqua, B. Solanky, A. Balducci, P. M. Crapo, S. F. Badylak, E. T. Ahrens, and M. Modo, "Non-invasive imaging of transplanted human neural stem cells and ECM scaffold remodeling in the stroke-damaged rat brain by (19)F- and diffusion-MRI.," *Biomaterials*, vol. 33, no. 10, pp. 2858–71, May 2012.

[110] E. Bible, D. Y. S. Chau, M. R. Alexander, J. Price, K. M. Shakesheff, and M. Modo, "The support of neural stem cells transplanted into stroke-induced brain cavities by PLGA particles.," *Biomaterials*, vol. 30, no. 16, pp. 2985–94, Jun. 2009.

[111] L. Wei, H. Dahnke, J. Rahmer, E. K. Jordan, and J. A. Frank, "Ultrashort T2* relaxometry for quantitation of highly concentrated superparamagnetic iron oxide (SPIO) nanoparticle labeled cells," *Magnetic Resonance in Medicine*, vol. 61, no. 4, pp. 761–766, 2009.

[112] R. M. Lebel, R. S. Menon, and C. V. Bowen, "Relaxometry model of strong dipolar perturbers for balanced-SSFP: application to quantification of SPIO loaded cells.," *Magnetic resonance in medicine : official journal of the Society of Magnetic Resonance in Medicine / Society of Magnetic Resonance in Medicine*, vol. 55, no. 3, pp. 583–91, Mar. 2006.

[113] W. Liu and J. A. Frank, "Detection and quantification of magnetically labeled cells by cellular MRI.," *European journal of radiology*, vol. 70, no. 2, pp. 258–64, May 2009.

[114] A. M. Rad, A. S. Arbab, A. S. M. Iskander, Q. Jiang, and H. Soltanian-Zadeh, "Quantification of superparamagnetic iron oxide (SPIO)-labeled cells using MRI.," *Journal of magnetic resonance imaging : JMRI*, vol. 26, no. 2, pp. 366–74, Aug. 2007.

[115] M. Stuber, W. D. Gilson, M. Schär, D. A. Kedziorek, L. V. Hofmann, S. Shah, E.-J. Vonken, J. W. M. Bulte, and D. L. Kraitchman, "Positive contrast visualization of iron oxide-labeled stem cells using inversion-recovery with ON-resonant water suppression (IRON).," *Magnetic resonance in medicine : official journal of the*

Society of Magnetic Resonance in Medicine / Society of Magnetic Resonance in Medicine, vol. 58, no. 5, pp. 1072–7, Nov. 2007.

[116] P. Boehm-Sturm, E. D. Pracht, M. Aswendt, N. Henn, and M. Hoehn, “B1 correction for quantitative in vivo 19F magnetic resonance imaging with surface coils,” *Proceedings of the International Society for Magnetic Resonance in Medicine*, 2012.

[117] E. K. Insko and L. Bolinger, “Mapping of the Radiofrequency Field,” *Journal of Magnetic Resonance Series A*, vol. 103, no. 1, pp. 82–85, 1993.

[118] K. Scheffler, “A pictorial description of steady-states in rapid magnetic resonance imaging,” *Concepts in Magnetic Resonance*, vol. 11, no. 5, pp. 291–304, 1999.

[119] A. Crabbe, C. Vandeputte, T. Dresselaers, A. A. Sacido, J. M. G. Verdugo, J. Eyckmans, F. P. Luyten, K. Van Laere, C. M. Verfaillie, and U. Himmelreich, “Effects of MRI contrast agents on the stem cell phenotype.,” *Cell transplantation*, vol. 19, no. 8, pp. 919–36, Jan. 2010.

[120] S. M. Cromer Berman, Kshitiz, C. J. Wang, I. Orukari, A. Levchenko, J. W. M. Bulte, and P. Walczak, “Cell motility of neural stem cells is reduced after SPIO-labeling, which is mitigated after exocytosis.,” *Magnetic Resonance in Medicine*, Feb. 2012.

[121] K. Kruttwig, C. Brueggemann, E. Kaijzel, S. Vorhagen, T. Hilger, C. Löwik, and M. Hoehn, “Development of a three-dimensional in vitro model for longitudinal observation of cell behavior: monitoring by magnetic resonance imaging and optical imaging.,” *Molecular imaging and biology*, vol. 12, no. 4, pp. 367–76, Aug. 2010.

[122] F. Bonetto, M. Srinivas, B. Weigelin, L. J. Cruz, A. Heerschap, P. Friedl, C. G. Figdor, and I. J. M. de Vries, “A large-scale (19) F MRI-based cell migration assay to optimize cell therapy.,” *NMR in biomedicine*, vol. 25, no. 9, pp. 1095–103, Sep. 2012.

[123] Y.-X. J. Wang, “Superparamagnetic iron oxide based MRI contrast agents: Current status of clinical application,” *Quantitative Imaging in Medicine and Surgery*, vol. 1, no. 1. pp. 35–40, 09-Jan-2011.

[124] M. Longmire, P. L. Choyke, and H. Kobayashi, “Clearance properties of nano-sized particles and molecules as imaging agents: considerations and caveats.,” *Nanomedicine (London, England)*, vol. 3, no. 5, pp. 703–17, Oct. 2008.

[125] J. W. M. Bulte and D. L. Kraitchman, “Iron oxide MR contrast agents for molecular and cellular imaging.,” *NMR in biomedicine*, vol. 17, no. 7, pp. 484–99, Nov. 2004.

[126] F. H. Wang, D. K. Kim, T. Yoshitake, S. M. Johansson, B. Bjelke, M. Muhammed, and J. Kehr, “Diffusion and clearance of superparamagnetic iron oxide nanoparticles infused into the rat striatum studied by MRI and histochemical techniques.,” *Nanotechnology*, vol. 22, no. 1, p. 015103, Jan. 2011.

[127] P. Boehm-Sturm, M. Aswendt, L. Breucker, N. Henn, L. Mengler, J. Adamczak, E. D. Pracht, A. Tennstaedt, C. Löwik, and M. Hoehn, "Imaging Structure and Function of Stem Cell Grafts in the Mouse Brain by combining 19F Magnetic Resonance Imaging with Bioluminescence Imaging," *Proceedings of the International Society for Magnetic Resonance in Medicine*, 2012.

[128] C. E. Badr and B. A. Tannous, "Bioluminescence imaging: progress and applications.," *Trends in biotechnology*, vol. 29, no. 12, pp. 624–33, Dec. 2011.

[129] M. Keyaerts, V. Caveliers, and T. Lahoutte, "Bioluminescence imaging: looking beyond the light.," *Trends in molecular medicine*, vol. 18, no. 3, pp. 164–72, Mar. 2012.

[130] P. E. De Almeida, J. R. M. Van Rappard, and J. C. Wu, "In vivo bioluminescence for tracking cell fate and function.," *American journal of physiology Heart and circulatory physiology*, vol. 301, no. 3, pp. H663–H671, 2011.

[131] P. Bahmani, E. Schellenberger, J. Klohs, J. Steinbrink, R. Cordell, M. Zille, J. Müller, D. Harhausen, L. Hofstra, C. Reutelingsperger, T. D. Farr, U. Dirnagl, and A. Wunder, "Visualization of cell death in mice with focal cerebral ischemia using fluorescent annexin A5, propidium iodide, and TUNEL staining.," *Journal of cerebral blood flow and metabolism : official journal of the International Society of Cerebral Blood Flow and Metabolism*, vol. 31, no. 5, pp. 1311–20, May 2011.

[132] C. Ruiz de Almodovar, D. Lambrechts, M. Mazzone, and P. Carmeliet, "Role and therapeutic potential of VEGF in the nervous system.," *Physiological reviews*, vol. 89, no. 2, pp. 607–48, Apr. 2009.

[133] P. Thored, J. Wood, A. Arvidsson, J. Cammenga, Z. Kokaia, and O. Lindvall, "Long-term neuroblast migration along blood vessels in an area with transient angiogenesis and increased vascularization after stroke," *Stroke*, vol. 38, no. 11, pp. 3032–3039, Nov. 2007.

[134] C. Geny, S. Naimisadaoui, R. Jeny, A. E. Belkadi, S. L. Juliano, and M. Peschanski, "Long-term delayed vascularization of human neural transplants to the rat-brain," *Journal of Neuroscience*, vol. 14, no. 12, pp. 7553–7562, 1994.

[135] H. J. Lee, K. S. Kim, I. H. Park, and S. U. Kim, "Human neural stem cells over-expressing VEGF provide neuroprotection, angiogenesis and functional recovery in mouse stroke model," *PLoS One*, vol. 2, no. 1, p. e156, 2007.

[136] A. Taguchi, T. Soma, H. Tanaka, T. Kanda, H. Nishimura, H. Yoshikawa, Y. Tsukamoto, H. Iso, Y. Fujimori, D. M. Stern, H. Naritomi, and T. Matsuyama, "Administration of CD34(+) cells after stroke enhances neurogenesis via angiogenesis in a mouse model," *Journal of Clinical Investigation*, vol. 114, no. 3, pp. 330–338, 2004.

[137] A. Moisan, N. Pannetier, E. Grillon, M.-J. Richard, F. Fraipont, C. Rémy, E. L. Barbier, and O. Detante, "Intracerebral injection of human mesenchymal stem cells impacts

cerebral microvasculature after experimental stroke: MRI study," *NMR in Biomedicine*, no. March, Apr. 2012.

5 Summary/Zusammenfassung

5.1 Summary

Molecular biology and stem cell research have had an immense impact on our understanding of neurological diseases, for which little or no therapeutic options exist today. Manipulation of the underlying disease-specific molecular and cellular events promises more efficient therapy. Angiogenesis, i.e. the regrowth of new vessels from an existing vascular network, has been identified as a key contributor for the progression of tumor and, more recently, for regeneration after stroke. Donation of stem cells has proved beneficial to treat cerebral lesions. However, before angiogenesis-targeted and stem cell therapies can safely be used in patients, underlying biological processes need to be better understood in animal models. Noninvasive imaging is essential in order to follow biological processes or stem cell fate in both space and time. We optimized steady state contrast enhanced magnetic resonance imaging (SSCE MRI) to monitor vascular changes in rodent models of tumor and stroke. A modification of mathematical modeling of MR signal from the vascular network allowed for the first time simultaneous measurements of relaxation time T_2 and SSCE MRI derived blood volume, vessel size, and vessel density. Limitations of SSCE MRI in tissues with high blood volume and non-cylindrically shaped vessels were explored. SSCE MRI detected angiogenesis and response to anti-angiogenic treatment in two rodent tumor models. In both tumor models, reduction of blood volume in small vessels and a shift towards larger vessels was observed upon treatment. After stroke, decreased vessel density and increased vessel size was found, which was most pronounced one week after the infarct. This is in agreement with two initial, recently published clinical studies. Overall, very little signs of angiogenesis were found. Furthermore, superparamagnetic iron oxide (SPIO) labels were used to study neural stem cells (NSCs) in vivo with MRI. SPIO labeling revealed a decrease in volume of intracerebral grafts over 4 months, assessed by T_2^* weighted MRI. Since SPIO labels are challenging to quantify and their MR contrast can easily be confounded, we explored the potential of in vivo ^{19}F MRI of ^{19}F labeled NSCs. Hardware was developed for in vitro and in vivo ^{19}F MRI. NSCs were labeled with little effect on cell function and in vivo detection limits were determined at ~10,000 cells within 1 h imaging time. A correction for the inhomogeneous magnetic field profile of surface coils was validated in vitro and applied for both sensitive and quantitative in vivo cell imaging. As external MRI labels do not provide information on NSC function we combined ^{19}F MRI with bioluminescence imaging (BLI). The BLI signal allowed quantification of viable cells whereas ^{19}F MRI provided graft location and density in 3D over 4 weeks both in the healthy and stroke brain. A massive decrease in number of viable cells was detected independent of the microenvironment. This indicates that functional recovery reported in many studies of NSC implantation after stroke, is rather due to release of factors by NSCs than direct tissue replacement. In light of these indirect effects, combination of the imaging methods developed in this dissertation with other functional and structural imaging methods is suggested in order to further elucidate interactions of NSCs with the vasculature.

5.2 Zusammenfassung

Die Molekularbiologie und Stammzellforschung haben unser Verständnis von neurologischen Erkrankungen, für die es momentan kaum Therapien gibt, immens verändert. Die Manipulation von erkrankungsspezifischen molekularen und zellulären Ereignissen stellt eine große Hoffnung für die effizientere Behandlung dar. Angiogenese, d.h. vaskuläres Neuwachstum ausgehend von existierenden Gefäßen, wurde als ein wichtiger Beitrag zum Tumorwachstum und zur Regeneration nach Schlaganfall erkannt. Stammzelltransplantationen haben sich als förderlich für die Behandlung zerebraler Läsionen erwiesen. Um angiogenese- oder stammzellbasierte Therapien sicher in Patienten benutzen zu können, müssen jedoch die zu Grunde liegenden biologischen Prozesse in Tiermodellen besser verstanden werden. Dabei spielt die nicht-invasive Bildgebung eine entscheidende Rolle, um diese Prozesse bzw. die Zellen sowohl räumlich als auch zeitlich zu verfolgen. Wir haben eine Magnet-Resonanz-Tomografie-Methode (SSCE-MRT) optimiert, um Änderungen der Gefäßstruktur in Maus- und Rattenmodellen des Tumors und des Schlaganfalls zu untersuchen. Das zu Grunde liegende mathematische Modell wurde erweitert, um erstmals die Relaxationszeit T_2, Blutvolumen, mittlere Gefäßdichte und Gefäßgröße simultan messen zu können. Die Grenzen des Modells in Gewebe mit hohem Blutvolumen und nicht-zylindrischen Gefäßen wurden erörtert. Angiogenese wurde in zwei unterschiedlichen Tumormodellen mit Hilfe der SSCE-MRT detektiert und die Wirkung anti-angiogenetischer Therapie untersucht. In beiden Tumormodellen induzierte die Therapie die Abnahme kleinerer Gefäße und Zunahme der Gefäßgröße. Nach Schlaganfall wurde eine Abnahme der Gefäßdichte und Zunahme der Gefäßgröße gefunden, die am stärksten eine Woche nach dem Infarkt ausgeprägt war. Diese Ergebnisse stimmen mit zwei erst kürzlich veröffentlichten ersten klinischen Studien überein. Insgesamt wurden nur geringe Anzeichen von Angiogenese nach Schlaganfall beobachtet. Darüber hinaus wurden Zellmarker basierend auf superparamagnetischen Eisenoxiden benutzt, um neurale Stammzellen (NSZ) in vivo mit MRT zu verfolgen. T_2^*-gewichtete MRT zeigte, dass das Volumen von intrazerebralen Eisenoxid-markierten NSZ-Transplantaten über 4 Monate abnahm. Da Zellmarker aus Eisenoxid kaum die Quantifizierung von NSZ zulassen und der Kontrast leicht verwechselt werden kann, wurde das Potenzial von fluorierten Zellmarkern, die mit ^{19}F-MRT detektiert werden können, untersucht. Hierzu wurde ein Aufbau für in vitro und in vivo ^{19}F-MRT entwickelt. NSZ konnten mit geringen Einschränkungen der Zellfunktion effizient mit einer ^{19}F-Verbindung markiert werden. In vivo wurde ein Detektionslimit von ca. 10.000 Zellen innerhalb 1 Std. Messzeit ermittelt. Eine Korrektur für das inhomogene Magnetfeld von Oberflächenspulen wurde in vitro validiert. Die Korrektur erlaubte es, NSZ sensitiv und quantitativ in vivo darstellen zu können. Da MRT-Zellmarker kaum Information über die Zellfunktion bereitstellen, wurde die ^{19}F-MRT mit Biolumineszenzbildgebung kombiniert. Diese diente der Quantifizierung der Zellvitalität. Die ^{19}F-MRT ermöglichte hingegen die Messung der Lage und der Zelldichte des Transplantats in 3D über einen Zeitraum von 4 Wochen – sowohl im gesunden als auch im Schlaganfallhirn. Ein massiver Rückgang der Zellvitalität wurde beobachtet unabhängig davon, in welche Umgebung die Zellen implantiert wurden. Dies ist ein Anhaltspunkt dafür, dass die funktionelle Erholung, die für Stammzellimplantation nach Schlaganfall gezeigt wurde, eher darauf zurückzuführen ist, dass die Zellen stimulierende Faktoren ins umliegende Gewebe absondern. Vor dem Hintergrund dieser indirekten Mechanismen wird vorgeschlagen, die Bildgebungsmethoden, die für diese Doktorarbeit entwickelt wurden, mit anderen funktionellen und strukturellen

Bildgebungsverfahren zu kombinieren, um speziell Interaktionen von NSZ und Gefäßbett zu untersuchen.

6 Appendix

Glossary and abbreviations

^{19}F	Most abundant, stable Fluorine isotope in nature. Nuclear spin ½.
^{1}H	Most abundant, stable Hydrogen isotope in nature. Nuclear spin ½.
Ang	Angiopoietin.
Angiogenesis	Regrowth of new vessels from an existing vascular network.
Apoptosis	A form of cell death in which a programmed sequence of events leads to the elimination of cells.
Arterial spin labeling	A MR image can be sensitized to the effect of inflowing blood spins if those spins are in a different magnetic state to that of the static tissue. Arterial spin labeling techniques use this idea by magnetically labeling blood flowing into the slices of interest.
Bevacizumab	Anti-angiogenic drug that blocks VEGF.
Bioluminescence	The production of light by living organisms.
BLI	Bioluminescence imaging
Bloch equations	Set of macroscopic differential equations that are used to calculate the nuclear magnetization $M = (M_x, M_y, M_z)$ as a function of time when relaxation times T_1 and T_2/ T_2^* are present.
Bloch-Torrey equation	Generalization of the Bloch equations, which includes added terms due to the transfer of magnetization by diffusion.
Blood flow	The rate at which a fluid passes through an organ or part, expressed as volume per unit of time.
BOLD effect	Blood oxygen level dependent effect. In MRI the changes in blood oxygenation level are visible. Oxyhaemoglobin (the principal haemoglobin in arterial blood) has no substantial magnetic properties, but deoxyhaemoglobin (present in the draining veins after the oxygen has been unloaded in the tissues) is strongly paramagnetic. It can thus serve as an intrinsic paramagnetic contrast agent in appropriately performed MRI.
C17.2	Widely used murine neural stem cell line. Transduced with an oncogene to increase proliferation.
Carcinoma	An invasive malignant tumor derived from epithelial tissue that tends to metastasize to other areas of the body.
Cascade	A chemical or physiological process that occurs in successive stages, each of which is dependent on the preceding one, and often producing a cumulative effect.

Caudal	Situated more toward the tail/posterior part of the animal
CD34	Gene expressed in a subset of cells of the human body including hematopoietic stem cells.
Cell tracker orange	Trade name for a fluorescent marker used in cell culture to label cells.
Cytoplasm	Part of a cell between cell membrane and nucleus.
Dentate gyrus	Brain structure within hippocampus.
Differential equation	Mathematical equation for an unknown function of one or several variables that relates the values of the function itself and its derivatives of various orders.
Diffusion coefficient	Mathematical quantity in Fick's law that describes diffusion.
Diffusivity	Ability of a substance to permit or undergo diffusion. Term sometimes used equivalently for diffusion coefficient.
Dynamic susceptibility contrast MRI	Method to measure blood flow and perfusion through acquisition of a fast series of MR images during passage of an intravascular, (super) paramagnetic MR contrast agent.
Endocytosis	A process of cellular ingestion by which the plasma membrane folds inward to bring substances into the cell.
Endosome	Intracellular vesicles formed from the cell membrane which are involved in intracellular transport.
Endothelial cell	Thin, flattened cell. A layer of them lines the inside surfaces of body cavities, blood vessels, and lymph vessels.
Epo	Erythropoietin.
Extracellular matrix	Any substance produced by cells and excreted to the extracellular space within the tissues, serving as a scaffolding to hold tissues together and helping to determine their characteristics.
Fluorescence	The emission of electromagnetic radiation, especially of visible light, stimulated in a substance by the absorption of incident radiation and persisting only as long as the stimulating radiation is continued.
Fractal geometry	Branch of mathematics concerned with irregular patterns made of parts that are in some way similar to the whole, e.g., twigs and tree branches, a property called self-similarity or self-symmetry.
Gadolinium^{3+}	Paramagnetic ion used in MR contrast agents. Efficiently shortens T_1 relaxation time of surrounding nuclei.
Genomics	The study of all the genes of a cell, or tissue, at the DNA (genotype), mRNA (transcriptome), or protein (proteome) levels.
GFAP	Glial fibrillary acidic protein. Intermediate filament protein

	that is expressed by numerous cell types of the central nervous system including astrocytes and ependymal cells.
Glia	The delicate web of connective tissue that surrounds and supports neurons.
Gradient echo	In MRI, a gradient echo is generated by using a pair of bipolar gradient pulses without the use of refocusing radiofrequency pulses. Signal in a gradient echo experiment decays exponentially with T_2^*.
Granular layer of the dentate gyrus	One of the three cell layers of the dentate gyrus. Consists of granule cells, i.e. very small neurons.
Growth factor	Any substance that promotes skeletal or somatic growth, usually a mineral, hormone, or vitamin.
Gyromagnetic ratio	Ratio of magnetic dipole moment and angular momentum.
HIF	Hypoxia inducible factor.
Hippocampus	Archicortical structures, which is multi-layered and folded/twisted resembling a hippocampus tail. Among manys other functions, it plays a central role in learning and memory.
hNSC	Human neural stem cell.
Hypoxia	Insufficient levels of oxygen in blood or tissue.
ICR	Outbred mouse strain. ICR stands for "imprinting control region."
In vitro	Made to occur outside the living organism in an artificial environment.
In vivo	In the living organism.
IPS cell	Induced pluripotent stem cell. A mature cell that is genetically modified to express certain factors. These factors drive the cell to a more potent and less differentiated state.
Ischemia	Insufficient supply of blood to an organ, usually due to a blocked artery.
Kupffer cell	Specialized cells in the liver that destroy bacteria, foreign proteins, and worn-out blood cells. Can take up MR contrast agents.
Larmor frequency	The Larmor precession frequency is the rate of precession of a spin packet under the influence of a magnetic field.
Luciferases	Group of oxidizing enzymes that acts with luciferines under production of light.
Luciferin	Group of substances that are oxydized by luciferases in an enzymatic reaction under production of light.
Metabolism	The sum of all the physical and chemical processes by which living organized substance is produced and maintained

	(anabolism), and also the transformation by which energy is made available for the uses of the organism (catabolism).
Middle cerebral artery occlusion	Most common ischemic stroke, for which the middle cerebral artery is blocked. Also refers to a certain type of surgery to model stroke in animals.
Molecular biology	The study of biology on a molecular level including the structure, function, and makeup of biologically important molecules such as DNA, RNA, and proteins.
Monocyte	A white blood cell that has a single nucleus and can ingest foreign material.
MRI	Magnetic resonance imaging.
MRS	Magnetic resonance spectroscopy
Neonate	Newly born infant.
Neurogenesis	Generation of new neurons.
Neuron	Any of the impulse-conducting cells that constitute the brain, spinal column, and nerves, consisting of a nucleated cell body with one or more dendrites and a single axon.
Neurosphere	A primitive neural tissue that arises when embryonic stem cells are grown in certain culture conditions.
NSC	Neural stem cell. Multipotent cell that has the capacity for self-renewal and can differentiate into cells of the central nervous system.
NuNu	Genetically modified mouse strain also referred to as nude mouse. Lacks an adaptive immune system and is therefore widely used in cell implantation studies to minimize graft rejection.
Olfactory bulb	Structure in the vertebrate forebrain involved in perception of odors.
Oncogene	A gene that causes the transformation of normal cells into cancerous tumor cells, especially a viral gene that transforms a host cell into a tumor cell.
Paracrine	Secretion released by cells into adjacent cells or tissue.
Paramagnetic	In an external magnetic field the induced magnetic field is parallel and proportional to the intensity of the magnetizing field.
Pax6	Gene involved in transcriptional regulation.
Perfusion	Passage of a fluid through the vessels of a specific organ.
PET	Positron emission tomography. Nuclear medicine tomographic imaging technique using positron emitters.
PFC	Perfluorocarbon. A hydrocarbon for which all hydrogen atoms

	have been replaced by fluorine atoms. Sometimes used as a shortcut for the specific perfluorocarbon Perfluoro-crown-ether.
PFPE	Perfluoropolyether. Linear perfluorocarbon molecule.
Phagocyte	A cell, such as a white blood cell, that engulfs and absorbs waste material, harmful microorganisms, or other foreign bodies in the bloodstream and tissues.
Phase coherence	The state in which two signals/spin packets maintain a fixed phase relationship with each other.
Phenotype	The observable physical or biochemical characteristics of an organism, as determined by both genetic makeup and environmental influences.
PlGF	Placenta growth factor.
Progenitor cell	Cell that, like a stem cell, has a tendency to differentiate into a specific type of cell, but is already more specific than a stem cell and is pushed to differentiate into its "target" cell. The most important difference between stem cells and progenitor cells is that stem cells can replicate indefinitely, whereas progenitor cells can divide only a limited number of times. Sometimes used equivalently to stem cell.
Proliferation	To grow or multiply by rapidly producing new tissue, parts, cells, or offspring.
PTK 787	Anti-angiogenic drug that inhibits protein tyrosine kinase and VEGF receptor kinase.
Relaxation rate	Inverse of relaxation time.
Reporter gene	Gene coding for an easily assayed protein, which is used to detect expression of the gene under different conditions.
Reticuloendothelial system	A group of cells having the ability to take up and sequester inert particles and vital dyes, including macrophages and macrophage precursors, specialized endothelial cells lining the sinusoids of the liver, spleen, and bone marrow, and reticular cells of lymphatic tissue (macrophages) and bone marrow (fibroblasts).
RF	Radiofrequency.
Rostral	Situated towards the oral/nasal region
Scaffold	A support, either natural or artificial, that maintains tissue contour.
Scratch assay	Widely used in vitro test for wound healing. A corridor is scratched through an adherent cell culture and the time is measured until the corridor is closed.
Sephadex	Trade name of a cross-linked dextran gel used for gel filtration columns.

Sinusoid (blood vessel)	A form of terminal blood channel consisting of a large, irregular anastomosing vessel having a lining of reticuloendothelium and found in the liver, heart, spleen, pancreas, and the adrenal, parathyroid, carotid, and hemolymph glands.
SNR	Signal-to-noise ratio, mean signal intensity divided by standard deviation of the noise
SPECT	Single photon emission computed tomography. Nuclear medicine tomographic imaging technique using gamma rays.
Spin echo	In MRI, a spin echo is generated by one or a series of refocusing radiofrequency pulses after the excitation pulse. Signal in a spin echo experiment decays exponentially with T_2.
SPIO	Superparamagnetic iron oxide
Subventricular zone	Paired brain structure situated throughout the lateral walls of the lateral ventricles.
Superparamagnetic	Form of magnetism, which appears in small ferromagnetic or ferrimagnetic nanoparticles. Without external magnetic field, the magnetization is on average zero, whereas magnetization is much higher than for paramagnetic substances inside an external magnetic field.
Susceptibility	Magnetic susceptibility is a proportionality constant that indicates the degree of magnetization of a material in response to an applied external magnetic field.
T_1	Empirical constant in Bloch equations. Longitudinal relaxation time.
T_2	Empirical constant in Bloch equations. Transverse relaxation time neglecting time-constant magnetic inhomogeneities.
T_2^*	Empirical constant in Bloch equations. Transverse relaxation including time-constant magnetic inhomogeneities
TGF	Transforming growth factor.
Transgene	A gene that is transferred from an organism of one species to an organism of another species by genetic engineering.
Trophic factor	Substance promoting cellular growth, differentiation, and survival.
Trypan blue	A dye that does not color intact cells and is therefore used in cell culture to measure cell viability through exclusion of stained cells.
Ultra short echo time sequence	MR pulse sequence with radial readout of k-space. Since each line acquired in k-space starts at k=0, very short echo times are possible <100 µs.
USPIO	Ultrasmall superparamagnetic iron oxide.
VEGF	Vascular endothelial growth factor.

White matter	The part of the brain that contains myelinated nerve fibers.

Eigener Anteil an den Veröffentlichungen

Paper I: Teilweise Durchführung der Experimente, teilweise Auswertung der Daten, teilweise Schreiben des Manuskripts.

Paper II: Entwicklung von Teilen des Versuchsaufbaus, Planung und Durchführung aller MRT Experimente, Auswertung aller MRT-Daten, Schreiben des Manuskripts und Gestaltung der Abbildungen.

Paper III: Entwicklung des Versuchsaufbaus, Planung und Durchführung aller MRT-Experimente, Auswertung der Daten, Schreiben des Manuskripts und Gestaltung der Abbildungen.

Paper IV: Entwicklung des MRT-Versuchsaufbaus, Planung und Durchführung aller MRT-Experimente, Auswertung der MRT-Daten, Schreiben des Manuskripts.

Paper V: Entwicklung des ^{19}F-MRT-Versuchsaufbaus, Planung und Durchführung aller MRT-Experimente, Auswertung der Daten, Schreiben des Manuskripts und Gestaltung aller Abbildungen.

Paper VI: Review, Schreiben des MR-methodischen Teils und des Ausblicks, Erstellen der Tabelle zum Vergleich der Sensitivitäten.

Danksagung

Ich möchte mich bei all den Menschen bedanken, die zu dieser Arbeit beigetragen haben.

Lieber Prof. Dr. Peter Reiter, vielen Dank, dass Sie seitens der Universität bereit waren, Ihre Rolle in diesem doch etwas komplizierten Betreuungskonstrukt äußerst gewissenhaft auszufüllen. Ich danke Ihnen für Ihr reges Interesse am Thema, für die exzellente Kommunikation bei der Bewältigung aller formaler Hürden und für unsere regelmäßigen Treffen.

Bei Mathias Hoehn möchte ich mich bedanken für die Überlassung und Betreuung dieses äußerst vielseitigen und spannenden Themas. Trotz anfänglicher Skepsis gegenüber der 19F-MRT habe ich von Dir die vollste Unterstützung erfahren. Besonders herausheben möchte ich das außergewöhnliche Maß an Verantwortung, dass Du mir bereits früh übertragen hast – sei es auf Konferenzen, in Gremien, bei meinen Auslandsaufenthalten oder bei der Betreuung von Studenten. Ich denke, dass dies nicht nur zu meiner fachlichen sondern in großem Maß auch zu meiner persönlichen Entwicklung in den letzten Jahren beigetragen hat.

I would also like to thank Prof. Dr. Michal Neeman and her group for the two great research visits to Israel. Michal, your way of scientific thinking is exceptional and truly inspiring to me. I would like to thank you and the whole group at the Weizmann Institute for the very warm welcome. Not only did this help to move forward with science but also I came back with many exceptional memories of wonderful people and of an exciting country. I would like to thank Reut Avni, Moriel Vandsburger, and Tal Raz for their support and the great times – see you soon!

Bei Stefan Wecker möchte ich mich besonders bedanken. Du hast mich mit dem MRT- und dem 19F-Virus infiziert und warst wie ein Mentor für mich – ohne Dich hätte diese Arbeit sicherlich so nicht stattgefunden.

Selbstverständlich sind große Teile dieser Arbeit im Team entstanden. Ich möchte mich deshalb bei der gesamten In-Vivo-NMR Gruppe für viele schöne Momente im Labor aber auch abseits der Arbeit bedanken. Ich möchte mich speziell bei Therése Kallur, Tracy Farr, und Markus Aswendt für die biologischen Teile meiner Arbeiten und für die vielen kleinen Crash-Kurse der „Biologie für Dummies“ bedanken. Tracy und Therése, ihr seid meine Vorbilder wenn es um gutes wissenschaftliches Arbeiten und außergewöhnliche Motivation geht. Danke an alle meine Doktoranden-Mitstreiter, insbesondere Joanna Adamczak, Daniel Kalthoff und Luam Mengler für gemeinsames Erleben und Verarbeiten von Freud und Leid. Mein Dank geht auch an Eberhart Pracht für die Einsetzung eines schwäbischen Traditionsvereins im gemeinsamen Büro und für die Verleihung eines informellen schwäbischen Doktortitels.

Ich danke meinen vielen Kooperationspartnern für die hervorragende Zusammenarbeit, insbesondere Thomas Viel, Roland Ullrich, Valerij Kiselev, Mathias Weigel und Mangala Srinivas.

Zu guter Letzt möchte ich mich bei meiner Familie für den wörtlich „bedingungs“-losen Rückhalt, für das Vertrauen und die Unterstützung bedanken. Außerdem danke ich Dir, Tina, für Dein Interesse, nicht nur an mir sondern auch an meiner Arbeit, für Dein Verständnis, Deine Unterstützung und die wunderbare gemeinsame Zeit.

Erklärung

Ich versichere, dass ich die von mir vorgelegte Dissertation selbständig angefertigt, die benutzten Quellen und Hilfsmittel vollständig angegeben und die Stellen der Arbeit – einschließlich Tabellen, Karten und Abbildungen –, die anderen Werken im Wortlaut oder dem Sinn nach entnommen sind, in jedem Einzelfall als Entlehnung kenntlich gemacht habe; dass diese Dissertation noch keiner anderen Fakultät oder Universität zur Prüfung vorgelegen hat; dass sie – abgesehen von unten angegebenen Teilpublikationen – noch nicht veröffentlicht worden ist sowie, dass ich eine solche Veröffentlichung vor Abschluss des Promotionsverfahrens nicht vornehmen werde. Die Bestimmungen der Promotionsordnung sind mir bekannt. Die von mir vorgelegte Dissertation ist von Prof. Dr. Peter Reiter seitens der Universität zu Köln und von Prof. Dr. Mathias Hoehn seitens des Max-Planck-Instituts für neurologische Forschung betreut worden.

Curriculum vitae

PERSÖNLICHE DATEN

Name	Philipp Gero Böhm-Sturm
Geburtsdatum	*19.05.1982
Geburtsort	Tübingen am Neckar
Familienstand	ledig
Staatsangehörigkeit	deutsch

SCHULE, STUDIUM, PROMOTION

seit 10/2009	Promotion im Bereich experimentelle Magnet Resonanz Tomographie, Max-Planck-Institut für neurologische Forschung in Köln, In-Vivo-NMR Labor, Prof. Dr. Mathias Hoehn Betreut von Prof. Dr. Reiter, Institut für Kernphysik, Universität zu Köln
10/2003-08/2009	Studium der Physik an der Universität zu Köln Abschluss als Diplom-Physiker Diplomarbeit im Bereich experimentelle Magnet Resonanz Tomographie, Max-Planck-Institut für neurologische Forschung in Köln, In-Vivo-NMR Labor, Prof. Dr. Mathias Hoehn Betreut von Prof. Dr. Reiter, Institut für Kernphysik, Universität zu Köln
08/1992-08/2002	Friedrich-List-Gymnasium Reutlingen Allgemeine Hochschulreife
10/1997-08/1998	Royal High School, Simi Valley, Kalifornien, USA
08/1988-08/1992	Mathäus-Beger-Schule Reutlingen